Statistical analysis of bacteria locomotion

Dissertation

zur Erlangung des Grades
des Doktors der Naturwissenschaften
der Naturwissenschaftlich-Technischen Fakultät
der Universität des Saarlandes

Von
Oliver KÖHN

Saarbrücken
2020

UNIVERSITÄT
DES
SAARLANDES

Tag des Kolloquiums:	18.09.2020
Dekan:	Prof. Dr. Guido Kickelbick
Berichterstatter:	Prof. Dr. Christian Wagner
	Prof. Dr. Frank Wilhelm-Mauch
Vorsitz:	Prof. Dr. Rolf Pelster
Akad. Mitarbeiter:	Dr. Herbert Wolf

UNIVERSITÄT DES SAARLANDES

Abstract

Naturwissenschaftlich-Technische Fakultät
Physics

Doktor der Naturwissenschaften

Statistical analysis of bacteria locomotion

by Oliver KÖHN

Many bacteria swim by employing their helical appendages, the flagella. We studied the statistics of this locomotion. To obtain more natural and especially long trajectories compared to two-dimensional tracking strategies, we developed a measurement-setup suitable to track bacteria in three-dimensions. The main component of this setup is an electrically focus tunable lens (ETL), able to adapt it's shape via an applied electrical current, resulting in a change of the current focal plane. This setup has no mechanical interaction with the sample to avoid adulteration of the measured trajectories. We found that for times smaller than the average running-time, the slope of the mean-squared displacement MSD of the tracked bacteria obeys a ballistic behavior, whereas for longer times we saw a clear diffusive behavior. To allow for a more efficient evaluation of the measured trajectories we introduce the Kalman-Filter. By using simulated trajectories we could show that the Kalman-Filter allows a more accurate determination of the rotational-diffusion coefficient than conventional methods. Furthermore we could show that evaluation of three-dimensional trajectories obeys slightly different statistics than the evaluation of projected two-dimensional trajectories due to missing information. Through the qualitative simulation of bacteria locomotion we could show that the flagella-positioning has a crucial impact on the tumbling dynamics.

UNIVERSITÄT DES SAARLANDES

Zusammenfassung

Naturwissenschaftlich-Technische Fakultät
Physics

Doktor der Naturwissenschaften

Statistische Auswertung der Bewegung von Bakterien

by Oliver KÖHN

Viele Bakterien schwimmen durch Nutzung ihrer spiralförmigen Anhänge, den Flagellen. Wir untersuchten die Statistik dieser Bewegung. Um natürlichere und vor allem längere Trajektorien - verglichen mit konventionellen zweidimensionalen Trackingmethoden - zu erhalten, haben wir einen Messaufbau zum dreidimensionalen tracken von Bakterien entwickelt. Die Hauptkomponente dieses Setups ist eine elektrische, fokusanpassbare Linse (ETL), welche ihre Form durch Anlegen eines elektrischen Stroms ändern kann, was zu einer Änderung der Fokusebene führt. Dieser Messaufbau hat keine mechanischen Wechselwirkungen mit der Probe, wodurch Verfälschungen der gemessenen Trajektorien verhindert werden. Wir konnten zeigen dass für Zeiten kleiner als die durchschnittliche *running*-Zeit (dt. *Renn*-Zeit), die mittlere quadratische Verschiebung (MSD) der getrackten Bakterien ein ballistisches Verhalten zeigt, wohingegen für längere Zeiten ein diffusives Verhalten vorliegt. Um eine effizientere Auswertung der gemessenen Trajektorien zu erlauben, führten wir den Kalman-Filter ein. Durch Nutzung simulierter Trajektorien konnten wir zeigen dass der Kalman-Filter eine genauere Bestimmung des Rotations-
Diffusionskoeffizienten - verglichen mit konventionellen Methoden - erlaubt. Weiterhin konnten wir zeigen, dass die Auswertung dreidimensionaler Trajektorien leicht andere Statistiken als die Auswertung zweidimensionaler Trajektorien liefert, was durch den Verlust an Information zu erklären ist. Durch die qualitative Simulation der Bewegung von Bakterien konnten wir zeigen dass die Position der Flagellen einen wesentlichen Einfluss auf die *Tumbling*-Dynamik (dt. *Taumel*-Dynamik) hat.

Acknowledgements

Zunächst möchte ich mich bei Prof. Dr. Christian Wagner bedanken, der mir nach meinem 18-monatigen Ausflug in die Wirtschaft die Möglichkeit bot, in seiner Arbeitsgruppe zu promovieren. Außerdem hat er mir durch seine guten Kontake in die ganze Welt ermöglicht, ein halbes Jahr in der Arbeitsgruppe von Prof. Michael David Graham in Wisconsin, USA, zu verbringen. Weiterhin danke ich Dr. Thomas John für die Betreuung in Form zahlreichen Diskussionen, insbesondere für seine interessanten Ideen und Ansätze. Furthermore I would like to thank Prof. Michael David Graham, who gave me the great opportunity to spend half a year in his group. I had a great time, especially because of his great group: Daniel, Xiaopo, RJ, Alec, Carlos, Ashwin, Eric, Kevin and all the people I met in the US.
Ein weiterer Dank geht an alle (ehemaligen) Mitglieder der AG Wagner, Alexander, Asena, Elke, Francois, Greta, Javad, Jorge, Karin, Matthias, Revaz, Rishab, Stefan, Stephan Zakaria und an alle die ich hier leider vergessen habe.
Ein ganz besonderer Dank geht auch an meine super WG, Vicky und Denise (Dennis!). Es war/ist super schön mit Euch und ich kann euch gar nicht genug für die zahlreichen unakademischen Dinge danken die ich durch Euch gelernt habe. Weiterhin möchte ich mich bei meiner *Schwester* Kim und Maya bedanken. Dafür dass ich Euch so lange kenne und es immer so schön ist Zeit mit Euch zu verbringen. Außerdem bin ich Maya und Christian sehr dankbar für das Korrekturlesen dieser Arbeit. Leonard bin ich für die stets interessanten, meist unphysikalischen Gespräche sehr dankbar. Diese waren stets eine willkommene Ablenkung. Andreas möchte ich dafür danken, dass er mir im Bachelorstudium durch die - für mich - nervigen Praktika geführt hat. Außerdem möchte ich mich bei meinem Tischtennisverein TTV Reisbach bedanken, der mir stets die Gelegenheit bot mich vom Promotionsstress abzulenken, insbesondere meiner Trainingspartnerin und guten Freundin Fabienne. Zu guter letzt möchte ich mich bei meiner Familie bedanken, insbesondere bei meinen Eltern Ralf und Barbara und Geschwistern Pascal und Jonas. Ich bin froh Euch zu haben.

To my family.

Contents

Chapter 1

Introduction

Despite bacteria have a size of only a few microns, their total biomass is larger than the one of plants and animals [84, 177]. Even the biomass of the planktonic microorganism *Cyanobacteria* exceeds the biomass of humans. Bacteria are found almost everywhere, e.g. in the air, water, skin, hair and even in the food we eat [125]. Many bacteria choose larger organisms as their habitat, which can be beneficial for both sides. For example several bacteria live in the gut functioning as a vital factor for digestion. Furthermore they help to prevent the outbreak of diseases, which are caused by other bacteria [146]. And there are many more bacterial cells in the human body. Their total amount is approximately ten times larger than the amount of human cells. Bacteria are also able to live in places where at a first glance no life was expected, e.g. at hot springs or salt lakes [84]. The most observed bacterium is *E. coli*, which acts as a standard model in bacteriology [94].
In general, bacteria are a type of biological cell. They are classified as *prokaryotic* microorganisms. The term *prokaryotic* refers to unicellular microorganisms without a membrane-bound nucleus or any other membrane-bound organelle [28]. The DNA and other genetic materials are contained as a single strand in their cytoplasm. Bacteria usually grow to a certain size until they reproduce through *binary fission*, a form of asexual reproduction [86, 176]. Many bacteria are able to maintain active swimming, with the two main goals to increase the efficiency in nutrient acquisition and the avoidance of toxic substances [12, 14]. The movement of bacteria is triggered by changes in the environment, such as changes in the light-intensity, changes in the temperature or changes in the chemical gradient. The corresponding technical terms are denoted as *phototaxis*, *thermotaxis* and *chemotaxis* [4, 12, 107, 141, 180].
To allow for active swimming, bacteria usually use their helical appendages, the flagella. Real (schematic) images of the bacterium *E. coli* during active swimming are represented in Fig. 1.1 (b) and (c) ((d) and (e)). Based on the placement of the flagella, one differentiates between *monotrichious* bacteria (only one flagellum), *lophotrichous* bacteria (multiple flagella attached to one spot), *amphitrichous* bacteria (two flagella on opposide ends) and *peritrichous* bacteria (multiple flagella at random locations). *Peritrichous* bacteria such as *E. coli* swim by rotating their helical flagella [12, 108]. The flagellum consists of three main parts, the helical filament, which is connected via the hook to a rotary motor, which generates the torque for flagella-rotation [105, 109]. The filament of the bacterium *E. coli* is only approximately $0.015\,\mu m$ in diameter and about $15\,\mu m$ in length [2]. It is generally very stiff, but can change

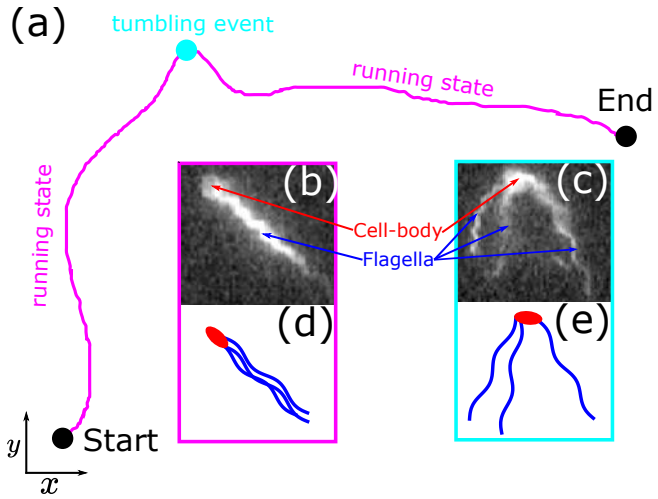

FIGURE 1.1: (a) Trajectory of the bacterium *E. coli* consisting of two running-states (magenta) separated by a tumbling-event (cyan). Real and schematic images of the bacterium during the running (tumbling) process are represented in (b) and (d) ((c) and (e)). (b) and (c) taken from [166].

between different helical shapes [43]. This behavior is denoted as polymorphism. The stiffness of the hook plays a key role to allow for bundling of the different flagella. This bundle allows for a more efficient swimming. In contrast to *prokaryotic* cells, there exist *eukaryotic* cells with a nucleus. Despite this basic difference, *eukaryotic* cells like *Chlamydomonas reinhardtii* or *spermatozoa* also use a flagellum to swim [78, 124], but their structure and functionality differs completely from the bacterial flagellum.
The swimming of bacteria consists of the running- (magenta) and tumbling-state (cyan), which can be seen in Fig. 1.1 (a). During the running-state, all flagella rotate counterclockwise (CCW, as seen from behind) in a bundle (Fig. 1.1 (b) and (d)). After several seconds in the running-state, one or more flagella start rotating clockwise (CW, as seen from behind). This reversing of the rotation-directory induces the tumbling-state, consisting of an unbundling of the flagella-bundle (Fig. 1.1 (c) and (e)), several polymorphic transformations of the CW-rotating flagella and a random reorientation of swimming-direction. This tumbling-state usually takes about $0.1\,s$ and all flagella start to rotate CCW again, building a new flagella bundle [43]. This behavior is known as the run-and-tumble strategy, leading to a random walk for bacteria locomotion. Polymorphic transformations can also be induced by the application of external forces or torques on the filament [43, 45, 66], changes in pH-value, salinity or temperature of the surrounding solvent [60, 76, 77], the addition of alcohol [67] or sugar [149]. It is interesting that bacteria that do not show any polymorphic transformations during swimming undergo polymorphic transformations by previous mentioned conditions [141]. It is possible to derive 12 different polymorphic forms of the flagellum based on the intrinsic structure, as first done by Asakura [5] and Calladine [31].
Due to their relatively small size, the swimming of bacteria occurs at the low

Reynolds-regime. Swimming at this scale, the micro-scale, was initially studied by Lighthill [100, 101] and Purcell [128]. The understanding of the helical filament [81, 172–174] is important to understand the bundling-process due to hydrodynamic interactions [70, 79, 81, 82, 131, 133].
The understanding of bacteria-swimming has inspired many applications in various disciplines, such as statistical physics [130], biology [169], robotics [27], social transport [62], soft matter [113], biomedicine [63, 64], transportation of colloids [9] and the pumping of fluids [44, 80].
This thesis is separated in six chapters. In this first chapter we give an overview about the research area of this thesis. In the second chapter we provide the required background to follow this thesis, consisting of experimental and mathematical facts about bacteria locomotion and the introduction of the Kalman-Filter. In the third chapter we describe an experimental setup consisting of an optical microscope extended with an electrically focus tunable lens (ETL). With this setup we are able to track particles in three dimensions. In chapter number four we apply the Kalman-Filter to extract trajectory-characteristics. The fifth chapter describes a method suitable for qualitative simulation of bacteria locomotion. The last chapter number six summarizes the results from this thesis and gives an outlook on possible future work.

Chapter 2

Background

2.1 Structure of the bacterium flagella

Several bacteria, such as *E. coli* or *B. subtilis*, are able to swim by using one or multiple appendages on their cell body, the flagella. This flagellum acts as a kind of propeller and generates thrust for the locomotion of the bacterium. A schematic representation of this flagellum for *E. coli* can be found in Fig. 2.1 (a), along with a reconstruction of the motor-core obtained from electron microscopy in Fig. 2.1 (b). The flagellum consists of several proteins, denoted as Flg, Fil and Mot in Fig. 2.1 (a). A detailed description of these proteins can be found in [17]. In this section we describe the three different parts of the flagellum

1. Filament: The largest component is known as the filament, shaped as a helix. The filament is a biopolymer constructed from a single protein called flagellin. We will discuss the filament in section 2.1.1

2. Motor: The filament is driven by the motor. It will be discussed in section 2.1.2

3. Hook: The hook connects the filament and the motor, transfering the torque generated by the motor to the filament. We will discuss the hook in section 2.1.3

2.1.1 The filament

Filaments can be distinguished in two main classes, based on their form: the plain form and the complex form. The complex form is brittle and forms a single, left-handed helix [141]. Compared to the plain filaments, their molecular structure is more complicated [165]. As we work with the bacterium *B. subtilis* in this thesis, we focus on the plain form, which arises in this kind of bacterium. In relation to their length of several μm, the filament is extremely thin with a diameter of only about $0.015\,\mu m$. Although the helical form of a filament is very stiff, the bacterium is able to switch between several helical forms, which is known as polymorphism. The change of a helical shape to another can be triggered by changes in pH value, salinity or the temperature of the surrounding fluid [60, 75, 76, 141, 150], or by the addition of alcohols or sugars [67, 149]. It also can be triggered by the application of external forces or torques to the filament [43, 45, 66, 108]. These different forms of the

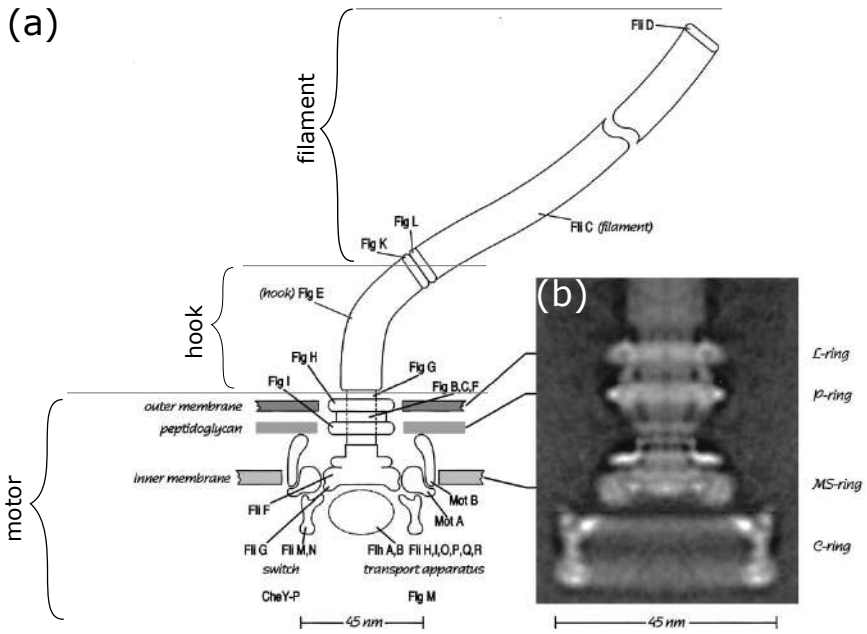

FIGURE 2.1: (a) Schematic representation of a bacterium-flagellum consisting of the motor, hook and filament consisting of different proteins Flg, Fli and Mot. (b) Image of the motor obtained by rotationally averaging images taken by electorn microscopy. Image taken from [17].

filament have been explained by Calladine 1975 [31, 33], who continued the work of Asakura [5]. The basic ideas of the work are summarized in Fig. 2.2 (a) and (b), resulting in 12 different helical forms first derivated by Calladine. These 12 helical forms are represented in Fig. 2.2 (c). In Fig. 2.2 (a) we see a schematic cross-section of a filament, consisting of 11 springs. These springs correspond to protofilaments. A filament consists of 11 protofilaments, and every protofilament consists of a stack of protein monomers, called flagellin [181, 182]. There are two different states of these monomers, called L- and R-state. Both states differ in length by approximately 0.8 Å [75, 138]. A single protofilament can only consist of a single type of monomer, therefore only two different types of protofilaments with two different lengths can be found in a filament. This observation is known as Calladine's rule [51]. Furthermore it was observed that protofilaments are mixed randomly, but they cluster to minimize elastic strain within the filament. Due to the different lengths of the protofilament, the filament starts to bend, resulting in a certain curvature as represented in Fig. 2.2 (a). In Fig. 2.2 (b) we see a *rolled-up* filament, which would result in the cylindric shape represented from fig. 2.2 (a) if we connected the left and the right side. To allow the creation of a chemical bond between the proteins, the protofilaments are slightly tilted against the centerline of the filament, represented through the angle α_t.

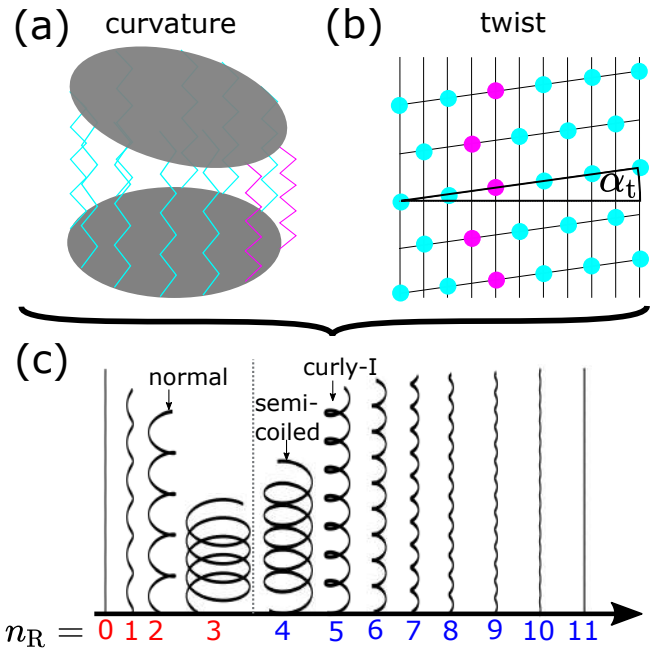

FIGURE 2.2: (a) Representation of a flagella-segment consisting of 11 protofilaments, where 9 are in the L- (cyan) and 2 are in the R-state (magenta). The protofilaments cluster and due to their different lengths the flagellum has a certain curvature. (b) To allow the creation of chemical bonds between the proteins, the protofilaments are slightly tilted against the centerline of the filament, represented through the angle α_t, resulting in a twist of the filament. (c) Based on curvature and twist, Calladine calculated 12 different shapes of the flagellum, where 4 ($n_R < 4$) are left handed, and 8 ($n_R \geq 4$) are right-handed.

This tilt results in a twist of the filament. A combination of the curvature and the twist of the filament results in its typical helical shape. Calladine derived all 12 possible shapes of the filament based on the properties of the protopolymers [31, 44], which can be quantified by the curvature and the twist

$$\kappa_n = \kappa_0 \sin\left(\frac{\pi n_R}{11}\right), \quad \tau_n = \tau_L + \frac{(\tau_R - \tau_L)\, n_R}{11}, \tag{2.1}$$

where n_R is the number of protofilaments in the R-state. The parameters κ_0, τ_L and τ_R where experimentally determined [45] to

$$\kappa_0 \approx 2.4\frac{1}{\mu m}, \quad \tau_L \approx -5.2\frac{1}{\mu m}, \quad \tau_R \approx 11.8\frac{1}{\mu m} \tag{2.2}$$

The obtained polymorphic forms are represented in Fig. 2.2 (c), where the shapes for $n_R < 4$ are left-handed, and the remaining shapes are right-handed. Most of these polymorphic forms have been observed experimentally [61, 181]. Several extensions based on Calledine's model have been developed [51, 61, 156–158].

2.1.2 The motor

The motor generates the torque to rotate the filament. For bacteria like *E. coli* the motor works at constant torque but can switch the direction of rotation. This change in the rotation from counterclockwise (CCW) to clockwise (CW) induces tumbling-events [155]. The torque for *E. Coli* is typically in the range from 1 $pN\,\mu m$ up to 4.6 $pn\,\mu m$ [17, 155]. There are other bacteria like *Rhizobium lupini* or *Rhodobacter sphaeroides* [3] which rather than changing from CCW to CW adapt the rotation velocity.
It is interesting to mention that the rotary motor of the bacterial flagellum does not use directly ATP as energy-source [49], in contrast to several other biological motors like myosine and kinesin. It rather uses protons [88, 112] or other ions [155] moving down an electro chemical gradient across the cell membrane. There exist several theoretical models suitable to describe these motors [93, 168]. Especially for the qualitative simulation of bacteria locomotion it is an important observation that the motor runs at constant torque over a broad range of angular velocities [17].

2.1.3 The hook

The hook is used to transfer the torque generated by the motor to the filament. The length of this hook is approximately 0.05 μm for *E. coli* or *S. typhimurium* and up to approximately 0.1, μm for *R. sphaeroides* and therefore much shorter than the filament [73, 85, 137, 151]. It has been shown that the flexibility of the hook is important to allow for a stable running state. In case of uni-flaggelated bacteria, a relatively stiff hook is required to avoid buckling, whereas for multiple flagella the hook needs to be more flexible in order to allow bundling of the flagella [119].

2.1.4 Swimming of bacteria

The first quantitative evaluation of *E. coli* locomotion was performed in 1972 by Howard C. Berg and Douglas A. Brown [19]. They used an optical microscope and followed the movement of single cells. One example of an observed trajectory from the original publication [19] is represented in Fig. 2.3 (a). We can qualitatively see that the trajectory consists of several straight paths, separated by a big change in the direction. The straight paths correspond to the running-state of the bacterium, whereas the events inducing big changes in the swimming direction are denoted as tumbling-events. In Fig. 2.3 (b) we see a quantitative evaluation of the swimming speed v for three different trajectories from [19]. We can clearly see large drops in the speed v, where tumbling-events are marked via black dots over the graphs. In this first publication [19], for the first time the run- and tumbling motion of bacteria was observed. Until 1973, it was expected that bacteria swim by using their flagella which perform helical waves [106]. In the year 1973, Howard C. Berg and Robert A. Anderson investigated the propulsion mechanics of bacteria and could demonstrate that rather than applying helical waves, that

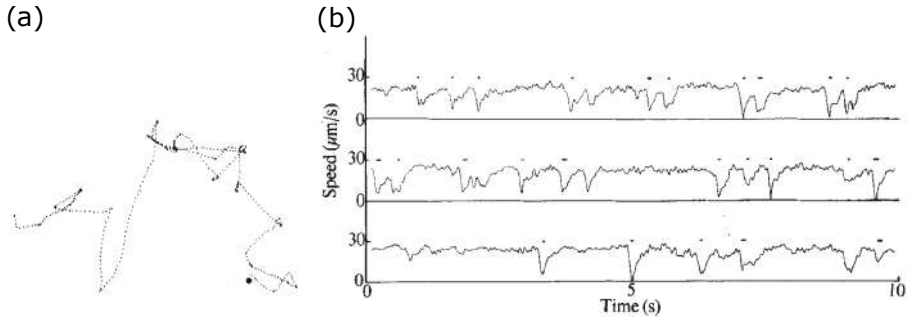

FIGURE 2.3: Original results presented in [19] for the bacterium *E. coli*: Measured trajectory (a) and speed v for three different trajectories (b).

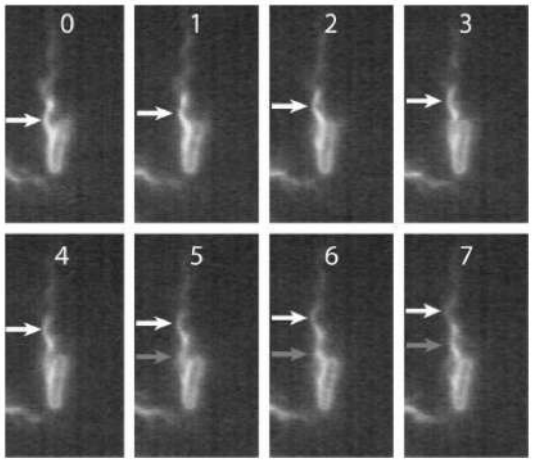

FIGURE 2.4: Images of the bacterium *E. coli* taken from [43]. The wavecrest of the flagella-bundle marked in image 5 has moved a whole wavelength in image 5, making it possible to denote the bundle-frequency to $\omega \approx 100\,Hz$.

a model where each filament rotates is favored [18]. This suggestion was experimentally proven by Silverman and Simon [154], who tethered bacteria to microscope slides and observed rotation of the bacteria-bodies. In a next step, Lahrsen et al. [89] used the same technique as Silverman and Simon [154] to show that the rotation-direction of the flagella can be manipulated by the environment. The addition of attractants causes counterclockwise-rotation (CCW) - the running-state - whereas the addition of repellents causes clockwise (CW) - the tumbling-state - rotations. From this publication [89] in the year 1974 it took approximately 30 years until Darnton et. al. were able to use a microscope to observe flagella during the running- and tumbling state, which allowed to observe the shape of the flagella as well as the angular velocity ω [43]. An example from the publication [43] showing a full rotation of a flagella-bundle is presented in Fig. 2.4. From these experiments, the rotation rate of flagella-bundles could be determined to $\omega \approx 100\,Hz$. Furthermore they were able to give a more detailed description of tumbling-events based on their measurements. The original image form the publication [43] summarizing the most frequent tumbling-process consisting of the

Polymorphic form	Pitch (P)	Radius (R)	Curvature (κ_0)	Twist (τ_o)
Normal (left-handed)	2.1611 μm	0.2161 μm	$\kappa_0^n = 1.3097$	$\tau_0^n = -2.0845$
Semicoiled (right-handed)	1.0766 μm	0.3810 μm	$\kappa_0^n = 2.1831$	$\tau_0^n = 0.9818$
Curly-I (right handed)	1.3199 μm	0.1975 μm	$\kappa_0^n = 2.3757$	$\tau_0^n = 2.5268$

TABLE 2.1: Experimentally values for the pitch P and radius R of the flagellum and the corresponding curvature κ_0 and twist values τ_o from [95].

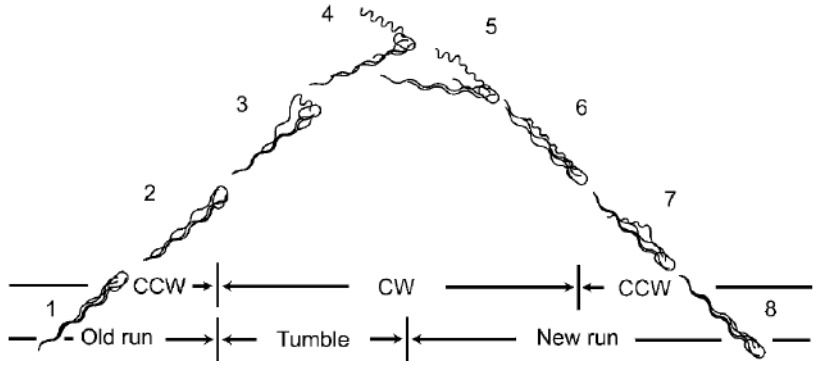

FIGURE 2.5: Schematically representation of the most common tumbling process consisting of the *normal-*, *semicoiled-* and *curly-I*-state of the flagella. Image taken from [43].

polymorphic-forms *normal-*, *semicoiled-* and *curly-I-* represented in Fig. 2.5. The corresponding parameters for the *normal-*, *semicoiled-* and *curly-I*-state of the flagella are summarized in table 2.1. Initially the bacterium is in the running state (1), where the bundle rotates CCW. At a certain time, one or more flagella start to rotate CW (2), initializing the unbundling-process, followed by a polymorphic-transformation of the unbundling flagellum to the semicoiled state (3). After a certain time, the polymorphic transformation is finished and the bacterium starts to reorientate (4). Now the bacterium moves in a new direction, with a bundle rotating CCW and one or more flagella rotating CW in the semicoiled state (5). After a certain time, the non-bundle flagella have transformed form the semicoiled to the curly-I state, which is loosely connected to the bundle. After a motor reversal from CW to CCW (7), the curly-I form changes to the normal form again and all flagella successfully bundle together again (8).

2.2 Properties of microswimmers

2.2.1 Dynamics at low Reynolds numbers

The main equation to describe dynamics of an incompressible Newtonian fluid is the Navier-Stokes equation:

$$\frac{\partial \boldsymbol{u}}{\partial t} + (\boldsymbol{u}\nabla)\,\boldsymbol{u} = -\frac{1}{\rho}\nabla p + \nu\nabla^2\boldsymbol{u} + \boldsymbol{g}. \tag{2.3}$$

where ρ is the density, p is the pressure, ν is the kinematic viscosity, $\boldsymbol{u}$ is the flow-velocity and $\boldsymbol{g}$ is the body acceleration field. The Navier-Stokes equation 2.3 can be understood as Newton's second law for small fluid-elements. Assuming mass conservation we obtain another equation

$$\nabla\boldsymbol{u} = 0. \tag{2.4}$$

Introducing a characteristic length-scale L, characteristic velocity-scale U, characteristic time-scale $T = \frac{L}{U}$ we can perform the following substitutions

$$\boldsymbol{r} = \tilde{\boldsymbol{r}}L,\ \ \nabla = \frac{\tilde{\nabla}}{L},\ \ \boldsymbol{u} = \tilde{\boldsymbol{u}}U \text{ and } t = \tilde{t}T, \tag{2.5}$$

transforming the Navier-Stokes equation to

$$\mathrm{Re}\frac{\partial \boldsymbol{u}}{\partial t} = -\mathrm{Re}\tilde{\boldsymbol{u}}\tilde{\nabla}\tilde{\boldsymbol{u}} - \tilde{\nabla}\tilde{p} + \nabla^2\boldsymbol{u} + \frac{\mathrm{Re}}{\boldsymbol{Fr}^2}\tilde{\boldsymbol{f}}. \tag{2.6}$$

Here the quantity Fr is the Froude-number defined as

$$\mathrm{Fr} \equiv \sqrt{\frac{\text{inertial forces}}{\text{gravitational forces}}} = \sqrt{\frac{\rho\frac{U^2}{L}}{\rho g}} = \frac{U}{\sqrt{gL}}. \tag{2.7}$$

The second quantity Re , known as the Reynolds number, defines the flow regime [116]. In the absence of external forces $\boldsymbol{f}$, the Reynolds-number Re is the ratio of the inertial term on the left-hand side of the Navier-Stokes equation 2.3 to the viscous force per unit volume on the right hand side of the Navier-Stokes equation 2.3 [116]:

$$\mathrm{Re} \equiv \frac{\text{inertial force}}{\text{viscous force}} = \frac{|\rho\boldsymbol{u}\nabla\boldsymbol{u}|\,|}{|\nu\nabla^2\boldsymbol{u}|} \propto \frac{\rho UL}{\nu}. \tag{2.8}$$

The Reynolds-number of a typical bacterium such as *E. coli* with a body length of approximately $L \approx 1\,\mu m$ swimming with a velocity $\boldsymbol{U} \approx 10\,\frac{mum}{s}$ in water ($\rho \approx 10^3\,\frac{kg}{m^3}$ and $\nu \approx 10^{-3}\,\mathrm{Pa}s$) can be calculated to $\mathrm{Re} \approx 10^{-5}$. In this case we can expect $\mathrm{Re} \ll 1$ and the left side of the Navier-Stokes equation 2.3 vanishes, simplifying the Navier-Stokes equation to

$$-\nabla p + \nu\nabla^2\boldsymbol{u} = 0. \tag{2.9}$$

Above equation 2.9 is denoted as *Stokes*-equation. For bacteria we can always expect to be in the regime Re $\ll 1$, enabling us to describe bacteria dynamics with the *Stokes*-equation 2.9, which is easier to solve than the original Navier-Stokes equation 2.3. It is important to mention that the Stokes-equation 2.9 is time-independent. The consequence is the fact that bacteria cannot use appendages moving with time reversal symmetry to generate thrust [128]. This phenomenon is known as the *scallop*-theorem [128] and was first discussed by Purcell. In the next section 2.2.2 we will describe how bacteria can generate thrust in the low Reynolds-number regime Re $\ll 1$.

2.2.2 Flagella propulsion for low Reynolds-numbers

We have seen in above section 2.2.1, that in the low Reynolds-number regime Re $\ll 1$ it is impossible to generate thrust for bacteria by using appendages moving with time reversal symmetry. This effect occurs as a result of the time-independence of the Stokes-equation 2.9. In general, it is impossible to generate thrust applying deformations with only one degree of freedom, as the net displacement will always sum up to zero. Therefore it is required for bacteria to employ deformations with $n_B > 1$ degrees of freedom. In a first step we discuss Purcells general idea of bacteria swimming in the low Reynolds-numbers regime [128]. Afterwards we will discuss the restrictive force theory (RFT), describing the propulsion based on drag. Finally Slender body Theory (SBT) will be discussed.

Propulsion of microswimmers

A bacterium swims by rotating one or more filaments, which are connected to the cell-body. Following Purcell [128], a bundle of flagella in the running-state can be approximated by a single flagellum. Due to the linearity of Stokes-equation 2.9, the thrust force $\boldsymbol{F}_{\text{fl}}$ and torque $\boldsymbol{T}_{\text{fl}}$ can be written as

$$-\boldsymbol{F}_{\text{fl}} = A\boldsymbol{v} - B\boldsymbol{\omega} \quad \text{and} \tag{2.10}$$

$$\boldsymbol{T}_{\text{fl}} = -B\boldsymbol{v} + D\boldsymbol{\omega}, \tag{2.11}$$

where $\boldsymbol{v}$ is the translational and $\boldsymbol{\omega}$ the angular velocity of the filament, as represented in Fig. 2.6 (a). The constant A and D represents the translational and rotational drag coefficient. To understand the meaning of constant B, let us assume a rotating helix. This rotating helix would start a translational motion, therefore a certain force is necessary to avoid this translational motion, quantified as $-B\boldsymbol{\omega}$ in equation 2.10. On the other hand, a helix moving through a fluid would start rotating, therefore a certain torque is necessary to avoid a rotation, quantified as $-B\boldsymbol{v}$ in equation 2.10 [91, 99]. Here the angular velocity $\boldsymbol{\omega}$ and the torque $\boldsymbol{T}_{\text{fl}}$ obey the right-hand rule for a left-handed helix, and the handness of the helix defines the sign in front of the coupling constant B [98, 128]. We can summarize both equations 2.10 and 2.11 into a

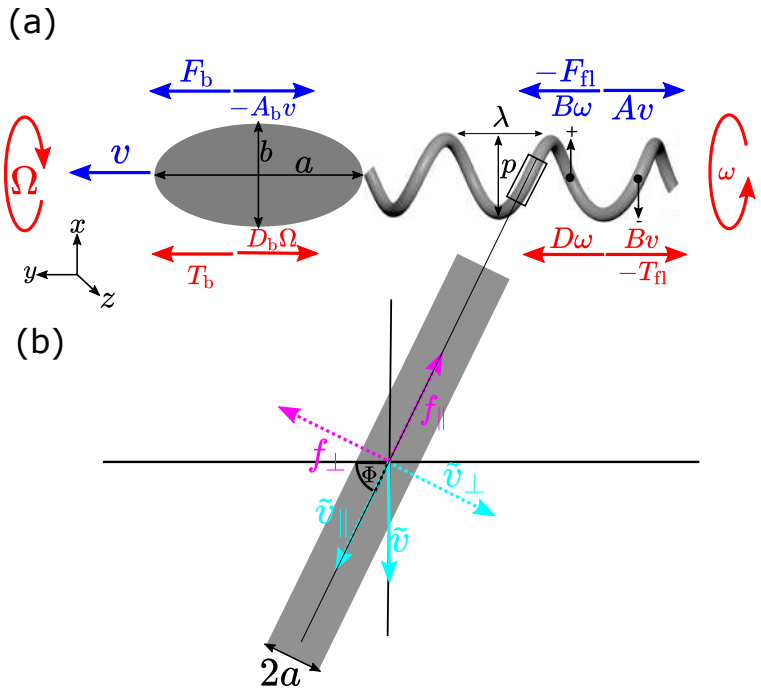

FIGURE 2.6: (a) Schematically representation of a bacterium consisting of the cell-body and the flagellum. Due to the rotation of the flagellum with angular frequency ω, the bacterium moves with a velocity $\boldsymbol{v}$. The total force $-\boldsymbol{F}_{\mathrm{fl}}$ (torque $\boldsymbol{T}_{\mathrm{fl}}$) on the flagellum consists of the propulsion-force $-B\boldsymbol{\omega}$ (torque $-B\boldsymbol{v}$) and the drag-force $A\boldsymbol{v}$ (torque $D\boldsymbol{\omega}$). (b) Zoom into a segment of the flagellum from (a). The drag-force $\tilde{\boldsymbol{f}}$ can be splitted into a component parallel $\tilde{\boldsymbol{f}}_\parallel$ and perpendicular $\tilde{\boldsymbol{f}}_\perp$ to the velocity $\tilde{\boldsymbol{v}}$ of the segment.

single matrix equation

$$\begin{pmatrix} -\boldsymbol{F}_{\mathrm{fl}} \\ \boldsymbol{T}_{\mathrm{fl}} \end{pmatrix} = \boldsymbol{M} \begin{pmatrix} \boldsymbol{v} \\ \boldsymbol{\omega} \end{pmatrix}, \quad \boldsymbol{M} = \begin{pmatrix} A & -A \\ -B & D \end{pmatrix}, \tag{2.12}$$

where the matrix $\boldsymbol{M}$ is known as propulsion or resistance matrix [128]. The propulsion matrix $\boldsymbol{M}$ depends on the pitch λ, radius R and thickness a of the helix. It can be determined by either using RFT or SLB, where the latter included interactions between individual segments of the helix. As the cell-body is approximated as an elongated ellipsoid, it cannot generate thrust due to its symmetry. The drag force and torque experienced by the cell-body can be described similar to the helical-case as

$$\boldsymbol{F}_{\mathrm{b}} = -A_{\mathrm{b}}\boldsymbol{v}, \tag{2.13}$$
$$\boldsymbol{T}_{\mathrm{b}} = -D_{\mathrm{b}}\boldsymbol{\Omega}, \tag{2.14}$$

where $A_0 = \frac{4\pi\eta b}{\ln\left(\frac{2b}{a}\right)-0.5}$ and $D_0 = \frac{16\pi a^2 b}{3}$ are the translational and rotational drag coefficients [16], a and b are the minor and major axis of the ellipsoid and η represents the viscosity of the medium. We expect the ellipsoid to

move along and rotate around the major axis. As the cell-body typically experiences larger drag as the flagella-bundle, the flagella-bundle has to rotate faster than the cell-body

$$\omega > \Omega, \tag{2.15}$$

to satisfy the torque-free condition. Similar to equation 2.16, we can summarize equations 2.13 and 2.14 into a single matrix equation

$$\begin{pmatrix} \boldsymbol{F}_\mathrm{b} \\ \boldsymbol{T}_\mathrm{b} \end{pmatrix} = \boldsymbol{M}_\mathrm{b} \begin{pmatrix} \boldsymbol{v} \\ \boldsymbol{\Omega} \end{pmatrix}, \quad \boldsymbol{M}_\mathrm{b} = \begin{pmatrix} -A_\mathrm{b} & 0 \\ 0 & -D_\mathrm{b} \end{pmatrix}. \tag{2.16}$$

Due to the fact that the cell body is not self propelled, we see that Matrix $\boldsymbol{M}_\mathrm{b}$, corresponding to the cell-body, has vanishing off diagonal elements, if we compare both matrices $\boldsymbol{M}$ and $\boldsymbol{M}_\mathrm{b}$. If we neglect external forces, the cell-body of a bacterium moving with constant velocity $\boldsymbol{v}$ experiences two forces $-\boldsymbol{F}_\mathrm{fl}$ and $\boldsymbol{F}_\mathrm{b}$. As the velocity $\boldsymbol{v}$ is assumed to be constant, these forces have to be equal

$$-\boldsymbol{F}_\mathrm{fl} = \boldsymbol{F}_\mathrm{b}, \tag{2.17}$$

resulting in

$$(A + A_\mathrm{b})\,\boldsymbol{v} = B\boldsymbol{\omega}. \tag{2.18}$$

Furthermore the torque must be balanced by the drag on the rotating cell-body

$$\boldsymbol{T}_{\hat{b}} = -\boldsymbol{T}_\mathrm{fl}, \tag{2.19}$$

resulting in

$$-B\boldsymbol{v} + D\boldsymbol{\omega} = D_\mathrm{b}\Omega. \tag{2.20}$$

By fixing a bacterium in an optical trap and vary the flow conditions, it is possible to extract the drag coefficients by applying equations 2.18 and 2.20 [35, 37, 43].

Resistive force theory

To understand how a rotating helix can generate thrust in the low Reynolds-number regime $\mathrm{Re} \ll 1$, we will follow the ideas from Gray and Hancock, who modeled the swimming of spermatozoa via a wave traveling through the viscous fluid [54, 55]. In the following we expect a left-handed, counter-clockwise (CCW) rotating helix of frequency $\boldsymbol{\omega}$ characterized by length L, radius R and pitch λ. In Fig. 2.6 (b) we zoom into a segment of the helix and introduce the pitch angle $\Phi = \mathrm{atan}\left(\frac{2\pi R}{\lambda}\right)$. This segment can be approximated as a cylinder of length l and radius a. For a moving helix, each segment moves with a certain velocity $\tilde{v}$ as illustrated in Fig. 2.6 (b). We can split the velocity $\tilde{v}$ into a component $\tilde{v}_\parallel$ parallel and a component $\tilde{v}_\perp$ perpendicular to the cylindric element. As we are in the Stokes regime, these

velocities $\tilde{v}_{\parallel}$ and $\tilde{v}_{\perp}$ result in proportional drag-forces

$$\tilde{f}_{\parallel} = -\zeta_{\parallel}\tilde{v}_{\parallel} = -\zeta_{\parallel}\tilde{v}\cos(\Phi), \tag{2.21}$$

$$\tilde{f}_{\perp} = -\zeta_{\perp}\tilde{v}\sin(\Phi), \tag{2.22}$$

where $\zeta_{\parallel}$ and $\zeta_{\perp}$ represent the drag coefficients of a cylinder pulled parallel or perpendicular to its main axis through the fluid. The component of the drag force in the y-direction can be obtained via

$$f_{\mathrm{p}} = \left(\zeta_{\parallel} - \zeta_{\perp}\right)\tilde{v}\sin(\Phi)\cos(\Phi)\,\boldsymbol{e}_y. \tag{2.23}$$

Here f_{p} describes the forward thrust force generated by each cylindric element of the helix in y-direction. The total propulsion force F_{p} can be obtained via

$$F_{\mathrm{p}} = \sum_{c} f_{\mathrm{p}}, \tag{2.24}$$

where c in equation 2.24 describes the summation over all propulsion forces f_{p} generated by the cylindric elements [36]. In general, there are two different sets of parameters $\zeta_{\parallel}$ and $\zeta_{\perp}$ used in literature [134], where for both of these sets its expected that the effect of small cylindric elements is just locally important. The first set of parameters $\zeta_{\parallel}$ and $\zeta_{\perp}$ has been calculated by Gray and Hancock in 1955 [54]

$$\zeta_{\parallel} = \frac{2\pi\eta}{\ln\left(\frac{2D}{r}\right) - 0.5}, \quad \zeta_{\perp} = \frac{4\pi\eta}{\ln\left(\frac{2D}{r}\right) + 0.5}. \tag{2.25}$$

A second, more accurate set was calculated by Lighthill in 1975 [101]

$$\zeta_{\parallel} = \frac{2\pi\eta}{\ln\left(\frac{0.18D}{r\cos(\Phi)}\right)}, \quad \zeta_{\perp} = \frac{2\pi\eta}{\ln\left(\frac{0.18D}{r\cos(\Phi)}\right) + 0.5}. \tag{2.26}$$

If we have a look at equation 2.23 it is important to realize that in case of an isotropic element with $\zeta_{\parallel} = \zeta_{\perp}$ it is impossible to generate thrust. However, in several experiments it was discovered that typically $\zeta_{\parallel} < \zeta_{\perp}$, Especially for very thin cylinders where approximately $\frac{\zeta_{\perp}}{\zeta_{\parallel}} = 2$ [55, 58]. Another important role plays the velocity $\tilde{v}$ and the pitch angle Φ of the cylindric elements from equation 2.23. If we assume the pitch angle Φ to be constant and the orientation of the velocity $\tilde{v}$ to change periodically, also the thrust force would change periodically. Therefore, for an effective propulsion, it is required that both the velocity $\tilde{v}$ and the pitch angle Φ of the cylindric elements change over time. In case of the helix, every change $\tilde{v} \to -\tilde{v}$ is connected to a change $\Phi \to -\Phi$, resulting in a constant direction of the propulsive force $\boldsymbol{F}_{\mathrm{p}}$.
Based on the local drag coefficients $\zeta_{\parallel}$ and $\zeta_{\perp}$ it is possible to calculate the elements of the propulsion matrix $\boldsymbol{M}$ by integrating the cylindric segments over the whole helix. These calculations have been performed in [163], resulting

in

$$A = \zeta_\perp L\left(1-\beta^2\right)\left(1+\gamma\frac{\beta^2}{1-\beta^2}\right), \quad B = \zeta_\perp\left(\frac{\lambda}{2\pi}\right)\left(1-\beta^2\right)(1-\gamma), \tag{2.27}$$

$$D = \zeta_\perp\left(\frac{\lambda}{2\pi}\right)^2 L\left(1-\beta^2\right)\left(1+\gamma\frac{\beta^2-1}{\beta^2}\right), \quad \beta = \cos(\Phi)^2, \quad \gamma = \frac{\zeta_\parallel}{\zeta_\perp} < 1. \tag{2.28}$$

From equation 2.27-2.28 we see that in case of $\gamma = 1$ we obtain $B = 0$, resulting in no swimming according to equation 2.18. Also in the case of a straight helix ($\Phi = 0$ or $\Phi = \frac{\pi}{2}$) no swimming is possible.

Slender body theory

To reconcile the shortcomings of RFT, the omission of hydrodynamic forces between different flagella segments and their cumulative effect on motion [72], the Slender body theory (SBT) was introduced. Instead of approximating the flagella by a chain of cylindric segments, Lighthill simulated the flagella as a distribution of point-forces, known as stokeslets, along the centerline of the flagella [100]. The impact of these Stokeslets decays as $\frac{1}{r}$ and therefore induce long-range effects that must be considered. Numerically this can lead to singularities, wherefore Cortez introduced a method of regularized stokeslets on the outer flagella surface to approximate forces and avoid singularities [41]. A comparison of the calculated drag coefficients of Gray and Hancock (RFT), Lighthill (RFT), Lighthill (SBT) and Cortez, concluding that the SBT applied by Lighthill and the Cortez model are in general more accurate than RFT [134].

2.2.3 Langevin equation

The motion of a small colloidal particle (*Brownian*-particle) in a bath of much smaller fluid particles, is denoted as Brownian motion [48]. The size of the colloidal particle can range from several nanometers up to micrometers. As there are several collisions of the colloidal particle with the fluid particles, this interaction can be modeled as a friction. When we denote the velocity of the colloidal particle as v, the friction force is given as $-\lambda v$, where $\lambda > 0$ is the friction coefficient. The friction $-\lambda v$ is known as Stokes friction. The friction coefficient for a sphere of radius r can be calculated via $\lambda_{\text{sphere}} = 6\pi\eta r$. To deal with random collisions with the surrounding particles, one can introduce a second, stochastic force $\sqrt{(2q)}\boldsymbol{\eta}(t)$. If we do not expect any additional forces on the Brownian particle, we can write Newton's equations

of motion for the position $\boldsymbol{r}(t)$ of the Brownian particle as

$$\frac{\mathrm{d}}{\mathrm{d}t}\boldsymbol{r}(t) = \boldsymbol{v}, \tag{2.29}$$

$$m\frac{\mathrm{d}}{\mathrm{d}t}\boldsymbol{v}(t) = -\lambda\boldsymbol{v} + \sqrt{(2q)}\boldsymbol{\eta}(t). \tag{2.30}$$

The first equation 2.29 simply defines the velocity $\boldsymbol{v}(t)$ of the Brownian particle. The second equation 2.30 is denoted as Langevin equation. The parameter q defines the strength of the force, and the stochastic part $\boldsymbol{\eta}(t)$ is Gaussian white noise satisfying

$$\langle \eta_i(t) \rangle = 0, \quad \langle \eta_i(t_1)\eta_j(t_2) \rangle \, \delta_{ij}\delta\left(t_1 - t_2\right). \tag{2.31}$$

The brackets $\langle ... \rangle$ denote an ensemble average over many realizations of the stochastic process. The noise strength q can be determined by applying the equipartition-theorem for systems in equilibrium at temperature T

$$\frac{m}{2}\left\langle \boldsymbol{v}^2 \right\rangle = d\frac{k_\mathrm{B}T}{2}. \tag{2.32}$$

Here the parameter d refers to the number of spatial dimensions and k_B is the Boltzmann constant. Integrating the particle-velocity from equation 2.30, we obtain

$$\boldsymbol{v}(t) = \exp\left(-\frac{t}{\tau_v}\right)\left(\boldsymbol{v}_0 + \frac{\sqrt{2q}}{m}\int_0^t \mathrm{d}t' \boldsymbol{\eta}\left(t'\right)\exp\left(\frac{t'}{\tau_v}\right)\right), \tag{2.33}$$

where $\tau_v = \frac{m}{\lambda}$ is an intrinsic time-constant. Taking the ensemble average from equation 2.33, the average over $\boldsymbol{\eta}$ yields zero and we obtain

$$\langle \boldsymbol{v}(t) \rangle = \boldsymbol{v}_0 \exp\left(-\frac{t}{\tau_v}\right). \tag{2.34}$$

This means that the mean velocity decays to zero on the time-scale τ_v. Applying both equations from 2.31, we can calculate the velocity correlation function for the velocity $\boldsymbol{v}(t)$ to

$$\langle \boldsymbol{v}(t_1)\boldsymbol{v}(t_2) \rangle = \boldsymbol{v}_0^2 \exp\left(-\frac{t_1 + t_2}{\tau_v}\right) + \frac{dq}{\lambda m}\left(\exp\left(-\frac{|t_1 - t_2|}{\tau_v}\right) - \exp\left(-\frac{|t_1 + t_2|}{\tau_v}\right)\right). \tag{2.35}$$

In the limit of large times $t \gg \tau_v$, above equation 2.35 simplifies to

$$\left\langle \boldsymbol{v}^2 \right\rangle = \frac{dq}{\lambda m}. \tag{2.36}$$

Combining the result in equation 2.36 with the equipartition-theorem from equation 2.32, we can determine the strength q of the random force to

$$q = \gamma k_\mathrm{B}T, \tag{2.37}$$

connecting the microscopic noise-strength q to the macroscopic friction coefficient λ. The fact that both quantities q and λ are not independent of each other is an example for the more general fluctuation-dissipation theorem [126]. After evaluating the velocity $\boldsymbol{v}$ of the Brownian particle, we will now focus on the trajectory $\boldsymbol{r}$ of the Brownian particle. The position $\boldsymbol{r}(t)$ can be obtained by integrating equation 2.29, yielding

$$\boldsymbol{r}(t) = \boldsymbol{r}(0) + \int_0^t \mathrm{d}t' \boldsymbol{v}\left(t'\right). \tag{2.38}$$

We can use equation 2.38 to calculate the mean displacement

$$\langle \boldsymbol{r}(t) - \boldsymbol{r}(0) \rangle = v_0 \tau_v \left(1 - \exp\left(-\frac{t}{\tau_v}\right)\right), \tag{2.39}$$

which will saturate to a fixed position for large times $t \gg \tau_v$. The random walk is usually characterized by the mean-squared displacement (MSD) defined as

$$\begin{aligned}
\left\langle \left[\boldsymbol{r}(t) - \boldsymbol{r}(0)\right]^2 \right\rangle &= \left\langle \left[\int_0^t \mathrm{d}t' \boldsymbol{v}\left(t'\right)\right] \cdot \left[\int_0^t \mathrm{d}t'' \boldsymbol{v}\left(t''\right)\right] \right\rangle \\
&= \int_0^t \mathrm{d}t \int_0^t \mathrm{d}t \left\langle \boldsymbol{v}\left(t'\right) \cdot v\left(t''\right) \right\rangle \qquad (2.40) \\
&= \frac{2dq\tau_v}{\lambda^2}\left(\frac{t}{\tau_v} - 1 + \exp -\frac{t}{\tau_v}\right) + \left(v_0^2 - \frac{dq}{\lambda m}\right)\left(\frac{1 - \exp\left(-\frac{t}{\tau_v}\right)}{\tau_v^{-1}}\right)^2. \qquad (2.41)
\end{aligned}$$

We are interested in the behavior of equation 2.41 in regimes for small and large times t compared to τ_v:

1. $t \ll \tau_v$: For small times t we can make a Taylor-expansion of the MSD, which yields

$$\left\langle \left[\boldsymbol{r}(t) - \boldsymbol{r}(0)\right]^2 \right\rangle \approx \left(\tilde{v}^2 t^2\right), \quad \tilde{v} = \sqrt{\frac{dk_\mathrm{B}t}{m}}. \tag{2.42}$$

2. $t \gg \tau_v$: For large times t, the second term of equation 2.41 vanishes due to the relation given by equation 2.36, yielding

$$\left\langle \left[\boldsymbol{r}(t) - \boldsymbol{r}(0)\right]^2 \right\rangle = \lim_{t\to\infty} D2dt, \quad D = \frac{q}{\lambda^2} = \frac{k_\mathrm{B}T}{\lambda}. \tag{2.43}$$

The relation

$$D = \frac{q}{\lambda^2} = \frac{k_\mathrm{B}T}{\lambda} \tag{2.44}$$

is known as the Stokes-Einstein relation.

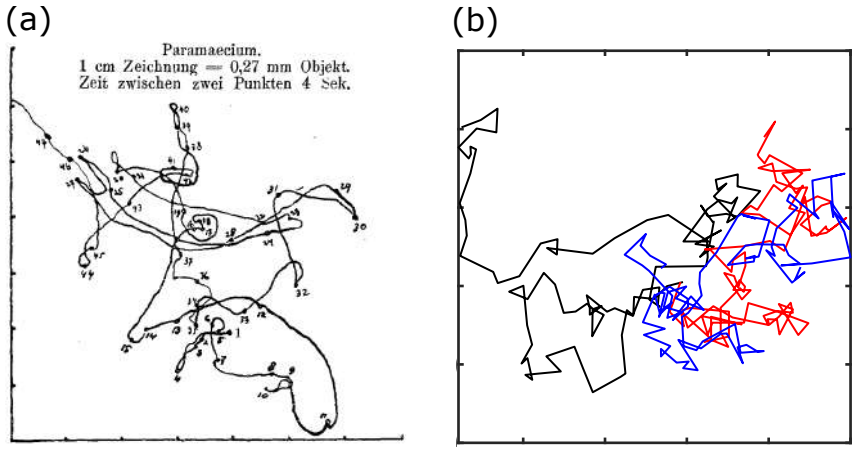

FIGURE 2.7: (a) Trajectory for the microorganism *Paramecium* measured by Przibram. Image taken from [127]. (b) Three different simulations of a Brownian particle.

Langevin equation and microswimmers

The Langevin-equation 2.30 was introduced in 1908. It was used to describe the stochastic motion of a Brownian, colloidal particle in a bath of smaller fluid particles at temperature T [96]. Nowadays, these Langevin-equations are used in several fields, such as Physics, Biology, Engineering and Finance [53, 83, 120]. The Langevin-equation can especially be used to describe the stochastic motion of cells observed under a microscope [1, 147]. The similarity between the observation of microorganism-trajectories and the trajectories of Brownian particles was first observed by Przibram in his article "Über die ungeordnete Bewegung niederer Tiere" (engl. "About the disordered locomotion of of low animals") from 1913 [127]. In Fig. 2.7 we compare original data from the work of Przibram [127] for the microorganism *Paramecium* (a) with three different trajectories of simulated Brownian particles (b). Qualitatively we see several similarities between both trajectories. Due to this good agreement, it is a valid approach to describe microorganisms in terms of stochastic differential equations. The noise terms - inducing random forces and torques - mimic the collisions of the microorganism with particles in the surrounding medium. On the other hand the noise terms can mimic internal cell processes that have an effect on the locomotion of the microorganism. We have seen in section 2.2.1, that the dynamics of microswimmers occur in the Low-Reynolds regime, where

$$\frac{\mathrm{d}}{\mathrm{d}t}\boldsymbol{v}(t) \ll \lambda \boldsymbol{v}(t), \tag{2.45}$$

meaning that inertial forces can be neglected. This simplifies equation 2.30 to the overdamped Langevin-equation

$$\frac{\mathrm{d}}{\mathrm{d}t}\boldsymbol{r}(t) = \sqrt{2D}\boldsymbol{\eta}(t). \tag{2.46}$$

Applying equation 2.31 we obtain

$$\langle \boldsymbol{v}(t_1)\,\boldsymbol{v}(t_2)\rangle = 2dD\delta(t_1 - t_2)\,, \tag{2.47}$$

for the velocity-correlation function. By applying equation 2.40 we see that the MSD for an overdamped particle can be calculated to

$$\left\langle [\boldsymbol{r}(t) - \boldsymbol{r}(0)]^2 \right\rangle = \int_0^t \mathrm{d}t \int_0^t \mathrm{d}t \left\langle \boldsymbol{v}(t') \cdot v(t'') \right\rangle = 2dDt. \tag{2.48}$$

We see from equation 2.48 that the MSD obtained from the overdamped Langevin-equation corresponds to the MSD obtained from the general Langevin-equation in the limit $t \gg \tau_v$ represented in equation 2.43.

2.2.4 Active particles

We have seen in above section 2.2 that the trajectories of Brownian particles and microswimmers have several similarities. Despite these similarities, there are huge physical differences. The Brownian particle is a passive colloid in the thermal equilibrium whose diffusion coefficient obeys the Stokes-Einstein relation 2.44 and the mean velocity tends to vanish for long times. This is a complete contradiction to the observation that active particles have an own mechanism of propulsion to maintain a certain speed $v > 0$. Therefore it will be necessary to make several adaptions to describe active particles in a Langevin-like approach. In this section, we will follow the ideas of Taktikos [160].
The reason why biological particles such as microswimmers can maintain a speed $v > 0$ over long times is due to their ability to absorb energy from their environment and store it in an internal depot. This internal stored energy can be transformed into kinetic energy, resulting in the swimming of the microorganism [145]. To model active swimming particles, one can introduce an efficient friction coefficient $\lambda(\boldsymbol{r}, \boldsymbol{v})$, depending on the current particle position $\boldsymbol{r}$ and velocity $\boldsymbol{v}$. The existence of energy (e.g. nutrition) can be modeled by a potential $U(\boldsymbol{r})$ that generates an attractive force $-\nabla U(\boldsymbol{r})$. There exist several approaches to model the friction coefficient λ based on the speed, such as [135]

$$\lambda(v) = \lambda - \frac{A}{B + Cv^2}, \quad \text{Schweitzer-Ebeling-Tilch,} \tag{2.49}$$

$$\lambda(v) = \lambda\left(\frac{v^2}{v_0^2} - 1\right), \quad \text{Rayleigh,} \tag{2.50}$$

$$\lambda(v) = \lambda\left(1 - \frac{v_0}{v}\right), \quad \text{Schienbein-Grule.} \tag{2.51}$$

$$\tag{2.52}$$

Here we will apply a different approach, which is based on the observation that for several microorganisms changes in orientation are independent of

changes in speed [121, 142]. This allows us to split the time-dependent velocity $\boldsymbol{v}(t)$ in two different parts to

$$\boldsymbol{v}(t) = v(t)\boldsymbol{e}(t), \tag{2.53}$$

where $v(t) > 0$ is the speed. The vector $\boldsymbol{e}(t)$ consisting of $d-1$ angles $\Omega(t)$ represents the current direction of motion. After splitting speed v and orientation $\boldsymbol{e}$, the probability density $p\left(v, \Omega\right)$ and the joint distribution $p\left(v, \Omega, t; v', \Omega', t'\right)$ factorize to

$$p\left(v, \Omega, t\right) = p\left(v, t\right) p\left(\Omega, t\right), \tag{2.54}$$

$$p\left(v, \Omega, t; v', \Omega', t'\right) = p\left(v, t; v', t'\right) p\left(\Omega, t; \Omega', t'\right). \tag{2.55}$$

Due to the factorization of equation 2.55, we can calculate the correlation function of the velocity to

$$\begin{aligned}\left\langle \boldsymbol{v}(t)\boldsymbol{v}(t')^2 \right\rangle &= \int_0^t \mathrm{d}^\mathrm{d} v \int_0^t \mathrm{d}^\mathrm{d} v' p\left(v, \Omega, t; v', \Omega', t'\right) v\boldsymbol{e} \cdot v'\boldsymbol{e}' \\ &= \left\langle v(t)v(t') \right\rangle \left\langle \boldsymbol{e}(t) \cdot \boldsymbol{e}\left(t'\right) \right\rangle. \end{aligned} \tag{2.56}$$

If we integrate the velocity $\boldsymbol{v}(t)$ to obtain the position $\boldsymbol{r}(t)$ via

$$\boldsymbol{r}(t) = \boldsymbol{r}(0) + \int_0^t \mathrm{d}t' v\left(t'\right) \boldsymbol{e}\left(t'\right) \tag{2.57}$$

we can calculate the MSD to

$$\left\langle \left[\boldsymbol{r}(t) - \boldsymbol{r}(0)\right]^2 \right\rangle = \int_0^t \mathrm{d}t' \int_0^t \mathrm{d}t'' \left\langle v(t')v(t'') \right\rangle \left\langle \boldsymbol{e}\left(t'\right) \cdot \boldsymbol{e}\left(t''\right) \right\rangle. \tag{2.58}$$

For simplification we will now assume a constant speed $v(t) = v$ whose direction of motion $\boldsymbol{e}(t)$ is driven by a Gaussian white noise. The strength of the rotational diffusion is set by the rotational diffusion coefficient D_r. To calculate the correlation function $\langle \boldsymbol{e}(t)\boldsymbol{e}(t') \rangle$, let us assume

$$p\left(\Omega, t\right) = \frac{1}{\Omega_0} \tag{2.59}$$

with ω_0 constant,representing stationary and uniform distribution. We can express the joint distribution $p\left(\Omega, t; \Omega', t'\right)$ in terms of the conditional probability $p\left(\Omega, t | \Omega', t'\right)$ via

$$p\left(\Omega, t; \Omega', t'\right) = p\left(\Omega, t | \Omega', t'\right) p\left(\Omega', t'\right). \tag{2.60}$$

The conditional probability satisfies the rotational diffusion equation

$$\partial_t p\left(\Omega, t; \Omega', t'\right) = D_\mathrm{r} \nabla_\Omega^2 p\left(\Omega, t; \Omega', t'\right), \tag{2.61}$$

where ∇^2_Ω denotes the angular part of the d-dimensional Laplace operator. Now we focus on calculating the correlation function

$$\left\langle \boldsymbol{e}(t)\boldsymbol{e}(t')\right\rangle = \int \mathrm{d}\boldsymbol{e} \int \mathrm{d}\boldsymbol{e}'\boldsymbol{e}\boldsymbol{e}' p\left(\Omega, t; \Omega', t'\right) p\left(\Omega', t'\right). \tag{2.62}$$

Calculating the time derivative on both sides and applying equation 2.61 yields

$$\partial_t \left\langle \boldsymbol{e}(t)\boldsymbol{e}(t')\right\rangle = D_\mathrm{r} \int \mathrm{d}\boldsymbol{e} \int \mathrm{d}\boldsymbol{e}'\boldsymbol{e}\boldsymbol{e}' \nabla^2_\Omega p\left(\Omega, t; \Omega', t'\right) p\left(\Omega', t'\right). \tag{2.63}$$

Performing two partial integrations with respect to Ω yields

$$\partial_t \left\langle \boldsymbol{e}(t)\boldsymbol{e}(t')\right\rangle = D_\mathrm{r} \int \mathrm{d}\boldsymbol{e} \int \mathrm{d}\boldsymbol{e}' \nabla^2_\Omega \boldsymbol{e}\boldsymbol{e}' p\left(\Omega, t; \Omega', t'\right) p\left(\Omega', t'\right). \tag{2.64}$$

Applying the relation

$$\nabla^2_\Omega \boldsymbol{e} = -(d-1)\boldsymbol{e} \tag{2.65}$$

from [143] simplifies equation 2.64 to

$$\begin{aligned}\partial_t \left\langle \boldsymbol{e}(t)\boldsymbol{e}(t')\right\rangle &= -(d-1)D_\mathrm{r} \int \mathrm{d}\boldsymbol{e} \int \mathrm{d}\boldsymbol{e}'\boldsymbol{e}\boldsymbol{e}' p\left(\Omega, t; \Omega', t'\right) p\left(\Omega', t'\right) \\ &= -(d-1)D_\mathrm{r} \left\langle \boldsymbol{e}(t) \cdot \boldsymbol{e}\left(t'\right)\right\rangle. \end{aligned} \tag{2.66}$$

The ordinary differential equation 2.66 can be solved by using the initial condition $\left\langle \boldsymbol{e}(t') \cdot \boldsymbol{e}\left(t'\right)\right\rangle = 1$ yielding

$$\left\langle \boldsymbol{e}(t) \cdot \boldsymbol{e}\left(t'\right)\right\rangle = \exp\left(-(d-1)D_\mathrm{r}(t-t')\right). \tag{2.67}$$

We see from the timescale τ_r for rotational diffusion that in case of larger spatial dimensions, the timescale τ_r decreases, resulting in a faster decay of correlations, due to a larger degree of freedom for directional reorientation. Applying equation 2.67 we can calculate the MSD from equation 2.58 to

$$\left\langle \left[\boldsymbol{r}(t) - \boldsymbol{r}(0)\right]^2 \right\rangle = 2v^2\tau_\mathrm{r}^2 \left(\frac{t}{\tau_\mathrm{r}} - 1 + \exp\left(-\frac{t}{\tau_\mathrm{r}}\right)\right). \tag{2.68}$$

It is interesting to realize that the MSD for an active particle from equation 2.68 equals the MSD of a classical Brownian particle from equation 2.48.

2.3 Kalman-Filter

In this section we want to introduce the Kalman-Filter [74] as a simple but efficient tool to extract bacteria-trajectory statistics. The Kalman filter was introduced by engineers and has a physical approach, resulting in several advantages such as the intrinsic distinction between process-noise (e.g. Brownian motion) and measurement noise (e.g. tracking errors), the possibility to estimate parameters which have not been measured by taking advantage of the specific underlying physical model, etc [56, 59]. The Kalman filter first introduced by Rudolf E. Kalman is suitable for linear problems. To deal with non-linear problems, there have been introduced several extensions such as the Extended-Kalman-Filter (EKF) [7, 59] or the Unscented-Kalman-Filter (UKF) [59]. To get an understanding what the Kalman-Filter can be used for, we can have a look at Fig. 2.8. In Fig. 2.8 (a) we see the information about the z-position of a particle in one dimension represented as a probability-density function (PDF). As we are not completely sure about the initial position, the PDF has a certain initial width $w_{x,k}$. The information about the position of the particle at time $t = k$ is denoted as x_k. Let us assume we have a certain knowledge about the velocity v_k of the particle at time t_k. Based on the information about the particle x_k and the velocity v_k we make a prediction $\tilde{x}_{k+1}$ for the position of the particle at time $t = k + 1$, represented as the blue distribution in Fig. 2.8 (b). The width of the predicted state $\tilde{x}_{k+1}$ is denoted as $\tilde{w}_{x,k+1}$. Due to the width $w_{v,k}$ of the distribution for velocity v_k, the relation between the width $w_{x,k}$ of the initial state x_k and the width $\tilde{w}_{x,k+1}$ of the predicted state $\tilde{x}_{k+1}$ is given as

$$\tilde{w}_{x,k+1} > w_{x,k}. \tag{2.69}$$

To summarize, the blue distribution in Fig. 2.8 (b) represents the PDF for the position of the particle at time $t = k + 1$ obtained by making a prediction based on a certain model and the applied on the state of the particle at time $t = k$. Another possibility to obtain the state of the particle at time $t = k + 1$ is performing a measurement of the particle position. For a car this can e.g. be a tracking via GPS, for smaller particles (e.g. bacteria) this can be a tracking using a microscope. In both scenarios, the tracked position has an underlying error due to the tracking process. Therefore the information about the tracked position y_{k+1} of the particle at time $t = k + 1$ can be described via a PDF with a certain width $w_{y,k+1}$. This information is represented as the cyan curve in Fig. 2.8 (c).
In total we have two possibilities to quantify the information about the position of the particle at time $t = k + 1$:

1. Based on a prediction involving previous time-step $t = k$ as represented in Fig. 2.8 (b)

2. Based on a measurement of the particle-position at time $t = k + 1$ as represented in Fig. 2.8 (c)

The task of the Kalman-Filter is the combination of both information $\tilde{x}_{k+1}$ and y_{k+1} to a state x_{k+1}, combining the predicted information $\tilde{x}_{k+1}$ and the

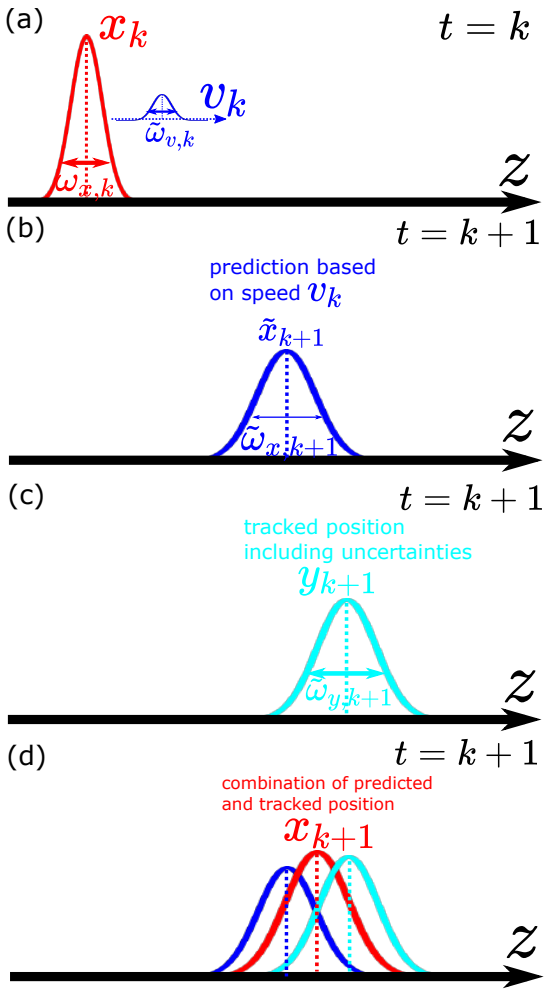

FIGURE 2.8: Schematic representation of the Kalman-Filter based on a one dimensional tracking problem. (a) Probability distribution x_k (red curve) for the position of the particle at time $t = k$. It moves with an uncertain velocity v_k (blue curve). (b) Based on the velocity v_k we can make a prediction about the position probability distribution $\tilde{x}_{k+1}$ (blue curve). (c) Rather than making a prediction, we can also perform an unprecise position measurement, resulting in the distribution y_{k+1} (cyan curve). (d) Combination of both position information $\tilde{x}_{k+1}$ and y_{k+1} about the particle position via the Kalman-Filter resulting in the new distribution x_{k+1} (red curve).

measured information y_{k+1} to the most reasonable assumption x_{k+1} about the particle position at time-step $t = k + 1$.
In the following section 2.3.1 we introduce the linear Kalman-Filter, suitable for the filtering of linear-processes. Here, we present the basic features relevant for the understanding of the Kalman-Filtering process. Subsequently in section 2.3.2 we extend the general Kalman-Filter introduced in section 2.3.1 to deal with non-linear processes, the Extended-Kalman-Filter (EKF). Finally in section 2.3.3 we extend the Kalman-Filter to deal with a system which can be described with multiple models, e.g. one model for the running- and one

model for the tumbling-state.

2.3.1 Linear Kalman-Filter

In this section we would like to introduce the mathematical framework of the linear Kalman-Filter (KF), inspired by an introduction from Reid [132]. After introducing the framework we give an example for an application of the KF. We want to use the KF to estimate the state $\hat{\boldsymbol{x}}(t)$ of a system. In a broader context, we seek to solve the problem of the continual estimation of a set of parameters whose values change over time. The observed measurements $\boldsymbol{z}(t)$ contain information about the signal of interest $\boldsymbol{x}(t)$. The KF is an estimator to provide an estimate $\hat{\boldsymbol{x}}(t)$ for the state of the system at time t.

Physical system

The KF can be applied to estimate the state $\boldsymbol{x}_k \in \mathcal{R}^{d_\mathrm{x}}$ of a system whose evolution can be described by the equation

$$\boldsymbol{x}_{k+1} = \boldsymbol{F}_k \boldsymbol{x}_k + \boldsymbol{G}_k \boldsymbol{u}_k + \boldsymbol{w}_k. \tag{2.70}$$

Here, the matrix $\boldsymbol{F}_k^{d_\mathrm{x} \times d_\mathrm{x}}$ is the state-transition matrix, quantifying the intrinsic time-evolution of the system. The matrix $\boldsymbol{G}_k^{d_\mathrm{u} \times d_\mathrm{x}}$ is the input-transition matrix, mapping the external input signal $\boldsymbol{u}_k \in \mathcal{R}^{d_\mathrm{u}}$ in the state-space ($\boldsymbol{x}$-space). The vector $\boldsymbol{w}_k \in \mathcal{R}^{d_\mathrm{x}}$ describes intrinsic system noise.
For the KF it is important to realize that the state-space and the measurement-space can differ, e.g. the measured quantities can be the position x and speed v and the state is described via the acceleration a. To map between the state-space and measurement-space we introduce a matrix $\boldsymbol{H}_k^{d_z \times d_z}$, transferring the state variable $\boldsymbol{x}_k$ in the measurement-space via equation

$$\boldsymbol{z}_k = \boldsymbol{H}_k \boldsymbol{x}_k + \boldsymbol{v}_k. \tag{2.71}$$

A schematic representation of a system whose state can be estimated is shown in Fig. 2.9. The time-evolution of the state $\boldsymbol{x}$ is described in the upper part of Fig. 2.9. It visualizes equation (2.70). The new state $\boldsymbol{x}_{k+1}$ is *created* at node (1), whose input is the transferred input-signal $\boldsymbol{u}$, the evolved old state $\boldsymbol{x}_k$ and the noise $\boldsymbol{w}$. It is a recursive process where each time the state x is evolved via matrix $\boldsymbol{F}$. The lower part of Fig. 2.9 visualizes equation (2.71). Based on the intrinsic system-state $\boldsymbol{x}$, the observable measurement $\boldsymbol{z}$ is *created* via matrix $\boldsymbol{H}$ and noise v.

Assumptions

For further calculations it is crucial to make some assumptions on the noise

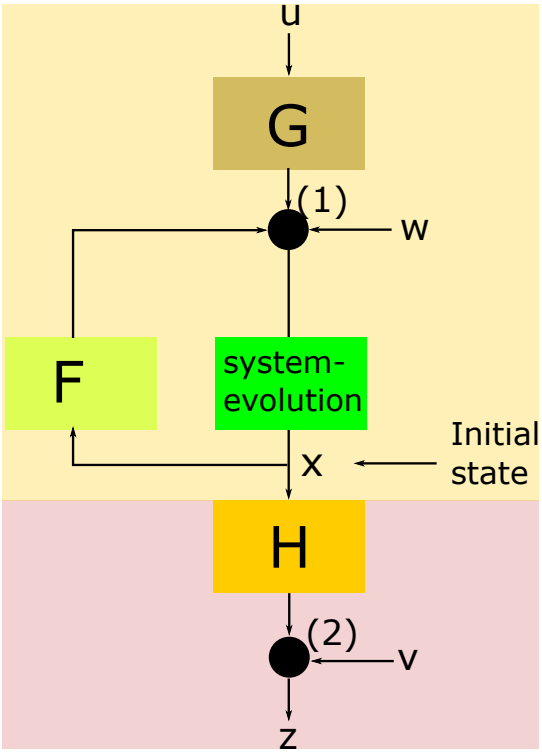

FIGURE 2.9: Schematic representation equations 2.70 and 2.71, where the state $\boldsymbol{x}$ evolves intrinsically via matrix $\boldsymbol{F}$, an external input $\boldsymbol{u}$ transferred via matrix $\boldsymbol{G}$ and process-noise $\boldsymbol{\omega}$. The state $\boldsymbol{x}$ is transformed into an experimentally observable quantity $\boldsymbol{z}$ via the matrix $\boldsymbol{H}$ and the addition of measurement-noise $\boldsymbol{v}$.

$\boldsymbol{w}_k$ and $\boldsymbol{v}_k$ from equations (2.70) and (2.71) respectively. These assumptions are:

1. The process noise $\boldsymbol{w}_k$ and the measurement noise $\boldsymbol{w}_k$ are uncorrelated:

$$\mathrm{E}\left[\boldsymbol{w}_k, \boldsymbol{v}_l\right] = 0 \text{ for all } k, l \tag{2.72}$$

2. The process-noise $\boldsymbol{w}_k$ is a zero-mean white-noise process with known covariance matrix:

$$\mathrm{E}\left[\boldsymbol{w}_k, \boldsymbol{w}_l\right] = \begin{cases} \boldsymbol{Q}_k & \text{if } k = l \\ \boldsymbol{0} & \text{otherwise} \end{cases} \tag{2.73}$$

3. The measurement-noise $\boldsymbol{v}_k$ is a zero-mean white-noise process with known covariance matrix:

$$\mathrm{E}\left[\boldsymbol{v}_k, \boldsymbol{v}_l\right] = \begin{cases} \boldsymbol{R}_k & \text{if } k = l \\ \boldsymbol{0} & \text{otherwise} \end{cases} \tag{2.74}$$

4. The initial system state $\boldsymbol{x}_0$ is a vector which is chosen randomly and is uncorrelated to the process-noise $\boldsymbol{w}_k$ and measurement-noise $\boldsymbol{v}_k$.

5. The mean
$$\hat{\boldsymbol{x}}_{0,0} = \mathrm{E}\left[\boldsymbol{x}_0\right] \tag{2.75}$$
of the initial state $\boldsymbol{x}_0$ is a known quantity.

6. The covariance-matrix
$$\boldsymbol{P}_{0,0} = \mathrm{E}\left[\left(\hat{\boldsymbol{x}}_{0,0} - \boldsymbol{x}_0\right)\left(\hat{\boldsymbol{x}}_{0,0} - \boldsymbol{x}_0\right)^T\right] \tag{2.76}$$
of the initial state $\boldsymbol{x}_0$ is a known quantity.

Making the above assumptions, we can describe the task of the KF as follows: Assuming $k > 0$ measurements $z_1, ..., z_k$, the KF shall estimate the state x_{k+1} of the system. This estimation is denoted as $\hat{x}_{k+1}$ and shall minimize the expectation of the squared-error loss function

$$\mathrm{E}\left[\left|\boldsymbol{x}_{k+1} - \hat{\boldsymbol{x}}_{k+1}\right|^2\right] = \mathrm{E}\left[\left(\boldsymbol{x}_{k+1} - \hat{\boldsymbol{x}}_{k+1}\right)\right]\mathrm{E}\left[\left(\boldsymbol{x}_{k+1} - \hat{\boldsymbol{x}}_{k+1}\right)^T\right]. \tag{2.77}$$

The minimization of above equation (2.77) is the definition of a minimum variance unbiased estimator (MVUE). As the KF is per definition a MVUE, it has to minimize above equation (2.77).

Prediction

We have already mentioned that the task of the KF is the estimation $\hat{\boldsymbol{x}}_{k+1}$ of state $\boldsymbol{x}_{k+1}$ based on previous measurements $\boldsymbol{z}_j$ for $j \leq k$. As the estimation $\hat{\boldsymbol{x}}_{k+1}$ depends on previous measurements, we can also denote the estimation as $\hat{\boldsymbol{x}}_{k+1,Z^k} = \hat{\boldsymbol{x}}_{k+1,k}$. To minimize equation (2.77) we have to estimate the state $\hat{\boldsymbol{x}}_{k+1,k}$ based on previous measurements up to time k:

$$\hat{\boldsymbol{x}}_{k+1,k} = \mathrm{E}\left[\boldsymbol{x}_{k+1}|\boldsymbol{z}_1, ..., \boldsymbol{z}_k\right] = \mathrm{E}\left[\boldsymbol{x}_{k+1}|\boldsymbol{Z}^k\right]. \tag{2.78}$$

Applying equation (2.70) for the time-evolution of the system we can rewrite equation (2.78) to

$$\begin{aligned}\hat{\boldsymbol{x}}_{k+1,k} &= \mathrm{E}\left[\boldsymbol{F}_k\boldsymbol{x}_k + \boldsymbol{G}_k\boldsymbol{u}_k + \boldsymbol{w}_k|\boldsymbol{Z}^k\right] \\ &= \mathrm{E}\left[\boldsymbol{F}_k\boldsymbol{x}_k\right] + \mathrm{E}\left[\boldsymbol{G}_k\boldsymbol{u}_k\right] + \mathrm{E}\left[\boldsymbol{w}_k|\boldsymbol{Z}^k\right] \\ &= \boldsymbol{F}_k\mathrm{E}\left[\boldsymbol{x}_k\right] + \boldsymbol{G}_k\mathrm{E}\left[\boldsymbol{u}_k\right] + \mathrm{E}\left[\boldsymbol{w}_k|\boldsymbol{Z}^k\right]\end{aligned} \tag{2.79}$$

As we know the external input $\boldsymbol{u}_k$ precisely and we know from equation (2.73) that the process-noise $\boldsymbol{w}_k$ has zero mean, we can rewrite equation (2.79) to

$$\hat{\boldsymbol{x}}_{k+1,k} = \boldsymbol{F}_k\boldsymbol{x}_{k,k} + \boldsymbol{G}_k\boldsymbol{u}_k. \tag{2.80}$$

The variance $\boldsymbol{P}_{k+1,k}$ is calculated as the mean squared error in the estimate $\hat{\boldsymbol{x}}_{k+1}$:

$$\boldsymbol{P_{k+1,k}} = \mathrm{E}\left[\left(\boldsymbol{x}_{k+1} - \hat{\boldsymbol{x}}_{k+1,k}\right)\left(\boldsymbol{x}_{k+1} - \hat{\boldsymbol{x}}_{k+1,k}\right)^T \middle| \boldsymbol{Z}^k\right]. \tag{2.81}$$

Applying again the time evolution for the state-vector $\boldsymbol{x}$ from equation (2.70), we can rewrite equation (2.81) to

$$\boldsymbol{P_{k+1,k}} = \mathrm{E}\left[\left(\boldsymbol{F}_k\boldsymbol{x}_k + \boldsymbol{G}_k\boldsymbol{u}_k + \boldsymbol{w}_k - \hat{\boldsymbol{x}}_{k+1,k}\right)\left(\boldsymbol{F}_k\boldsymbol{x}_k + \boldsymbol{G}_k\boldsymbol{u}_k + \boldsymbol{w}_k - \hat{\boldsymbol{x}}_{k+1,k}\right)^T \middle| \boldsymbol{Z}^k\right]. \tag{2.82}$$

We can simplify equation (2.82) by applying the fact that the noise $\boldsymbol{w}_k$ and the state $\boldsymbol{x}_k$ are uncorrelated. Furthermore the external input $\boldsymbol{u}_k$ is known precisely. This simplifies equation (2.82) to

$$\boldsymbol{P_{k+1,k}} = \boldsymbol{F}_k\boldsymbol{P}_{k,k}\boldsymbol{F}_k^T + \boldsymbol{Q}_k, \tag{2.83}$$

where $\boldsymbol{Q}_k$ is the process-noise matrix as introduced in equation (2.73). Applying equations (2.80) and (2.83) we can estimate the new state $\hat{\boldsymbol{x}}_{k+1,k}$ and the new variance $\hat{\boldsymbol{P}}_{k+1,k}$ using measurements z_j for $j \leq k$. In a next step we have to add the information from measurement z_{k+1} to make a more accurate assumption $\hat{\boldsymbol{x}}_{k+1,k+1}$ for the state $\boldsymbol{x}_{k+1}$ at time $k+1$. Therefore let us assume we can calculate the estimate $\hat{\boldsymbol{x}}_{k+1,k+1}$ as a weighted sum of both the estimate $\hat{\boldsymbol{x}}_{k+1,k}$ and the current measurement $\boldsymbol{z}_{k+1}$ via

$$\hat{\boldsymbol{x}}_{k+1,k+1} = \tilde{\boldsymbol{K}}_{k+1}\hat{\boldsymbol{x}}_{k+1,k} + \boldsymbol{K}_{k+1}\boldsymbol{z}_{k+1}, \tag{2.84}$$

where $\tilde{\boldsymbol{K}}_k \in \mathcal{R}^{d_x \times d_x}$ and $\boldsymbol{K}_k \in \mathcal{R}^{d_x \times d_z}$ are so called gain-matrices. Via equation 2.84 we have reduced our initial problem in finding the state $\hat{\boldsymbol{x}}_{k+1} = \hat{\boldsymbol{x}}_{k+1,k+1}$ which minimizes equation (2.77) to finding the matrices $\tilde{\boldsymbol{K}}_k$ and $\boldsymbol{K}_k$. The error in the estimation of the state $\boldsymbol{x}_{k+1}$ is given as

$$\mathrm{err}\left(\hat{\boldsymbol{x}}_{k+1}\right) = \hat{\boldsymbol{x}}_{k+1,k+1} - \boldsymbol{x}_k. \tag{2.85}$$

The unbiased condition

As the KF aims on estimating the state $\boldsymbol{x}_{k+1}$, we have to require that

$$\mathrm{E}\left[\hat{\boldsymbol{x}}_{k+1,k+1}\right] = \mathrm{E}\left[\boldsymbol{x}_{k+1}\right], \tag{2.86}$$

making the KF unbiased. Let us now in a first step combine equations 2.84 and (2.71), yielding the equation

$$\begin{aligned}
\mathrm{E}\left[\hat{\boldsymbol{x}}_{k+1,k+1}\right] &= \mathrm{E}\left[\tilde{\boldsymbol{K}}_{k+1}\hat{\boldsymbol{x}}_{k+1,k} + \boldsymbol{K}_{k+1}\boldsymbol{z}_{k+1}\right] \\
&= \mathrm{E}\left[\tilde{\boldsymbol{K}}_{k+1}\hat{\boldsymbol{x}}_{k+1,k} + \boldsymbol{K}_{k+1}\boldsymbol{H}_{k+1}\boldsymbol{x}_{k+1} + \boldsymbol{K}_{k+1}\boldsymbol{v}_{k+1}\right] \\
&= \tilde{\boldsymbol{K}}_{k+1}\mathrm{E}\left[\hat{\boldsymbol{x}}_{k+1,k}\right] + \boldsymbol{K}_{k+1}\boldsymbol{H}_{k+1}\mathrm{E}\left[\boldsymbol{x}_{k+1}\right] + \boldsymbol{K}_{k+1}\mathrm{E}\left[\boldsymbol{v}_{k+1}\right] \\
&= \tilde{\boldsymbol{K}}_{k+1}\mathrm{E}\left[\hat{\boldsymbol{x}}_{k+1,k}\right] + \boldsymbol{K}_{k+1}\boldsymbol{H}_{k+1}\mathrm{E}\left[\boldsymbol{x}_{k+1}\right].
\end{aligned} \tag{2.87}$$

Furthermore, by applying the time-evolution introduced in equation (2.70), we can calculate the expectation value $\mathrm{E}\left[\hat{\boldsymbol{x}}_{k+1,k}\right]$ to

$$\begin{aligned}\mathrm{E}\left[\hat{\boldsymbol{x}}_{k+1,k}\right] &= \mathrm{E}\left[\boldsymbol{F}_k\hat{\boldsymbol{x}}_{k,k} + \boldsymbol{G}_k\boldsymbol{u}_k\right] \\ &= \boldsymbol{F}_k\mathrm{E}\left[\hat{\boldsymbol{x}}_{k,k}\right] + \boldsymbol{G}_k\boldsymbol{u}_k \\ &= \mathrm{E}\left[\boldsymbol{x}_{k+1}\right]. \end{aligned} \tag{2.88}$$

Replacing $\mathrm{E}\left[\hat{\boldsymbol{x}}_{k+1,k}\right]$ in equation (2.87) with the result from equation (2.88) gives the expectation-value $\mathrm{E}\left[\hat{\boldsymbol{x}}_{k+1,k+1}\right]$ of the state $\hat{\boldsymbol{x}}_{k+1,k+1}$ in dependence of the gain-matrices $\tilde{\boldsymbol{K}}_{k+1}$ and $\boldsymbol{K}_{k+1}$ as

$$\mathrm{E}\left[\hat{\boldsymbol{x}}_{k+1,k+1}\right] = \left(\hat{\boldsymbol{x}}_{k+1,k+1} + \tilde{\boldsymbol{K}}_{k+1}\boldsymbol{H}_{k+1}\right)\mathrm{E}\left[\boldsymbol{x}_{k+1}\right]. \tag{2.89}$$

If we now remember the unbiased-condition introduced in equation (2.86), this yields the relation

$$\hat{\boldsymbol{x}}_{k+1,k+1} + \tilde{\boldsymbol{K}}_{k+1}\boldsymbol{H}_{k+1} = \mathbf{1} \tag{2.90}$$

or

$$\hat{\boldsymbol{x}}_{k+1,k+1} = \mathbf{1} - \tilde{\boldsymbol{K}}_{k+1}\boldsymbol{H}_{k+1}. \tag{2.91}$$

If we expect our estimator to be unbiased, the estimator has to satisfy equation (2.91). If we replace $\hat{\boldsymbol{x}}_{k+1,k+1}$ from equation (2.91) in equation 2.84, the resulting, unbiased equation reads

$$\begin{aligned}\hat{\boldsymbol{x}}_{k+1,k+1} &= \left(\mathbf{1} - \tilde{\boldsymbol{K}}_{k+1}\boldsymbol{H}_{k+1}\right)\hat{\boldsymbol{x}}_{k+1,k} + \boldsymbol{K}_{k+1}\boldsymbol{z}_{k+1} \\ &= \hat{\boldsymbol{x}}_{k+1,k} + \boldsymbol{K}_{k+1}\left[\boldsymbol{z}_{k+1} - \boldsymbol{H}_{k+1}\boldsymbol{x}_{k+1,k}\right]. \end{aligned} \tag{2.92}$$

Here $\boldsymbol{K}$ is known as the Kalman-gain. If we have a look at equation (2.92), we see that the new state-estimate $\hat{\boldsymbol{x}}_{k+1,k+1}$ is a sum of a prediction $\hat{\boldsymbol{x}}_{k+1,k+1}$ and a second term, which is the difference between the actual measurement $\boldsymbol{z}_{k+1}$ and the predicted state $\boldsymbol{x}_{k+1,k}$ transferred into the measurement space, weighted with the Kalman-gain $\boldsymbol{K}_{k+1}$.

Finding the error-covariance

After we estimated the state $\hat{\boldsymbol{x}}_{k+1,k+1}$ via equation (2.92), we have to calculate the corresponding variance-matrix $\boldsymbol{P}_{k+1,k+1}$ via

$$\begin{aligned}\boldsymbol{P}_{k+1,k+1} &= \mathrm{E}\left[\left(\hat{\boldsymbol{x}}_{k+1,k+1} - \boldsymbol{x}_k\right)\left(\hat{\boldsymbol{x}}_{k+1,k+1} - \boldsymbol{x}_k\right)^T\right] \\ &= \left(\mathbf{1} - \boldsymbol{K}_{k+1}\boldsymbol{H}_{k+1}\right)\boldsymbol{P}_{k+1,k}\left(\mathbf{1} - \boldsymbol{K}_{k+1}\boldsymbol{H}_{k+1}\right)^T + \boldsymbol{K}_{k+1}\boldsymbol{R}_{k+1}\boldsymbol{K}_{k+1}^T, \end{aligned} \tag{2.93}$$

where in the last step we used the definition of the measurement-noise matrix $\boldsymbol{R}$ introduced in equation (2.74) and the fact that measurements and noise are uncorrelated, quantified as

$$\mathrm{E}\left[\mathrm{err}\left(\hat{\boldsymbol{x}}_{k+1}\right)\mathrm{err}\left(\hat{\boldsymbol{x}}_{k+1}\right)^T\right] = 0. \tag{2.94}$$

Choosing the Kalman-gain

We started with the initial problem to find a state $\boldsymbol{x}_{k+1}$ minimizing the expectation of the squared-error loss function (SELF) defined in equation (2.77). This problem is now reduced to finding the Kalman-gain $\boldsymbol{K}$ creating a state $\boldsymbol{x}_{k+1,k+1}$ as described via equation (2.92). To summarize, we want to minimize the quantity L with respect to the Kalman-gain $\boldsymbol{K}$:

$$\begin{aligned} L &= \min_{\boldsymbol{K}_{k+1}} \mathrm{E}\left[\mathrm{err}\left(\hat{\boldsymbol{x}}_{k+1}\right)\mathrm{err}\left(\hat{\boldsymbol{x}}_{k+1}\right)^T|\boldsymbol{Z}^{k+1}\right] \\ &= \min_{\boldsymbol{K}_{k+1}} \mathrm{trace}\left(\mathrm{E}\left[\mathrm{err}\left(\hat{\boldsymbol{x}}_{k+1}\right)\mathrm{err}\left(\hat{\boldsymbol{x}}_{k+1}\right)^T|\boldsymbol{Z}^{k+1}\right]\right) \\ &= \min_{\boldsymbol{K}_{k+1}} \mathrm{trace}\left(\boldsymbol{P}_{k+1,k+1}\right). \end{aligned} \tag{2.95}$$

To find the minimum of L defined in equation (2.95) we solve

$$\frac{\partial L}{\partial \boldsymbol{K}_{k+1}} = \frac{\partial\left(\min_{\boldsymbol{K}_{k+1}} \mathrm{trace}\left(\boldsymbol{P}_{k+1,k+1}\right)\right)}{\partial \boldsymbol{K}_{k+1}} = 0 \tag{2.96}$$

where we used the relation

$$\frac{\partial}{\partial \boldsymbol{A}}\left(\mathrm{trace}\left(\boldsymbol{A}\boldsymbol{B}\boldsymbol{A}^T\right)\right) = 2\boldsymbol{A}\boldsymbol{B} \tag{2.97}$$

for any matrix $\boldsymbol{A}$ and a symmetric matrix $\boldsymbol{B}$. From equation (2.96) we obtain the relation

$$\boldsymbol{K}_{k+1} = \boldsymbol{P}_{k+1,k}\boldsymbol{H}_{k+1}^T\left[\boldsymbol{H}_{k+1}\boldsymbol{P}_{k+1,k}\boldsymbol{H}_{k+1}^T + \boldsymbol{R}_{k+1}\right]^{-1} \tag{2.98}$$

for the Kalman-gain $\boldsymbol{K}$. Now with equation (2.98) we can calculate both quantities $\hat{\boldsymbol{x}}_{k+1,k+1}$ and $\boldsymbol{P}_{k+1,k+1}$ from equation (2.92) and (2.93).

Summary Kalman-equations

To summarize, the Kalman-filtering process consists of two steps.

1. Prediction: In the prediction step, we calculate a prediction $\hat{\boldsymbol{x}}_{k+1,k}$ for the state $\boldsymbol{x}_{k+1}$ at time $k+1$ based on previous measurements via

$$\hat{\boldsymbol{x}}_{k+1,k} = \boldsymbol{F}_k\hat{\boldsymbol{x}}_{k,k} + \boldsymbol{G}_k\boldsymbol{u}_k \tag{2.99}$$

$$\boldsymbol{P}_{k+1,k} = \boldsymbol{F}_k\boldsymbol{P}_{k,k}\boldsymbol{F}_k^T + \boldsymbol{Q}_k. \tag{2.100}$$

2. Update: In the update step, we adapt the predicted state $\hat{\boldsymbol{x}}_{k+1,k}$ for time $k+1$ based on the current measurement $\boldsymbol{z}_{k+1}$ at time $k+1$ via

$$\hat{\boldsymbol{x}}_{k+1,k+1} = \hat{\boldsymbol{x}}_{k+1,k} + \boldsymbol{K}_{k+1}\left[\boldsymbol{z}_{k+1} - \boldsymbol{H}_{k+1}\boldsymbol{x}_{k+1,k}\right] \tag{2.101}$$

$$\boldsymbol{P}_{k+1,k+1} = \left(\boldsymbol{1} - \boldsymbol{K}_{k+1}\boldsymbol{H}_{k+1}\right)\boldsymbol{P}_{k+1,k}\left(\boldsymbol{1} - \boldsymbol{K}_{k+1}\boldsymbol{H}_{k+1}\right)^T + \boldsymbol{K}_{k+1}\boldsymbol{R}_{k+1}\boldsymbol{K}_{k+1}^T \tag{2.102}$$

A schematic representation of the Kalman-equations (2.99) - (2.101) for the estimation of the state $\hat{\boldsymbol{x}}_{k+1,k+1}$ can be found in Fig. 2.10. The prediction process

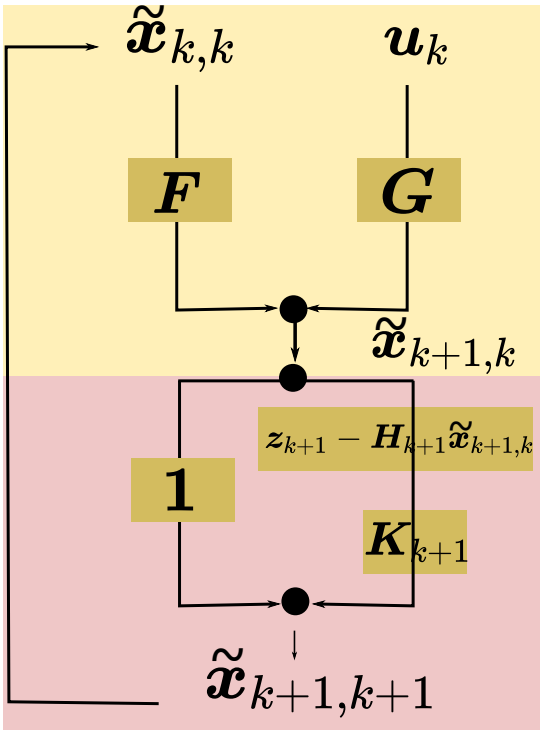

FIGURE 2.10: Representation of the Kalman-equations (2.99)-(2.102). Based on the old state $\tilde{\boldsymbol{x}}_{k,k}$ and the external input $\boldsymbol{u}_k$ the predicted state $\tilde{\boldsymbol{x}}_{k+1,k}$ is calculated. Based on the difference between the predicted state $\tilde{\boldsymbol{x}}_{k+1,k}$ and the measurement $\boldsymbol{z}_{k+1}$ the new estimate $\tilde{\boldsymbol{x}}_{k+1,k+1}$ is calculated.

is represented in the upper part of Fig. 2.10. Based on the old state-estimate $\hat{\boldsymbol{x}}_{k,k}$ and the input-vector $\boldsymbol{u}_k$, the predicted state-estimate $\hat{\boldsymbol{x}}_{k+1,k}$ is calculated. The bottom part of Fig. 2.10 represents the updating process, where the new state-estimate $\hat{\boldsymbol{x}}_{k+1,k+1}$ is calculated as a weighted sum of the predicted state-estimate $\hat{\boldsymbol{x}}_{k+1,k}$ and the difference between the predicted state-estimate $\hat{\boldsymbol{x}}_{k+1,k}$ and the current measurement $\boldsymbol{z}_{k+1}$.

Understanding the process- and measurement noise

If we have a look at the Kalman-equations (2.99) - (2.102) we see that we have to choose both matrices $\boldsymbol{Q}$ and $\boldsymbol{R}$, which define the process- and the measurement noise. To get an understanding of the impact of both matrices $\boldsymbol{Q}$ and $\boldsymbol{R}$ we present a simple application for the Kalman-filter. Let us assume a particle in one dimension, whose state is described via its position $x(t)$ and speed $v(t) = \dot{x}(t)$. We can only meassure the position $x(t)$ of the particle. Furthermore let us assume the particle undergoes random accelerations $a_{\mathrm{r}}(t)$ for each time t. The state of the system can be described via the vector

$$\boldsymbol{x}(t) = \begin{pmatrix} x(t) \\ v(t) \end{pmatrix}. \tag{2.103}$$

The time evolution of the state $\boldsymbol{x}(t)$ is given as

$$\begin{aligned} \dot{\boldsymbol{x}}(t) &= \boldsymbol{A}\boldsymbol{x}(t) + \boldsymbol{w}(t), \\ z(t) &= \boldsymbol{H}\boldsymbol{x}(t) + \boldsymbol{v}(t), \end{aligned} \tag{2.104}$$

where

$$\boldsymbol{A} = \begin{pmatrix} 0 & 1 \\ 0 & 0 \end{pmatrix}, \boldsymbol{H} = \begin{pmatrix} 1 & 0 \\ 0 & 0 \end{pmatrix}, \boldsymbol{w}(t) = \begin{pmatrix} 0 \\ a_{\mathrm{r}} \end{pmatrix}, \tag{2.105}$$

and $\boldsymbol{v}(t)$ is the measurement-noise.
The time-evolution analogue to equation (2.70) is given as

$$\boldsymbol{x}_{k+1} = \boldsymbol{F}_k \boldsymbol{x}_k + \boldsymbol{w}_k, \tag{2.106}$$

with

$$\boldsymbol{F}_k = \begin{pmatrix} 1dt & \\ 0 & 1 \end{pmatrix}. \tag{2.107}$$

The measurement-equation analog to equation (2.71) is given as

$$\boldsymbol{z}_k = \boldsymbol{H}\boldsymbol{x}_k + \boldsymbol{v}_k. \tag{2.108}$$

To apply the Kalman-filter, we have to make assumptions for

1. $\hat{\boldsymbol{x}}_{0,0}$: Initial assumption for the state of the system.
2. $\boldsymbol{P}_{0,0}$: Initial assumption for the covariance.
3. $\boldsymbol{Q}$: Assumption for the process-noise matrix.
4. $\boldsymbol{R}$: Assumption for the measurement-noise matrix.

Let us assume the following values and afterwards discuss their impact individually.

$$\hat{\boldsymbol{x}}_{0,0} = \begin{pmatrix} 0 \\ 0 \end{pmatrix}, \boldsymbol{P}_{0,0} = \begin{pmatrix} 1 & 0 \\ 0 & 1 \end{pmatrix}, \boldsymbol{Q} = \begin{pmatrix} 1 & 0 \\ 0 & 1 \end{pmatrix} \text{ and } \boldsymbol{R} = 1. \tag{2.109}$$

A realization of the particle-trajectory according to equation (2.104) is represented in Fig. 2.11 (a). The black dots represent the system-state x. The blue dots are the measurements affected by the process-noise. We applied a Kalman-Filter for the parameters defined in equation (2.109) to estimate the state $\boldsymbol{x}$ of the system based on the noisy measurements z_k. The corresponding estimated positions $\hat{x}$ are represented as the red dots in Fig. 2.11 (a). We see qualitatively that the estimated position $\hat{x}$ follows the evolution of the true position x. To understand the impact of the initial guess $\hat{\boldsymbol{x}}_{0,0}$ of the system-state, required as an input-parameter for the Kalman-Filter, we applied a Kalman-Filter for different initial guesses $\hat{\boldsymbol{x}}_{0,0}$. The corresponding results are represented as the red, blue, green and magenta curve in Fig. 2.11 (b). We see that initially the estimated positions are different from each other, but tend to move to the true system-state x. After approximately 50 time-steps,

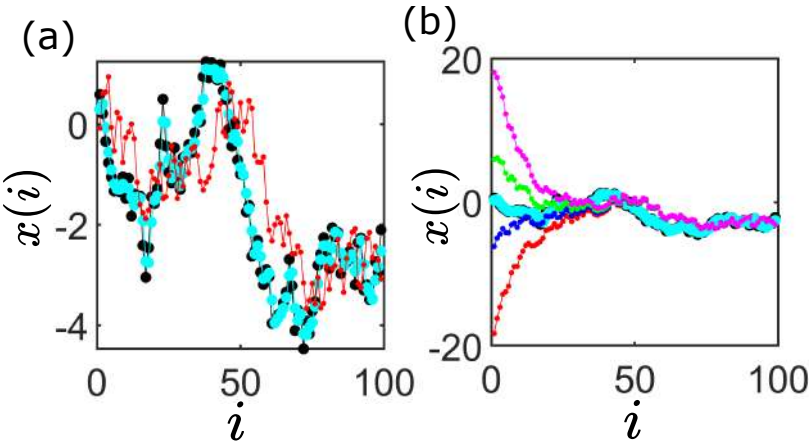

FIGURE 2.11: (a) Plot of a simulated system state (black), system state-including process-noise (cyan) and estimated positions (red). (b) Simulated system state (black) with included process-noise (cyan). Estimated positions for different initial positions $\hat{\boldsymbol{x}}_{0,0}$ are represented in magenta, green, blue and red.

the impact of different initial guesses $\hat{\boldsymbol{x}}_{0,0}$ has vanished and the estimated positions are identical for all different initial guesses $\hat{\boldsymbol{x}}_{0,0}$. This is a general behavior of the Kalman-Filter. For long-times, the estimated solution does not depend on initial guesses $\hat{\boldsymbol{x}}_{0,0}$. In a next step, we investigated the impact of the initial covariance matrix $\boldsymbol{P}_{0,0}$ on the estimated positions $\hat{x}$. The results are represented in 2.12 (a). Here the black dots represent the system state x_k

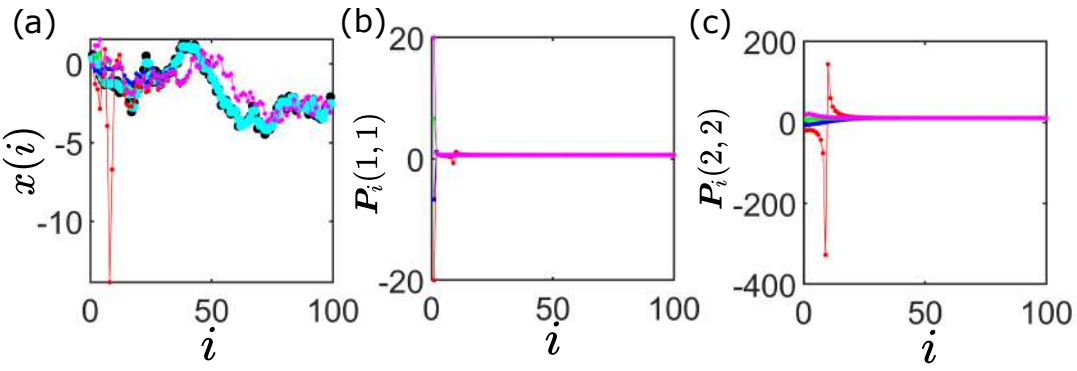

FIGURE 2.12: (a) Simulated state (black) including process-noise (cyan) and estimated state red, blue, green and magenta for different initial values of $\boldsymbol{P}_{0,0}$. For $i > 20$ all estimated states overlap and only the magenta dots are visible. (b),(c) Representation of the components $\boldsymbol{P}_i\,(1,1)$ and $\boldsymbol{P}_i\,(2,2)$ for different initial values as red, blue, green and magenta curve. For $i > 20$ all curves overlap.

and the cyan dots represent the measurements z_k. The red, blue, green and magenta dota correspond to the estimated positions using a Kalman-Filter for different initial guesses $\boldsymbol{P}_{0,0}$ of the covariance matrix $\boldsymbol{P}$. Similar to the impact of the initial guess for the state $\hat{\boldsymbol{x}}_{0,0}$, the impact of the initial guess for the covariance-matrix $\boldsymbol{P}_{0,0}$ leads to a difference of the first few estimates $\hat{x}$.

But after approximately 30 measurement-steps, all the estimates are identical. This is a general feature of the Kalman-Filter, as the estimate after long times shall not depend on initial guesses. The evolution of the diagonal-elements $\boldsymbol{P}_k\,(1,1)$ and $\boldsymbol{P}_k\,(2,2)$ of the covariance-matrix $\boldsymbol{P}_k$ are represented in 2.12 (b) and (c). We see that after approximately 20 measurement-steps they converged to the same value, leading to the same estimates for the position $\hat{x}$ as shown in Fig. 2.12 (a). To understand the impact of the process-noise matrix $\boldsymbol{Q}$ we can have a look at Fig. 2.13 (a). Here we used the Kalman-Filter

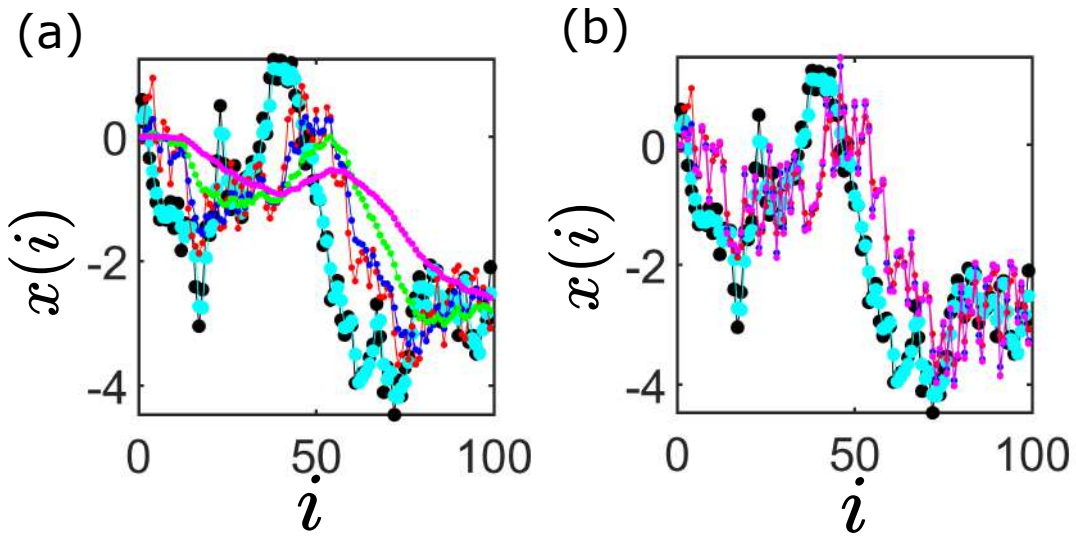

FIGURE 2.13: Representation of the state (black) including process noise (cyan). (a) Estimation of the state with fixed matrix $\boldsymbol{Q}$ and $r = 1$ (red), $r = 10$ (blue), $r = 100$ (green) and $r = 1000$ (magenta). (b) Estimation of the state with $\boldsymbol{Q}$ and $\boldsymbol{R}$ chosen from equation (2.111) and $r = 1$ (red), $r = 10$ (blue), $r = 100$ (green) and $r = 1000$ (magenta).

with four different measurement-noise matrices

$$\boldsymbol{R} = r \tag{2.110}$$

for $r = 1$ (red), $r = 10$ (blue), $r = 100$ (green) and $r = 1000$ (magenta). We see that for larger values of r, the curve of the estimated positions $\hat{x}$ gets smoother. This is due to the fact that a larger matrix for the measurement-noise means a lower importance of the measured positions z_k and a higher importance of the state evolution described via equation (2.70). Therefore before applying the Kalman-Filter it is crucial to quantify the measurement errors and choose a measurement-noise matrix $\boldsymbol{R}$ in accordance to the model. To understand the impact of the process noise matrix $\boldsymbol{Q}$ we choose four different combinations for the process-noise matrix and the measurement-noise matrix

$$\boldsymbol{Q} = \begin{pmatrix} r & 0 \\ 0 & r \end{pmatrix} \text{ and } \boldsymbol{R} = r \tag{2.111}$$

with $r = 1$ (red), $r = 10$ (blue), $r = 100$ (green) and $r = 1000$ (magenta) and show the results in Fig. 2.13 (b). We see that all the curves overlap if the ratio between the diagonal-elements of the process-noise matrix $\boldsymbol{Q}$ and the measurement-noise matrix $\boldsymbol{R}$ keeps the same. This is another important feature of the Kalman-Filter. It can be interpreted in a way that the values represent the amount of trust in the measured and predicted values. Their absolute values do not matter, but their ratio indicated which values are more trustworthy.
In this example we have seen how the Kalman-Filter can be applied to a simple system. Furthermore we have seen that the initial guess for the state of the system $\hat{\boldsymbol{x}}_{0,0}$ as well as the initial guess for the covariance-matrix $\boldsymbol{P}_{0,0}$ only affect the first few measurement steps but do not affect the estimates for large times. Another important fact of the Kalman-Filter is that the absolute values of the diagonal elements of the measurement-noise matrix $\boldsymbol{R}$ and the process-noise matrix $\boldsymbol{Q}$ do not matter. Only their ratio has an impact on the performance of the Kalman-Filter. The Kalman-Filter in this section is suitable to estimate the state of a linear system. To estimate the state of a non-linear system the linear Kalman-Filter can be extended, as explained in the following section 2.3.2.

2.3.2 Extended Kalman-Filter

In this thesis, we investigate systems whose development cannot be described using a linear model. Therefore we cannot apply the *normal* linear Kalman-Filter. To solve this problem, we want to extend the linear Kalman-Filter (KF) from the previous section 2.3.1 to deal with nonlinear problems. This Kalman-Filter will be called Extended Kalman-Filter (EKF). The EKF can be used to estimate the state of a system whose time-evolution is given by the equation

$$\boldsymbol{x}_{k+1} = \boldsymbol{f}\left(\boldsymbol{x}_k, \boldsymbol{u}_k, k\right) + \boldsymbol{u}_k, \tag{2.112}$$

and the transformation from state-space to measurement-space is done via equation

$$\boldsymbol{z}_k = \boldsymbol{h}\left(\boldsymbol{x}_k, k\right) + \boldsymbol{v}_k. \tag{2.113}$$

Here the function $\boldsymbol{f}$ is a function mapping from the state space to the state-space

$$\boldsymbol{f}: \ \mathcal{R}^{d_\mathrm{x}} \rightarrow \mathcal{R}^{d_\mathrm{x}} \tag{2.114}$$

and the function $\boldsymbol{h}$ maps from the state-space to the measurement-space

$$\boldsymbol{h}: \ \mathcal{R}^{d_\mathrm{x}} \rightarrow \mathcal{R}^{d_\mathrm{y}}. \tag{2.115}$$

The expectations for the measurement-noise $\boldsymbol{v}_k$ and process-noise $\boldsymbol{w}_k$ are the same as for the KF:

$$\begin{aligned} \mathrm{E}\left[\boldsymbol{w}_k\right] = 0, \ \mathrm{E}\left[\boldsymbol{v}_k\right] = 0, \ \mathrm{E}\left[\boldsymbol{v}_k \boldsymbol{w}_j^\mathrm{T}\right] = 0 \\ \mathrm{E}\left[\boldsymbol{w}_k \boldsymbol{w}_j^\mathrm{T}\right] = \delta_{kl} \boldsymbol{Q}_k \ \text{ and } \ \mathrm{E}\left[\boldsymbol{v}_k \boldsymbol{v}_j^\mathrm{T}\right] = \delta_{kl} \boldsymbol{R}_k. \end{aligned} \tag{2.116}$$

In the next section we derivate the prediction equations of the EKF.

Prediction

We denote estimation $\hat{\boldsymbol{x}}_{k,k}$ of the state $\boldsymbol{x}_k$ at time k based on the measurements $\boldsymbol{Z}_k = \{z_i | i \leq k\}$ as

$$\hat{\boldsymbol{x}}_{k,k} = \mathrm{E}\left[\boldsymbol{x}_k | \boldsymbol{Z}_k\right]. \tag{2.117}$$

The corresponding covariance matrix $\boldsymbol{P}$ is given as

$$\boldsymbol{P}_{k,k}. \tag{2.118}$$

For further calculations we can expand the function $\boldsymbol{f}$ from equation (2.112) in a Taylor-Series around the point $\hat{\boldsymbol{x}}_{k,k}$, leading to

$$\boldsymbol{x}_{k+1} = \boldsymbol{f}\left(\hat{\boldsymbol{x}}_{k,k}, \boldsymbol{u}_k, k\right) + \boldsymbol{J}\left(\boldsymbol{x}_k - \hat{\boldsymbol{x}}_{k,k}\right) + \mathcal{O}\left[\left(\boldsymbol{x}_k - \hat{\boldsymbol{x}}_{k,k}\right)^2\right] + \boldsymbol{w}_k, \tag{2.119}$$

where the matrix

$$\boldsymbol{J} = \left[\frac{\partial \boldsymbol{f}}{\partial \boldsymbol{x}}\right]_{x=\hat{\boldsymbol{x}}_{k,k}} \tag{2.120}$$

is the Jacobian of the function $\boldsymbol{f}$. Taking the expectation-value of equation (2.119) by ignoring higher than first-order terms leads to

$$\begin{aligned}
\boldsymbol{x}_{k+1} &= \mathrm{E}\left[\boldsymbol{f}\left(\hat{\boldsymbol{x}}_{k,k}, \boldsymbol{u}_k, k\right)\right] + \mathrm{E}\left[\boldsymbol{J}\left(\boldsymbol{x}_k - \hat{\boldsymbol{x}}_{k,k}\right)\right] + \mathcal{O}\left[\left(\boldsymbol{x}_k - \hat{\boldsymbol{x}}_{k,k}\right)^2\right] + \mathrm{E}\left[\boldsymbol{w}_k\right] \\
&= \mathrm{E}\left[\boldsymbol{f}\left(\hat{\boldsymbol{x}}_{k,k}, \boldsymbol{u}_k, k\right)\right] + 0 + 0 \\
&= \boldsymbol{J}\left(\hat{\boldsymbol{x}}_{k,k}, \boldsymbol{u}_k, k\right).
\end{aligned} \tag{2.121}$$

Therefore the predicted state $\hat{\boldsymbol{x}}_{k+1,k}$ is given as

$$\hat{\boldsymbol{x}}_{k+1,k} = \boldsymbol{f}\left(\hat{\boldsymbol{x}}_{k,k}, \boldsymbol{u}_k, k\right). \tag{2.122}$$

To calculate the covariance-matrix $\boldsymbol{P}$, we first have a look at the prediction error $\mathrm{err}\left[\boldsymbol{x}_{k+1}\right]$ at time $k+1$, which is given as

$$\begin{aligned}
\mathrm{err}\left[\boldsymbol{x}_{k+1}\right] &= \boldsymbol{x}_{k+1} - \hat{\boldsymbol{x}}_{k+1,k} \\
&= \boldsymbol{f}\left(\hat{\boldsymbol{x}}_{k,k}, \boldsymbol{u}_k, k\right) + \boldsymbol{J}\left[\boldsymbol{x}_k - \hat{\boldsymbol{x}}_{k,k}\right] + \mathcal{O}\left[\left(\boldsymbol{x}_k - \hat{\boldsymbol{x}}_{k,k}\right)^2\right] + \boldsymbol{w}_k - \boldsymbol{f}\left(\hat{\boldsymbol{x}}_{k,k}, \boldsymbol{u}_k, k\right) \\
&\approx \boldsymbol{J}\left[\boldsymbol{x}_k - \hat{\boldsymbol{x}}_{k,k}\right] + \boldsymbol{w}_k \\
&= \boldsymbol{J}\mathrm{err}\left[\boldsymbol{x}_k\right] + \boldsymbol{w}_k.
\end{aligned} \tag{2.123}$$

The predicted covariance $\boldsymbol{P}_{k+1,k}$ is then given as

$$\begin{aligned}\boldsymbol{P}_{k+1,k} &= \mathrm{E}\left[\mathrm{err}\left[\boldsymbol{x}_{k+1}\right]\mathrm{err}\left[\boldsymbol{x}_{k+1}\right]^{\mathrm{T}}\right] \\ &\approx \mathrm{E}\left[\left(\boldsymbol{J}\mathrm{err}\left[\boldsymbol{x}_{k}\right]+\boldsymbol{w}_{k}\right)\left(\boldsymbol{J}\mathrm{err}\left[\boldsymbol{x}_{k}\right]+\boldsymbol{w}_{k}\right)^{\mathrm{T}}\right] \\ &= \boldsymbol{J}\mathrm{E}\left[\mathrm{err}\left[\boldsymbol{x}_{k}\right]\mathrm{err}\left[\boldsymbol{x}_{k}\right]^{\mathrm{T}}\right]\boldsymbol{J}^{\mathrm{T}}+\mathrm{E}\left[\boldsymbol{w}_{k}\boldsymbol{w}_{k}^{\mathrm{T}}\right] \\ &= \boldsymbol{J}\boldsymbol{P}_{k,k}\boldsymbol{J}^{\mathrm{T}}+\boldsymbol{Q}_{k}. \end{aligned} \tag{2.124}$$

If we compare equations (2.121) and (2.124) with equations (2.99) and (2.100), we see that the Jacobian $\boldsymbol{J}$ in the nonlinear case corresponds to the transition matrix $\boldsymbol{F}_k$ in the linear case.

Update

To update the predicted state-estimate $\boldsymbol{x}_{k+1}$ and covariance-matrix $\boldsymbol{P}_{k+1,k}$, we have to include the measurement z_{k+1}. Expanding equation (2.113) around the predicted state $\boldsymbol{x}_{k+1}$, the equation reads

$$z_{k+1} = \boldsymbol{h}\left(\hat{\boldsymbol{x}}_{k+1,k}\right)+\boldsymbol{J}_{h}\left(\hat{\boldsymbol{x}}_{k+1,k}-\boldsymbol{x}_{k+1}\right)+\mathcal{O}\left[\left(\hat{\boldsymbol{x}}_{\boldsymbol{k+1,k}}-\boldsymbol{x}_{k+1}\right)^{2}\right]+v_{k}, \tag{2.125}$$

where the matrix

$$\boldsymbol{J}_{h} = \left[\frac{\partial \boldsymbol{h}}{\partial \boldsymbol{x}}\right]_{\boldsymbol{x}=\hat{\boldsymbol{x}}_{k,k}} \tag{2.126}$$

is the Jacobian of the function $\boldsymbol{h}$. Taking the expectation value of equation (2.126) yields

$$\hat{\boldsymbol{z}}_{k+1,k} \approx \boldsymbol{h}\left(\hat{\boldsymbol{x}}_{k+1,k}\right). \tag{2.127}$$

The innovation - the difference between predicted-state $\hat{\boldsymbol{x}}_{k+1,k}$ and measured-state - is given as

$$\boldsymbol{v}_{k+1} = \boldsymbol{z}_{k+1}-\boldsymbol{h}\left(\hat{\boldsymbol{x}}_{k+1,k}\right). \tag{2.128}$$

The covariance of the innovation $\boldsymbol{v}_{k+1}$ yields

$$\begin{aligned}\boldsymbol{S}_{k+1} &= \mathrm{E}\left[\boldsymbol{v}_{k+1}\boldsymbol{v}_{k+1}^{\mathrm{T}}\right] \\ &= \mathrm{E}\left[\left(\boldsymbol{z}_{k+1}-\boldsymbol{h}\left(\hat{\boldsymbol{x}}_{k+1,k}\right)\right)\left(\boldsymbol{z}_{k+1}-\boldsymbol{h}\left(\hat{\boldsymbol{x}}_{k+1,k}\right)\right)^{\mathrm{T}}\right] \\ &\approx \mathrm{E}\left[\left(\boldsymbol{J}_{h}\left(\boldsymbol{x}_{k+1,k}-\boldsymbol{x}_{k}\right)+\boldsymbol{v}_{k+1}\right)\left(\left(\boldsymbol{x}_{k+1,k}-\boldsymbol{x}_{k}\right)^{\mathrm{T}}\boldsymbol{J}_{h}^{\mathrm{T}}+\boldsymbol{v}_{k+1}^{\mathrm{T}}\right)\right] \\ &= \boldsymbol{J}_{h}\boldsymbol{P}_{k+1,k}\boldsymbol{J}_{h}^{\mathrm{T}}+\boldsymbol{R}_{k+1}. \end{aligned} \tag{2.129}$$

If we again compare equation (2.129) with equation (2.98), we see that the matrix $\boldsymbol{H}_k$ in the linear case corresponds to the Jacobian $\boldsymbol{J}_h$ in the nonlinear case. If we use again the fact that the Kalman-Filter minimizes the quantity L defined in equation (2.96), we find for the EKF that the Kalman-gain $\boldsymbol{K}$ equals the Kalman-gain $\boldsymbol{K}$ from the linear Kalman-Filter, and therefore is given as

$$\boldsymbol{K}_{k+1} = \boldsymbol{P}_{k+1,k}\boldsymbol{J}_{h}^{\mathrm{T}}\boldsymbol{S}_{k+1}^{-1}. \tag{2.130}$$

The corresponding state- and covariance update equations are given as

$$\begin{aligned} \boldsymbol{x}_{k+1,k+1} &= \boldsymbol{x}_{k+1,k} + \boldsymbol{K}_{k+1}\left(\boldsymbol{z}_{k+1} - \boldsymbol{h}\left(\hat{\boldsymbol{x}}_{k+1,k}\right)\right) \\ \boldsymbol{P}_{k+1,k+1} &= \boldsymbol{P}_{k+1,k} - \boldsymbol{K}_{k+1}\boldsymbol{S}_{k+1}\boldsymbol{K}_{k+1}^{\mathrm{T}}. \end{aligned} \tag{2.131}$$

Summary of the EKF-equations

To summarize, the equations for the EKF consist - as the equations for the KF - of two steps:

1. Prediction: In the prediction step, the *old* estimate $\hat{\boldsymbol{x}}_{k,k}$ and *old* covariance $\boldsymbol{P}_{k,k}$ are updated via the function $\boldsymbol{f}$ from equation (2.112), quantifying the time-evolution of the system:

$$\hat{\boldsymbol{x}}_{k+1,k} = \boldsymbol{f}\left(\hat{\boldsymbol{x}}_{k,k}, \boldsymbol{u}_k, k\right) \tag{2.132}$$

$$\boldsymbol{P}_{k+1,k} = \boldsymbol{J}_f \boldsymbol{P}_{k,k} \boldsymbol{J}_f^{\mathrm{T}} + \boldsymbol{Q}_k. \tag{2.133}$$

2. Update: The predicted quantities $\hat{\boldsymbol{x}}_{k+1,k}$ and $\boldsymbol{P}_{k+1,k}$ are updated based on the *new* measurement $\boldsymbol{z}_{k+1}$ via

$$\hat{\boldsymbol{x}}_{k+1,k+1} = \hat{\boldsymbol{x}}_{k+1,k} + \boldsymbol{K}_{k+1}\left[\boldsymbol{z}_{k+1} - \boldsymbol{h}\left(\hat{\boldsymbol{x}}_{k+1,k}\right)\right] \tag{2.134}$$

$$\boldsymbol{P}_{k+1,k+1} = \boldsymbol{P}_{k+1,k} - \boldsymbol{K}_{k+1}\boldsymbol{S}_{k+1}\boldsymbol{K}_{k+1}^{\mathrm{T}}, \tag{2.135}$$

where

$$\boldsymbol{K}_{k+1} = \boldsymbol{P}_{k+1,k}\boldsymbol{J}_h^{\mathrm{T}}\boldsymbol{S}_{k+1}^{-1} \tag{2.136}$$

and

$$\boldsymbol{S}_{k+1} = \boldsymbol{J}_h \boldsymbol{P}_{k+1,k}\boldsymbol{J}_j^{\mathrm{T}} + \boldsymbol{R}_{k+1}. \tag{2.137}$$

In this section we introduced the Extended Kalman-Filter(EKF). The EKF is an extension to the linear Kalman-Filter (KF), suitable to estimate the state of a nonlinear system described via equations 2.112 and 2.113. In the next section we present another extension of the KF/EKF, suitable to estimate a state of a system whose evolution is based on multiple models.

2.3.3 Multiple-Model Kalman-Filter

In the previous sections 2.3.1 and 2.3.2 we introduced the KF and the EKF. Both of these filters a suitable to estimate the state of a system whose time-evolution is based on a single model. But in reality, the time-evolution of a system can be based on multiple, interacting models. Therefore, in this section we present an extension of the KF/EKF, the interacting multiple-model Kalman-Filter (IMM) introduced in [7], suitable to estimate the state of a system described via the equations

$$\boldsymbol{x}_{k+1} = \boldsymbol{F}_k^j \boldsymbol{x}_k + \boldsymbol{G}_k^j \boldsymbol{u}_k + \boldsymbol{w}_k^j, \tag{2.138}$$

$$\boldsymbol{z}_k = \boldsymbol{H}_k^j \boldsymbol{x}_k + \boldsymbol{v}_k^j. \tag{2.139}$$

Here, the evolution of the system consists of N different models, indicated via the superscript j. If we apply the total probability theorem,

$$p\left(A|C\right) = \sum_{n} p\left(A|C, B_n\right) p\left(B_n|C\right) \tag{2.140}$$

we can calculate the probability of state $\boldsymbol{x}_k$ given the measurements $\boldsymbol{Z}_k$ as

$$\begin{aligned} p\left(\boldsymbol{x}_k|\boldsymbol{Z}_k\right) &= \sum_{j=1}^{N} p\left(\boldsymbol{x}_k|\boldsymbol{M}_k^j, \boldsymbol{Z}_k\right) p\left(\boldsymbol{M}_k^j|\boldsymbol{Z}_k\right) \\ &= \sum_{j=1}^{N} p\left(\boldsymbol{x}_k|\boldsymbol{M}_k^j, \boldsymbol{z}_k, \boldsymbol{Z}_{k-1}\right) \mu_k^j, \end{aligned} \tag{2.141}$$

where the probability-density function (pdf) of the state $\boldsymbol{x}$ is given as

$$p\left(\boldsymbol{x}_k|\boldsymbol{M}_k^j, \boldsymbol{z}_k, \boldsymbol{Z}_{k-1}\right) = \frac{p\left(\boldsymbol{z}_k|\boldsymbol{M}_k^j, \boldsymbol{x}_k\right)}{p\left(\boldsymbol{z}_k|\boldsymbol{M}_k^j, \boldsymbol{Z}_{k-1}\right)} p\left(\boldsymbol{x}_k|\boldsymbol{M}_k^j, \boldsymbol{Z}_{k-1}\right), \tag{2.142}$$

where $p\left(\boldsymbol{x}_k|\boldsymbol{M}_k^j, \boldsymbol{z}_k, \boldsymbol{Z}_{k-1}\right)$ is denoted as the posterior and $p\left(\boldsymbol{x}_k|\boldsymbol{M}_k^j, \boldsymbol{Z}_{k-1}\right)$ is denoted as the prior. The term $\frac{p\left(\boldsymbol{z}_k|\boldsymbol{M}_k^j, \boldsymbol{x}_k\right)}{p\left(\boldsymbol{z}_k|\boldsymbol{M}_k^j, \boldsymbol{Z}_{k-1}\right)}$ is a measurable quantity, suitable to update the prior, resulting in the posterior. This is a basic feature also known in Bayesian probability theory [20, 21, 23]. The total probability theorem from equation 2.140 can also be applied on the prior from equation 2.142, yielding

$$\begin{aligned} p\left(\boldsymbol{x}_k|\boldsymbol{M}_k^j, \boldsymbol{Z}_{k-1}\right) &= \sum_{i=1}^{N} p\left(\boldsymbol{x}_k|\boldsymbol{M}_k^j, \boldsymbol{M}_{k-1}^i, \boldsymbol{Z}_{k-1}\right) p\left(\boldsymbol{M}_{k-1}^i|\boldsymbol{M}_k^j, \boldsymbol{Z}_{k-1}\right) \\ &\approx \sum_{i=1}^{N} p\left(\boldsymbol{x}_k|\boldsymbol{M}_k^j, \boldsymbol{M}_{k-1}^i, \left\{\hat{\boldsymbol{x}}_{k-1,k-1}^l, \boldsymbol{P}_{k-1,k-1}^l\right\}_{l=1}^{r}\right) \mu_{k-1,k-1}^{i,j}. \end{aligned} \tag{2.143}$$

Here we used the fact that the past $k-1$ measurements can be approximated by the N model approximated-states $\hat{\boldsymbol{x}}_{k-1,k-1}^l$ and covariances $\boldsymbol{P}_{k-1,k-1}^l$. The term $\mu_{k-1,k-1}^{i,j}$ can be understood as a transition-probability from model $\boldsymbol{M}^i$ to model $\boldsymbol{M}^j$. As we are only interested in the transition from mode i to j, we can simplify equation 2.143 to

$$p\left(\boldsymbol{x}_k|\boldsymbol{M}_k^j, \boldsymbol{Z}_{k-1}\right) \approx \sum_{i=1}^{N} p\left(\boldsymbol{x}_k|\boldsymbol{M}_k^j, \boldsymbol{M}_{k-1}^i, \hat{\boldsymbol{x}}_{k-1,k-1}^i, \boldsymbol{P}_{k-1,k-1}^i\right) \mu_{k-1,k-1}^{i,j}. \tag{2.144}$$

From equation 2.144 we see that the pdf of state $\boldsymbol{x}_k$ is a weighted sum of probabilities $p\left(\boldsymbol{x}_k|\boldsymbol{M}_k^j, \boldsymbol{M}_{k-1}^i, \hat{\boldsymbol{x}}_{k-1,k-1}^i, \boldsymbol{P}_{k-1,k-1}^i\right)$, where the weight is given

as $\mu^{i,j}_{k-1,k-1}$. We assume that this mixture is a mixture of Gaussian sums, meaning that the pdf for the state $\boldsymbol{x}_k$ is given as a Gaussian sum. The Gaussian sum from equation 2.144 can then be approximated ba a single Gaussian via

$$\begin{aligned} p\left(\boldsymbol{x}_k|\boldsymbol{M}^j_k, \boldsymbol{Z}_{k-1}\right) &\approx \sum_{i=1}^{N} \mathcal{N}\left[\boldsymbol{x}_k; \mathrm{E}\left[\boldsymbol{x}_k|\boldsymbol{M}^j_k, \hat{\boldsymbol{x}}^i_{k-1,k-1}\right]\right] \mu^{i,j}_{k-1,k-1} \\ &\approx \mathcal{N}\left[\boldsymbol{x}_k; \sum_{i=1}^{N} \mathrm{E}\left[\boldsymbol{x}_k|\boldsymbol{M}^j_k, \hat{\boldsymbol{x}}^i_{k-1,k-1}\right]\right] \mu^{i,j}_{k-1,k-1}. \end{aligned} \tag{2.145}$$

If we now use the linearity of the Kalman-Filter, equation 2.145 simplifies to

$$p\left(\boldsymbol{x}_k|\boldsymbol{M}^j_k, \boldsymbol{Z}_{k-1}\right) \approx \mathcal{N}\left[\boldsymbol{x}_k; \mathrm{E}\left[\boldsymbol{x}_k|\boldsymbol{M}^j_k, \sum_{i=1}^{N} \hat{\boldsymbol{x}}^i_{k-1,k-1}\right]\right] \mu^{i,j}_{k-1,k-1}. \tag{2.146}$$

From equation 2.146 we see that the pdf for the state $\boldsymbol{x}_k$ is calculated as a mixing over all models $\boldsymbol{M}^i$, where the state $\hat{\boldsymbol{x}}^i_{k-1,k-1}$ is weighted with a certain factor $\mu^{i,j}_{k-1,k-1}$, which are called mixing probabilities.

The IMM-algorithm

The IMM-filtering process consists of five different steps, which are explained in the following

1. Mixing-probabilities: To calculate the mixing-probabilities $\mu^{i,j}_{k-1,k-1}$ from equation 2.146, we have to understand that the term $\mu^{i,j}_{k-1,k-1}$ has the meaning of being in mode $\boldsymbol{M}^i$ at time $k-1$ given that we know that we are in state $\boldsymbol{M}^j$ at time k. This can be quantified via

$$\begin{aligned} \mu^{i,j}_{k-1,k-1} &= p\left(\boldsymbol{M}^i_{k-1}|\boldsymbol{M}^j_k, \boldsymbol{Z}_{k-1}\right) \\ &= \frac{1}{\bar{c}_j} p\left(\boldsymbol{M}^j_k|\boldsymbol{M}^i_{k-1}, \boldsymbol{Z}_{k-1}\right) p\left(\boldsymbol{M}^i_{k-1}|\boldsymbol{Z}_{k-1}\right). \end{aligned} \tag{2.147}$$

   Above equation 2.147 is usually rewritten as

$$\mu^{i,j}_{k-1,k-1} = \frac{1}{\bar{c}_j} p_{ij} \mu^i_{k-1} \quad i,j \in [1,N], \tag{2.148}$$

   where the normalization constants are given as

$$\bar{c}_j = \sum_{i=1}^{N} p_{i,j} \mu^i_{k-1} \quad j \in [1,N]. \tag{2.149}$$

2. Mixing: We can apply equation 2.146 to calculate the mixed state $\hat{\boldsymbol{x}}_{k-1}^{0,j}$ based on the single state $\hat{\boldsymbol{x}}_{k-1}^{i}$ via

$$\hat{\boldsymbol{x}}_{k-1}^{0,j} = \sum_{i} = 1^{N} \hat{\boldsymbol{x}}_{k-1}^{i} \mu_{k-1,k-1}^{i,j} \quad j \in [1, N] \,. \tag{2.150}$$

The corresponding covariance calculates to

$$\begin{aligned} \boldsymbol{P}_{k-1,k-1}^{0,j} = & \sum_{i=1}^{N} \mu_{k-1,k-1} \cdot \\ & \left(\boldsymbol{P}_{k-1,k-1}^{i} + \left(\hat{\boldsymbol{x}}_{k-1,k-1}^{i} - \hat{\boldsymbol{x}}_{k-1}^{0,j} \right) \left(\hat{\boldsymbol{x}}_{k-1,k-1}^{i} - \hat{\boldsymbol{x}}_{k-1}^{0,j} \right)^{\mathrm{T}} \right) \\ j \in [1, N] \,. \end{aligned} \tag{2.151}$$

3. Mode-matched-filtering: The likelihood Λ_k^j of the measurement $\boldsymbol{z}_k$ for a certain model $\boldsymbol{M}^j$ is given as

$$\Lambda_k^j = p\left(\boldsymbol{z}_k | \boldsymbol{M}_k^j, \boldsymbol{Z}_{k-1} \right), \tag{2.152}$$

and can be computed via the single state-estimate $\hat{\boldsymbol{x}}_{k-1}^{0,j}$ and covariance $\boldsymbol{P}_{k-1,k-1}^{0,j}$ from equation 2.150 and 2.151 as

$$\begin{aligned} \Lambda_k^j &= p\left(\boldsymbol{z}_k | \boldsymbol{M}_k^j, \hat{\boldsymbol{x}}_{k-1,k-1}^{0,j}, \boldsymbol{x}_{k-1,k-1}^{0,j} \right) \\ &= \mathcal{N}\left[\mathrm{err}\left(\hat{\boldsymbol{x}}_k \right); 0, \boldsymbol{S}_k^j \right]. \end{aligned} \tag{2.153}$$

4. Mode probability update: The probability μ_k^j of being in mode $\boldsymbol{M}^j$ at time k is calculated as

$$\begin{aligned} \mu_k^j &= p\left(\boldsymbol{M}_k^j | \boldsymbol{Z}_k \right) \\ &= \frac{1}{c} p\left(\boldsymbol{z}_k | \boldsymbol{M}_k^j, \boldsymbol{Z}_{k-1} \right) p\left(\boldsymbol{M}_k^j | \boldsymbol{Z}_{k-1} \right) \\ &= \frac{1}{c} \Lambda_k^j \sum_{i=1}^{N} p\left(\boldsymbol{M}_k^j | \boldsymbol{M}_{k-1}^i, \boldsymbol{Z}_{k-1} p\left(\boldsymbol{M}_{k-1}^i | \boldsymbol{Z}_{k-1} \right) \right) \\ &= \frac{1}{c} \Lambda_k^j \sum_{i=1}^{N} p^{i,j} \mu_{k-1}^i \\ &= \frac{1}{c} \Lambda_k^j \bar{c}_j \quad j \in [1, N] \,, \end{aligned} \tag{2.154}$$

where the normalization constant c is calculated as

$$c = \sum_{j=1}^{N} \Lambda_k^j \bar{c}_j. \tag{2.155}$$

5. Estimate and covariance combination: Applying the probability μ_k^j defined in equation 2.154 we can calculate the state-estimate $\hat{\boldsymbol{x}}_{k,k}$ and the state covariance $\boldsymbol{P}_{k,k}$ at time k via

$$\hat{\boldsymbol{x}}_{k,k} = \sum_{j=1}^{N} \hat{\boldsymbol{x}}_{k,k}^j \mu_k^j,$$

$$\boldsymbol{P}_{k,k} = \sum_{j=1}^{N} \mu_k^j \left(\boldsymbol{P}_{k,k}^j + \left(\hat{\boldsymbol{x}}_{k,k}^j - \hat{\boldsymbol{x}}_{k,k} \right) \left(\hat{\boldsymbol{x}}_{k,k}^j - \hat{\boldsymbol{x}}_{k,k} \right)^{\mathrm{T}} \right). \tag{2.156}$$

In this section we introduced the IMM, suitable to estimate the state $\boldsymbol{x}$ of a system whose time-evolution can consist of N different models $\boldsymbol{M}^i$. Furthermore, for each time-step k the IMM-filter yields the probability μ_k^i of the system being in state $\boldsymbol{M}^i$.

Chapter 3

3D Particle-Tracking

Understanding the underlying dynamics of bacteria locomotion is still a challenging task. It requires the acquisition of high frequency and high quality images of bacteria-locomotion over a long period of time. In the past 40 years there has been a huge improvement starting from the first 2D-images acquired by Berg [19]. Through their - at this time - outstanding experimental set-up [15] they observed the so called run- and tumbling dynamics of *E. coli* bacteria. In the following years, 2D imaging and tracking of multiple different bacteria was optimized [13, 39, 87, 92, 180]. However, these conventional 2D tracking techniques cannot hold up with the 3D movement of bacteria - especially for free swimming bacteria. Bacteria tend to leave the focal plane z_f, resulting in short trajectories if the focal plane z_f cannot be adapted. Furthermore statistics might be biased if only the 2D projection is observed. To deal with the 3D movement of bacteria, 3D imaging and tracking techniques have been developed, such as a piezo-stage without feedback [40] or defocussing rings [179]. However, these so called Eulerian-type methods [38, 115, 136, 162] struggle with the problem that the volume of observation is fixed in the laboratory reference frame, allowing no feedback to the tracking process. To deal with this problem, Lagrangian methods have been developed to allow 3D tracking with feedback control to the measurement-setup. These Lagrangian methods either mechanically move the sample in z-direction [42, 104] or use phase-contrast [167] to adapt the measurement-settings, providing the possibility to follow bacteria over larger distances compared to a fixed setup. However, both of these methods have intrinsic problems. The mechanical interaction with the sample can lead to undesired effects, especially in case of high frequency oscillations of the sample. Furthermore it is nearly impossible following fast-moving bacteria due to mechanical limitations. Using phase-contrast for 3D tracking has a small z-width and struggles in case of high particle densities.
In this chapter we present a method allowing us 3D tracking over several mm in the xy and $1\,mm$ in the z-range without any mechanical interaction with the sample. In the next section we will describe the experimental setup. The interesting new part in this bacterium is the electrically focus tunable lens (ETL) mounted between camera and objective, allowing us to adjust the focal plane z_f inside the sample without any mechanical interaction [26, 52, 68, 102, 122, 152]. The focal plane z_f is changed by applying a current to the lens, forcing it to change shape. Through this change in the focal-plane z_f we are able to track particles in three dimensions. We will compare three methods

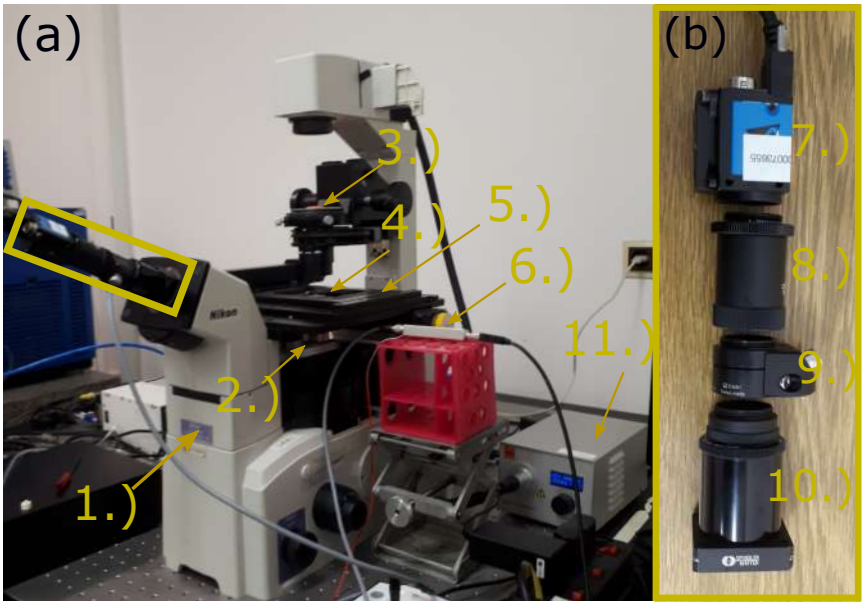

FIGURE 3.1: (a) Representation of the measurement setup with 1.) microscope, 2.) objective, 3.) modification for Darkfield-microscopy, 4.) sample, 5.) xy-moving stage, 6.) driver for the electrically focus tunable lens (ETL) and 11.) the light-source. (b) Zoom for several components marked in (a) with 7.) camera, 8.) adapter, 9.) electrically focu stunable lens (ETL) and 10.) mount.

in section 3.4 to determine the current height z of a particle. In section 3.5 we will present our algorithm to track particles in three dimensions. We applied this tracking algorithm on beads, which allows us to compare the calculated MSD based on the three-dimensional tracked bead-trajectories with the theoretical value. Afterwards we apply the tracking algorithm on bacteria.

3.1 Experimental setup

The size of the particles observed in this thesis is in the range of several μm. In this section we will describe the setup to image particles of this size. The experimental setup we use is represented in Fig. 3.1. We first give a brief overview about the different components, and will have a detailed discussion about all the components used afterwards. The following components are represented in Fig. 3.1:

1.) Optical Microscope: The optical microscope is a device to obtain a magnified image of a specimen using visible light. The working principle of an optical microscope is described in section 3.1.1.

2.) Objective: The objective belongs to the general setup of an optical microscope and is a crucial part to obtain a magnified image of the sample. A discussion about objectives and its impact to image quality is given in section 3.1.2.

3.) Coin: We use a simple coin to perform darkfield-microscopy. This kind of microscopy is used to increase the contrast. The principle of darkfield-microscopy is explained in section 3.1.3.

4.) Specimen: The specimen we want to observe is placed at this position.

5.) xy-movable-stage: This stage can be used to move the specimen in the x- and y-direction. We use a connection to the computer to control the stage-position via the programming language Python. A discussion about the stage is given in section 3.1.4.

6.) ETL-Driver: This driver is connected to the electrically-focus tunable lens (ETL) and the computer. We control the ETL by sending signals via our measurement-code in Python to the Driver, which transfers the control to a certain current c applied to the ETL.

7.) Camera: We use a digital camera to transfer the image obtained via microscope to the computer. This allows a quantitative evaluation of the observed images.

8.) Adapter: We can use adapters of different length to tune the distance between camera and ETL, which has a huge impact on the obtained image. The relation between the obtained image via the microscope and the length of the adapter is discussed in section 3.2.4.

9.) Electrically focus tunable lens (ETL): The ETL is a lens distributed by *optotune* which changes its shape based on the applied current. The impact of the ETL to the obtained image is discussed in section 3.2.

10.) Mount: Custom build mount to connect the ETL and/or the camera to the microscope.

11.) Light-source: Provides light to the microscope to obtain an image of the sample.

In the following sections we will discuss the several pieces of the measurement setup. We will start with the main component, the microscope, in the following chapter.

3.1.1 Optical microscope

In our experiments we use an optical microscope to obtain magnified images of the specimen. The term *optical* refers to the fact that we work with optical visible light. For our setup, the used light is provided as red light with a wavelength of $\lambda = 635\,nm$ by the light-source denoted as 11 in Fig. 3.1. In Fig. 3.2 we see the setup of a *simple* optical microscope (Fig. 3.2 (a)) and a *compound* optical microscope (Fig. 3.2 (b)).

First we will have a brief discussion about the *simple* optical microscope. A more detailed explanation of this microscope can be found in [46].

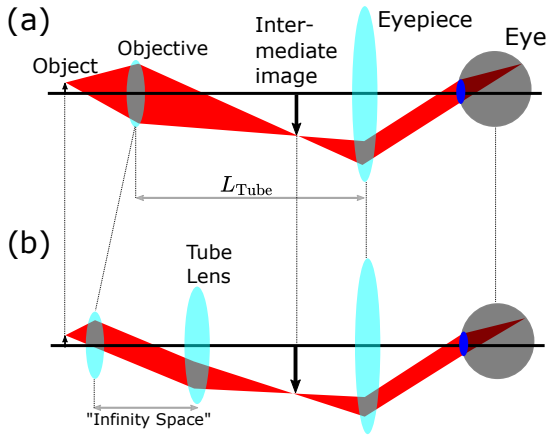

FIGURE 3.2: (a) Schematic representation of a *simple* optical microscope. The light coming from an object passes the objective, creating an intermediate image at a fixed distance L_{Tube} behind the objective. After the light is passed through the eyepiece a magnified image of the object can be observed. (b) Schematic representation of the compound optical microscope. The main difference to the simple optical microscope represented in (a) is the tube-lense, creating parallel light-rays between the object and the objective, the *Infinity-Space*. The tube lens creates an intermediate image. After passing through the eyepiece, the magnified image of the object can be observed.

Simple optical microscope

The first optical microscopes are denoted as simple optical microscopes. Their working principle is schematically represented in Fig. 3.2 (a). Light emerging from an object passes the objective, resulting in an intermediate, magnified image. The intermediate image is further magnified by the eyepiece and thereafter can be observed by the human eye. As the distance L_{Tube} is fixed - typically as $L_{\text{Tube}} = 160\,mm$, only a limited amount of additional optical devices can be brought in the space between the objective and the intermediate image. Furthermore, if these additional optical devices change the effective length of the light path, even more additional optical devices have to be brought into the light path to rearrange the effective length of the light path to L_{Tube}. As the *simple* optical microscope introduces several problems due to its fixed tube length L_{Tube}, a new kind of microscope, the *infinity-corrected* (or *compound*-) optical microscope was invented.

Compound optical microscope

The setup of a compound optical microscope is represented in Fig. 3.2 (b). We see that compared to the *simple* optical microscope an additional lens , the Tube Lens is brought in the light path between objective and eyepiece. The distance between objective and specimen is arranged so that the light-rays in the *infinity*-space , the space between the objective and the Tube Lens, are parallel. The Tube Lens creates the intermediate image and the eyepiece

FIGURE 3.3: (a) Image of two different objectives with magnification $m = 10$ and numerical aperture NA $= 0.3$ (left) and magnification $m = 4$ and numerical aperture NA $= 0.1$ (left).

magnifies the intermediate image and finally the image can be observed. The advantage of this setup lies within the fact that the light-rays in the *infinity*-space are parallel, meaning that this distance can be adapted to an arbitrary value, as no intermediate image is created in this space. Therefore any additional optical devices can be brought into the *infinity*-space as the effective light-path is not relevant as in the setup of the *simple* optical microscope. Due to the ability to include an arbitrary amount of additional optical devices in the light-path, modern optical microscopes are usually compound optical microscopes. These microscopes are marked with a printed ∞-symbol.

3.1.2 The objective

The objective used in the microscopical-setup has a huge impact on image quality and the magnification. An objective is mainly characterized by two different quantities, the magnification m and the numerical aperture NA, usually labeled as "m/NA" on the objective. E.g. the magnification m and numerical aperture NA of the left objective represented in Fig. 3.3 are $m = 10$ and NA $= 0.3$, and $m = 4$ and NA $= 0.1$ for the right objective in Fig. 3.3. Whereas the magnification m refers only to the magnification of the objective, the numerical aperture NA has an impact on several quantities, such as image quality and depth of field. After introducing the numerical aperture NA, we will discuss its impact on image quality and depth of field. The numerical aperture NA characterizes the range of angles over which the system can accept light. It is defined as [117]

$$\text{NA} = n \sin(\alpha), \tag{3.1}$$

where n describes the refraction index of the medium between specimen and objective, and α is the maximal half-angle of the cone of light that can enter or exit the lens. In Fig. 3.4 we visualized both the impacts of the angle α (Fig. 3.4 (a)) and refraction index n (Fig. 3.4 (b)). It can be seen from Fig.

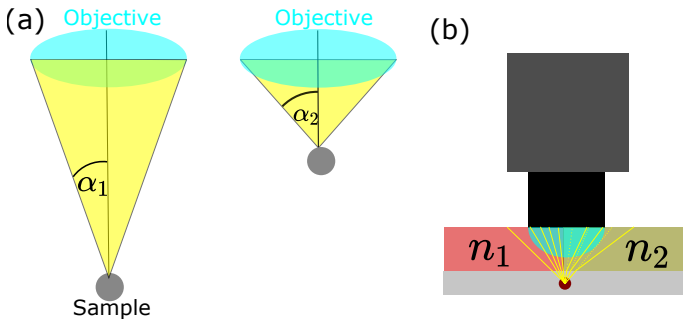

FIGURE 3.4: (a) Impact of the angle α from equation 3.1. A larger angle α enables the microscope to *collect* more light, resulting in more information and therefore better image quality. (b) Impact of the refraction-index n from equation 3.1 for two materials with $n_1 > n_2$. Due to the higher refraction of the material with n_1, more light can be collected, resulting in a better image quality.

3.4 (a) that in case of a larger angle α the objective is able to accept more light from the specimen. The range of the light which can be accepted by the objective is furthermore influenced by the refraction index n (Fig. 3.4 (b)), as this index describes the refraction of the light leaving the specimen. A larger refraction index n_1 results in a smaller refraction and therefore more light can be observed by the objective as in case of a lower refraction index n_2.

Image quality

The quality of the obtained image is heavily influenced by the numerical aperture NA of the objective. To understand the impact of the numerical aperture NA on the image quality, it is crucial to understand the image obtained for a point source [117]. In Fig. 3.5 (a) and (d), we see the light captured for an objective with a lower (a) and higher (d) numerical aperture NA. We see that in case of a larger numerical aperture NA, the objective is able to capture light for a broader angle α. The corresponding three dimensional observed signal for a point source is represented in Fig. 3.5 (b) and (e). This signal of a point-source can be described by an airy disk [103]. It is important to realize that in case of a lower numerical aperture NA, the signal appears broader, resulting in lower image quality. This broadening furthermore influences the minimal distance d_{min} between two point sources which can be distinguished. Therefore we show the signal for two identical point-sources having the same wavelength λ separated by a distance d obtained via an objective with a low numerical aperture NA in Fig. 3.5 (c) and the corresponding signal obtained via an objective with a larger numerical aperture NA in Fig. 3.5 (f). We see from Fig. 3.5 (c) that the main maxima overlap and it is hard to distinguish both point-sources. The minimal distance d_{min} for which individual point-sources can be distinguished was calculated by Abbe to [103]

$$d_{\text{min}} = \frac{0.61\lambda}{\text{NA}}, \tag{3.2}$$

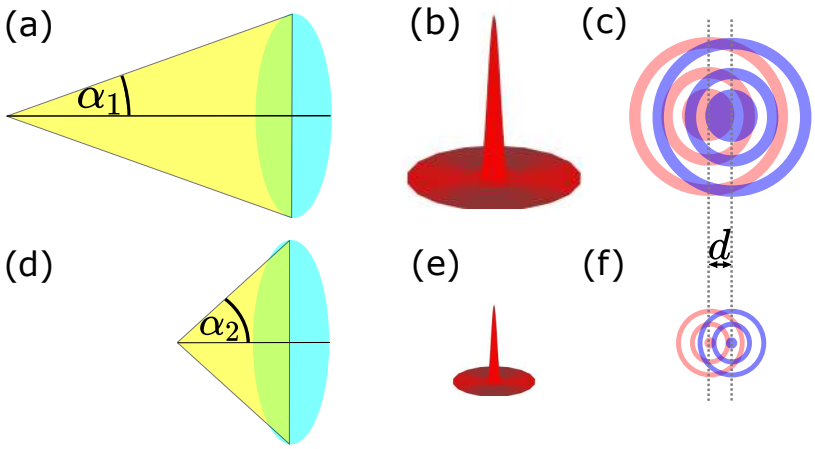

FIGURE 3.5: Comparison between the detected signal of a two point-sources with low ((a),(b),(c)) and high ((d),(e),(f)) NA. In case of a low NA, the signal (b), an Airy-disk, appears broader compared to a higher NA (e). The broadness of the signal in case of low NA makes it impossible to distinguish the signal of close points separated by a distance d (c), whereas in case of high NA (f) it is possible to distinguish the center of both signals.

where λ describes the wavelength of the illuminating light.

Depth of field

Besides the image quality, the numerical aperture NA also influences the depth of field, usually denoted as DOF. To understand what depth of field means, we can have a look at Fig. 3.6. In Fig. 3.6 (b) we can see the image of a μm-scale rotated around the axis represented as the red solid line. We put the part of the μm-scale corresponding to the red solid line in the focal plane of the microscope. Due to the tilting it is impossible that the whole scale is in the focal-plane of the microscope, hence we see the scale over the whole x-range of the image. For positions (x, y) with increasing distances x to the red solid line, the scale gets more and more blurred. The range Δz_{DOF} in which we obtain sharp images of a specimen around the focal plane is denoted as depth of field. The depth of field Δz_{DOF} is represented in Fig. 3.6 (a) and can be calculated via

$$\Delta z_{\text{DOF}} = \frac{\lambda \sqrt{n^2 - \text{NA}^2}}{\text{NA}^2}, \tag{3.3}$$

where n denotes the refractive index between sample and objective, λ the wavelength of the illuminating light and NA the numerical aperture of the objective.

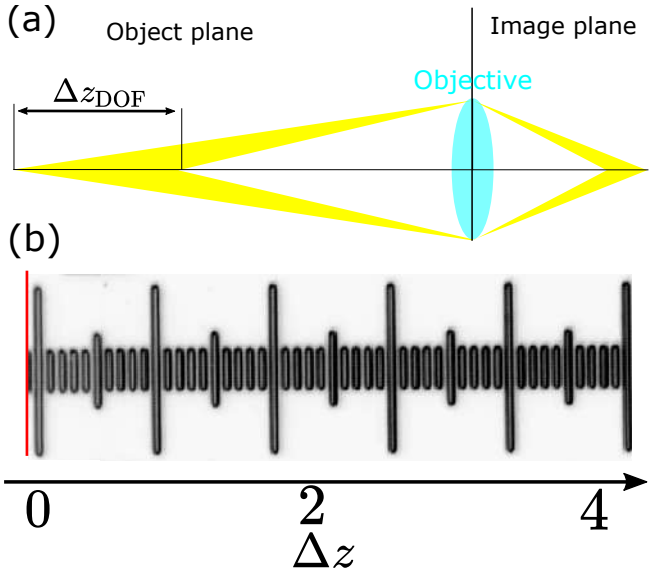

FIGURE 3.6: (a) Representation of the depth of field Δz_{DOF}, representing the area around the focal plane where objects can be detected. (b) Image of a scale out of the horizontal plane. The distance Δz of the scale to the focal plane increases to the right. Due to the depth of field Δz_{DOF}, a certain range of the scale can be observed as a sharp although it is not in the focal plane.

3.1.3 Brightfield- vs Darkfield-microscopy

The microscope-setup introduced in Fig. 3.2 (b) is suitable for bright-field (BF) microscopy. The principle of this method is schematically represented in Fig. 3.7 (a). The light provided by a light source is focused by a condenser and illuminates the transparent sample. The light passing through the specimen is collected via the objective. As light cannot pass the structures in the specimen, the structure appears as black spots on white ground. An example for an image obtained via brightfield-microscopy can be seen in Fig. 3.7 (c). In contrast to brightfield-microscopy, we can block the light passing through the sample and reaching the objective, as represented in Fig. 3.7 (b). Now light passing through the sample cannot be detected by the objective anymore. The only light detected by the objective is light which is scattered at a structure in the specimen. An example for an image obtained via darkfield-microscopy is represented in Fig. 3.7 (d). We see a black ground as non-scattered light is not entering the objective. The white structure is observed as the scattered light changes its direction and therefore can enter the objective. The advantage in darkfield-microscopy is its higher contrast. Due to this higher contrast, smaller structures can be observed. In Fig. 3.7 (c) and (d) we marked two positions with a red circle. Both images have been obtained for the same sample. In case of darkfield-microscopy we can observe small structures inside the red circles. For the image obtained via brightfield-microscopy no structure can be observed. Furthermore brightfield-microscopy is much more sensitive to dust in the optical setup. The positions marked as blue dots in Fig. 3.7 (c) show a certain structure.

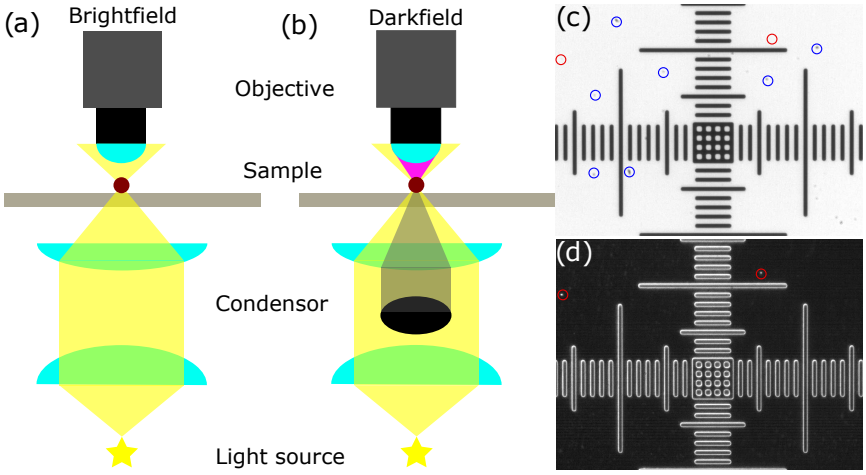

FIGURE 3.7: Comparison between brightfield- (a) and darkfield-microscopy (b). For brightfield microscopy, the light emitted by a light-source passes the sample. This creates an image as represented in (c), where the white background arises from the passing light and the dark areas correspond to the observed structure. In case of darkfield-microscopy, the directly passing light is blocked and only scattered light inside the sample can be detected. This results in a dark background, whereas the structure is visible as the white areas.

But this structure does not arise based on the sample but based on dust in the optical path and dust-particles on the lenses. In Fig. 3.7 (d) we do not observe this dust.

3.1.4 XY-Stage

Active particles move with velocities up to 40 $\frac{\mu m}{s}$, and therefore tend to leave the focal plane z_f as well as the region of interest (ROI) in the x- and y-direction. To deal with the second problem, we mounted our sample on a stage which can be moved in both the x- and the y-direction. The stage is connected to the computer and can be controlled by a Communication port (COM). We use the python-programming language to communicate with the stage. While live tracking a particle, we only move the stage if a particle tend to leave the focal plane.

3.2 Electrically-focus-tunable lens

In section 3.1.1 we described the setup of a standard optical microscope. This optical microscope has a certain focal plane z_f, in which we can observe sharp particles. It is sharp when the light-rays from the specimen meet in the intermediate image plane. This is schematically represented in Fig. 3.8 (a). We see that the light-rays from the specimen pass the objective and Tube Lens, crossing each other in the intermediate image plane at distance L_{TI} from the Tube Lens. As for the microscopic setup we have a fixed distance L_{TI}, changing the

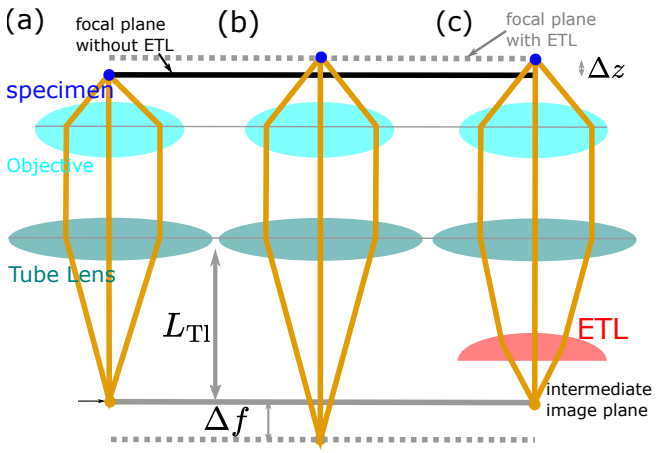

FIGURE 3.8: (a) A specimen placed right at the focal plane of the microscope will create an intermediate image at distance L_{TI} behind the Tube Lens. (b) Changing the height z of the specimen by a distance Δz will shift the position of the intermediate image by a distance Δf. (c) To compensate the shifting of the specimen by a distance Δz we can mount a new lens, ETL, between the Tube Lens and the intermediate image position. Due to the additional refracting, the intermediate image is now located again at a distance L_{TI} behind the Tube Lens.

specimen height z will create the intermediate image at a different position. In Fig. 3.8 (b) we simulated the impact of moving the height z of the particle by a distance Δz. We see that the intermediate image will shift by a distance Δf and therefore the obtained image will not be sharp anymore. There are several tracking methods where the specimen is placed on a mountable stage in z direction, and the height of the specimen will be adapted so that the particle always keeps in the focal plane. However this method has the intrinsic disadvantage of interacting with the sample. Furthermore the speed by mechanically adapting the sample height has its limitations, especially in case of fast moving particles. Another method to counter the effect of moving the specimen out of focus by a distance Δz is the mounting of an additional lens between Tube Lens and image plane. The effect of this additional lens, named as ETL, is represented in Fig. 3.8 (c). Due to the additional refraction of the light, the intermediate image is shifted to the desired distance of L_{TI} behind the Tube Lens. In this example the ETL is able to correct the impact of shifting the height of the specimen by Δz. For changes of the specimen height different than Δz, the intermediate image will again be at a different position than L_{TI} behind the Tube Lens. For an arbitrary distance Δz of changing the height z of the specimen, we need a lens which can change its shape to map the intermediate image to a distance L_{TI} behind the Tube Lens. A lens which is able to adapt is shape is the electrically focus tunable lens (ETL) provided by the company *optotune* (Bernstrasse 388, 8953 Dietikon, Switzerland). The change of the ETL-shape is controlled by a certain electrical current in the range from $I = 0\,mA$ to $I = 300\,mA$. The ETL has a broad range of applications, e.g. optical coherence tomography (OCT) [161], medicine [183],

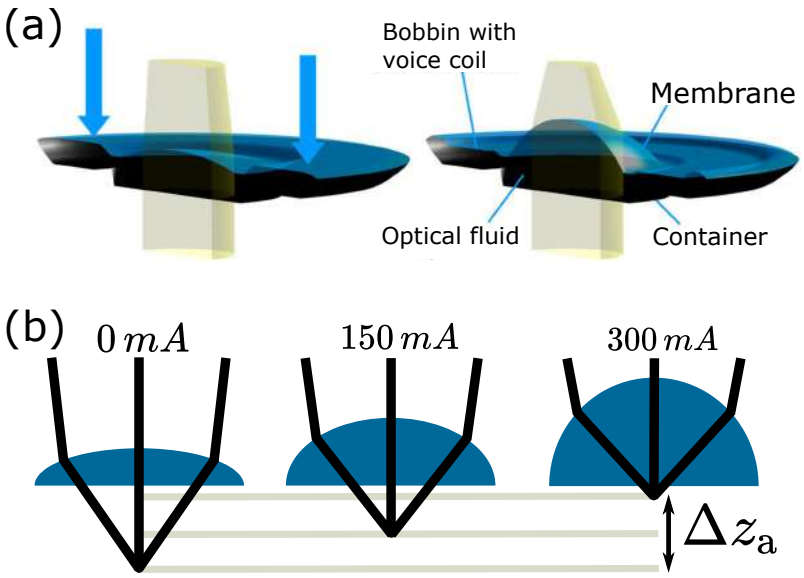

FIGURE 3.9: (a) Working principle of the ETL: By applying a current c on the ETL pressure is exerted on the membrane, forcing it to change shape. (b) Imapct on different shapes of the ETL on the intersection point of transmitting light-rays.

dielectric structures [6, 110, 152], neuronal cell populations [57], optics [26], digital holographic microscopy [144] and confocal-microscopy [69].
In the following section 3.2.1 we describe the working principle of the ETL. Afterwards in sections 3.2.2 and 3.2.3 we will discuss the impact of the ETL to the observed images compared to the images obtained without an ETL.

3.2.1 Working principle

To understand the working principle, we can first have a look at Fig. 3.9 (a). This image is taken from the datasheet provided by *optotune* to describe the ETL. We see that the ETL consits of an optical fluid, which is confined by a container to the bottom and by a membrane to the top. The upper deflection of the lens is proportional to the pressure in the optical fluid. The ETL has an electromagnetic actuator which exerts pressure when current is applied. Hence, the shape of the ETL can be controlled by applying a current. The current is typically chosen in the range from $I = 0\,mA$ to $I = 300\,mA$. In 3.9 (a) we see the impact of the shape of the ETL on passing light. The more current is applied to the ETL, the closer the focal point approaches the ETL. The maximal change in the focal plane defined via the quantity Δz_a can be varied by changing the distance L between camera and ETL. A quantitative discussion of this topic is done in section 3.2.4.

3.2.2 Influence of the ETL: Shifting

In this section we investigate the impact of the ETL to the obtained images. We distinguish two cases. First we compare images $\mathrm{im}_{\mathrm{nE}}$ obtained without an ETL and images im_0 obtained with an ETL for no applied current ($c = 0\,mA$).

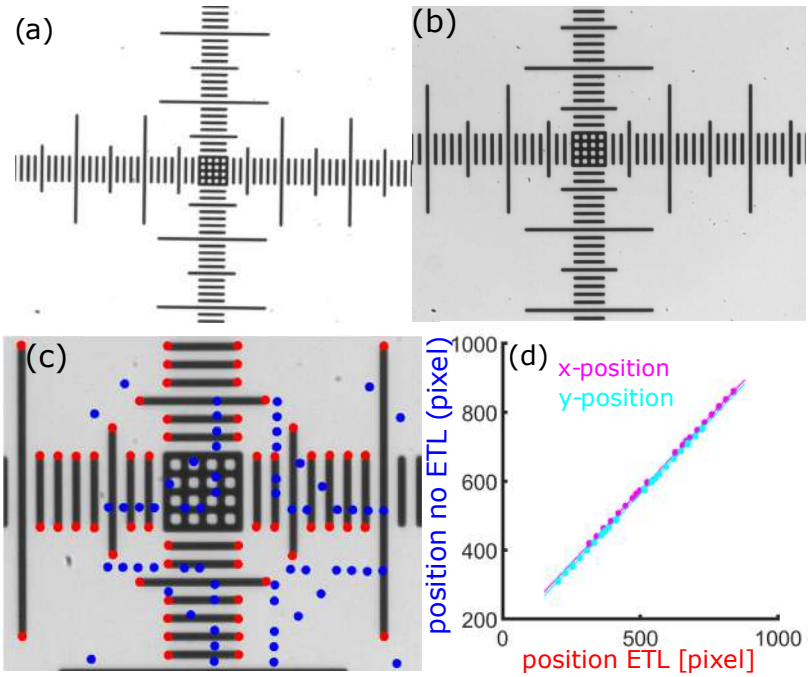

FIGURE 3.10: Comparison between images $\mathrm{im}_{\mathrm{nE}}$ (a) and im_0 (b). A comparison between corresponding tracked positions $\boldsymbol{p}_{\mathrm{nE}} = (x_{\mathrm{nE}}, y_{\mathrm{nE}})$ (blue) and $\boldsymbol{p}_0 = (x_0, y_0)$ (red) in (c) indicates that the ETL shifts positions. (c) Linear relation between positions $\boldsymbol{p}_{\mathrm{nE}} = (x_{\mathrm{nE}}, y_{\mathrm{nE}})$ and $\boldsymbol{p}_0 = (x_0, y_0)$.

Afterwards we compare images im_{150} obtained with an ETL and an applied current $c = 150\,\mu m$ and images im_c obtained with an ETL for the applied current c. Correspondingly we denote tracked positions observed without an ETL as $\boldsymbol{p}_{\mathrm{nE}} = (x_{\mathrm{nE}}, y_{\mathrm{nE}})$ and tracked positions obtained with an ETL as $\boldsymbol{p}_c = (x_c, y_c)$, where c denotes the applied current.

No applied current

In Fig. 3.10 a first comparison between images $\mathrm{im}_{\mathrm{nE}}$ (a) and im_0 (b) can be seen. We see that there is a shift between both images $\mathrm{im}_{\mathrm{nE}}$ and im_0. To quantify this observation we tracked corresponding parts of the images represented in Fig. 3.10 (a) and (b). In Fig. 3.10 (c) we show an image im_0 with tracked positions $\boldsymbol{p}_0$ represented as the red dots. The corresponding positions $\boldsymbol{p}_{\mathrm{nE}}$ are represented as the blue dots. To analyze the relation between positions $\boldsymbol{p}_{\mathrm{nE}}$ and $\boldsymbol{p}_0$ we plotted the x- (magenta) and y (cyan) -component of positions $\boldsymbol{p}_{\mathrm{nE}}$ vs the x- and y-components of positions $\boldsymbol{p}_{\mathrm{nE}}$ in Fig. 3.10 (d). We observe a linear relation between x_{nE} and x_0, as well as between y_{nE} and y_0. Fitting a second order polynomial yields

$$x_{\mathrm{nE}} = a_x + b_x\, x_0 + c_x \cdot 10^{-7}\, x_0^2 \tag{3.4}$$
$$y_{\mathrm{nE}} = a_y + b_y\, y_0 + c_y \cdot 10^{-7}\, y_0^2. \tag{3.5}$$

where $a_x = 152.5$, $b_x = 0.84$, $c_x = 1.2$, $a_y = 140.7$, $b_y = 0.84$, $c_y = 2.1$. We

see from equations (3.4) and (3.5) that the ETL introduces a linear shift to the image, as the nonlinear parameters can be neglected. As both coefficients b_x and b_y are smaller 0, the ETL shrinks the image.

Applied current

In this section we compare positions obtained from images $\mathrm{im}_{c_{\mathrm{re}}}$ for an applied current $c = c_{\mathrm{re}}$ with positions obtained from images im_c for an applied current c. The images $\mathrm{im}_{c_{\mathrm{re}}}$ can be seen as a reference image. To quantify position-shifts we tracked the positions $\boldsymbol{p}_c$ of several beads attached to the surface of a microscope-slide for different applied currents c. The tracked positions are represented as red dots in Fig. 3.11 (a).

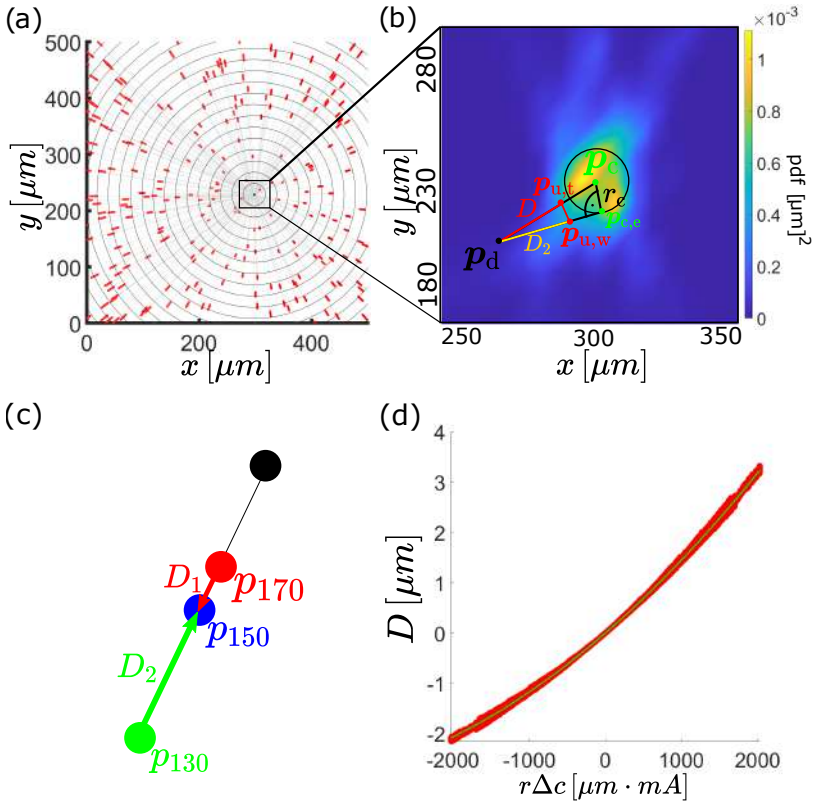

FIGURE 3.11: (a) Positions $\boldsymbol{p}_c$ tracked for multiple attached beads to the surface of a microscope slide for different applied currents c with linear fits through corresponding positions. (b) Probability density function for the intersection of linear fits from (a). The mean of the pdf defines the center of distortion $\boldsymbol{p}_{\mathrm{ce}}$. (c) We set our reference-frame to $c_{\mathrm{r}} = 150\,mA$. For currents $c < c_{\mathrm{r}}$ (green), positions move away from the center of distortion $\boldsymbol{p}_{\mathrm{ce}}$ (black). For currents $c > c_{\mathrm{r}}$ (red), positions move closer from the center of distortion $\boldsymbol{p}_{\mathrm{ce}}$ (black). (d) Relation between the shift D and the product $r\Delta c$.

We performed a linear fit for the tracked positions for each bead $\boldsymbol{p}_c = (x_c, y_c)$. All these linear fits meet in a small region, represented as a probability-density function in Fig. 3.11 (b) for the marked region in Fig. 3.11 (a). (To

be strict, this is only true in case of frequencies $f < 50\,Hz$. The limitations in using the ETL are discussed in section 3.2.5. But as we use frequencies $f \leq 10\,Hz$ we can assume that the linear fits in Fig. 3.11 (b) meet in a small circle.) We denote the mean of the region represented in Fig. 3.11 (b) as the center of distortion

$$\boldsymbol{p}_{\mathrm{ce}} = (x_{\mathrm{ce}}, y_{\mathrm{ce}})\,. \tag{3.6}$$

The black circle of radius $r_{\mathrm{ce}} = 5.4\,\mu m$ in Fig. 3.11 (b) displays the area which contains more than 98 % of the crossing-points of the linear fits. For each tracked bead-position $\boldsymbol{p}_c$ we calculate the distance r to the center via

$$r = \sqrt{(x_{\mathrm{ce}} - x_c)^2 + (y_{\mathrm{ce}} - y_c)^2}. \tag{3.7}$$

Furthermore for each tracked position we calculate the difference in current Δc between the applied current c and the reference-current $c_{\mathrm{re}} = 150\,mA$

$$\Delta c = (c_{\mathrm{re}} - c)\,. \tag{3.8}$$

For different currents c we track fixed particles at a different position $\boldsymbol{p}_c$. To provide an example we can have a look at Fig. 3.11 (c). There we see the tracked position $\boldsymbol{p}_c$ of a bead for three different currents $c = 130\,mA$ (green dot), $c = 150\,mA$ (blue dot) and $c = 170\,mA$ (red dot). The green and the red arrows represent the shift which is required to map positions $\boldsymbol{p}_{130}$ and $\boldsymbol{p}_{170}$ to their reference-position $\boldsymbol{p}_{c_{\mathrm{re}}}$ with $c_{\mathrm{re}} = 150\,mA$. We see that both arrows $\boldsymbol{D}_1$ and $\boldsymbol{D}_2$ point in different directions, which is due to the fact that Δc from equation (3.8) can either be positive or negative. It is important to mention that the absolute value of the shift D_1 obtained for $\Delta c = a > 0$ and the shift D_2 obtained for $\Delta c = -a < 0$ are not equal but rather $D_1 < D_2$. To shift the position $\boldsymbol{p}_c$ to its reference position $\boldsymbol{p}_{c_{\mathrm{re}}}$ we make the following Ansatz:

$$\boldsymbol{D} = \left(\gamma_1 r\Delta c + \gamma_2 \left(r\Delta c\right)^2\right)\boldsymbol{u}. \tag{3.9}$$

For above $\boldsymbol{u}$ acts as the unity vector between the tracked position $\boldsymbol{p}_c$ and the center of distortion $\boldsymbol{p}_{\mathrm{ce}}$

$$\boldsymbol{u} = \frac{1}{|\boldsymbol{p}_c - \boldsymbol{p}_{\mathrm{ce}}|}\boldsymbol{p}_c - \boldsymbol{p}_{\mathrm{ce}}. \tag{3.10}$$

The reference-position $\boldsymbol{p}_{c_{\mathrm{re}}}$ can be obtained via

$$\boldsymbol{p}_{c_{\mathrm{re}}} = \boldsymbol{p}_c + \boldsymbol{D}. \tag{3.11}$$

To obtain the parameters γ_1 and γ_2 we applied a least-square-fit on equation (3.9). The parameters are determined to $\gamma_1 = 0.0013\,(1)\,\frac{1}{mA}$ and $\gamma_2 = 1.20\,(3)\,10^{-7}\frac{1}{\mu m(mA)^2}$ for the 10 x-magnification and $\gamma_1 = 0.0012\,(1)\,\frac{1}{mA}$ and $\gamma_2 = 1.30\,(4)\,10^{-8}\frac{1}{\mu m(mA)^2}$ for the 4 x-magnification.
By applying equation (3.9) we are able to shift an arbitrary position $\boldsymbol{p}_c$ with

$c \in [0\,mA, 300\,mA]$ to a position $\boldsymbol{p}_{c_{\text{re}}}$ corresponding to a certain reference-current c_{re}. This allows us to obtain trajectories for a single reference frame determined by c_{re}.
The accuracy for the recalculated particle-positions $\boldsymbol{p}_{c_{\text{re}}}$ is heavily influenced by the obtained center of distortion $\boldsymbol{p}_{\text{ce}}$ as shown in Fig. 3.11 (b). This center is obtained through the calculation of the mean of all intersection points for all lines represented in Fig. 3.11 (a). The probability-density function (PDF) of all these intersection-points is shown as a heat-map in Fig. 3.11 (b) for the marked region in Fig. 3.11 (a). A circle of radius $r_{\text{ce}} = 5.4\ \mu m$ around the center of distortion $\boldsymbol{p}_{\text{ce}}$ represents the area containing more than 98% of all intersection points. To estimate the error introduced by the recalculation process we can assume a particle tracked at position $\boldsymbol{p}_{\text{d}}$. The recalculation process regarding the center of distortion $\boldsymbol{p}_{\text{c}}$ shifts the point $\boldsymbol{p}_{\text{d}}$ to the position $\boldsymbol{p}_{\text{u,t}}$. If we assume the center of distortion on the edge of the circle represented in Fig. 3.11 (b), the point $\boldsymbol{p}_{\text{d}}$ is shifted to the position $\boldsymbol{p}_{\text{u,w}}$. The error E can be calculated through

$$E = \sqrt{D^2 + {D_2}^2 - 2DD_2 \frac{\text{d}\left(\boldsymbol{p}_{\text{d}}, \boldsymbol{p}_{\text{c,e}}\right)}{r_c}}. \tag{3.12}$$

The maximum for the error defined in equation (3.12) is observed for the maximum current $c = 300\,mA$. The corresponding error yields $E = 2.8\,\mu m$. As we always start our tracking process with a current of $c = 150\,mA$, the effective error due to the recalculation of the distortion is $E_{\text{eff}} = \frac{E}{2} = 1,4 \mu m$. This is the maximal observed error due to the recalculation of the distortion effects.

3.2.3 Influence of the ETL: Image quality

We have seen that the ETL introduces a shift to the image im_0 compared to the image im_{nE}. In this section we are interested in the impact of the ETL to the image quality of image im_0. Therefore we compare the pixel-intensities of the images im_{nE} (a) and im_0 (b) represented in Fig. 3.12 on the marked horizontal and vertical lines.

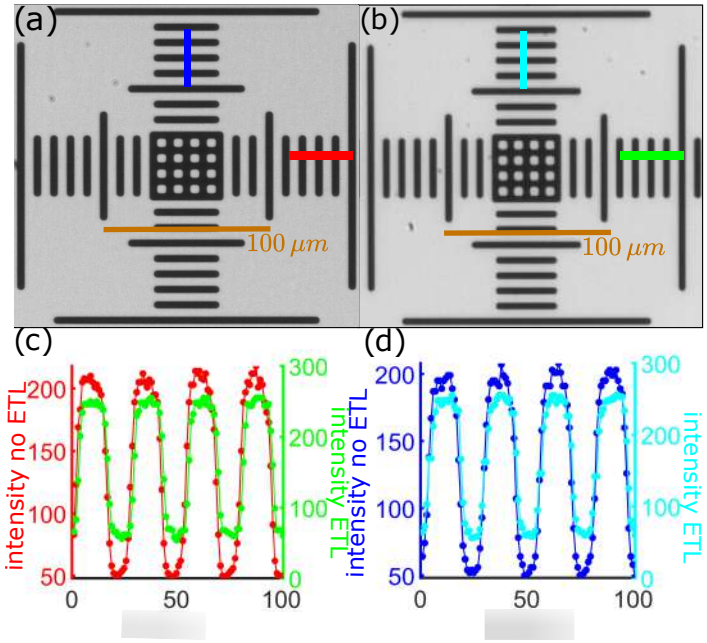

FIGURE 3.12: Comparison between the image quality with no ETL (a) and with ETL (b). Plot of the intensity along the horizontal (c) and vertical (d) lines marked in (a) and (b).

We see based on Fig. 3.12 (c) and (d) that the presence of the ETL changes the absolute value of the observed pixel-intensities. However, we see that the presence of the ETL does not broaden or shrink the observed patterns represented in Fig. 3.12 (a) and (b) as the black stripes.

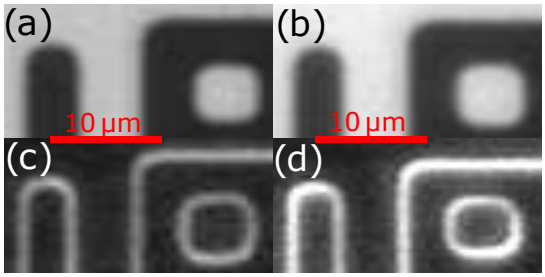

FIGURE 3.13: Comparison of the image quality for a structure obtained for: brightfield-no ETL (a), brightfield-ETL (b), darkfield-no ETL (c), darkfield-ETL (d).

Furthermore we compare a smaller structure compared to Fig. 3.12 in Fig. 3.13. Here the images in Fig. 3.13 (a) and (b) have been obtained for brightfield-microscopy and the images in Fig. 3.13 (c) and (d) for darkfield-microscopy. The images from Fig. 3.13 (a) and (c) are obtained without ETL and the images from Fig. 3.13 (b) and (d) with ETL. We see that there is no significant difference in the image quality due to the presence of the ETL.
We have seen that the ETL does not reduce the image quality of the image im_0. In the next section we investigate the impact of the distance L between ETL and camera on the obtained images im_0.

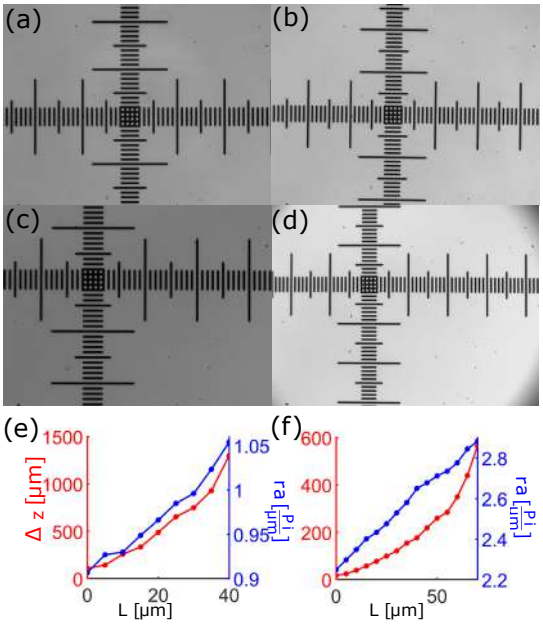

FIGURE 3.14: Comparison between images im_0 for distances $L = 5\,mm$ (a) and $L = 40\,mm$ (c) and corresponding images im_{300} for distances $L = 5\,mm$ (b) and $L = 40\,mm$ (d). (e)-(f) Plot of the tunable range Δz (red) and the ratio ra (blue) of pixels per μm for the 4 x-magnification (e) and for the 10 x-magnification (f).

3.2.4 Impact distance between camera and ETL

We have seen that the ETL introduces a shift to the image im_0 compared to image im_{nE}, which can be recalculated using equations (3.4) and (3.5). In this section we are interested in the impact of the distance L between ETL and camera on the obtained images im_c, where c denotes the applied current to the ETL in mA resulting in image im_c. In Fig. 3.14 (a) and (c) we show images im_0 for distances $L = 5\,mm$ (a) and $L = 40\,mm$ (c). The corresponding images im_{300} are represented in Fig. 3.14 (b) and (d). For all images im_c represented in Fig. 3.14 (a) - (d) we manually matched the focal plane z_f with the height z of the observed structure. The distance Δz between the focal planes z_f used to obtain the image in Fig. 3.14 (a) and Fig. 3.14 (b) is $\Delta z = 15\,\mu m$. The distance Δz between the focal planes z_f used to obtain the image in Fig. 3.14 (c) and Fig. 3.14 (d) with a bigger distance L is $\Delta z = 210\,\mu m$. We see that by increasing the distance L we can increase the width Δz in which we can observe particles.

To quantify this result we plotted the quantity Δz for different lengths L between camera and ETL. The results are shown as the red curve in Fig. 3.14 (e) for the 4 x-magnification and in Fig. 3.14 (f) for the 10 x-magnification. We see that by adapting the length L between camera and ETL over several millimeter, this changes the width Δz over several orders of magnitude. Therefore the ETL can be used to investigate a broad spectrum of phenomena, arising at different length-scales. A smaller spacing in the width Δz allows a finer tuning in the focal plane z_f, larger values of the width Δz allow

tracking particles over large distances.
Adapting the distance L between camera and lens L not only affects the width Δz, but also the relation

$$ra = \frac{\text{pixels}}{\mu m} \tag{3.13}$$

representing the number of pixels per μm is represented as the blue curve in Fig. 3.14 (e) for the 4 x-magnification and in Fig. 3.14 (f) for the 10 x-magnification. For an increasing distance L we obtain an increased ratio ra. The impact of the distance L on the ratio ra is much smaller than the impact on the distance Δz.

3.2.5 Frequency limitations

It is possible to tune the ETL with frequencies f_{ETL} up to a maximal frequency of $f_{\text{ETL,max}} = 1000\,\text{Hz}$. As we have seen in section 3.2.2, applying different currents c to the ETL results in a shift $\text{D}(c, r)$, where c denotes the applied current and r the distance of the tracked object to the center of distortion $\boldsymbol{p}_{\text{ce}}$. We mentioned in section 3.2.2 that the impact of this-position shift can be recalculated and we can map positions $\boldsymbol{p}_c$ to a reference position $\boldsymbol{p}_{c_{\text{re}}}$ corresponding to a reference current c_{re}. But this recalculation process is only possible if we have a fixed center of distortion $\boldsymbol{p}_{\mathbf{ce}}$. For *fast changing currents* c we observe multiple centers of distortion. In this cases we did not find a way to map positions $\boldsymbol{p}_c$ to an arbitrary reference-position $\boldsymbol{p}_{c_{\text{re}}}$. To quantify the term *fast changing currents* let us assume a triangular current of amplitude A_{c} and frequency f_{c}. In Fig. 3.15 (a) we see the position of a fixed particle represented as the black dot. We tracked this particle for different combinations of amplitudes A_{c} and frequencies f_{c}.

We denote the corresponding tracked positions as $p_{c,A_{\text{c}},f_{\text{c}}}$. In Fig. 3.15 (a) we show the tracked positions for $A_{\text{c}} = 10\,mA$ and $f_{\text{c}} = 1\,Hz$ (green dots), $A_{\text{c}} = 10\,mA$ and $f_{\text{c}} = 20\,Hz$ (blue dots) and $A_{\text{c}} = 10\,mA$ and $f_{\text{c}} = 60\,Hz$ (red dots). We qualitatively cannot observe a significant difference between the positions $p_{c,10,1}$ and $p_{c,10,20}$. But for a high frequency $f_{\text{c}} = 60\,Hz$ we see that the corresponding points $\boldsymbol{p}_{c,10,60}$ do not shift according to a single center of distortion $\boldsymbol{p}_{\text{ce}}$ anymore, resulting in a spreading of the points $\boldsymbol{p}_{c,10,60}$. To quantify this spreading, for each combination of amplitudes A_{c} and frequencies f_{c} we calculated the mean of the difference between the true position $\boldsymbol{p}_{150}$ and the recalculated positions $p_{c,A_{\text{c}},f_{\text{c}},c_{\text{re}}}$ based on equation (3.11)

$$E_{A_{\text{c}},f_{\text{c}}} = \text{mean}\left(p_{150} - p_{c,A_{\text{c}},f_{\text{c}},c_{\text{re}}}\right). \tag{3.14}$$

From Fig. 3.15 (b) we see that the error $E_{A_{\text{c}},f_{\text{c}}}$ increases for increasing amplitudes A_{c} as well as increasing frequencies f_{c}. This is due to the fact that the speed in changing the current c increases for larger products $A_{\text{c}}f_{\text{c}}$. Especially at the turning points of the triangular system the speed in changing the current c is very high. This leads to mechanical stresses on the ETL making it unable to obtain a symmetric shape resulting in multiple centers of distortion. Due to these multiple centers of distortion, the true position $\boldsymbol{p}_{150}$ is

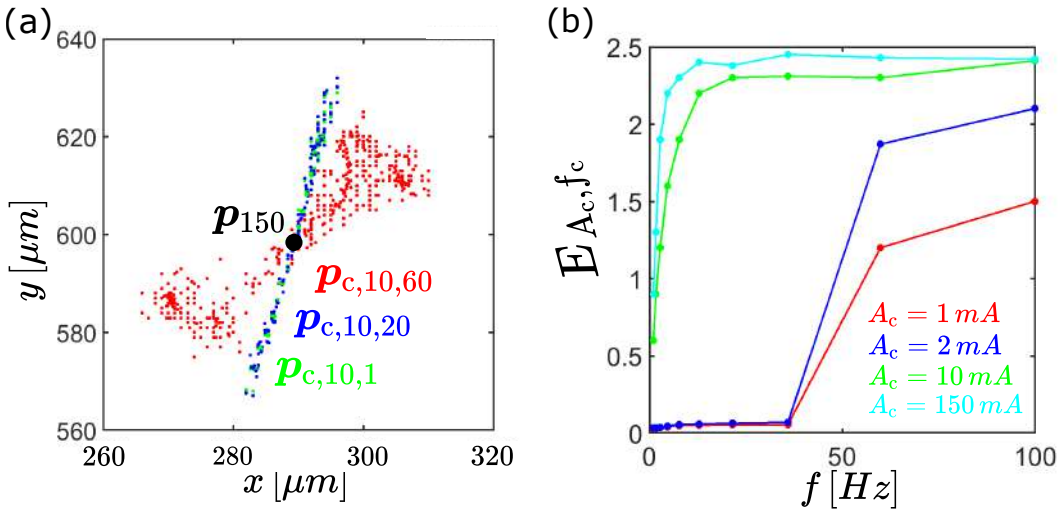

FIGURE 3.15: (a) Tracking of a fixed particle represented as the black dot at position $\boldsymbol{p}_{150}$ for $A_c = 10\,mA$ and $f_c = 1\,Hz$ (green dots), $A_c = 10\,mA$ and $f_c = 20\,Hz$ (blue dots) and $A_c = 10\,mA$ and $f_c = 60\,Hz$ (red dots). We see qualitatively that in case of a high frequency the tracked particles $\boldsymbol{p}_{c,10,60}$ spread. This increases the error in the recalculation process. (b) A quantitative discussion on the impact of the quantities amplitude A_c and frequency $f = f_c$ on the error E_{A_c,f_c} as described in equation (3.14).

shifted towards multiple centers of distortion $\boldsymbol{p}_{ce,i}$, resulting in a spread of positions p_{c,A_c,f_c} as can be seen from the red dots corresponding to $\boldsymbol{p}_{c,10,60}$ in Fig. 3.15 (a). The quantity E_{A_c,f_c} is therefore a crucial value to determine the accuracy of the tracking process.

3.3 xy-Detection

We have discussed the experimental setup we are using to track particles in section 3.1. Using this setup, we imaged certain bacteria (*E. coli*) in Fig. 3.16 (a). The pixel intensity of the obtained image are in the range from 0 (black) to 255 (white) and therefore these images are denoted as gray-scale images. In the following we denote these images as $\tilde{\text{im}}$. By eye we can qualitatively detect several bacteria in Fig. 3.16 (a). To perform a quantitative *xy*-detection of particles - tracking - we can have a look at Fig. 3.16 (c), where we show the intensity profiles along the red and blue solid lines added to Fig. 3.16 (a). We see for both curves a huge rise according to the visible white spot, but just the red intensity profile corresponds to a bacterium, whereas the blue intensity profile corresponds to a dust particle. It is beneficial for the tracking algorithm, to remove dust particles in a first step. To do so we make use of the fact that typically dust particles have a much lower maximal intensity than particles we want to track. Based on this assumption we binarize the

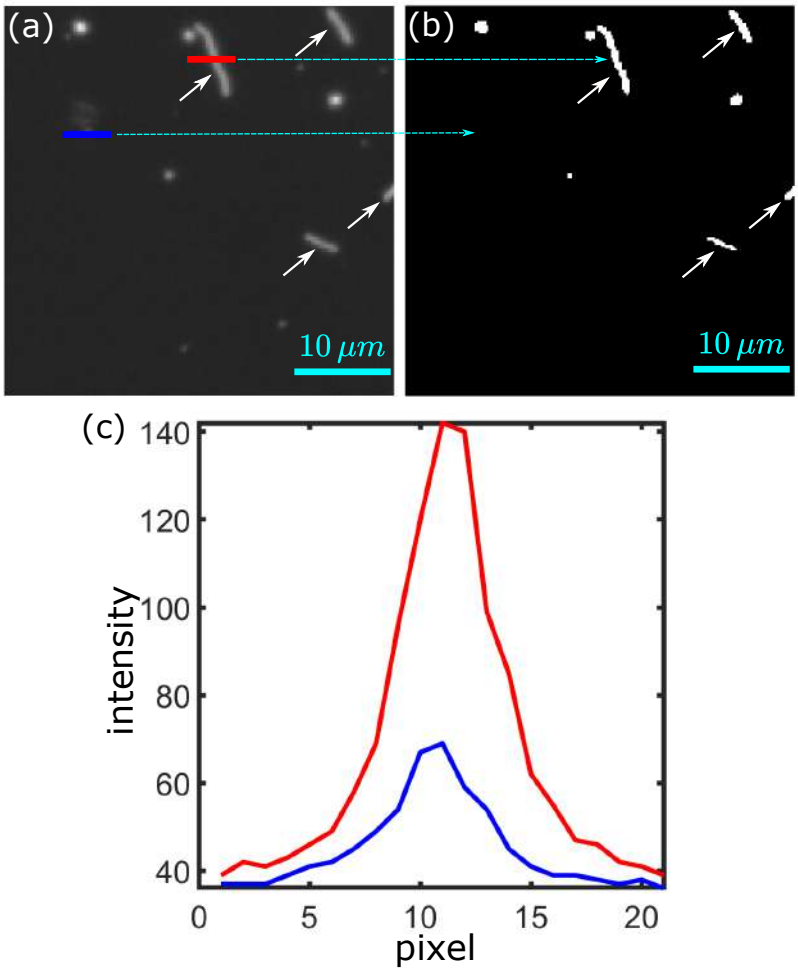

FIGURE 3.16: (a) Image of multiple bacteria marked via a white arrow. The remaining signals correspond to dust particles. (b) Binariation of the image represented in (a). (c) Intensity profiles along the red and blue line represented in (a).

images $\tilde{\text{im}}$ to a new image im via

$$\text{im}\,(i,j) = \begin{cases} 255 & \text{im}\,(i,j) \geq t_B \\ 0 & \text{else.} \end{cases} \tag{3.15}$$

The resulting image im is represented in Fig. 3.16 (b). We can see that the bacterium marked via the red line in Fig. 3.16 (a) is still present in Fig. 3.16 (b), whereas the dust particle has vanished. Based on the image im we can detect the positions $\boldsymbol{p}_i = (x_i, y_i)$ of the different particles p_i. To do so, we apply an algorithm introduced in [159], based on topological structural analysis of binary images by border following. In Fig. 3.17 (a) and (b) we show a zoom of the image represented in Fig. 3.16 (a) and (b), where we marked the tracked contour (red) as well as the center of mass (blue). Here Fig. 3.17 (a) corresponds to the original image $\tilde{\text{im}}$ whereas Fig. 3.17 (b) corresponds to the binarized image im.

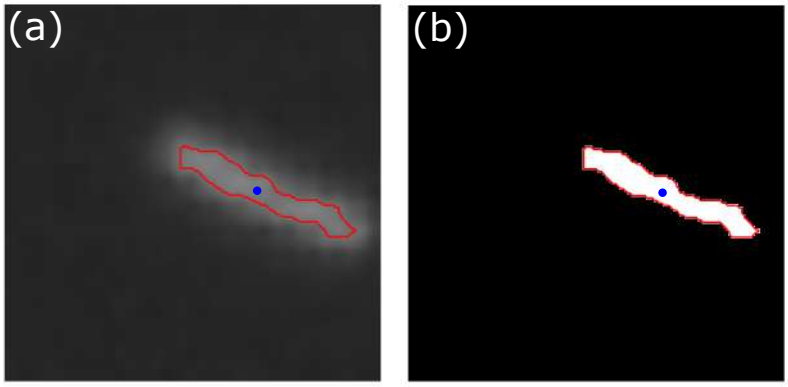

FIGURE 3.17: (a) Image of a bacterium. The red line marks the boundary of the bacterium, and the blue dot the center of mass. (b) Binarization of the image presented in (a).

3.4 z-Detection

We have seen in section 3.2 that we can modify a standard optical microscope with an ETL to adapt the focal plane z_f of the microscope without any mechanical interaction on the sample. In this section we discuss the impact of the quantity Δz , the distance between the focal plane of the microscope z_f and the height z of a particle, on the obtained image. In Fig. 3.18 we show an image of a particle for different values of Δz, where we defined the position $\Delta z = 0\,\mu m$ by manually adapting the height z of the particle until it qualitatively appeared as the sharpest image.

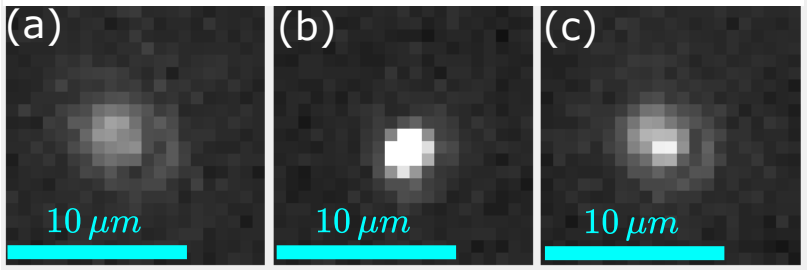

FIGURE 3.18: Image of a particle for a distance $\Delta z = -4\,\mu m$ (a), $\Delta z = 0\,\mu m$ (b) and $\Delta z = 4\,\mu m$ (c) between the height of the particle z and the focal plane of the microscope z_f.

For the human eye it is an easy task to detect that the particle represented in Fig. 3.18 (b) is the image where the particle is closest to the focal plane. It turns out that a quantification of this process is very challenging. In the following sections we will present several methods to

1. quantify which image was obtained for the smallest distance Δz
2. quantify the distance Δz based on the obtained image

for images of a particle obtained for several distance Δz.

3.4.1 Quantify with area

There are several approaches to track particles in three dimensions via adapting their height to keep them in focus, as done in [40, 42]. In these publications, the measurements had a feedback to the z-stage and the height z_s of the stage is adapted to keep the particle in focus. They used the diameter w of the tracked particle - connected to the area via $a = \pi \left(\frac{w}{2}\right)^2$ - to quantify the defocussing of the tracked particle. The obtained relation between the half diameter $\frac{w}{2}$ of the spherical particle and the distance Δz is represented in Fig. 3.19 (a).

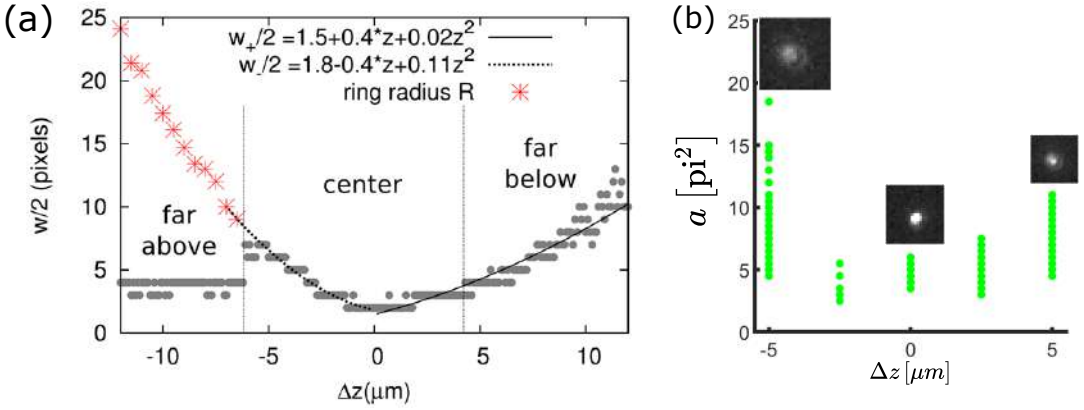

FIGURE 3.19: (a) Relation between radius r of the tracked spherical particle and the distance to true particle height Δz from [42]. (b) Relation between the area a of the tracked particle represented in Fig. 3.18 and the distance to true particle height Δz.

We see from Fig. 3.19 (a) that they are able to map the obtained half diameter $\frac{w}{2}$ of the tracked particle to the distance Δz to the true particle height z_t. As they are using brightfield-microscopy they furthermore can distinguish based on diffraction rings whether the particle is below or above the applied focal plane. As our particles have arbitrary shapes, we apply the area a of the tracked particles rather than the diameter w. If we use the particle represented in Fig. 3.18 to plot the area a vs the distance Δz, we obtain the data represented in Fig. 3.19 (b). We can see that there is no mapping possible between the observed area a and the distance Δz. The main reason because we cannot do a similar calibration as represented in Fig. 3.19 (a) is the huge difference in the experimental setup. The curve in Fig. 3.19 (a) was obtained for a 100 x-objective, resulting in images of 128 x 128 pixels of the tracked object. We are using a 10 x-objective, resulting in a 20 x 20 image of the tracked object, resulting in 40-times less pixels for an image of the same particle size. Due to the ETL we are limited to 10 x-objectives, as otherwise the range in the adaption of the z-width by the ETL would shrink under several μm. Having only several pixels of the tracked particle to determine its area a, this method is

1. very sensitive to random pixel fluctuations, resulting in the big spread of the obtained area for a fixed distance Δz as represented in Fig. 3.19 (b)

2. not suitable to distinguish images obtained for close focal planes as represented in Fig. 3.19 (b).

To summarize, the area a of a particle is a suitable quantity for creating a calibration curve to map between the area a and the distance to the distance Δz to the true particle height z_t. However, in case of low magnifications, the area a cannot be used to recalculate the distance Δz to the true particle height z_t. In addition we would like to remark that using the area a of a particle only uses a very small amount of the image-information. The area just takes into account a very small amount of pixels defining the border of the particle and therefore is non-optimal as a lot of information is not used. We will see that the methods presented in the next sections use more information of the image and therefore result in a better quantity to obtain the distance Δz.

3.4.2 Deconvolution

In this section we describe the deconvolution technique, which is based on the assumption that the observation process of a *true* structure im_{tr} is disturbed by a disturbance h_{ob} resulting in the observation of the structure im_{ob}. Deconvolution tries to recalculate the true structure im_{tr} by estimating the disturbance h_{ob} and inverting the disturbing-process. In the following we start to explain how this disturbance h_{ob} is estimated. In a second step we show how the disturbance h_{ob} can be used to quantify the distance Δz of a particle from the focal plane z_f.

Estimation of the disturbance

In our work we are observing structures of the size of several μm. Let us denote the signal of these structures as f. To get a magnified image of these structures we use a combination of an optical microscope and a camera. These additional devices have a certain impact g on the signal f we would like to detect. To simulate this impact, one can make the approach that the observed signal h is obtained via a convolution of the true signal f and the measurement setup, quantified via the transfer function g. The relation between f, g and h can be described via

$$f * g = h. \tag{3.16}$$

This problem can be generalized in a way that we are interested in a certain signal f we are detecting with a device which introduces the transfer function g. This is a well known, well investigated problem. In the following we present the general idea to obtain the signal f based on the observed signal h. We follow the ideas presented in [178]. The observed signal can be described

via equation (3.16). The general approach to obtain the true signal f is the transformation

$$F = \mathscr{F}(f) \tag{3.17}$$
$$G = \mathscr{F}(g) \tag{3.18}$$
$$H = \mathscr{F}(h) \tag{3.19}$$
$$\tag{3.20}$$

of the problem in the Fourier-space and solve equation (3.16) for F:

$$F = \frac{H}{G}. \tag{3.21}$$

The desired signal f can be obtained via a back-transformation of F. A first application of this approach was done by astrophysicists to obtain the true signal f of a galaxy obtained via the Hubble-Telescope. An example of the observed signal h and the true signal f is represented in Fig. 3.20 [34]. We

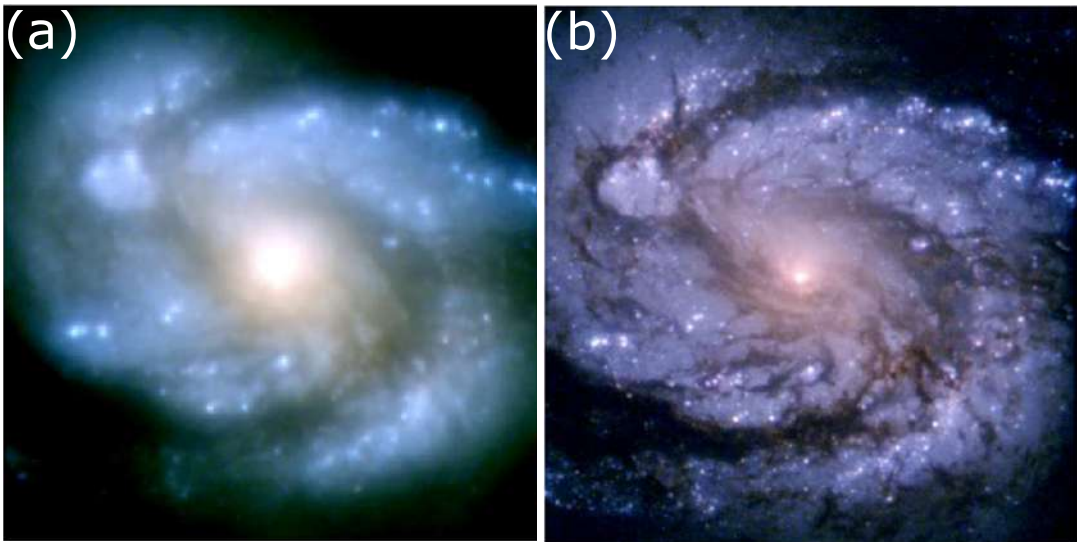

FIGURE 3.20: (a) Original obtained signal h recorded by the Hubble telescope. (b) Recalculated signal f from (a) based on the calculated transfer function g. Both images taken from [34].

see that the original image Fig. 3.20 (a) obtained via the Hubble-telescope appears very blurry, which results from the impact of the Hubble-telescope to the original signal f. In case of the Hubble-telescope it is possible to calculate the impact g of the telescope on the original signal f. Based on equation (3.21) it is possible to obtain the true signal f, represented in Fig. 3.20 (b). The Hubble-telescope is an example for the recalculation of the true signal f through the known transfer-function g.
In many scenarios the transfer-function g remains unknown. Hence there exist iterative methods to approximate the transfer-function g so that the original signal f can be recalculated. These methods are explained in [24, 65, 71, 97]. The general process of these iterative methods is represented in Fig. 3.21. We would like to detect a certain signal f. The microscope trans-

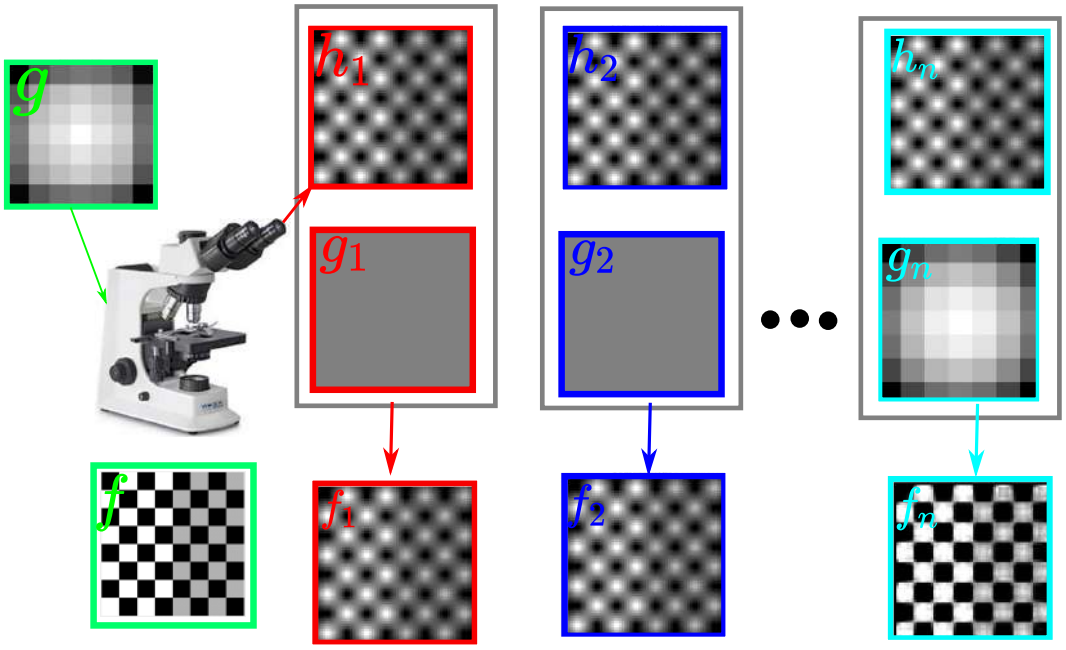

FIGURE 3.21: Observation of the original signal f via a microscope introduces the transfer-function g resulting in the observed signal h_1. Via an algorithm the transfer-function g_i is iteratively adapted until a certain threshold is reached and the best estimation f_n of the original observed state f is obtained.

forms the signal f through the transfer function g and we observe the signal h. As we would like to obtain the signal f without specific knowledge of the transfer-function g, the method to obtain f in such a case is called blind deconvolution. In a first step we make an arbitrary assumption g_1 about the transfer-function g and perform the deconvolution step described in equation (3.21). Based on the obtained signal f_1, the initially assumed transfer-function g_1 will be optimized to the function g_2. This process continues until a certain threshold in the optimization process is reached. We see from Fig. 3.21 that the obtained signal f_n and the corresponding transfer-function g_n look very similar to the true signal f and transfer-function g.

Quantification of height z

We can use the obtained transfer-function g to quantify the distance Δz of the tracked particle to the current focal plane z_f. To explain this process, we can have a look at Fig. 3.22. In Fig. 3.22 (a) we see a visual representation of a transfer function g. Plotting the mean $m(i) = \text{mean}(\boldsymbol{m}_i)$ of each column-vector $\boldsymbol{m}_i$ results in the curves shown in Fig. 3.22 (b), where each color represents the vector $m(i)$ for a certain distance Δz. In a next step we need to quantify the curves $m(i)$ by a single value. It turned out that taking the maximum of the vector $m(i)$ gives a better quantification than the area under the curve or the full-width,half-maximum value (FWHM). This can be explained by the small dimension (in our case 10 x 10) of the transfer function

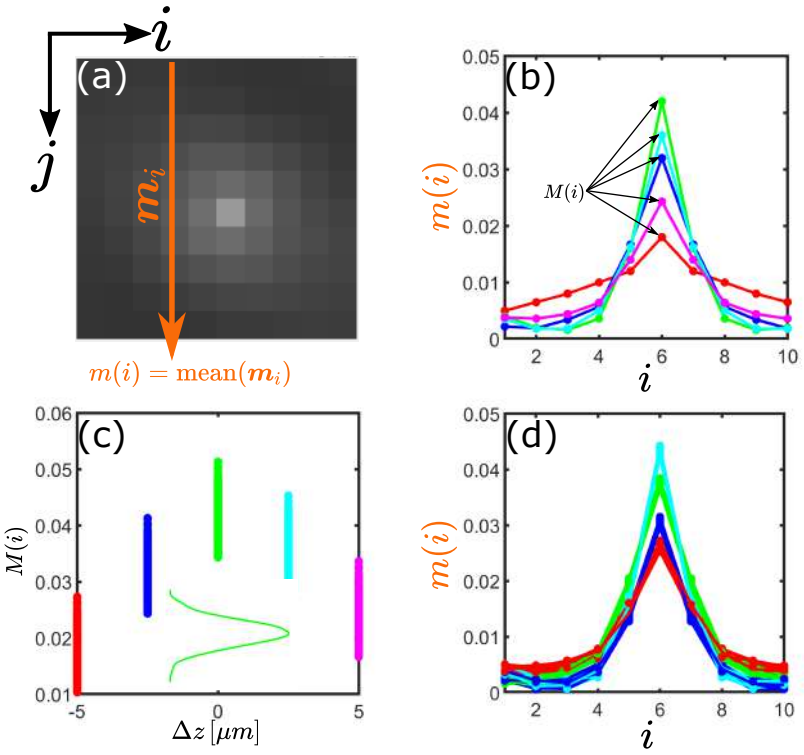

FIGURE 3.22: (a) Quantification of the transfer-function g to a vector $\boldsymbol{m}$. (b) Representation of the vector $\boldsymbol{m}$ for tracked particles obtained for different distances Δz. (c) Relation between a single value quantification of the transfer-function g and the distance Δz to the true particle height z_t. (d) Impact of different light intensities on the vector $\boldsymbol{m}$.

g. But as described in [97], transfer-functions always have a small dimension. Therefore the area under the curve $m(i)$ as well as the FWHM are no precise quantities and we choose the maximum value of $m(i)$ to quantify the distance Δz. We see in Fig. 3.22 (c) the relation between the maximum of $m(i)$ and the distance Δz for multiple measurements. We see that for a fixed distance Δz there is a certain distribution, caused by the random pixel fluctuations as described in 3.4.1. Despite these random fluctuations it is still possible to map between M and Δz. But it becomes problematic in case of different light-intensities as observed in experiments. In Fig. 3.22 (c) we plot different curves $m(i)$ for the same distance Δz but for different light-intensities. We see that the curves $m(i)$ as well as the value M are very sensitive to the light intensity. As this intensity randomly changes in experiments for different heights z as well as for different xy-positions in the sample, it is not possible to obtain a calibration curve mapping a value M to a certain distance Δz.

3.4.3 Quantification via sharpness

The focal plane z_f of a microscope is the plane where the sharpest focus is attained. Here in this section we make the assumption that the sharpness is a monotonous decreasing function of the distance Δz of the object to the focal

plane z_f. Therefore quantifying the sharpness s of an image can be mapped to the distance Δz. Although there exist multiple methods to quantify the sharpness of images of size $m \times n$ for $m, n > 400$ pixels, we could not find a suitable method to define the sharpness of tracked particles of size $m, n < 20$. Therefore we developed our own method to quantify the sharpness s of a tracked object. Let us have a view at the images represented in Fig. 3.23 (b)-(d). It is easy to see for the human eye that image Fig. 3.23 (c) is the sharpest

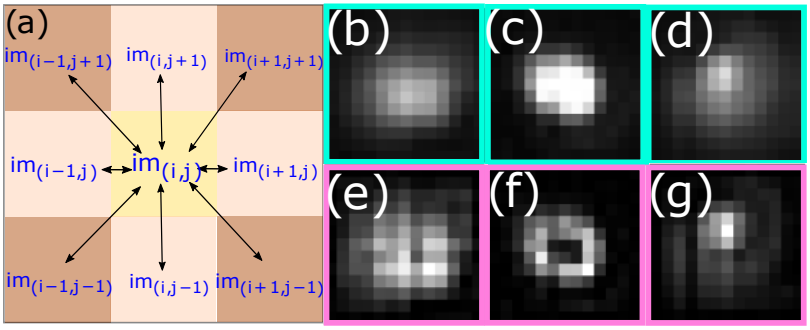

FIGURE 3.23: (a) Visualization of equation (3.22). (b)-(d) Images im of a tracked particle for different heights $\Delta z = -5\,\mu m$ (b), $\Delta z = 0\,\mu m$ (c) and $\Delta z = -5\,\mu m$ (d). (e)-(f) Images $\tilde{\text{im}}$ obtained from the image im obtained via equation (3.22) of a tracked particle for different heights $\Delta z = -5\,\mu m$ (b), $\Delta z = 0\,\mu m$ (c) and $\Delta z = -5\,\mu m$ (d).

image. We see that Fig. 3.23 (b) and (d) appear very blurry as neighboring pixels tend to have similar intensities, whereas Fig. 3.23 (c) has a well located (compared to the other images) bright spot in the middle, resulting in a larger gap in neighboring pixel-intensities. This difference in neighboring pixel-intensities is the origin of our sharpness quantification. As represented in Fig. 3.23 (a) we check for a single pixel the differences to its neighboring pixel-intensities. Summing up this value for all pixels results in a new image $\tilde{\text{im}}$ defined as

$$\tilde{\text{im}}\,(i,j) = \sum_{(a,b)\in \text{nh}} \text{abs}\left(p_{(i,j)} - p_{(a,b)}\right). \tag{3.22}$$

These new images $\tilde{\text{im}}$ representing the difference in neighboring pixel-intensities are represented in Fig. 3.23 (e)-(g). We see that the sharp image im represented in Fig. 3.23 (c) transfers to an image $\tilde{\text{im}}$ represented in 3.23 (f) with a dark region in the center, as the intensities of the centered pixels in the original image im appear very bright. This black center in the middle is surrounded by brighter pixels. Altogether we see that if we compare the image represented in 3.23 (f) with the images represented in 3.23 (e) and (g), there is a broader range in the variation of pixel-intensities represented in 3.23 (f). To quantify this observation we finally define the sharpness s as the standard deviation of the pixel intensities of the image $\tilde{\text{im}}$:

$$s = \text{std}\left(\tilde{\text{im}}\right). \tag{3.23}$$

We applied our method in the quantification of the sharpness s on experimental data as well as simulated data. In the case of simulated data we were able to easily apply our method on different shapes and sizes of the tracked object. This showed us that our method can be applied to quantify the sharpness of a broad range of objects.

Application on experimental data

Here we show the performance of our method on experimental data application. We tracked a fixed particle for different distances Δz. In Fig. 3.24

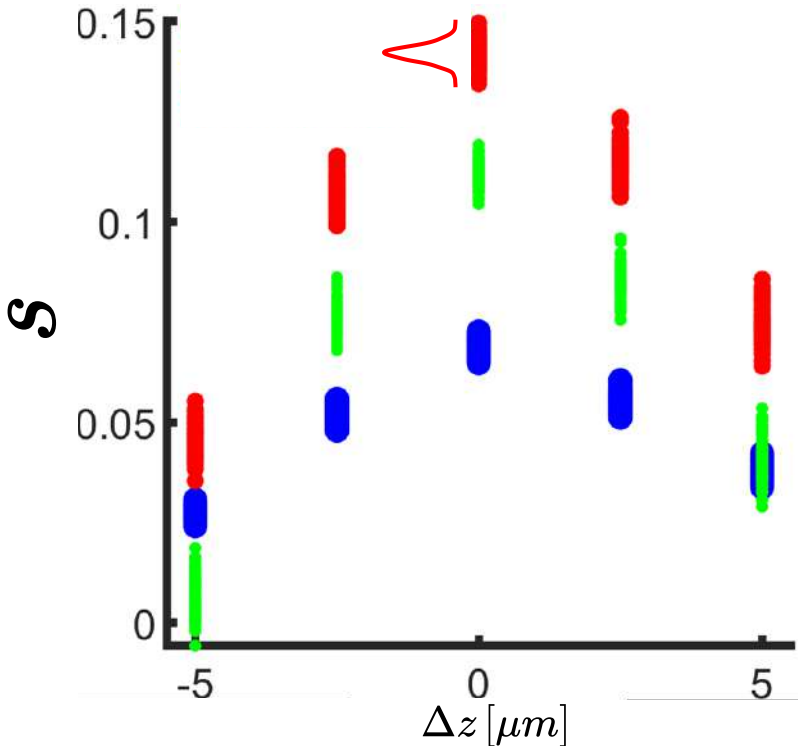

FIGURE 3.24: Calculation of the sharpness s of an experimentally observed particle for different distances Δz and different light-intensities.

(a) we see the obtained sharpness-value s for different distances Δz in red. Due to random pixel fluctuations, as explained in section 3.4.1, we observe a certain distribution for the sharpness s at a certain position as represented via the inset in Fig. 3.24 (a). The impact of a changing light intensity as observed in experiments leads to different calculated sharpness values s (blue). Also the shape of the tracked particle results in a change of the calculated sharpness s, as can be seen from the green dots in Fig. 3.24 (a).

Application on simulated particles

To test the performance of our method in estimating the sharpness s on a large number of different shapes and objects, we created computer simulated images. To simulate the impact of defocussing we used Gaussian blurring as described in [47]. The steps in creating computer simulated images are the following:

1. creating a white square/circle (intensity $= 1$) on dark ground (intensity $= 0$)
2. applying a Gaussian blur to the image for different standard deviations σ_{Gaussian}
3. adding noise to the image by summing a normal-distributed-value ($\sigma = 0.025$) to any pixel of the image. Intensity values larger than 1 will be set to 1, values smaller than 0 will be set to 0.

We quantified squares and circles for images of size $\text{s}_{\text{image}} \in [20, 50, 75, 100]$, length (diameter) of the squares (circles) corresponding to $\text{f}_{\text{shape}} \in [0.30, 0.42, 0.56, 0.7]$ multiplied the image-size s_{image}. To compare the sharpness for images of different size s_{image} we scale the standard deviation σ_{Gaussian} of the Gaussian-filter with the image size s_{image}. The standard-deviation σ_{Gaussian} of the Gaussian-filter is obtained by multiplying a factor $\tilde{\sigma}_{\text{Gaussian}}$ with the corresponding image-size s. For $\tilde{\sigma}_{\text{Gaussian}}$ we choose 25 equally spaced values in the interval $[0.05, 0.3]$. In Fig. 3.25 (b) we present the calculates sharpness values s for squares as the red shaded area. Different curves belong to different values of s_{image} and f_{shape}. The median is represented as the red solid line. We compared our method to a similar method where we apply a Laplacian-of-Gaussian filter to the initial image im and calculate the sharpness s_{LoG} as the standard deviation of the filtered images $\tilde{\text{im}}_{\text{LoG}}$. We did the same for circles in Fig. 3.25 (d). We see that the calculated sharpness s decreases for increasing blurring of the images, in contrast to the sharpness s_{LoG}, which initially decreases, but starts to increase after a certain blurring. This indicates that our method is suitable for quantifying the sharpness of an image for different sizes of the tracked objects as well as different sizes of the images.

3.5 Online single particle-3D-tracking

3.5.1 Method

We have seen that based on the experimental setup explained in section 3.1 we can obtain images im of several particles from which we can

1. extract the positions $\boldsymbol{p}_i = (x_i, y_i)$ of the visible particles p_i (section 3.3) and
2. determine for a set of n images im_i of a particle p_i which image im_j was recorded for the smallest distance Δz between particle and focal plane z_f of the microscope (section 3.4).

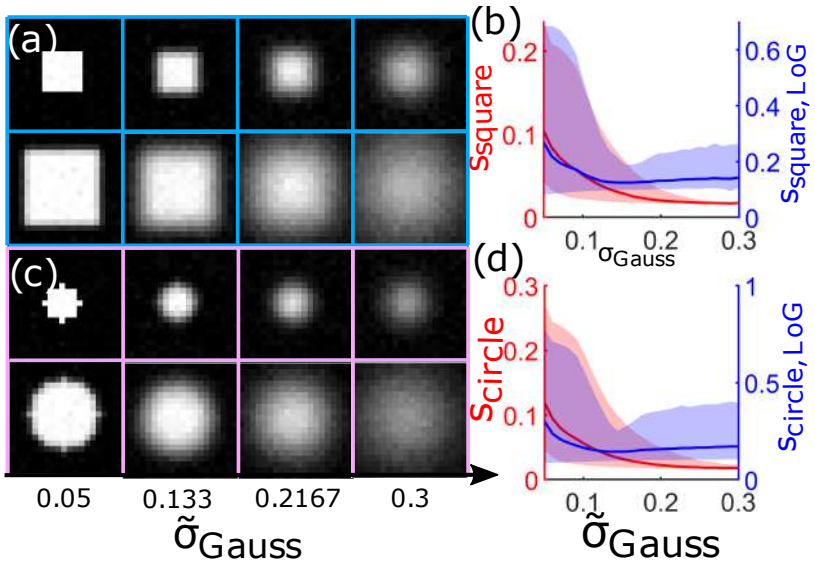

FIGURE 3.25: Computer-generated images of a square (a) and circle (c) with increasing blurring. The sharpness s (red shaded area) as well as a sharpness obtained after applying the Log-filter s_{LoG} (blue shaded area) are calculated for the squares (b) and circles (d). The median of the curves is given as the corresponding solid line. The sharpness-values s decrease with increasing blurring.

By combining both points we can perform online (live) 3D-tracking of a single particle. Online means that the we adapt the measurement settings during the experiment and therefore perform live-tracking. The measurement process is summarized in Fig. 3.26. We see in Fig. 3.26 (a) a certain region of interest (ROI) of an image of bacteria. The current focal plane is set to a certain value $z_{f,1}$. Once we left-click at a certain position $\boldsymbol{p}_{\text{clicked}}$, the tracking process is initiated. The particle $\boldsymbol{p}_k$ closest to the clicked position $\boldsymbol{p}_{\text{clicked}}$ will be tracked, the corresponding position will be denoted as $\boldsymbol{p}_{k,1}$. We see in Fig. 3.26 (a) that based on the clicked position $\mathrm{p}_{\text{clicked}}$ we will track the particle $\boldsymbol{p}_3$. The ROI shrinks around the position $\boldsymbol{p}_{3,1}$. We denote the new ROI as ROI_1. The corresponding sharpness of the particle is denoted as s_1. Once we obtained the position $\boldsymbol{p}_{3,1}$ and sharpness s_1 of particle $\boldsymbol{p}_3$ at time-step t_1, we increase the focal plane to $z_{f,2}$. In the next measurement step we perform a tracking of particles in the region ROI_1 to minimize computational time. At time-step t_2 the particle $\boldsymbol{p}_3$ was tracked at position $\boldsymbol{p}_{3,2}$. We again adapt the region around position $\boldsymbol{p}_{i,2}$ to ROI_2 and calculate the corresponding sharpness s_2. The steps can be summarized as follows:

1. At time-step t_k the tracked position of particle $\boldsymbol{p}_i$ is denoted as $\boldsymbol{p}_{i,k}$ for focal-plane $z_{f,k}$.

2. We change the region of interested to a square of width w centered around position $\boldsymbol{p}_{i,k}$. The new ROI is denoted as ROI_k

3. We calculate the sharpness s_k of particle $\boldsymbol{p}_i$

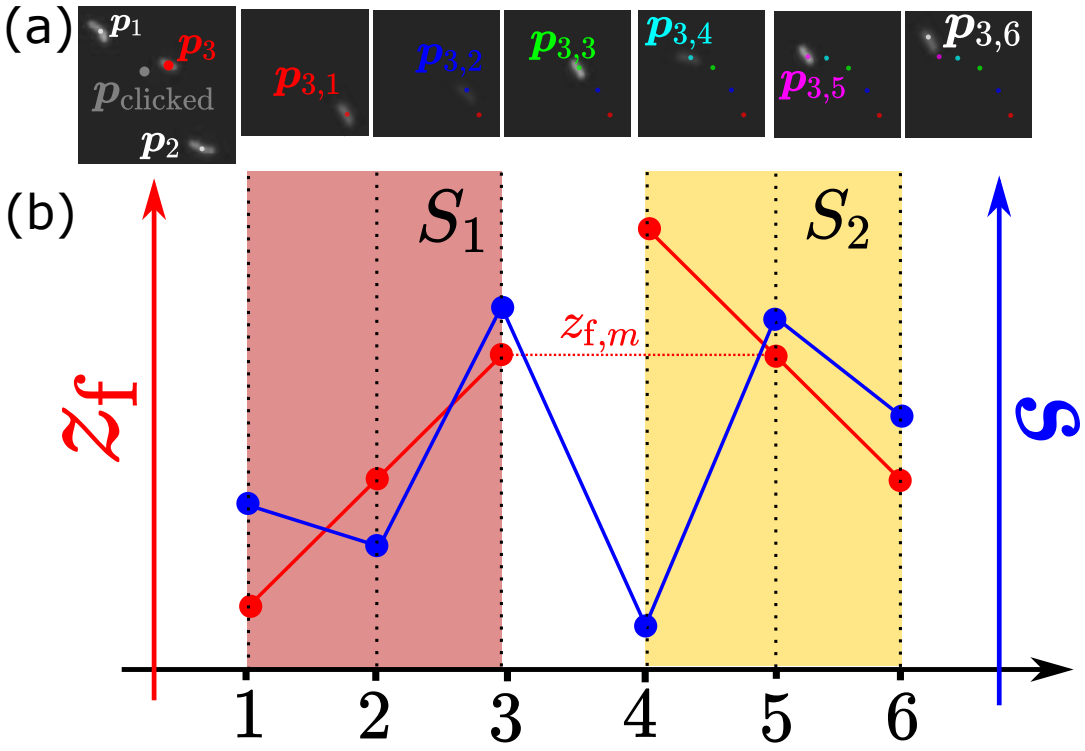

FIGURE 3.26: (a) After clicking at a certain position p_{clicked}, the tracking-algorithm starts with tracking the closest particle p_3. (b) Representation of the focal plane z_{f} and sharpness s for the tracked particles from (a). After session S_1 ended, the focal planes z_{f} for session S_2 are centered around the focal plane corresponding to the highest sharpness s from session S_1 (see red dotted line).

4. After obtaining the tracked position $\boldsymbol{p}_{i,k}$ and sharpness s_k, we adapt the ROI to ROI_k

5. At time-step t_{k+1} we track particles in the region ROI_k. We denote the tracked position closest to position $\boldsymbol{p}_{i,k}$ as $\boldsymbol{p}_{i,k+1}$

The five points mentioned above are repeated n times. All these n measurements belong to a session S_1 as represented in Fig. 3.26 (b). In this session we successively increased the focal plane. After performing these n measurements we define the focal plane $z_{\text{f},k}$ associated with the highest sharpness as the height z_m of particle $\boldsymbol{p}_i$ at time-step t_m. In the next session S_2 we successively decrease the focal plane $z_{\text{f},k}$ in a way that the focal plane in the middle equals $z_{\text{f},m}$ (b, horizontal dotted red line). This ensures that the focal-plane z_{f} is adapted in a way that the particle is kept approximately in the middle. To summarize, the tracking process consists of sessions S_j, where we

1. subsequently increase the focal plane z_{f} by a distance Δz_{S} if j is odd,

2. and subsequently decrease the focal plane z_{f} by a distance Δz_{S} if j is even.

For each session S_j we assign the height $z_{f,k}$ corresponding to the highest sharpness s_k of session S_j to the height z_k of particle $\boldsymbol{p}_i$ at time-step t_k.

3.5.2 Accuracy

As we have discussed in section 3.4.3, we did not find a method to map between a certain sharpness s and the corresponding distance Δz to the focal plane z_f. Therefore we only use a single value out of the n measurements performed in session S_i to define the particles height z. This reduces the frequency f_z for which we can obtain heights z of a tracked particle to

$$f_z = \frac{f}{n}, \tag{3.24}$$

where n denotes the number of measurements per session S_i. The accuracy in the detection of the height z is limited by

1. The ability to distinguish different focal planes z_f and
2. by the choice of the parameter n determining the number of measurements per session S_i and the spacing Δ_s between two successive focal planes z_f. The total spacing of a session S_i.

We denote the whole spacing of a session S_i as

$$\Delta_w = n\Delta_w. \tag{3.25}$$

In Fig. 3.27 we represent the impact of both parameters n and Δ_s.

In Fig. 3.27 (a) we show a particle trajectory as the blue dots. The measurements have been performed at the focal planes represented via the black dots with parameters $n = 3$ and $\Delta_s = \Delta_{s_1}$. For session S_1 we marked the focal plane which corresponds to the highest sharpness s as a red dot. As the particle at time $t = t_2$ was detected inside the red shaded region, the error E is limited by

$$E_{max} = \frac{\Delta_s}{2}. \tag{3.26}$$

But this holds only true if the focal plane $z_{f,1,2}$ is bounded by both focal planes $z_{f,1,1}$ and $z_{f,1,3}$. If we have a look at Fig. 3.27 (c) we see that $\Delta_{w,2} = \Delta_{w,1}$ but $n = 6$. The sharpest particle was detected for $t = t_6$. As t_6 corresponds to a focal plane $z_{f,2,6}$ at the edge of session S_6, we only can bound the error E_2 to the below focal plane $z_{f,2,5}$ but not to the top. Therefore the error E_2 remains undefined. As we need to quantify the error of our measurements, we need to choose the width Δ_w so that the sharpest position gets not detected at the edge of a session S_i. Therefore in Fig. 3.27 (c) we kept the parameter $n = 6$ but increased Δ_w. This increases the spacing Δ_s and therefore the maximal obtained error E_{max} regarding equation (3.26).
To summarize, choosing a small n increases the frequency f_z of the z-detection, but tends to detect the z-position of the tracked particle at the edge of session S_i, leaving the error of the height z undefined. To deal with this problem, one

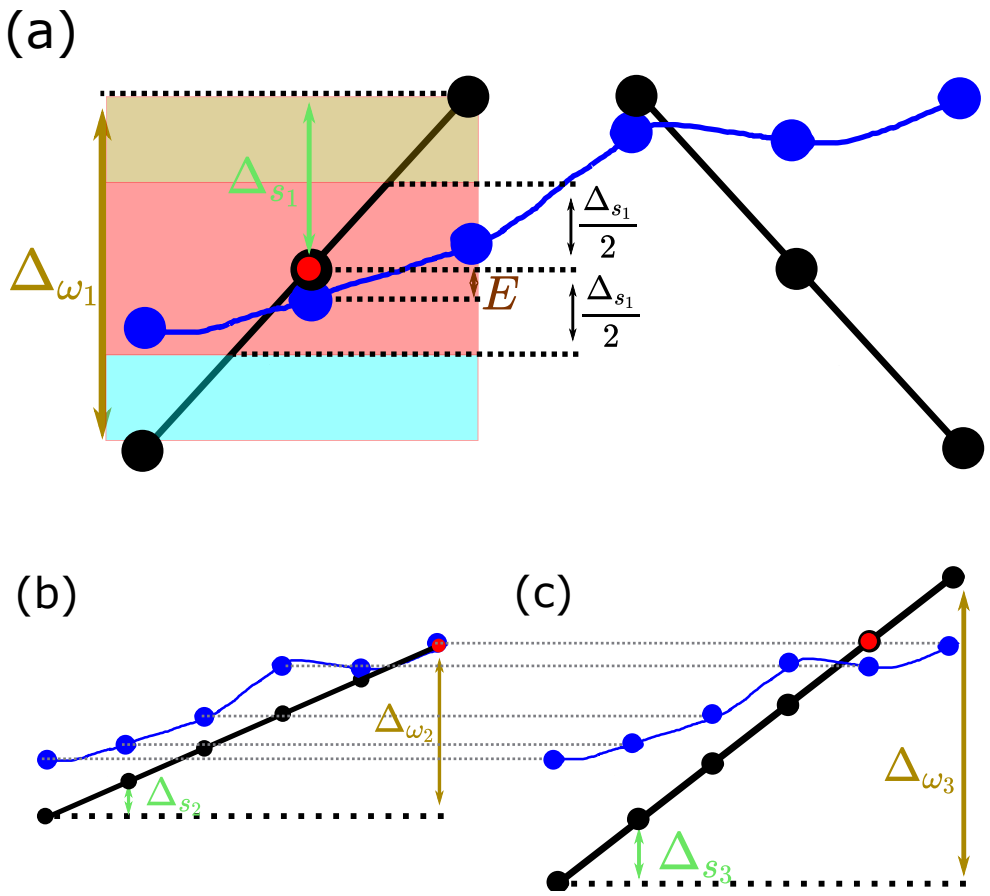

FIGURE 3.27: (a) Representation of the current focal-plane z_f (black dots) and particle height z (blue dots). The error in the detection of the height z is limited by $\frac{\Delta_{s_1}}{2}$. (b) and (c) Impact of the spacing Δ_s on the tracking performance. For the smaller spacing Δ_{s_2} (b) it is likely that the sharpest particle is tracked at the edge of a session S_n, making it impossible to estimate the error in the tracking process. A larger spacing Δ_{s_3} (c) enables us to estimate the error in the detected height z.

can increase the spacing Δ_s resulting in a larger maximal error E_{max} regarding equation (3.26). A second solution is to increase n, resulting in a decrease of the frequency f_z of the z-detection. Therefore the choice of parameters n and Δ_s depends on the experimental requirements and needs to be initially discussed.

3.5.3 Application on beads

In this section we apply our three-dimensional tracking algorithm on beads. By calculating the MSD from the measured bead-trajectories, we can compare the measured diffusion coefficient D_m with the theoretical diffusion coefficient D_t. We track beads of radius $r = 2.5\,\mu m$ and density $\rho = 1.05\,\frac{g}{cm^3}$. We tracked $n = 20$ beads for $t = 5\,m$. The tracked positions are shown in Fig. 3.28 (a). For each of the beads we calculated the mean-squared-displacement (MSD). The mean of the MSD for all particles is shown in Fig. 3.28 (b) for the

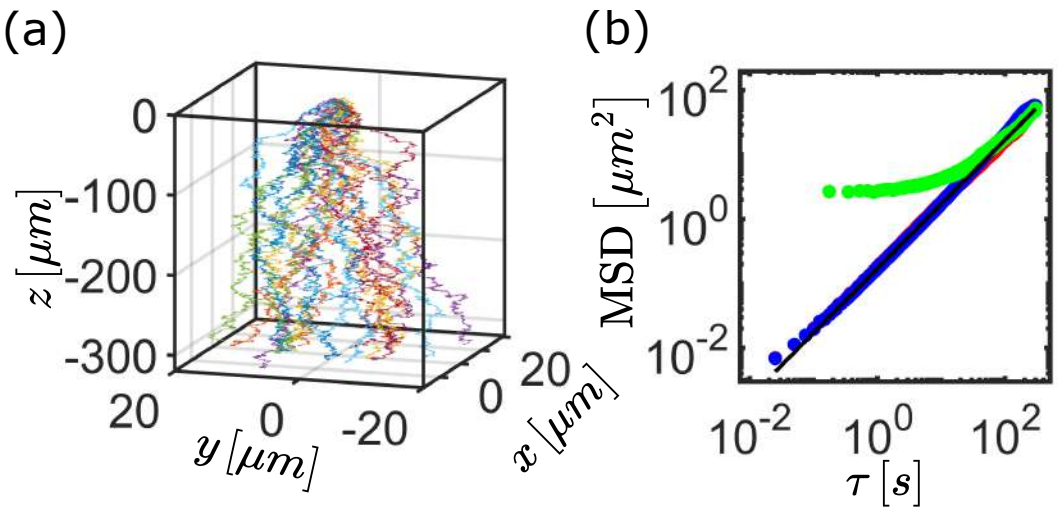

FIGURE 3.28: (a) Trajectories of $n = 20$ beads. For better visibility we choose a different scale for the x- and y-axis than for the z-axis. (b) Calculated MSDs for the tracked beads in (a) for the x- (red), y- (blue) and z- (green) components. The theoretical value is represented as the black solid line.

x (red), y (blue) and

$$\tilde{z} = z - v_{\mathrm{st}} t \tag{3.27}$$

(green) component. Here $v_{\mathrm{st}} = 1.04\,\frac{\mu m}{s}$ is the theoretical sink-speed for the beads. The theoretical curve for the MSD is shown as the black solid line. Due to the initial error of the MSD-curves we obtain the diffusion coefficient for the x-, y, and z-component through a linear fit in the range $t \in [1s, 20s]$. The calculated diffusivity constants D_{m} based on the data represented in Fig. 3.28 (b) are $D_{\mathrm{m},x} = 0.0896\frac{\mu m^2}{s}$, $D_{\mathrm{m},y} = 0.0926\frac{\mu m^2}{s}$ and $D_{\mathrm{m},z} = 0.077\frac{\mu m^2}{s}$. The theoretical value is $D_{\mathrm{t}} = 0.0858\,\frac{\mu m^2}{s}$. We see that the error for the diffusivity constants $D_{\mathrm{m},x}$ and $D_{\mathrm{m},y}$ is far smaller than for the diffusivity constant $D_{\mathrm{m},z}$. The reason is the difference in the methods for determining the position in the plane. x and y, and the estimation of the height z. We discussed in section 3.3 that the maximal error in the estimation of x and y is limited by equation 3.12 to $E = 0.81\,\mu m$. It is important to mention that this is the maximal error. Typical errors are way smaller. Furthermore as we transform the distorted, tracked position $(\tilde{x}, \tilde{y})$ to the undistorted particle-position (x, y) via a linear transformation, the role of error E is even more minimized. In total, the error in the detection of the x and y position is mainly given by the used microscope, which in our-case is in the sub-μm-region.
The error for the detection of the z-component, as discussed in section 3.4 is larger than $1\,\mu m$. Therefore we see in 3.28 (b) a big disagreement between the theoretical (black) and the calculated MSD (green) for the z-component. The advantage in using the ETL is clearly visible when we see that we can track the beads over several μm in height z. For long trajectories, the error in the estimation of the z becomes less and less important, and the curve for the estimated MSD for the z component gets closer to the theoretical curve. With this

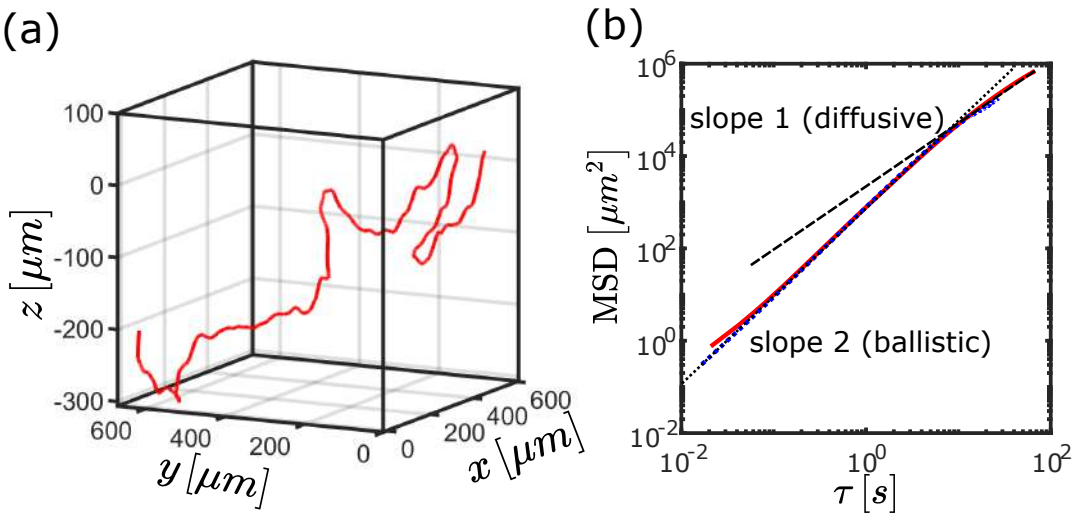

FIGURE 3.29: (a) Example for a trajectory of the bacterium *B. subtilis*. (b) Comparison of the MSD for the bacterium *B. subtilis* from [118] (blue), our three-dimensional tracking method (red). Black dotted and dashed line represent the ballistic and diffusive regime.

knowledge about the precision of our tracking-algorithm we tracked bacteria *B. subtilis* in the next section.

3.5.4 Application on bacteria

We tracked several bacteria *B. subtilis*. An example for a bacteria-trajectory is represented in Fig. 3.29 (a). The mean of the MSD obtained for 50 trajectories of the bacterium *B. subtilis* is represented as the red line in Fig. 3.29 (b). The MSD obtained for the same bacterium published in [118] is represented as the blue line. The black dotted line represents the slope in the initial, ballistic regime, the black solid line the slope in the second, diffusive regime. We see a good agreement of the red and blue curve for times between approximately $t = 0.1\,s$ and $t = 10\,s$. The reason for the difference for smaller times is due to the lower precision of our tracking algorithm, as already discussed in previous section for the tracked beads. This inaccuracy only plays a minor role for larger times, leading to a better agreement between the red and blue curve for times $t > 0.1\,s$. The difference for times $t > 10\,s$ is due to the difference in data quality. The length of trajectories measured in [118] are in the range of $t = 10\,s$, the trajectories we measured are in the range of several minutes. As the MSD is less and less trustworthy for times closer to the maximal tracking time, there is a big uncertainty for the last part of the blue trajectory. As with our new method, the trajectories are measured for longer times, the MSD is precise for several minutes. Despite this inaccuracy, one can already see a change from the initial ballistic regime to the diffusive regime for the blue MSD. This switch is visible even more clear for the MSD represented as the red curve. Therefore by applying the three-dimensional tracking method, we can show a clear switch from the ballistic to the diffusive

regime. In the next chapter we will present a technique for the evaluation of bacteria-trajectories. We will show how we can apply this technique to evaluate run- and tumble-dynamics of trajectories obtained with our three-dimensional tracking method.

3.6 Discussion

In this chapter we showed how a general optical microscope can be adapted via an ETL for being capable of three-dimensional particle tracking. By adapting the distance L between ETL and camera, we are able to tune the distance Δz of possible focal plane z_f adaption over certain orders of magnitude. This feature makes our method applicable on phenomena arising on several length-scales. The adaption of the focal plane z_f occurs due to an the deformation of the ETL in the presence of an electrical current c. As this electrical current c not only has the desired effect of adapting the focal plane z_f but also introduces an undesired effect of shifting positions, we compensate this undesired effect via a calibration curve as summarized in equation 3.11. To demonstrate the effectiveness of this calibration-function, we tracked several beads of known size and density, allowing us to compare the calculated diffusion coefficient D with the theoretical obtained diffusion coefficient, leading to a good agreement. To obtain the positions x, y and z of the tracked beads, we applied separate methods to obtain the x-y-position in the plane and the height z. For the height detection z we tested three different methods. A first approach was a mapping between the area of the tracked particle and the distance Δz to the focal plane z_f as already done in [42]. This method was not suitable in our case, as we are restricted to a low magnification due to the ETL. This low magnification makes it impossible to accurately map between the area a of the observed particle and distance Δz to the focal plane z_f. In a second approach we used a technique inspired by astrophysicists which is e.g. applied to remove noise from images of the Hubble-telescope. Here we also deal with the problem of low magnification, making this method unsuitable for our purpose. In a final approach we apply the relation between the sharpness s of a tracked particle and the distance Δz to the focal plane z_f. This does not allow us to map between sharpness s and distance Δz, but enables us to choose the sharpest image of a particle of a set of several images obtained for different focal planes z_f. This sharpest image corresponds to the image obtained for the smallest distance Δz to the focal plane z_f. Based on this principle we build our tracking method, consisting of several sessions S_i with n tracked positions $(x_{i,j}, y_{i,j})$ each, where $j \in [1, n]$. For each session S_i we obtain n x-y-positions and 1 z-position of the observed particle. During the tracking process we adaptively change the focal plane z_f to keep the particle in focus. As in the x-y-plane we apply a general tracking technique, the corresponding accuracy is in the sub-pixel regime of several nm. The accuracy in the determination of the height z is given by the distance Δs of subsequent focal planes z_f. This spacing Δs has to be chosen according to the experimental conditions and the observed particles. The minimal

spacing Δs is set due to random pixel fluctuations. Large values of Δs decrease the accuracy in the tracking of the z-position, as the maximal error is given by $\frac{1}{2}\Delta s$. In our experiments the accuracy in the determination of the height z is approximately $1\mu m$, and therefore about two orders of magnitude worse than the accuracy in the z-detection. This is clearly visible in Fig. 3.28 (b), where the measured MSD for the x- (y-) component of the beads is represented in red (blue), and the measured MSD for the z-component is represented in green. We see that there is a good agreement between the red and blue curve and the theoretical MSD represented as the black solid line. For times $\tau < 50s$, there is a big disagreement between the green and the black curve. This disagreement vanishes for greater times. It is important to realize that the effectiveness of our tracking method depends on the experimental situation, especially which kind of particles are tracked and for which times. If particles only move in the sub-μm-regime, our method is hardly applicable, but if we increase the timescale or the velocity of the observed particles, and they move several microns, then the error of approximately 1 μm has a relatively low weight and our method is an effective one in tracking the particle position. A second observation from Fig. 3.28 (b) is the mentioned fact that we have less tracked heights z than positions x and y, as for each session S_i we only use the particle with the highest sharpness for height-determination z. If rather than tracking beads, moving at relatively low speed v, we focus on tracking bacteria, the error in the tracking of the z-position has a lower impact. As bacteria tend to move with velocities up to 40 $\frac{\mu m}{s}$, the impact of a tracking error of 1 μm vanishes. With our tracking method, we are able to observe particles over hundreds of μm, allowing us to obtain trajectories of several minutes at times. We showed an example for a trajectory of the bacterium *B. subt.* in Fig. 3.29 (a). We were able to compare our results with results of [118], who tracked the same bacteria. Their result for the MSD is represented as the blue curve in Fig. 3.29 (b). We see the initial ballistic regime which tends to change to the diffusive regime. As this is a double logarithmic plot, it requires approximately 10 times longer trajectories in time to confirm the diffusive regime. Applying our three-dimensional tracking method, we were able to obtain trajectories for times that long. Evaluating these trajectories, we see a clear transition to the diffusive regime. The power of our method can be seen from Fig. 3.29. Although in the very beginning, the red curve has larger errors compared to the blue curve, the impact of these errors can be neglected for larger times. The possibility of observing trajectories over several minutes weights more than small inaccuracies in the beginning.

Chapter 4

Trajectory-Evaluation

An efficient and accurate evaluation of trajectories is a crucial point for the understanding of the underlying dynamics in bacteria locomotion. It is well known that their motion can be separated in two different states, denoted as running- and tumbling-state [19], where the state is determined by the rotation directory of flagellum attached to the bacterium [12, 18, 91]. Evolutionary advantages in the movement of these two different states are the enhancement of search efficiency [8, 10, 11] as well as aiming to or avoiding special regions [175]. Evaluating of bacteria-trajectories can mainly be separated in two different parts: 1.) Distinguish between running- and tumbling-states and 2.) in detail description of running-states. The running-state is determined by a smooth forward-movement of the bacterium with approximately a constant velocity whereas the tumbling-state is determined by a quick change in the bacterium orientation and a drop in the bacterium velocity [19]. A simulated, three-dimensional trajectory of a bacterium is represented as the black-solid line in Figure 4.1 (a), where the tumbling-events are marked as dots. Unlike in the experiments done in [42, 129], many experimental-

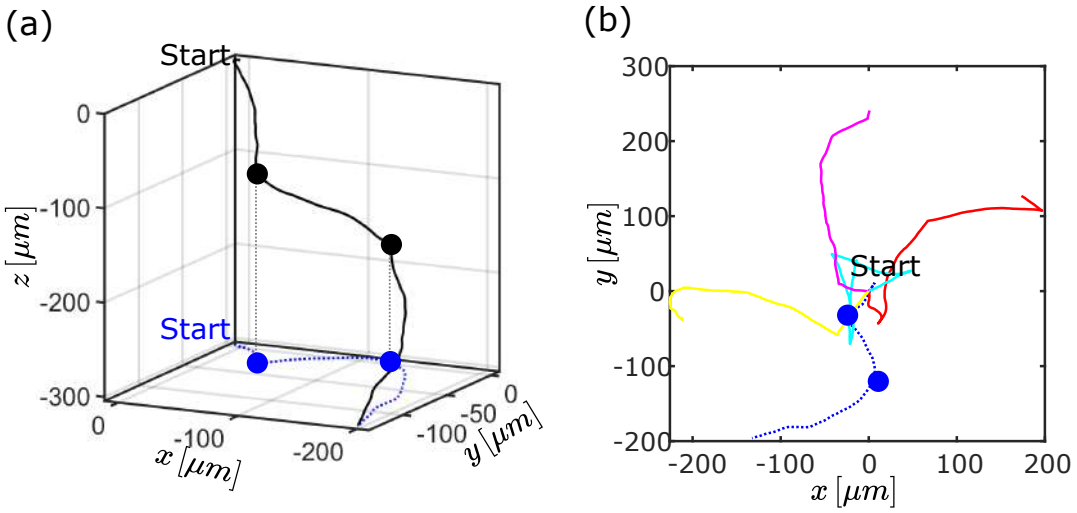

FIGURE 4.1: (a) Example for a three-dimensional simulated trajectory (black-solid line) and the corresponding projection in the x-y-plane (blue-dotted-line). Tumbling-events are marked as dots. (b) Plot of measured trajectories for Bacillus subtilis (solid lines) and a simulated trajectory (blue-dotted line) and tumbling-events marked as dots.

setups do not provide the possibility to detect the height (z-position) of the bacterium [30, 111, 123, 139, 166, 180]. Therefore it is only possible to evaluate the projection of the trajectory in the x-y-plane, represented as the blue-dotted line in Figure 4.1 (a). To compare the simulated trajectory with real trajectories, the projection of the simulated line is also plotted as the blue-dotted line in Figure 4.1 (b), whereas the real trajectories are plotted as the solid lines.
Although there exist many methods to evaluate bacteria-trajectories [114, 123, 164], they mainly follow the same principle: Extracting orientation- and velocity information from the measured trajectories and afterwards applying an algorithm to distinguish between running- and tumbling-states. In this chapter we introduce the Kalman-Filter [74] as a method suitable to parallelize the extraction- and distinction-process. The advantage of this filter is 1.) an intrinsic distinction between measurement- and process-noise [56, 59] and 2.) the possibility of an intrinsic distinction between running- and tumbling-states [59].

In section 4.1 we describe the simulation-process of the running-state, in section 4.2 we include tumbling-events. In the next section 2.3 we introduce the Kalman-Filter as a powerful tool to extract parameters of bacteria locomotion. Afterwards we extend the Kalman-Filter to include the possibility to not only extract trajectory-parameters of the running-state but also distinguish between running- and tumbling-states. Finally in section 4.3 we use the Kalman-filter to extract parameters of simulated trajectories and experimental data.

4.1 Simulate trajectories - running state

In this section we will discuss how we can simulate the running state of bacteria. To simulate bacteria trajectories, there are two approaches:

1. qualitative simulation: In a qualitative-simulation, we simulate the cell body as well as the flagella of the bacterium. A motor torque forces the flagellum to rotate. The physical interactions of the flagellum with its surroundings forces the simulated bacterium to move, creating a trajectory. These kind of simulations are described in chapter 5.

2. quantitative simulation: The trajectory of a certain kind of bacterium is defined via several parameters, such as diffusion coefficient D, tumbling-times t_t, tumbling angle θ_t. Based on these parameters D, t_t, θ_t. We can create random numbers $\boldsymbol{r}_{\text{simulation}}$, simulating the quantitative behavior of the trajectory. These random numbers $\boldsymbol{r}_{\text{simulation}}$ define a trajectory with the same statistical properties as the trajectory of real bacteria.

We are interested in the extraction of statistical trajectory-properties, such as the rotational diffusion coefficient D_r. Therefore, in this chapter, we will perform quantitative trajectory simulations using parameters $\boldsymbol{p}_{\text{simulation}}$ and will compare different methods in the efficiency of extracting these parameters

$\boldsymbol{p}_{\text{simulation}}$ from the simulated trajectories. Furthermore we split the simulation process in two parts:

1. 2D: In section 4.1.1 we simulate two dimensional-trajectories as they are observed using a conventional optical microscope.
2. 3D: In section 4.1.2 we expand the method defined in section 4.1.1 suitable to simulate 3D-trajectories, as free bacteria tend to swim in three dimensions.

In the following section 4.1.1 we start with the simulation of 2D-trajectories:

4.1.1 Running state: 2D

To quantitatively simulate the running state in two dimensions, we can have a look at Fig. 4.2 (a). The blue dots $\boldsymbol{P}_j$ mark the particle position at time-

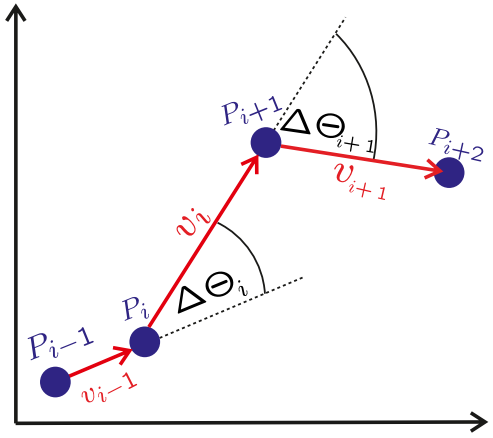

FIGURE 4.2: Representation of the simulation-process for two-dimensional trajectories. Based on the positions $\boldsymbol{P}_{i-1}$ and $\boldsymbol{P}_i$, the change in direction $\Delta\Theta_i$ and the speed v, the position $\boldsymbol{P}_{i+1}$ is absolutely defined.

step t_j. The vectors $\boldsymbol{v}_j$ define the velocity between positions $\boldsymbol{P}_{j-1}$ and $\boldsymbol{P}_j$. The angle $\Delta\theta_j$ defines the difference in the orientation between successive vectors $\boldsymbol{v}_{j-1}$ and $\boldsymbol{v}_j$. Rather than using the variable $\Delta\Theta_i$ it is more intuitive to use the variable

$$\Theta_i = \sum_{j=0}^{i} \Delta\Theta_j, \tag{4.1}$$

representing the absolute orientation of velocity $\boldsymbol{v}_j$ with respect to the x-axis. The quantity θ_j is also represented in Fig. 4.2. A bacterial trajectory in its running-state can be defined via the distribution of angles $\Delta\theta_j$ and speed $v_j = \text{abs}\left(\boldsymbol{v}_j\right)$. The orientations $\Delta\theta_j$ are normal-distributed

$$\boldsymbol{\Delta\Theta} \leftarrow \mathcal{N}\left(N\right)\sqrt{2D_{\text{r}}\Delta t}, \tag{4.2}$$

where $\mathcal{N}$ denotes a normal distributed random variable, N the number of elements of the trajectory, D_{r} the rotational diffusion coefficient and Δt the

time-spacing. Calculating the cumulative sum $\boldsymbol{\theta}$ of angles $\boldsymbol{\Delta\Theta}$ as defined via equation (4.1) results in a random walk for the orientation $\boldsymbol{\theta}$. Several examples for realizations of orientation $\boldsymbol{\theta}$ are represented in Fig. 4.3 (a). The black

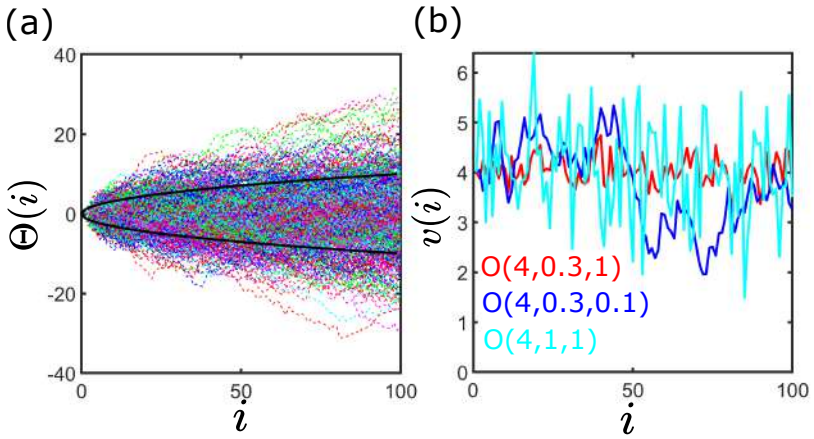

FIGURE 4.3: (a) Dashed lines represent realizations of a Random Walk. The black solid lines mark the standard-deviation. (b) Realization of the Ornstein-Uhlenbeck-process as mentioned in equation (4.3) for $\mu_{\mathrm{OU}} = 4$, $\sigma_{\mathrm{OU}} = 0.3$ and $\theta_{\mathrm{OU}} = 1$ (red), $\mu_{\mathrm{OU}} = 4$, $\sigma_{\mathrm{OU}} = 0.3$ and $\theta_{\mathrm{OU}} = 0.1$ (blue) and $\mu_{\mathrm{OU}} = 4$, $\sigma_{\mathrm{OU}} = 1$ and $\theta_{\mathrm{OU}} = 1$ (cyan).

solid lines represent the interval of the standard deviation.
The distribution of bacteria speeds v_j show different statistical properties than the angle $\Delta\theta_j$. The bacteria speed v_j in the running state oscillates randomly around a certain value μ. To simulate this behavior, we simulate the speed v_j as an Ornstein-Uhlenbeck-process

$$dv_j = \theta_{\mathrm{OU}} \left(\mu_{\mathrm{OU}} - v_j\right) dt + \sigma_{\mathrm{OU}} \sqrt{dt} \mathcal{N}. \tag{4.3}$$

The parameter θ_{OU} defines the *strength* with which the speed v_j is dragged back to its mean speed μ_{OU}. The parameter σ_{OU} defines the size of random fluctuations to the process. The impact of both parameters θ_{OU} and σ_{OU} can be seen in Fig. 4.3 (b), where we plotted three different realizations of the Ornstein-Uhlenbeck-process as described in equation (4.3) for $\mu_{\mathrm{OU}} = 4$, $\sigma_{\mathrm{OU}} = 0.3$ and $\theta_{\mathrm{OU}} = 1$ (red), $\mu_{\mathrm{OU}} = 4$, $\sigma_{\mathrm{OU}} = 0.3$ and $\theta_{\mathrm{OU}} = 0.1$ (blue) and $\mu_{\mathrm{OU}} = 4$, $\sigma_{\mathrm{OU}} = 1$ and $\theta_{\mathrm{OU}} = 1$ (cyan).
As an example for the simulation of a trajectory we show a simulation of a RW for the orientation θ_j (red solid line) and a simulation of an Ornstein-Uhlenbeck-process for the speed v_j (blue solid line) in Fig. 4.4 (a). The corresponding trajectory is shown in Fig. 4.4 (b). To check that this simulation process produces trajectories resulting in the desired rotational-diffusion-coefficient D_{r}, we simulated $N = 1000$ trajectories in two dimensions and plotted the Mean-Square-Angular-Displacement (MSAD)

$$\mathrm{MSAD}\left(\tau\right) = \frac{1}{N} \sum_{n=1}^{N} \left(\theta_n\left(\tau\right) - \theta_n\left(0\right)\right)^2. \tag{4.4}$$

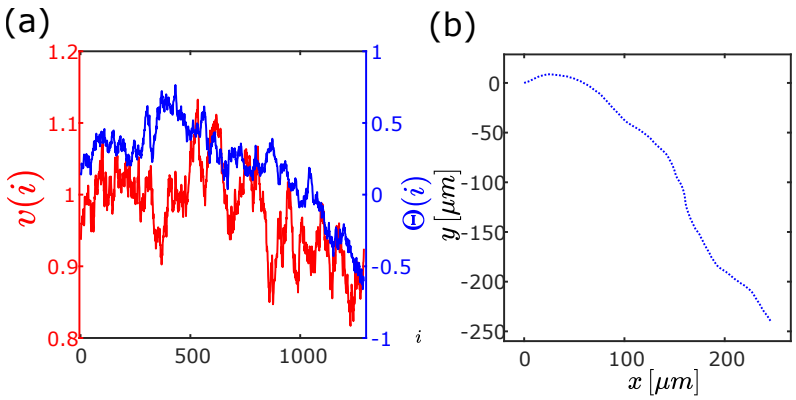

FIGURE 4.4: (a) Simulation of the speed $v(i)$ (red line) and the orientation $\Theta(i)$ (blue line). (b) Obtained trajectory based on both quantities represented in (a).

The rotational-diffusion-coefficient D_r is obtained via the relation

$$\text{MSAD}\,(\tau) = 2D_r t. \tag{4.5}$$

In Fig. 4.5 (a) we see five simulated trajectories for a rotational-diffusion-coefficient $D_r = 0.003$. The corresponding D_r-curves are represented in Fig. 4.5 (b). The calculated rotational diffusion-coefficient based on the MSAD-curves is $D_{r,\text{calculated}} = 0.0031$, indicating our method for creating two-dimensional trajectories covers the desired statistical properties. In Fig. 4.5 (c) and (e) we simulated the impact of measurement-noise via

$$\tilde{x} = x + \mathcal{N} * \sigma_x, \tag{4.6}$$
$$\tilde{y} = y + \mathcal{N} * \sigma_y, \tag{4.7}$$

for $\sigma_x = \sigma_y = 0.1$ (c) and $\sigma_x = \sigma_y = 0.25$ (e). Here $\tilde{x}$ ($\tilde{y}$) represents a position with a normal distributed position error with standard-deviation σ_x (σ_y). The corresponding MSAD-curves are represented in Fig. 4.5 (d) and (f). For the error $\sigma_x = \sigma_y = 0.1$ we calculated a rotational-diffusion-coefficient $D_{r,\text{calculated}} = 0.27$ and for the error $\sigma_x = \sigma_y = 0.25$ we calculated a rotational-diffusion-coefficient $D_{r,\text{calculated}} = 0.31$.
If we have a look at the trajectories represented in Fig. 4.5 (a), (c) and (e) it is impossible to observe qualitative differences. Nevertheless the corresponding calculated rotational diffusion coefficients D_r differ by 2 orders of magnitude. Therefore in real experiments it is crucial to estimate the tracking error. If the tracking error is too large, this means larger than 10 % of the average distance the particle moves in one second, it is impossible to calculate the rotational diffusion coefficient D_r with a reasonable accuracy.

After we have shown how to simulate the running-state of bacteria in two-dimensions, we will extend this method to simulate bacteria-trajectories in three dimensions in the next section 4.1.2.

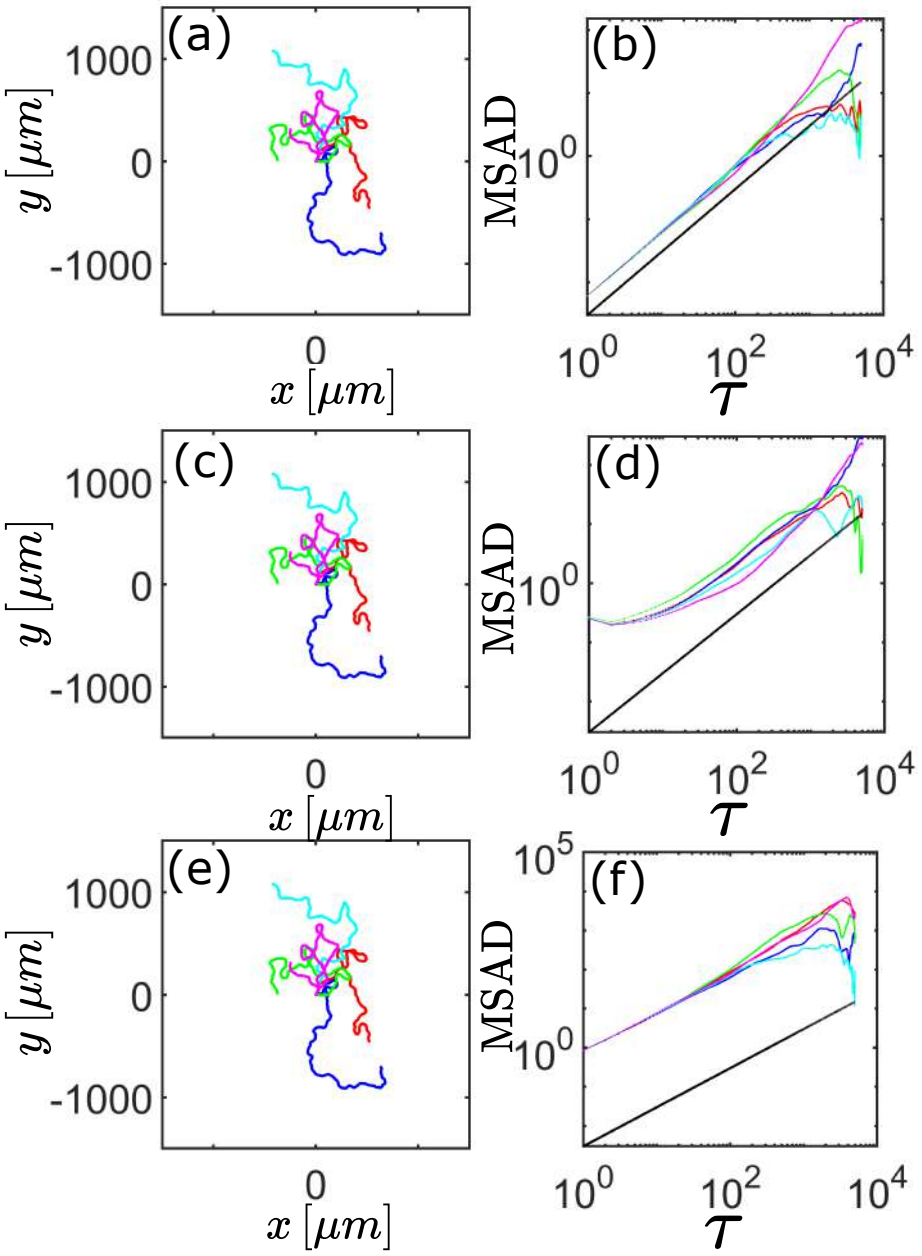

FIGURE 4.5: (a),(c),(e) Simulation of two dimensional trajectories for $D_r = 0.003$ for $\sigma = 0$ (a), $\sigma = 0.1$ (c), $\sigma = 0.25$ (e). (b),(d),(f) Calculated MSAD for the corresponding trajectories in (a), (c) and (e). The black solid line represents the theoretical obtained MSAD.

4.1.2 Running state: 3D

Using the quantities speed v_j and orientation θ_j, we are able to simulate two-dimensional bacteria trajectories. To simulate three-dimensional trajectories, we need to introduce a third quantity ϕ_j enabling us to leave the two-dimensional plane. The impact of this third component is visualized in Fig. 4.6 (a). Rather than choosing the point $\boldsymbol{P}_{i+1}$ as the unique position defined in the paper plane via speed v_{i+1} and angle Θ_i as in Fig. 4.2, we now choose

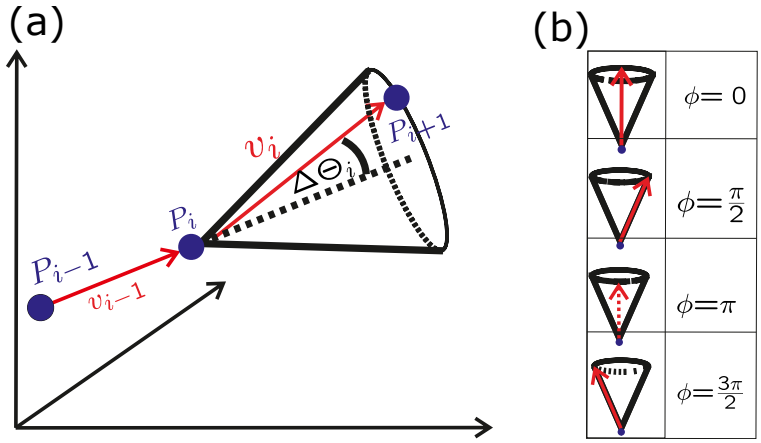

FIGURE 4.6: (a) To simulate three-dimensional trajectories we introduce a new parameter Φ. In this method, the position $\boldsymbol{P}_{i+1}$ is not absolutely defined based on the positions $\boldsymbol{P}_{i-1}$ and $\boldsymbol{P}_i$, the change in direction $\Delta\Theta_i$ and the speed v. These quantities only define the edge of the cone. The quantity Φ_i defines the position on the cone. The selection of the position on the edge of the cone is represented in (b).

the position $\boldsymbol{P}_{i+1}$ at the edge of a cone. Every point on the edge of the cone is separated by a distance v_i from point $\boldsymbol{P}_i$ and at an angle $\Delta\theta_i$. The position on the cone is defined via the uniform distributed random variable

$$\phi \in [0, 2\pi[. \tag{4.8}$$

As in the previous section 4.1.2 we have to verify that this method in creating three-dimensional trajectories replicates the desired statistical properties. Therefore we simulated several three-dimensional trajectories for a certain rotational diffusion coefficient D_r. These trajectories can be seen in Fig. 4.5 (a), (c) and (e) for $\sigma_x = \sigma_y = 0$ (a), $\sigma_x = \sigma_y = 0.1$ (c) and $\sigma_x = \sigma_y = 0.25$ (e). The corresponding MSAD-curves are represented in Fig. 4.5 (b), (d) and (f). As in this chapter we experimentally only observe bacteria-trajectories in two-dimensions, we calculated the MSAD based on the projection of the simulated three-dimensional trajectories on the x-y-plane. For the error $\sigma_x = \sigma_y = \sigma_z = 0.0$ we calculated a rotational-diffusion-coefficient $D_{\mathrm{r,calculated}} = 0.0032$, for the error $\sigma_x = \sigma_y = \sigma_z = 0.1$ we calculated a rotational-diffusion-coefficient $D_{\mathrm{r,calculated}} = 0.05$ and for the error $\sigma_x = \sigma_y = \sigma_z = 0.25$ we calculated a rotational-diffusion-coefficient $D_{\mathrm{r,calculated}} = 0.089$. We see that our method for simulating three-dimensional trajectories imitates the desired statistical properties.

As we have seen now how we can simulate the running state of bacteria in two- as well as in three dimensions, we will focus on the simulation of tumbling-events in the next section 4.2.

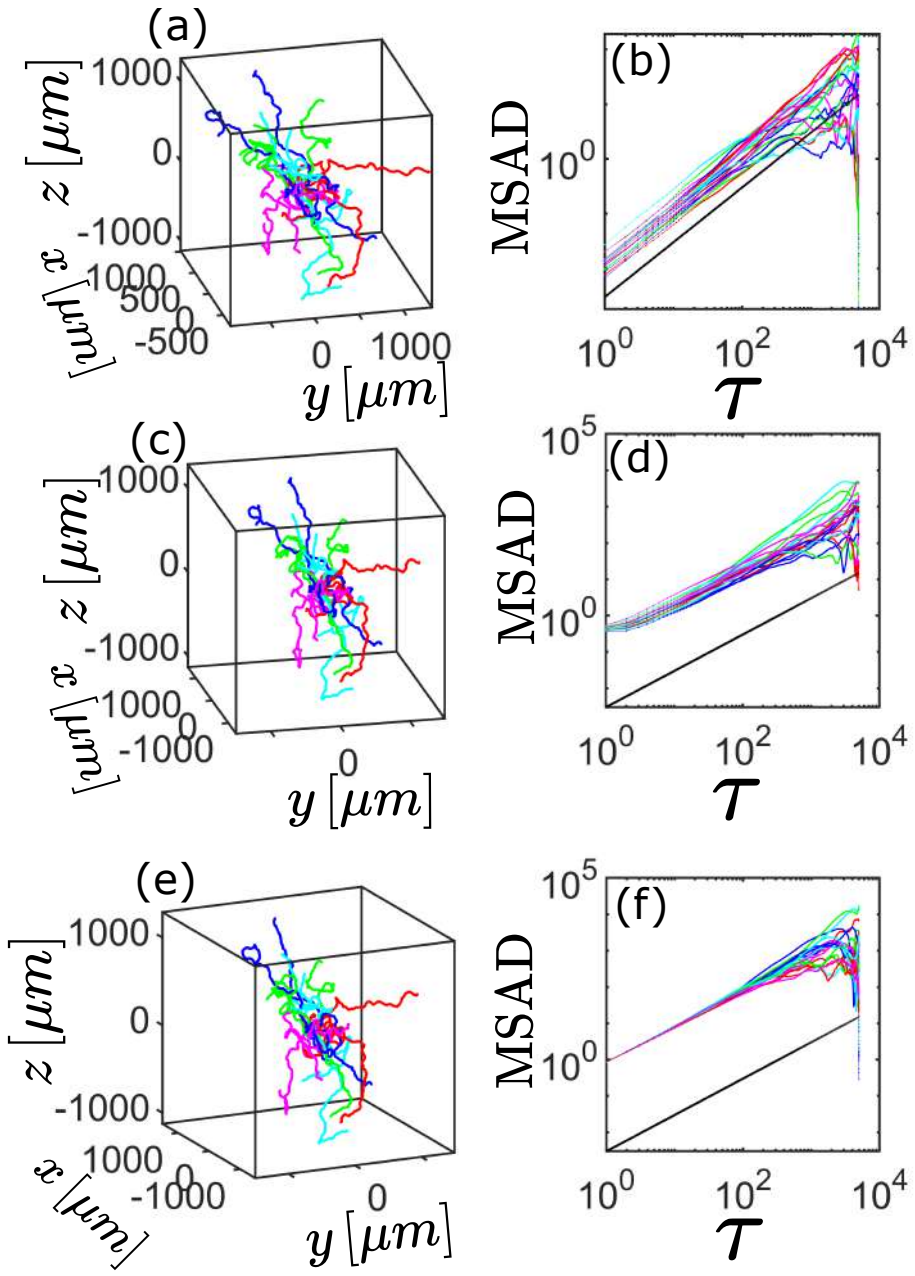

FIGURE 4.7: (a),(c),(e) Simulation of three dimensional trajectories for $D_r = 0.003$ for $\sigma = 0$ (a), $\sigma = 0.1$ (c), $\sigma = 0.25$ (e). (b),(d),(f) Calculated MSAD for the corresponding trajectories in (a), (c) and (e). The black solid line represents the theoretical obtained MSAD.

4.2 Simulate trajectories: tumbling state

In section 4.1.2 we have shown how to simulate the running state of bacteria. In this section we aim on simulating the tumbling state. Therefore we remember the two main facts about tumbling-events:

1. The speed v_j of the bacterium shows a large drop.

2. The distribution of tumbling angles θ_t defined via the change in orientation before and after the tumbling-events obeys a certain distribution $D(\theta_t)$.

To explain the process for simulating tumbling-events, let us assume a trajectory consisting of four running states and three tumbling-events. Let us define seven time-intervals $t_{r,1}$, $t_{r,2}$, $t_{r,3}$, $t_{r,4}$, $t_{t,1}$, $t_{t,2}$ and $t_{t,3}$ of length $T_{r(t),i}$. An example for a two-dimensional trajectory is represented in Fig. 4.8 (a). The

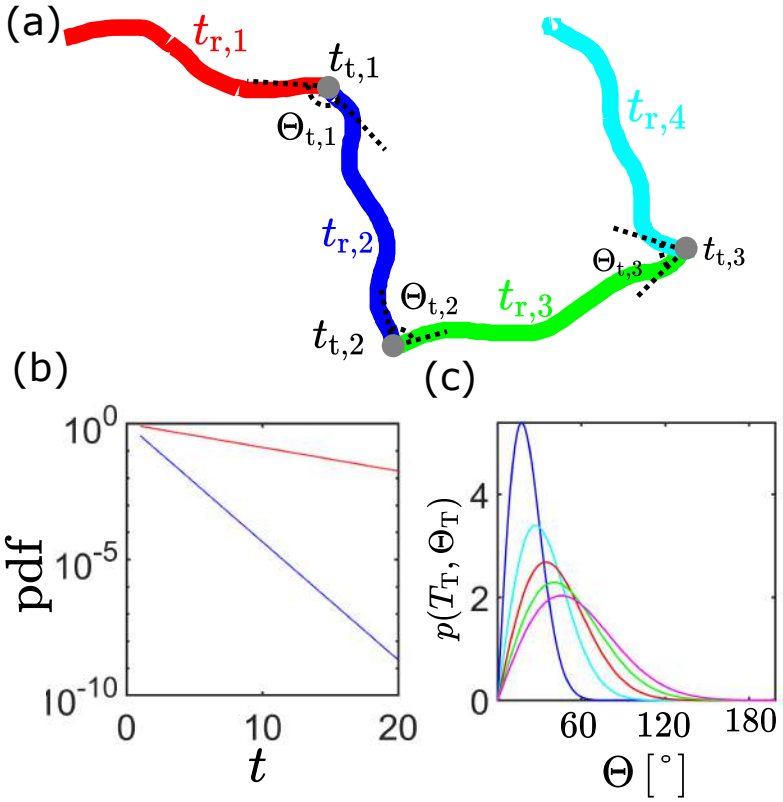

FIGURE 4.8: (a) Simulation of a trajectory consisting of four running states at time-intervals $t_{r,1}$, $t_{r,2}$, $t_{r,3}$ and $t_{r,4}$ and three tumbling states at time-intervals $t_{t,1}$, $t_{t,2}$ and $t_{t,3}$. (b) PDF for the duration of tumbling-times T_t (blue) and running times T_r (red). (c) Probability $p(\theta_t, T_{t,i})$ for the tumbling angle θ_t based on a certain tumbling-time $T_{t,i}$.

length $T_{r,i}$ of a running state is chosen based on experimental data from [118]. The corresponding probability-density function (PDF) is represented as the red curve in Fig. 4.8 (b). The corresponding PDF for the tumbling-times $T_{t,i}$ is represented as the blue curve in Fig. 4.8 (b). The tumbling-angle θ_t is simulated based on the experimental data from [118, 140] and depends on the length of the tumbling-time $T_{t,i}$ via

$$p(\theta_t, T_{t,i}) = \sum_{l=0}^{\infty} \frac{2l+1}{2} \exp(-D_r l(l+1) T_{t,i}) P_l(\cos\theta_t) \sin\theta_t, \qquad (4.9)$$

where P_l is the Legendre's polynomial of order l (see corresponding pdf in Fig. 4.8 (c)). In Fig. 4.9 (a) we see the simulation of orientations θ_j (blue),

angle ϕ_j (red) and speed v_j (green) to create a trajectory without tumbling-events. The corresponding trajectory is represented as the magenta dashed line in Fig. 4.9 (c). To understand the impact of the tumbling-events on

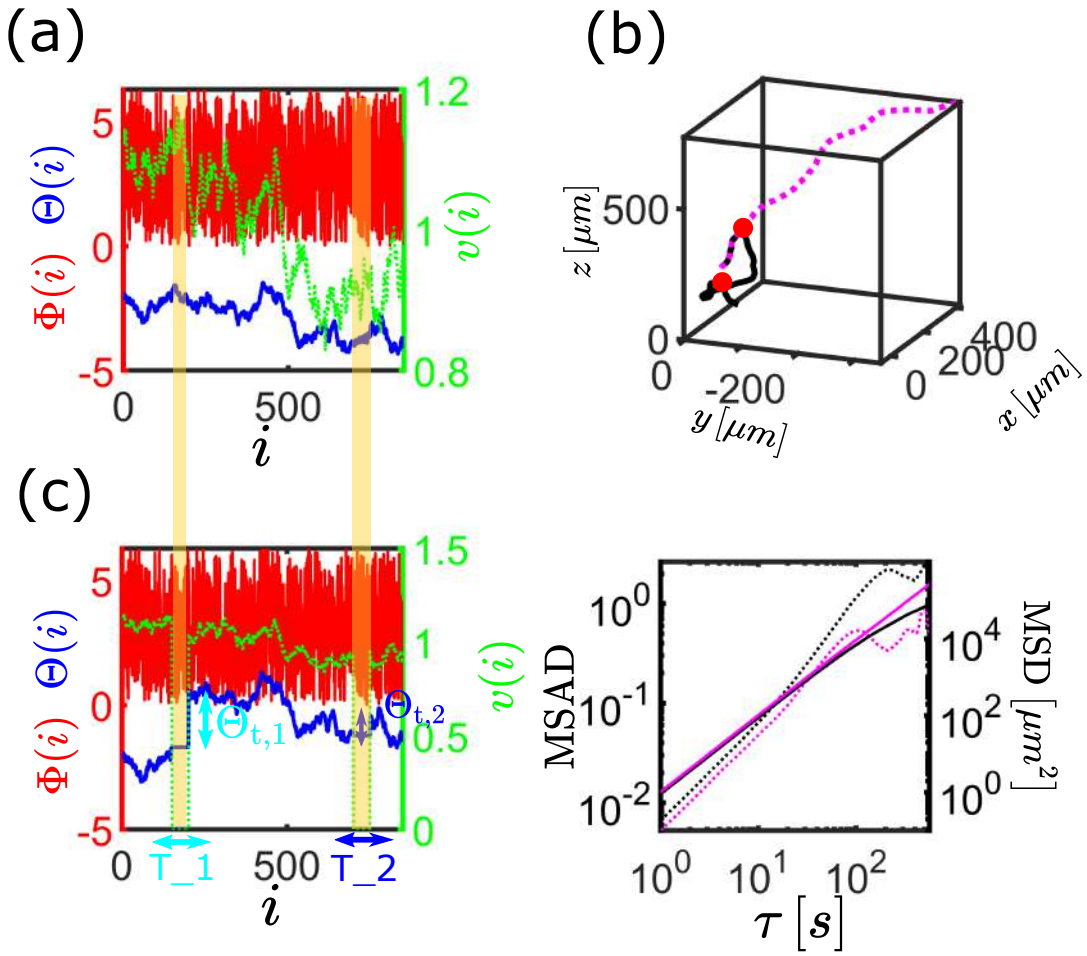

FIGURE 4.9: (a) (c) Simulation of the quantities $\Theta(i)$ (blue), $\Phi(i)$ (red) and $v(i)$ (green) without (a) and including (c) tumbling-events. During the time-interval $T_1 = [150, 200]$ ($T_2 = [750, 800]$) a tumbling event with tumbling angle $\Theta_{t,1}$ ($\Theta_{t,2}$) occurs. (b) Simulating of a three dimensional trajectory based on the quantities $\Theta(i)$, $\Phi(i)$ and $v(i)$ represented in (a) ((c)) as the magenta dotted (black-solid) line. (d) Representation of the MSAD (solid lines) and MSAD (dashed-lines) of the trajectories represented in (b), where magenta corresponds to the trajectory without tumbling-events and black to the trajectory including tumbling-events.

trajectory-properties, the quantities orientations θ_j (blue), angle ϕ_j (red) and speed v_j (green) represented in Fig. 4.9 (c) are chosen as in Fig. 4.9 (a) and only differentiate during the tumbling-processes highlighted in yellow. For other times, the speed v and the angle ϕ are equal and the orientation θ differs only in a constant factor Θ_t. The corresponding trajectory including tumbling-events is represented as the black solid line in Fig. 4.9 (b). Initially, both trajectories are equal. After the first tumbling event, both trajectories

start to separate. We see from Fig. 4.9 (c) that in both tumbling-events T_1 and T_2, the speed v_j drops to zero. The difference between the first orientation θ_{200} after tumbling event T_1 and the last orientation θ_{150} before tumbling event T_1 defines the tumbling angle $\theta_{t,1}$. The tumbling angle $\theta_{t,2}$ is defined accordingly. In Fig. 4.9 (d) we compare the MSAD (dashed lines) and the MSD (dashed lines) for both trajectories represented in Fig. 4.9 (b). The MSAD for the trajectory including tumbling-events is larger, which can be explained due to the fact that tumbling-events introduce a larger angle between the orientation of different parts of the trajectory. In contrast, a trajectory without tumbling-events appears very smooth, therefore the difference in orientation between different parts of the trajectory is - compared to a trajectory including tumbling-events - smaller. The opposite is observed for the MSD. Here, tumbling-events lead to a *slower* separation from the origin of the trajectory, resulting in a smaller MSD for trajectories including tumbling-events. This effect can clearly be observed from the solid lines in Fig. 4.9 (d), where both MSDs are very similar at the beginning, but after a certain time the impact of tumbling-event occurs, resulting in a lower value of the black-solid curve, corresponding to the trajectory with tumbling-events.
In this chapter we wanted to give an overview about the quantitative simulation of bacteria trajectories. In the next section we present a powerful tool, the Kalman-Filter, to extract statistics from particle-trajectories.

4.3 Extract 2D-trajectory characteristics

We have seen that the relevant quantities of a three dimensional trajectory $\boldsymbol{X}$ to distinguish between the running- and the tumbling state are the speed v and the orientation θ. The angle ϕ can be neglected, as it has no influence on run- and tumble dynamics. Therefore it is sufficient to evaluate two-dimensional trajectories $\boldsymbol{X}_{\text{ma}}$ mapped in the two dimensional plane based on speed v and orientation θ. It is important to mention that a mapped trajectory $\boldsymbol{X}_{\text{ma}}$ is different to a projected trajectory $\boldsymbol{X}_{\text{pr}}$ which is typically observed via a general optical microscope, where the height of the particle is projected in the plane. A comparison between trajectories $\boldsymbol{X}$ (red), $\boldsymbol{X}_{\text{pr}}$ (blue) and $\boldsymbol{X}_{\text{ma}}$ (cyan) is shown in Fig. 4.10. We see from Fig. 4.10, that the projected trajectory $\boldsymbol{X}_{\text{pr}}$ appears very smooth and loses several features of the original trajectory $\boldsymbol{X}$. These features are still visible in the mapped trajectory $\boldsymbol{X}_{\text{ma}}$. In this section we investigate

1. how precise statistics can be extracted from projected trajectories $\boldsymbol{X}_{\text{pr}}$ and

2. how precise statistics can be extracted from mapped trajectories $\boldsymbol{X}_{\text{ma}}$.

By evaluating measured projected trajectories TR we additionally have to deal with measurement errors included in the measured trajectory TR. In Fig. 4.11 (a) we show a *true* simulated trajectory TR_{tr} as the red red curve. In Fig. 4.11 (b) we see a zoom of the region marked in Fig. 4.11 (a). To simulate a measurement error, we added a uniformly distributed error, resulting in

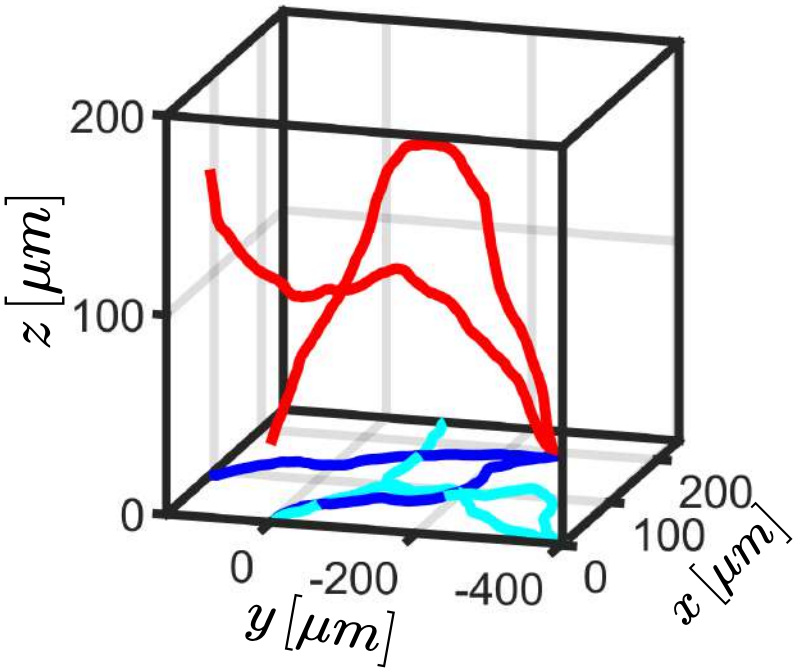

FIGURE 4.10: Comparison between trajectories $\boldsymbol{X}$ (red), $\boldsymbol{X}_{\text{pr}}$ (blue) and $\boldsymbol{X}_{\text{ma}}$ (cyan)

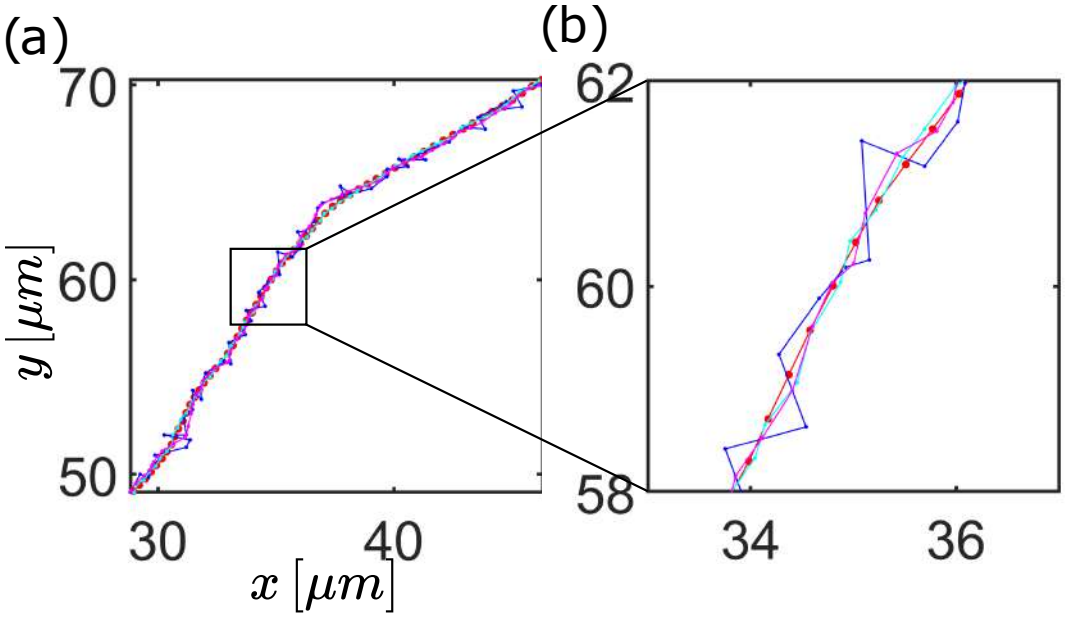

FIGURE 4.11: (a) Simulation of a trajectory (red) with added noise (blue). We applied a median-filter (magenta) and a Kalman-Filter (cyan). (b) Zoom into the region marked in (a).

the blue curve in Fig. 4.11 (a). We see a big difference between the red and the blue curve, due to the measurement error. Therefore, instead of evaluating the measured trajectory TR, it is better to first apply a filter $\mathcal{F}$ to the measured trajectory TR resulting in the trajectory $\text{TR}_{\text{filter}}$. The filter $\mathcal{F}$ should

reduce the influence of the measurement-errors. In Fig. 4.11 we show the impact of two different filters $\mathcal{F}$. As a first filter we use a standard median-filter with filter-length $fl = 40$. The corresponding filtered trajectory $\mathrm{TR}_{\mathrm{m},40}$ is represented as the magenta curve in Fig. 4.11. The next filter we applied is the Kalman-Filter introduced in section 2.3.2. The corresponding trajectory $\mathrm{TR}_{\mathrm{KF}}$ is represented as the cyan curve in Fig. 4.11. We see qualitatively that both curves $\mathrm{TR}_{\mathrm{m},40}$ and $\mathrm{TR}_{\mathrm{KF}}$ both reduce the impact of the measurement noise. In section 4.3.1, we simulate trajectories TR and apply a filter $\mathcal{F}$ to extract statistical quantities like the rotational diffusion coefficient D_{r}, tumbling-angle Θ_{t} and tumbling-time t_{t} of the trajectories TR. As we know the true quantities $D_{\mathrm{r,true}}$, tumbling-angle $\Theta_{\mathrm{t,true}}$ and tumbling-time $t_{\mathrm{t,true}}$ used for the creation of a certain trajectory TR, we can quantify the performance of a certain filter $\mathcal{F}$. After we quantified the performance of the Kalman-Filter, we apply it to estimate quantities of experimental measured trajectories $\mathrm{TR}_{\mathrm{exp}}$ in section 4.3.2. Furthermore we can compare our results of the evaluation of trajectories $\mathrm{TR}_{\mathrm{exp}}$ with another evaluation of the same trajectories done with another method from [114, 118, 164]. Subsequently we evaluate three-dimensional trajectories obtained with the measurement-setup described in chapter 3.

4.3.1 Simulated Trajectories

In this section we apply the Kalman-Filter to extract statistical quantities of simulated trajectories TR. First we show how the Kalman-Filter can be applied on particle trajectories $\mathrm{TR} = (x_i, y_i)$. Afterwards we show the performance of the Kalman-Filter in estimating the running-state as simulated in section 4.1.2. In a last step we apply the Kalman-Filter to detect tumbling-events as simulated in section 4.2.

Application of the Kalman-Filter

In 2D-tracking experiments, we measure the absolute positions $\mathrm{TR} = (x_i, y_i)$ of particles. In this thesis, we are mainly interested in the rotational diffusion coefficient D_{r} as well as tumbling-events of the underlying trajectory. Therefore, rather than the absolute positions, it is more efficient to have a look at the speed v_i and orientation Θ_i of the particle for each time t_i. The relation between absolute position (x_i, y_i) (blue) and speed/orientation (v_i, Θ_i) (red) is represented in Fig. 4.12 (a). To switch between positions (x_i, y_i) and speed/orientation (v_i, Θ_i) we can use the following equation

$$\tan(\theta_i) = \frac{\Delta y_i}{\Delta x_i}, \tag{4.10}$$

$$v_i = \frac{\sqrt{\Delta x_i^2 + \Delta y_i^2}}{\Delta t}, \tag{4.11}$$

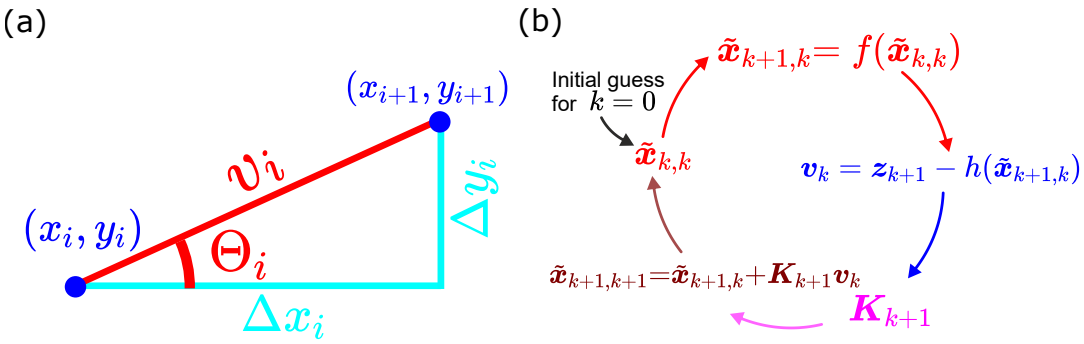

FIGURE 4.12: (a) Representation of the experimentally measured quantities (x_i, y_i) and (x_{i+1}, y_{i+1}). Based on these quantities we can calculate the displacements Δx_i and Δy_i, suitable to obtain the quantities Θ_i and v_i used in the EKF-process. (b) Visualization of the EKF-process.

where

$$\Delta x_i = x_i - x_{i-1}, \tag{4.12}$$
$$\Delta y_i = y_i - y_{i-1}. \tag{4.13}$$

As we are especially interested in estimating the quantities speed v_i and orientation Θ_i of the particle, a first approach for the state-vector would be

$$\hat{\boldsymbol{x}}_i = \begin{pmatrix} v_i \\ \Theta_i \end{pmatrix}, \tag{4.14}$$

where the orientation Θ_i and the speed v_i are defined as represented in Fig. 4.12 (a) or in equations 4.10 and 4.11. We found that using the state-vector as introduced in equation 4.14 introduces several problems. The main problem is the fact that this state-vector is not unique. To understand this problem, let us assume two states $\hat{\boldsymbol{x}}_1$ and $\hat{\boldsymbol{x}}_2$ defined via the state-vectors

$$\hat{\boldsymbol{x}}_1 = \begin{pmatrix} v_1 \\ \Theta_1 \end{pmatrix}, \quad \hat{\boldsymbol{x}}_2 = \begin{pmatrix} -v_1 \\ \Theta_1 + \pi \end{pmatrix}. \tag{4.15}$$

Both states $\hat{\boldsymbol{x}}_1$ and $\hat{\boldsymbol{x}}_2$ are the same. This introduces several numerical problems and we need a possibility to make the estimated states $\hat{\boldsymbol{x}}$ unique. To do so, rather than using the speed v_i, we introduce a second variable $\tilde{v}_i$, denoted as effective speed. The connection between speed v_i and effective speed $\tilde{v}_i$ is given via equation

$$v_i = \exp \tilde{v}_i. \tag{4.16}$$

Defining the estimated state-vector of the system as

$$\hat{\boldsymbol{x}}_i = \begin{pmatrix} \tilde{v}_i \\ \Theta_i \end{pmatrix} \tag{4.17}$$

makes the states unique, as now the speed $v = \exp \tilde{v}$ is restricted to positive values. As a last step before applying the Kalman-Filter, we have to define

the measurement-noise matrix $\boldsymbol{R}$ and the process-noise matrix $\boldsymbol{Q}$. As there is no connection between the measurement-noise in x- and y-direction, and the statistical properties for the errors in both directions are the same, we can expect the measurement-noise matrix $\boldsymbol{R}$ as

$$\boldsymbol{R} = \begin{pmatrix} r & 0 \\ 0 & r \end{pmatrix}. \tag{4.18}$$

Furthermore we assume that there is no connection between the process noise of the v- and Θ-component, resulting in the process-noise matrix

$$\boldsymbol{Q} = \begin{pmatrix} q_1 & 0 \\ 0 & q_2 \end{pmatrix}. \tag{4.19}$$

We have seen in section 2.3.1, that only the ration of measurement-noise matrix and process-noise matrix is important. Therefore we set $r = 1$, setting the measurement-noise matrix to

$$\boldsymbol{R} = \begin{pmatrix} 1 & 0 \\ 0 & 1 \end{pmatrix}. \tag{4.20}$$

The Kalman-Filtering process is summarized in Fig. 4.12 (b). The remaining quantities to run this process are the functions $\boldsymbol{f}$ and $\boldsymbol{h}$. As we always assume that the particle keeps its current speed v_i and orientation θ_i, the function $\boldsymbol{f}$ is set as

$$\boldsymbol{f}(\hat{\boldsymbol{x}}) = \hat{\boldsymbol{x}}. \tag{4.21}$$

The function $\boldsymbol{h}$ maps between measurement- and state-space. Therefore the function $\boldsymbol{h}$ is given as

$$\boldsymbol{h}(\hat{\boldsymbol{x}}) = \begin{pmatrix} \exp(\hat{x}_1)\cos(\hat{x}_2) \\ \exp(\hat{x}_1)\sin(\hat{x}_2) \end{pmatrix}. \tag{4.22}$$

All the relevant parameters for the Kalman-Filtering process are summarized in table 4.1.

Parameter	Size	Explanation
$\boldsymbol{Q}_t = \begin{pmatrix} q_1 & 0 \\ 0 & q_2 \end{pmatrix}$	$d_\mathrm{P} \times d_\mathrm{P}$	Process noise matrix.
$\boldsymbol{R}_t = \begin{pmatrix} 1 & 0 \\ 0 & 1 \end{pmatrix}$	$d_\mathrm{M} \times d_\mathrm{M}$	Measurement noise matrix.
n	$\mathbb{N}$	Number of measurements.
$d_\mathrm{P} = 2$	$\mathbb{N}$	Parameter dimension.
$d_\mathrm{M} = 2$	$\mathbb{N}$	Measurement dimension.
$\boldsymbol{Y}_t$	$\mathbb{R}^{(d_\mathrm{M} \times n)}$	Measurements at time t.
$\boldsymbol{f}$	$\mathbb{R}^{d_\mathrm{P}} \to \mathbb{R}^{d_\mathrm{P}}$	Function describing the system-evolution for small timesteps.
$\boldsymbol{h}$	$\mathbb{R}^{d_\mathrm{P}} \to \mathbb{R}^{d_\mathrm{M}}$	Function giving the link between measurement-space and parameter-space.
$\boldsymbol{F}_t$	$\mathbb{R}^{d_\mathrm{P} \times d_\mathrm{M}}$	Jacobian of $\boldsymbol{f}$ at time t.
$\boldsymbol{H}_t$	$\mathbb{R}^{d_\mathrm{P} \times d_\mathrm{M}}$	Jacobian of $\boldsymbol{h}$ at time t.

TABLE 4.1: Relevant parameters for the Extended-Kalman-Filter (EKF).

With the defined state-vector $\hat{\boldsymbol{x}}$ and the process- and measurement-noise matrices $\boldsymbol{Q}$ and $\boldsymbol{R}$ we can run the Kalman-Filtering process, summarized in Fig. 4.12 (b).

Calculation of the rotational diffusion coefficient

We have seen in section 2.2.4, that the rotational diffusion coefficient D_r can be calculated based on the Mean Squared Displacement (MSD) applying equation

$$\mathrm{MSD} = \frac{2{v^2}^2}{q_\phi} \left(q_\phi t - 1 + \exp\left(-q_\phi t\right)\right), \quad \tau_\mathrm{r} = \frac{1}{q_\phi}, \quad D_\mathrm{r} = \frac{1}{(d-1)\tau_\mathrm{r}}. \tag{4.23}$$

Furthermore the rotational diffusion coefficient D_r can be calculated by calculating the Mean Angular Squared Displacement (MSAD) and applying the equation

$$\mathrm{MSAD} = 2dD_\mathrm{r}t. \tag{4.24}$$

Here d is the dimension of the system. In the following we apply four different methods for the calculation of the rotational diffusion coefficient D_r, where two of them are based on the original measured data, and two of them have an intermediate step of Kalman-Filtering.
We have summarized four methods for the calculation of the rotational diffusion coefficient in Fig. 4.13. Based on the measured trajectories, the di-

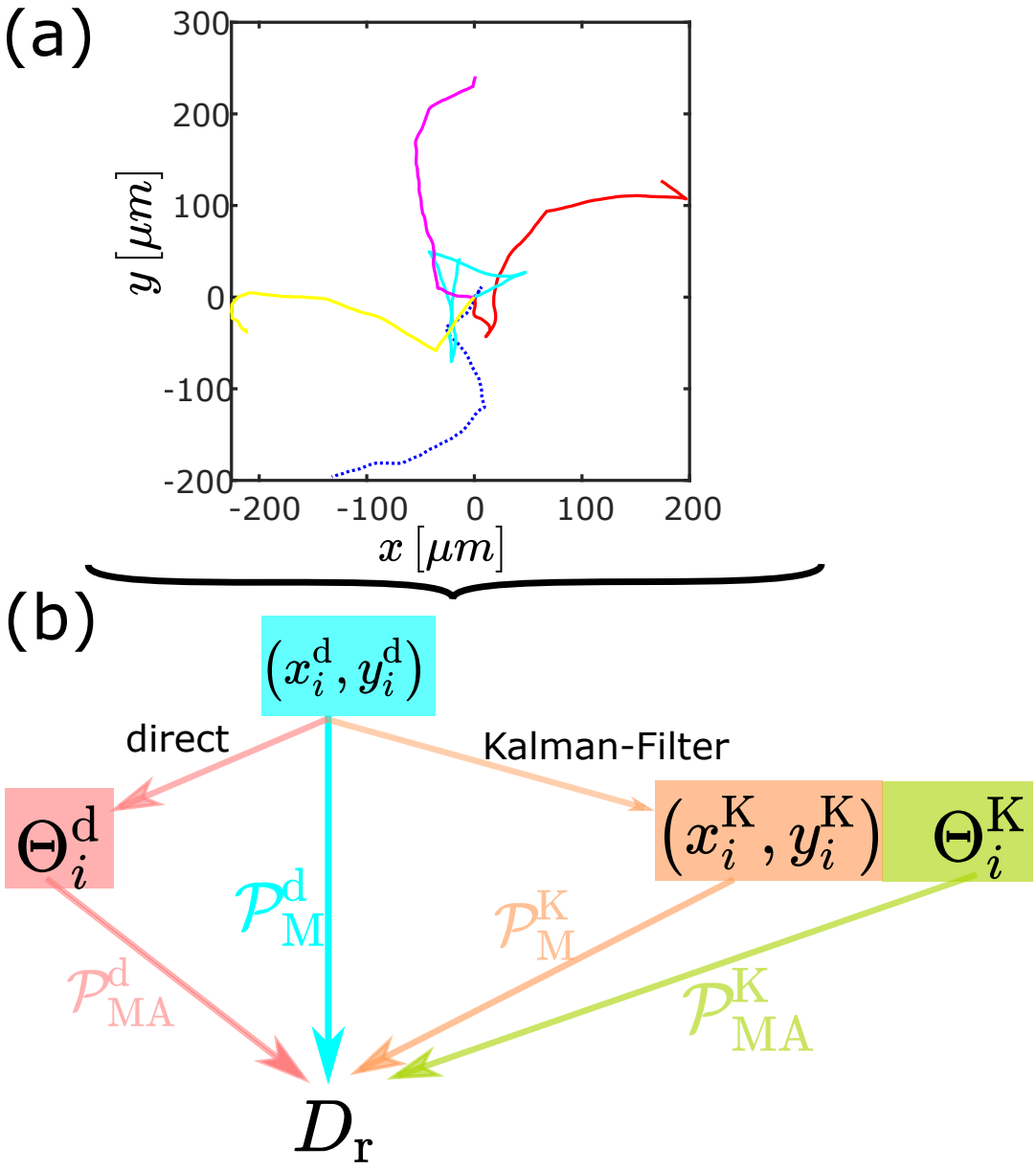

FIGURE 4.13: (a) Representation of certain trajectories. (b) Representation of the for different methods $\mathcal{P}_{\mathrm{M}}^{\mathrm{d}}$, $\mathcal{P}_{\mathrm{MA}}^{\mathrm{d}}$, $\mathcal{P}_{\mathrm{M}}^{\mathrm{K}}$ and $\mathcal{P}_{\mathrm{MA}}^{\mathrm{K}}$ to extract the rotational diffusion coefficient D_{r}.

rectly measured positions $(x_{i,d}, y_{i,d})$ for each trajectory are extracted. Based on the positions $(x_i^{\mathrm{d}}, y_i^{\mathrm{d}})$, the rotational diffusion-coefficient D_{r} can be calculated by applying equation 4.23. This policy for the calculation of D_{r} is denoted as $\mathcal{P}_{\mathrm{M}}^{\mathrm{d}}$. Rather than directly calculating D_{r} from the measured positions $(x_i^{\mathrm{d}}, y_i^{\mathrm{d}})$, we can add an intermediate step to calculate the orientations Θ_i^{d}. Based on these orientations Θ_i^{d}, we can apply equation 4.24 to calculate D_{r}. This policy will be determined as $\mathcal{P}_{\mathrm{MA}}^{\mathrm{d}}$. Rather than evaluating the measured data $(x_{i,d}, y_{i,d})$, we can add an intermediate step, the Kalman-Filter. After applying the Kalman-Filter on the measured data $(x_i^{\mathrm{d}}, y_{i^{\mathrm{d}}})$, we obtain the Kalman-Filtered positions $(x_i^{\mathrm{K}}, y_{i^{\mathrm{K}}})$ as well as the orientation Θ_i^{K}. Here

we can rather apply equation 4.23 to calculate D_r, denoted as policy $\mathcal{P}_M^K$. Or we can apply equation 4.23, denoted as policy $\mathcal{P}_{MA}^K$.
To quantify the efficiency in the calculation for the rotational diffusion coefficient D_r for each policy $\mathcal{P}$, we create a certain number $n = 1000$ of simulated trajectories Tr in the running state for a certain rotational diffusion-coefficient D_r. For each trajectory Tr we estimate the rotational-diffusion coefficient D_r applying a certain policy $\mathcal{P}$. The efficiency Eff $(\mathcal{P}, D_r)$ of a certain policy $\mathcal{P}$ in the estimation of the rotational diffusion coefficient D_r is given as median of the normalized error:

$$\text{Eff}\,(\mathcal{P}, D_r) = \text{median}\left(\frac{\boldsymbol{D}_e - D_r}{D_r}\right). \tag{4.25}$$

The efficiencies Eff $(\mathcal{P}, D_r)$ for different values of the *true* rotational diffusion coefficient D_r are represented in Fig. 4.14. We see that the performance

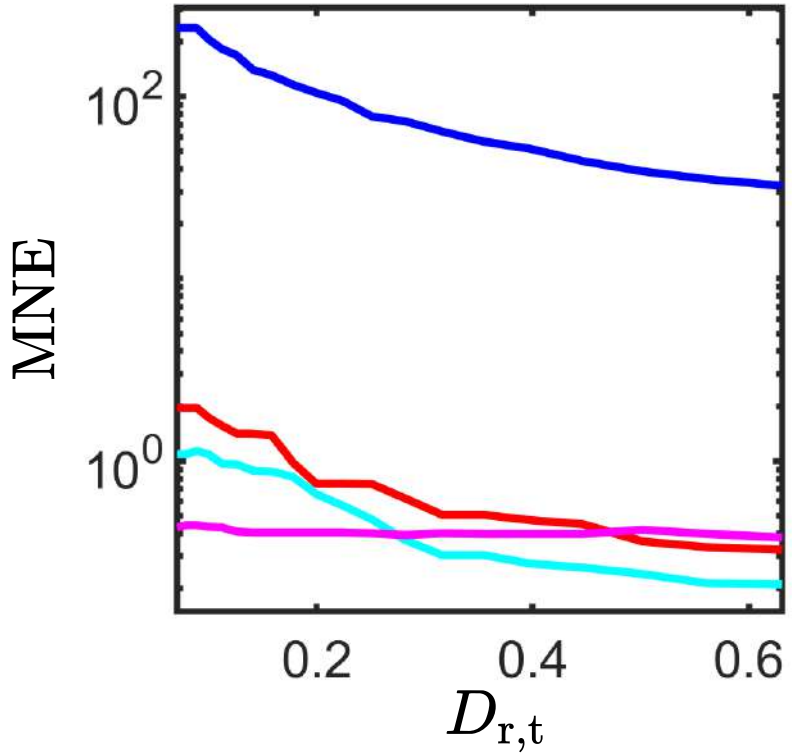

FIGURE 4.14: Comparison of the performance of policies $\mathcal{P}_M^d$ (red), $\mathcal{P}_{MA}^d$ (blue), $\mathcal{P}_M^K$ (cyan) and $\mathcal{P}_{MA}^K$ (magenta).

of the policy $\mathcal{P}_{d,MSAD}$ is the worst of all policies. The reason is that if we use the orientation Θ obtained via direct measurements, the error in these orientations is very large due to noise in the position-measurements. Up to a rotational-diffusion coefficient D_r of approximately $D_r = 0.5\,\frac{1}{s^2}$, both Kalman-methods $\mathcal{P}_{\text{Kalman, MSD}}$ and $\mathcal{P}_{\text{Kalman, MSAD}}$ have a better performance than the policy $\mathcal{P}_{\text{Kalman, MSD}}$. The policy $\mathcal{P}_{\text{Kalman, MSD}}$ has always a better performance than the policies based on direct-measurements, but choosing the best policy depends on the range of diffusion coefficients we want to estimate. As it is known that the rotational-diffusion coefficient of Bacillus

Subtillis is approximately $D_\mathrm{r} = 0.2\,\frac{1}{\mathrm{s}^2}$, the best policy to choose would be $\mathcal{P}_{\mathrm{Kalman,\,MSAD}}$ although it performs worse than the other policies for larger rotational-diffusion coefficients D_r. It is important to realize that we simulated the trajectories in three dimensions, but evaluated only the projection of the trajectory in the two-dimensional plane. Nevertheless we are able to determine the rotational-diffusion-coefficient D_r of the three-dimensional trajectory.

Tumbling-events of projected trajectories

Now we are able to extract the rotational diffusion coefficient D_r from a simulated three-dimensional trajectory $\boldsymbol{X} = (x_i, y_i, z_i)$ mapped in the two dimensional plane $\boldsymbol{X}_\mathrm{pr}\,(x_i, y_i)$. In a next step we would like to use the EKF introduced in section 2.3.2 to detect tumbling-events TE of simulated three-dimensional trajectories $\boldsymbol{X}$. As we would like to simulate the tracking of bacteria with a conventional light-microscope, these three-dimensional trajectories are also restricted in the two-dimensional plane, denoted as $\boldsymbol{X}_\mathrm{pr}$. An example of a simulated three dimensional trajectory $\boldsymbol{X}$ can be seen as the red curve in Fig. 4.15 (a). tumbling-events are represented as cyan dots. The corresponding projection $\boldsymbol{X}_\mathrm{pr}$ is represented as the blue curve in Fig. 4.15 (a), tumbling-events are marked as magenta dots. The corresponding speeds v_i and orientations Θ_i of the trajectory $\boldsymbol{X}$ are represented as the red lines in Fig. 4.15 (b) and (c). Here, the beginning and the end of a tumbling-events is marked via a black vertical line. If we have a look at Fig. 4.15 (b), we see that tumbling-events occur when there is a drop in the speed v. But as we are only able to detect the trajectory $\boldsymbol{X}_\mathrm{pr}$, the projection of the trajectory $\boldsymbol{X}$ in the xy-plane, we can only observe the speed $\tilde{v}_i$ in this plane, represented as the blue curve in Fig. 4.15 (b). We see that there are several events with a large drop in speed $\tilde{v}$, which do not belong to a tumbling event of the original trajectory $\boldsymbol{X}$. This is due to the fact that a movement of the particle in the z detection cannot be observed in the xy-plane. Therefore a particle only moving in the z-direction would result in a speed $\tilde{v} = 0$ in the xy-plane. The impact of the projection in the xy-plane is also visible through the projected orientation $\tilde{\Theta}$. In Fig. 4.15 (c) we see several jumps in the blue curve - representing $\tilde{\Theta}$ - which do not correspond to a tumbling event. Our main goal in this section is to investigate how precise we are able to detect tumbling-events despite the limitation of dealing with projections $\boldsymbol{X}_\mathrm{pr}$ in the xy-plane. A crucial experimental quantity which impacts the ability to observe a three-dimensional trajectory is the depth of field. Only a particle in the depth of field can be observed via the microscope. In the following, the notation $\boldsymbol{X}_{\mathrm{pr},w}$ denotes a trajectory with

$$w = \max\left(z_i\right) - \min\left(z_i\right). \tag{4.26}$$

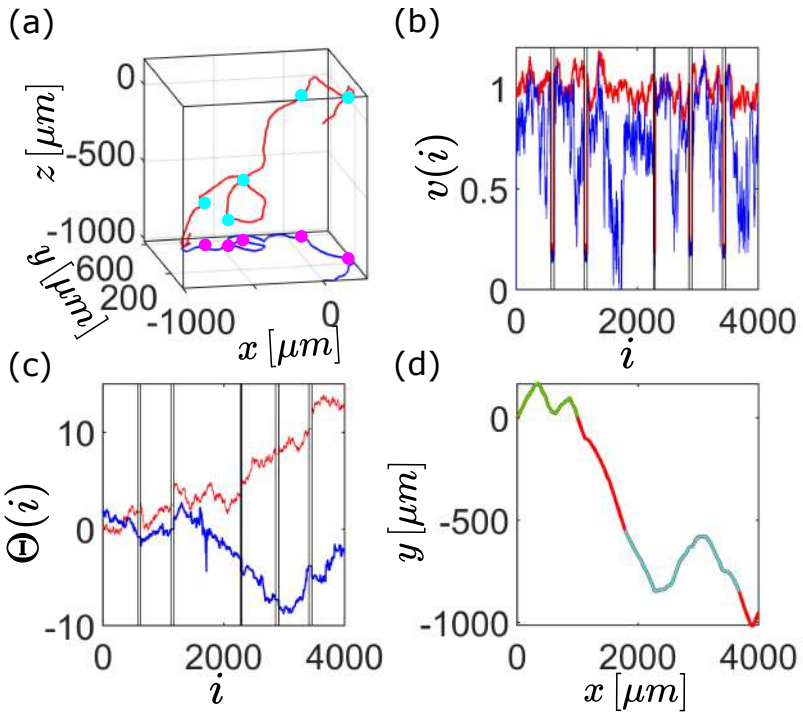

FIGURE 4.15: (a) Simulation of a three dimensional trajectory (red) and the corresponding projection in the xy-plane (blue). Tumbling-events are marked as cyan and magenta dots. (b),(c) Representation of the speed $v(i)$ (orientation $\Theta(i)$) for the three dimensional (red) and projected (blue) trajectory. (d) Representation of the height-profile of the trajectory from (a). Longest possible tracked trajectory corresponding to depth of field $\boldsymbol{X}_{\text{pr},160}$ (green) and $\boldsymbol{X}_{\text{pr},300}$ (cyan).

This allows us to quantify the performance in detecting tumbling-events TE based on the width w. In Fig. 4.15 (d) we see the high-profile z of the trajectory $\boldsymbol{X}$ represented in Fig. 4.15 (a). We included two trajectories $\boldsymbol{X}_{\text{pr},160}$ (green) and $\boldsymbol{X}_{\text{pr},300}$ (cyan). To detect tumbling-events, we apply the IMM-filter introduced in section 2.3.3. The main-feature of the IMM-filter is the possibility to distinguish between different models describing a process. If we have a look at Fig. 4.15 (b) and (c), we see that the speed v_i and orientation Θ_i undergoes a relative smooth development in case of being in the running state. We already applied the EKF to estimate the running state. The main-input matrices are the process-noise matrix $\boldsymbol{Q}_{\text{ru}}$ and the measurement noise-matrix $\boldsymbol{R}_{\text{ru}}$, where the subscript ru denotes that the matrices are used to describe the running-state. In a tumbling-events, the measurement noise remains the same, therefore the measurement-noise matrix $\boldsymbol{R}_{\text{tu}}$ during a tumbling state can be chosen as $\boldsymbol{R}_{\text{tu}} = \boldsymbol{R}_{\text{ru}} = \boldsymbol{R}$. But the beginning and the end of a tumbling event show a large process-noise, visible as the big jumps in Fig. 4.15 (b) and (c). Therefore we set the process noise-matrix $\boldsymbol{Q}_{\text{tu}}$ during a tumbling event to

$$\boldsymbol{Q}_{\text{tu}} = \begin{pmatrix} f_1 & 0 \\ 0 & f_2 \end{pmatrix} \boldsymbol{Q}_{\text{ru}}, \tag{4.27}$$

where $f_1, f_2 > 1$. Here the definition 4.27 reflects the fact that the process noise during a tumbling event is larger than during a running event.
Let us now apply the IMM-filter on the trajectory represented in Fig. 4.15 (a). For each time-step i this yields the probability p_r of the system being in the running state and the probability $p_t = 1 - p_r$ of the system being in the tumbling state. To be precise, the p_r reflects the probability of the system being in the running state. But for the tumbling-state we do not have a *clean* model. We expect it to have a larger process noise, reflected by the parameters f_1 and f_2 form equation 4.27. So the probability p_t can be better described as the probability not being in the running state. In Fig. 4.16 (a) we plot the probability p_r of the system being in the running-state for the trajectory represented in Fig. 4.15 (a) as the red curve. The beginning and the end

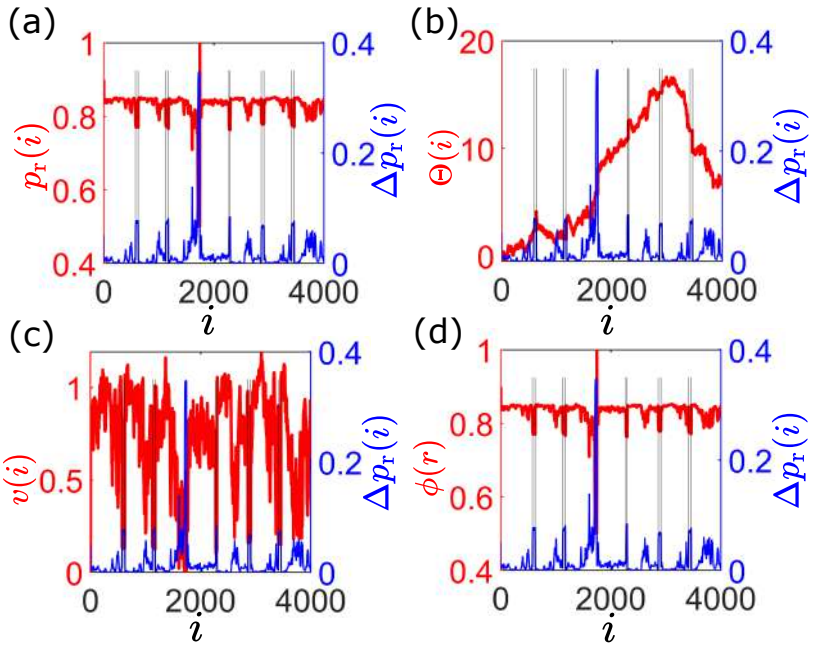

FIGURE 4.16: Representation of the relation between the quantity Δp_r (blue) and p_r (red, (a)), Θ (red, (b)), v (red, (c)) and ϕ (red, (d)). Black vertical lines represent tumbling intervals.

of tumbling-events are represented as black vertical lines. We see that in case of tumbling-events, there is a clear dip in the probability p_r, indicating that at these times the probability of being in the running state is lower, indicating the system switched to the tumbling state. It turns out that rather than evaluating the probability p_r to detect tumbling-events, it is more efficient - especially in the case of experimental data - to evaluate the quantity

$$\Delta p_r(i) = p_r(i) - p_r(i-1), \tag{4.28}$$

representing the change of the probability $p_r(i)$. The quantity Δp_r is represented as the blue curve in Fig. 4.16 (a). We see that in case of tumbling-events, there is a local peak in the quantity Δp_r, but there are also peaks when no tumbling occurs. To understand this fact, we show the speed in the xy-plane v_k, the orientation Θ_k as well as the orientation ϕ_z between the

position difference $\Delta \boldsymbol{X}\left[(x_i - x_{i-1})\,;(x_i - x_{i-1})\,;(x_i - x_{i-1})\right]$ and the xy-plane as the red curve in Fig. 4.16 (b), (c) and (d). The blue curve represents the quantity Δp_{r}. We see in Fig. 4.16 (b) and (c) that during a tumbling event, the current speed v_{k} obeys a minimum and/or there a jump in the orientation Θ_{k}. But there are also peaks in the quantity Δp_{r} if no tumbling-events occur, especially the largest peak around the time-step 1700. The reason for these spurious peaks is the fact that due to the projection of the original three-dimensional trajectory in the two-dimensional plane we lose information. If we have a look at Fig. 4.16 (d), we see that for time-steps $a = 1700 \pm 20$ the orientation ϕ_z is close to $\phi_z(a) \approx \frac{pi}{2}$, meaning the vector $\Delta \boldsymbol{X}(a)$ is perpendicular to the xy-plane. Due to the projection in the xy-plane this movement cannot be observed, resulting in a drop in the speed v_{k} resulting in a peak of the quantity Δp_{r}.
Until now we detected tumbling-events in a qualitative way, as a peak in the quantity Δp_{r}. In a next step we define a quantitative method $\mathcal{T}$ to detect tumbling-events. Afterwards we discuss the efficiency of the method $\mathcal{T}$. To understand how the policy $\mathcal{T}$ works in order to detect tumbling-events, we can have a look at Fig. 4.17 (a). There we see three different trajectories $\tilde{\boldsymbol{X}}_w$

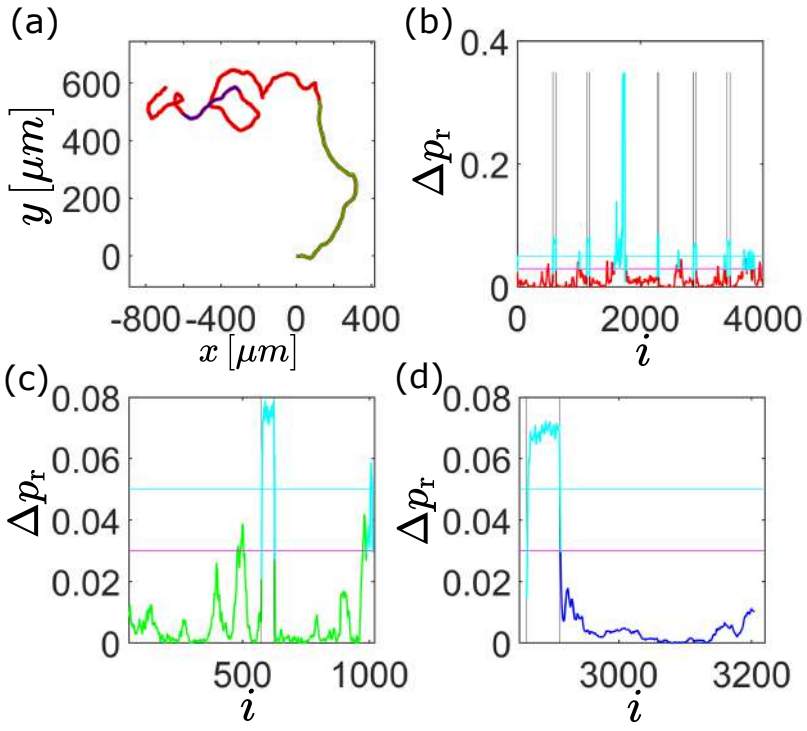

FIGURE 4.17: (a) Representation of three different trajectories $\tilde{\boldsymbol{X}}_{40}$ (blue), $\tilde{\boldsymbol{X}}_{80}$ (green) and $\tilde{\boldsymbol{X}}_{500}$ (red). (b),(c),(d) Plot of the quantity Δp_{r} for $\tilde{\boldsymbol{X}}_{40}$ (d), $\tilde{\boldsymbol{X}}_{80}$ (c) and $\tilde{\boldsymbol{X}}_{500}$ (b).

for $w_1 = 500\,\mu m$ (red), $w_2 = 80\,\mu m$ (green) and $w_3 = 40\,\mu m$ (blue). In Fig. 4.17 (b) we see the probability Δp_{r} obtained via the IMM-filter for the trajectory $\tilde{\boldsymbol{X}}_{w_1}$. We see two different thresholds, one represented as the horizontal cyan line at the value $b_{\mathrm{top}} = 0.05$, and the other one represented as the magenta one at the value $b_{\mathrm{bottom}} = 0.025$. To define a tumbling event, we use the following steps:

1. Find a time-step i satisfying

$$\Delta p_{\mathrm{r}}(j) \geq b_{\mathrm{top}}. \tag{4.29}$$

2. Find the greatest index $l \leq i$ satisfying

$$\Delta p_{\mathrm{r}}(l) \geq b_{\mathrm{bottom}}. \tag{4.30}$$

3. Find the smallest index $r \geq i$ satisfying

$$\Delta p_{\mathrm{r}}(r) \geq b_{\mathrm{bottom}}. \tag{4.31}$$

The tumbling event occurs during the time-steps j with $j \in [l, r]$. The obtained tumbling-events are represented as the cyan line in Fig. 4.17 (b), (c) and (d). We see from Fig. 4.17 (b) that five times a tumbling event is detected although no tumbling occured. In Fig. 4.17 (c) we see that two tumbling-events were falsely detected and in Fig. 4.17 (d) no false tumbling event was detected. The observed performance in Fig. 4.17 (b) for the tumbling-events of the trajectory $\tilde{\boldsymbol{X}}_{w_1}$ is quite bad. But in real experiments we can not observe trajectories in a z-range of w_1 using a conventional optical microscope due to the limitations in the depth of field. Realistic values for the depth of field are in the range around $50\,\mu m$. In the following we investigate the performance in detecting tumbling-events for different values w. We investigate the two quantities

$$p_{\mathrm{missed}} = \frac{n_{\mathrm{missed\,detected}}}{n_{\mathrm{tumblings}}} \tag{4.32}$$

quantifying the percentage of missed tumbling-events and

$$p_{\mathrm{false}} = \frac{n_{\mathrm{false\,detected}}}{n_{\mathrm{tumblings}}} \tag{4.33}$$

quantifying the percentage of falsely detected tumbling-events. The results are represented as histograms in Fig. 4.18, where we show the results for $w = 60\,\mu m$ in (a), the results for $w = 120\,\mu m$ in (b), the results for $w = 300\,\mu m$ in (c) and the results for $w = 800\,\mu m$ in (d). We see that under reasonable experimental conditions with $w \leq 150\mu m$ nearly all tumbling-events are detected. Also the number of falsely detected tumbling-events can be neglected. In the experimentally unreasonable condition of $w = 800\,\mu m$ also nearly all tumbling-events are detected, indicating that our method $\mathcal{T}$ for detecting tumbling-events is unlikely to miss tumbling-events. But the amount of falsely detected tumbling-events is quite high. This is due to the fact that for $w = 800\,\mu m$ it happens quite often that the particle moves almost purely in the z-direction, resulting in a loss of information due to the projection in the z-plane. The fact that under reasonable experimental conditions it is impossible to track particles for large distances in the z-direction is therefore beneficial to avoid falsely detected tumbling-events. In the next

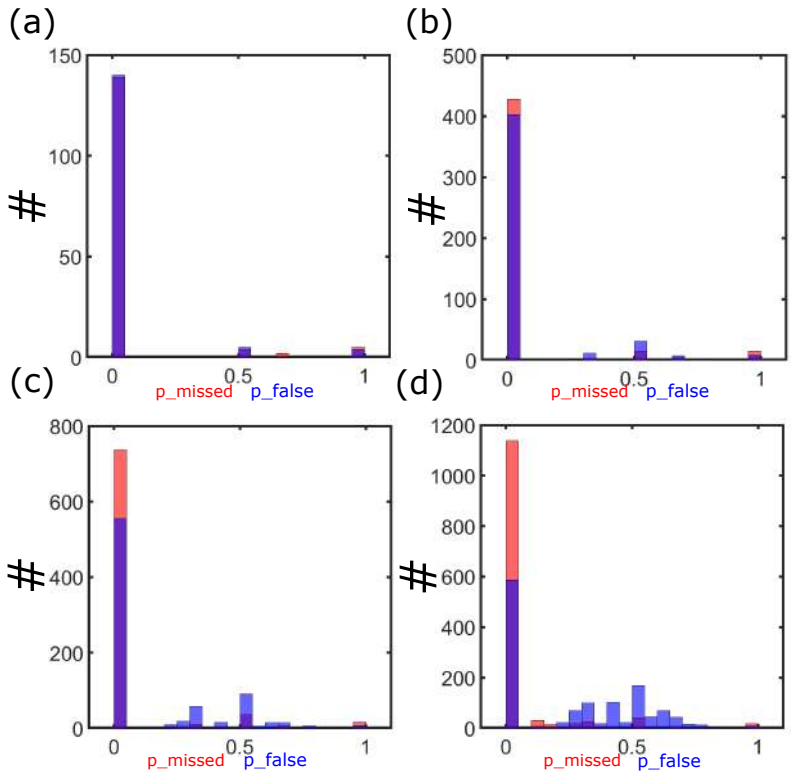

FIGURE 4.18: Histogram for the amount of missed (red) and falsely detected (blue) tumbling-events for $w = 60\,\mu m$ (a), $w = 120\,\mu m$ (b), $w = 300\,\mu m$ (c) and $w = 800\,\mu m$ (d).

section we apply the Kalman-Filter on experimental data to obtain the rotational diffusion-coefficient D_r as well as tumbling-events, tumbling-angles Θ_t, tumbling-times t_t and running-times tr.

4.3.2 Experimental data

Application on two-dimensional trajectories

In this section we apply the Kalman-Filter on experimental data. We evaluate the same dataset as in [118], so we can compare the performance of the Kalman-Filter in detecting tumbling-events to a conventional method. To understand the conventional method in detecting tumbling-events, we can have a look at Fig. 4.19. We see a trajectory in Fig. 4.19 (a), where the current speed is color-coded. In Fig. 4.19 (a) we see the corresponding speeds v_i and angular velocity ω_i. Based on drops in the speed v_i and peaks in the angular velocity ω_i, tumbling-events are quantified. A more detailed description of the method can be found in [114, 164]. The resulting tumbling-events are represented as black bars in the bottom graph of Fig. 4.19 (b).
To compare the conventional method in detecting tumbling-events with our method, we can have a look at Fig. 4.20. A trajectory of an experimentally measured bacterium is shown as the red curve in Fig. 4.20 (a). tumbling-events based on the conventional-method are represented in blue, tumbling-events based on our new method in cyan. For the detected tumbling-events,

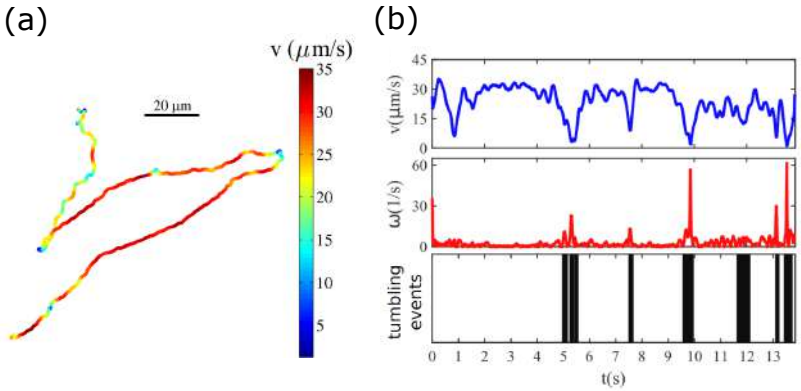

FIGURE 4.19: (a) Trajectory with color-coded speed v. (b) Speed v, angular-velocity ω and time-intervals for tumbling-events represented via black bars. Image taken from [118].

zoomed representations are shown as nine different, numbered curves. Here the measured trajectory is represented as red dots, tumbling-events based on the conventional method as blue dots and tumbling-events based on the new method as cyan dots. The orientations Θ_i and speeds v_i corresponding to the trajectory represented in Fig. 4.20 (a) are represented in Fig. 4.20 (b) and (c), where vertical lines mark tumbling-events. We see that the conventional algorithm detects much more tumbling-events than the new method. This can be explained by the different conditions for the speeds v_i and angular velocity ω_i to detect a tumbling event for the conventional method. Nearly each drop in the speed v_i results in a tumbling event. In contrast, our policy quantifies the probability for a tumbling event in a single quantity, avoiding to detect a tumbling event in case of minor tracking-errors resulting a drop in speed v_i.
The obtained probability density function for the tumbling-angle Θ_t, tumbling-time t_t and running-time tr applying the policy from [114, 164] on $n = 260$ trajectories are represented as the red curves in Fig. 4.21. The corresponding curves for our policy are represented as the blue curves in Fig. 4.21. The main difference between the conventional method and our new method can be seen in the distribution of the tumbling angle Θ_t. Where the tumbling-distribution for the conventional policy obeys a double peak at angles $\Theta_t \approx \pm 30°$, the distribution based on the new method has a peak at orientations $\Theta = 0°$. To understand why the conventional policy obeys this double peak, we evaluated all trajectory manually and found that very often the well known effect of wobbling [22] is detected as a tumbling event. One example where the wobbling is falsely detected as a tumbling event applying the conventional policy is represented in Fig. 4.21 (d), where the trajectory is represented as the red dots and the tumbling state based on the conventional policy is marked as blue dots. Here the tumbling angle is $\Theta_t = -28°$ corresponding to the left peak of Fig. 4.21 (a). These wobbling events are not detected as tumbling-events applying the new policy. Therefore the new policy is peaked around $\Theta_t = 0$. The difference in running times t_r is represented in Fig. 4.21 (b) and can be neglected, but tumbling-times t_t are chosen slightly

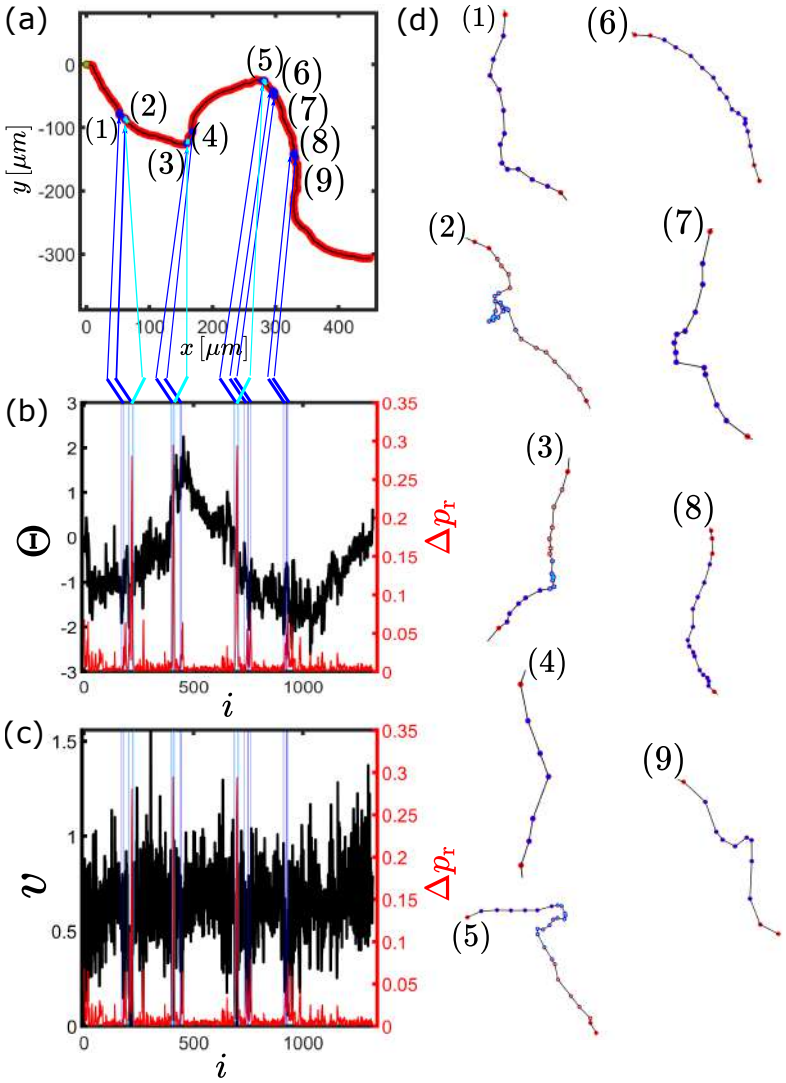

FIGURE 4.20: (a) Two dimensional projection of an experimentally measured trajectory of the bacterium *B. subtilis*. tumbling-events based on the conventional method are marked as blue dots, tumbling-events based on the IMM-filter are marked as cyan dots. The corresponding orientation Θ and speed v are represented as the black curve in (b) and (c). The quantity Δp_r is represented as the red line in (b) and (c). (d) Zoom of the trajectory for the marked tumbling-events from (a).

greater in case of the new policy. This can also be explained with the wobbling events. These events are typically in the order of $t_{\text{wobbling}} = 0.2\,s$, corresponding to the peak in Fig. 4.21 (c). As our new method does not classify these wobbling events as tumbling-events, several short events - compared to the conventional method - are not taken into account anymore, resulting in a shift of tumbling-times t_t to slightly greater values.

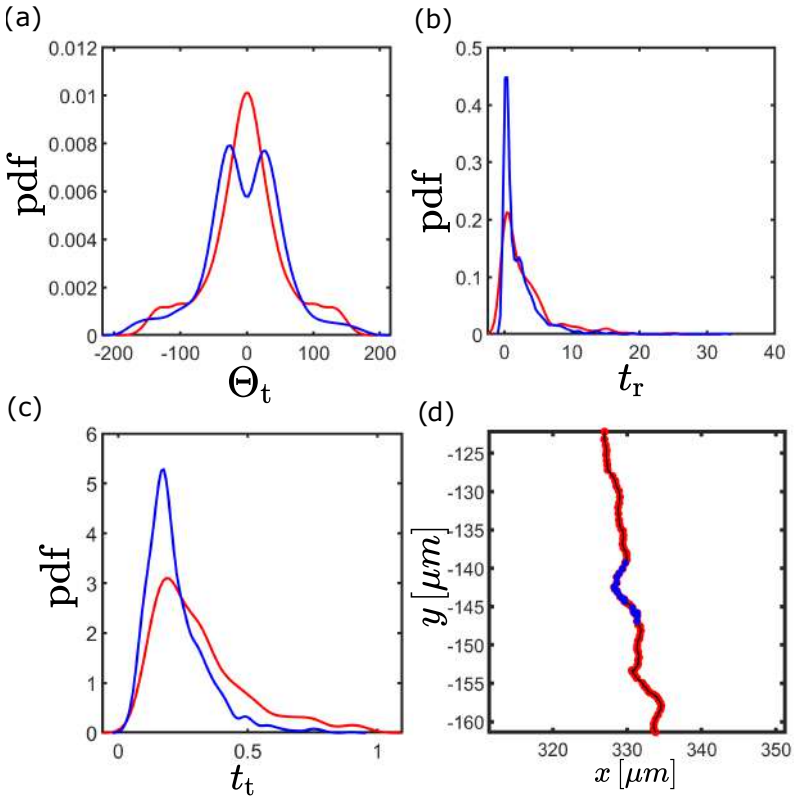

FIGURE 4.21: (a),(b),(c) Probability density function (pdf) for the tumbling-angle Θ_t (a), tumbling-time t_t (c) and running time t_r (b) for the conventional (blue) and Kalman-(red) method. (d) Two dimensional projection of a trajectory (red), where blue dots mark two short tumbling-events based on the conventional technique separated by a small running-state.

Application on three-dimensional trajectories

In this section we apply the IMM-filter to evaluate tumbling-events for three-dimensional trajectories measured as described in previous chapter 3. In Fig. 4.22 we compare the probability-density function (pdf) for the tumbling-angle Θ_t (a), tumbling-time t_t (b) and running-time t_r (c) for experimental trajectories $\boldsymbol{X}_{pr}$ (red) and $\boldsymbol{X}_{ma}$ (blue). The vertical lines represent the mean of the corresponding distribution, with $\langle t_r \rangle (\boldsymbol{X}_{pr}) = 0.31\,s$, $\langle t_t \rangle (\boldsymbol{X}_{ma}) = 0.314\,s$, $\langle t_r \rangle (\boldsymbol{X}_{pr}) = 3.07\,s$ and $\langle t_r \rangle (\boldsymbol{X}_{ma}) = 3.44\,s$. We see nearly no difference in the pdf for tumbling-angles Θ_t and tumbling-times t_t, but a difference in the pdf for the running-times t_r. The difference in the running-times t_r is because by evaluating projected trajectories $\boldsymbol{X}_{pr}$, several wrong tumbling-events are detected as a movement in the z-direction is classified as a tumbling-event due to the drop in speed v. This problem is avoided when trajectories $\boldsymbol{X}_{ma}$ are evaluated, as for these trajectories the z-information is included, therefore longer running-times are observed.

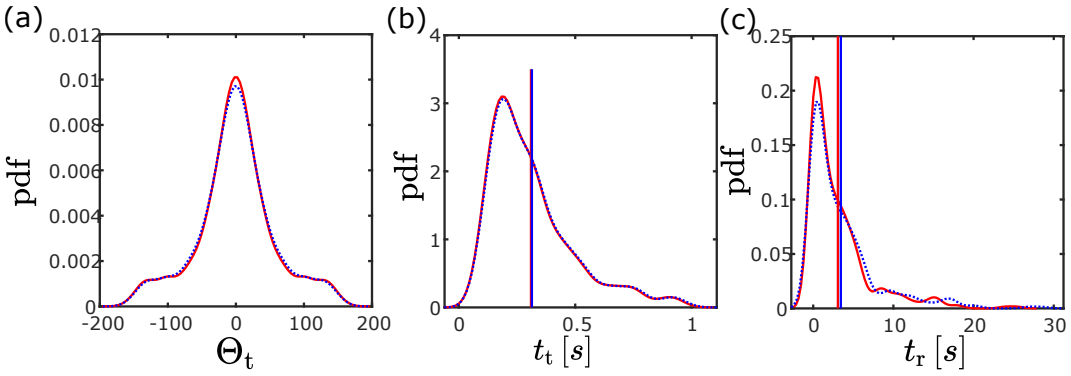

FIGURE 4.22: Comparison of the probability-density function (pdf) for the tumbling-angle Θ_t (a), tumbling-time t_t (b) and running-time t_r (c) for experimental trajectories $\boldsymbol{X}_{pr}$ (red) and $\boldsymbol{X}_{ma}$ (blue). Vertical lines mark the mean of the corresponding pdf.

4.4 Discussion

In this chapter we applied the Kalman-Filter to extract statistical properties of bacteria-trajectories, especially the (rotational) diffusion coefficient $D_{(r)}$ as well as run- and tumble characteristics such as running-time t_r, tumbling-time t_t and tumbling-angle Θ_t. To quantify the accuracy of this extraction process, in a first step we introduced a process for the quantitative simulation of bacteria-trajectories. This process consisted of the simulation of speeds v, orientations Θ and angles ϕ. Based on these quantities we were able to create three-dimensional trajectories and extract statistical properties. We have seen from Fig. 4.14 that for different regimes of the rotational diffusion coefficient D_r, different methods are beneficial for the extraction of the rotational diffusion coefficient D_r. But methods based on the Kalman-Filter are always superior. Now as we were confident that the Kalman-Filter is a suitable method for the evaluation of the running-state, we applied an extension of the Kalman-Filter, the IMM to distinguish between different states of a trajectory, the running and the tumbling-state. In several experiments, only the two-dimensional projected trajectory $\boldsymbol{X}_{pr}$ is observed. Therefore in a first step, we investigated how the information-loss due to the projection of a three-dimensional trajectory $\boldsymbol{X}$ in the two dimensional plane $\boldsymbol{X}_{pr}$ influences the obtained run- and tumbling dynamics. Therefore we simulated three-dimensional trajectories and only evaluated the projection in the two-dimensional plane $\boldsymbol{X}_{pr}$. We have seen in Fig. 4.18 that the efficiency in the evaluation of the run- and tumble-dynamics depends mainly on the depth of field w we observe. For large depth of fields, several tumbling-events are wrongly detected, as a pure movement in the z-direction appears as zero velocity in the x-y-plane. For large depth of fields, these events occur relatively often, leading to a bad efficiency in the evaluation of run- and tumbling dynamics. But in experiments, depth of fields are typically lower than approximately $w \approx 50\mu m$. If we apply realistic depth of fields in our simulations, the amount of movements purely in the z-direction vanishes, and the efficiency

in the evaluation of run- and tumble-dynamics rises. Therefore, as in real experiments we have relatively low depth of fields, events where wrongly detected tumbling-events occur are relatively rare. In a next step, we evaluated run- and tumble dynamics of experimental data. Therefore we evaluated the same data-set as [118]. The comparison can be seen in Fig. 4.21, where the results from [118] are represented in blue and our results are represented in red. The main difference is the distribution in tumbling-angles Θ_t. To understand the difference, we manually evaluated the bacteria-trajectories and found that the peaks of the blue curve from Fig. 4.21 correspond to two corresponding close tumbling-events as represented in Fig. 4.21 (d). The trajectory represented in Fig. 4.21 (d) most likely occurs due to wobbling and not tumbling. Our method $\mathcal{T}$ for detection of tumbling-events based on the Kalman-Filter does not detect these special events as tumbling-events, hence we do not observe a double peak in Fig. 4.21 (a). The main difference between our policy $\mathcal{T}$ and the policy introduced in [118] is the fact that rather than threatening speed v and orientation Θ as two different quantities for detecting tumbling-events, the Kalman-Filter provides a single, intrinsic quantity for the distinction of different models. This single quantity is less susceptible for fluctuations than two separate quantities. In a last step, we compared the evaluation of projected trajectories $\boldsymbol{X}_{\text{pr}}$ and mapped trajectories $\boldsymbol{X}_{\text{ma}}$. We see from Fig. 4.22 only minor differences, proving the simulation results, that in the case of low depth of fields, the run-and tumbling dynamics are very accurate as wrong tumbling-events are very unlikely.

Chapter 5

Qualitative Trajectory-Simulation

5.1 Bacterial swimmer model

In this section we describe the model we use for the simulation of bacteria locomotion. It has been developed and used by Frank Nguyen [119] to investigate the running-state of bacteria. In the next section 5.1.1 we model the relevant parts of the bacterium, namely the cell-body and the flagellum. Afterwards in section 5.1.2 we define the equations of motion representing the interaction of the bacterium with the environment. After introducing the model and the relevant interactions with the environment, we describe the time evolution in section 5.1.3. Before we show how we can induce polymorphic-transformations of a certain flagellum in section 5.2.1, we briefly review the main results of Frank Nguyen in section 5.1.4. Afterwards in section 5.2.2 we simulate tumbling-events.

5.1.1 Discretization of the bacterium

The bacterium consists of a cell body and the flagellum, where the flagellum consists of the filament, which is connected to the cell body via the hook. In this section we develop a theoretical model of the bacterium which can be used to simulate bacteria locomotion. The theoretical model of the bacterium is represented in Fig. 5.1 (a). Here we see the cell-body modeled as a rigid sphere of radius R_b. Its position is described via its center of mass and denoted as $\boldsymbol{x}_\mathrm{b}$. The orientation is quantified via a union quaternion $\boldsymbol{q}_\mathrm{b}$. The flagellum is modeled as a helix of radius R, pitch λ, end-to-end length L and filament radius a. A bacterium consists of N flagella, where the flagellum is connected to the cell-body at an anchor-point. In Fig. 5.1 (b) we see a zoom inside the flagellum. It consists of different nodes $\boldsymbol{x}_i$ connected via edges $\boldsymbol{e}_i$. The first edge $\boldsymbol{e}_0$ of length L_h connecting the anchor-point and the filament is denoted as hook, and represented as the red line in Fig. 5.1 (a). The hook is initialized perpendicular to the body surface. The remaining edges $\boldsymbol{e}_i$ with $i > 0$ are flagella segments of length l. The points $\boldsymbol{x}_i$ connecting the edges $\boldsymbol{e}_i$ are denoted as nodes, the node $\boldsymbol{e}_0$ is the anchor-point. Each edge $\boldsymbol{e}_i$ between nodes $\boldsymbol{x}_{i-1}$ and $\boldsymbol{x}_i$ defines a local orthonormal coordinate system $\{\boldsymbol{e}_i^1, \boldsymbol{e}_i^2, \boldsymbol{e}_i^3\}$, where $\boldsymbol{e}_i^3 = \boldsymbol{e}_i$ is the edge defined by

$$\boldsymbol{e}_i^3 = \frac{\boldsymbol{x}_i - \boldsymbol{x}_{i-1}}{|\boldsymbol{x}_i - \boldsymbol{x}_{i-1}|}, \quad i \in [i, N-1]\,. \tag{5.1}$$

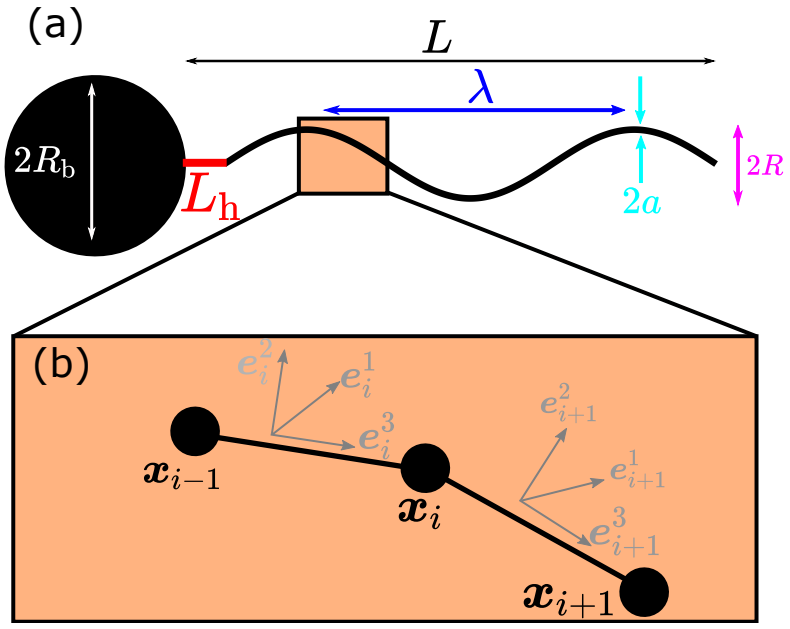

FIGURE 5.1: (a) Schematic representation of the swimmer consisting of the cell-body, a sphere with radius R_b, and the flagellum, consisting of the hook of length L_h and the filament with pitch λ, radius R and diameter a. (b) The flagellum is simulated via several nodes $\boldsymbol{x}_i$, where each node defines a local coordinate-system with basis $\{\boldsymbol{e}_i^1, \boldsymbol{e}_i^2, \boldsymbol{e}_i^3\}$.

The initial edge $\boldsymbol{x}_0^3$ is defined via the anchor-point $\boldsymbol{x}_0$ and the cell-body position $\boldsymbol{x}_\mathrm{b}$ via

$$\boldsymbol{e}_i = \frac{\boldsymbol{x}_0 - \boldsymbol{x}_\mathrm{b}}{R_\mathrm{b}}. \tag{5.2}$$

The remaining components $\boldsymbol{e}_i^1$ and $\boldsymbol{e}_i^2$ of the orthonormal-coordinate system $\{\boldsymbol{e}_i^1, \boldsymbol{e}_i^2, \boldsymbol{e}_i^3\}$ are defined perpendicular to the plane created by $\boldsymbol{e}_{i-1}^3$ and $\boldsymbol{e}_i^3$ via

$$\boldsymbol{e}_i^1 = \frac{\boldsymbol{e}_{i-1}^3 \times \boldsymbol{e}_i^3}{\left|\boldsymbol{e}_{i-1}^3 \times \boldsymbol{e}_i^3\right|}, \tag{5.3}$$

and perpendicular to components $\boldsymbol{e}_i^1$ and $\boldsymbol{e}_i^3$ via

$$\boldsymbol{e}_i^2 = \boldsymbol{e}_i^1 \times \boldsymbol{e}_i^3. \tag{5.4}$$

Based on the orthonormal coordinate system $\{\boldsymbol{e}_i^1, \boldsymbol{e}_i^2, \boldsymbol{e}_i^3\}$ we subsequently can define a bend-angle Θ_i and a twist angle ϕ_i. Based on the angles Θ_i and ϕ_i

we can transform the system $\{e_i^1, e_i^2, e_i^3\}$, to $\{e_{i+1}^1, e_{i+1}^2, e_{i+1}^3\}$ via

$$\Theta_i = \arccos\left(e_i^3 \cdot e_{i+1}^3\right), \tag{5.5}$$

$$\phi_i = \arctan\left(\frac{\tilde{e}_i^1 \cdot e_i^2}{e_i^1 \tilde{e}_i^1}\right), \tag{5.6}$$

$$\tilde{e}_i^1 = [nn + \cos(\Theta_i)(\delta - nn)] \cdot e_{i+1}^1 - \sin(\Theta_i)\left(n \times e_i^1\right), \tag{5.7}$$

$$n = \frac{e_i^3 \times e_{i+1}^3}{\sin(\Theta_i)} = e_{i+1}^1. \tag{5.8}$$

Here δ is the identity tensor and $\tilde{e}_i^1$ can be interpreted as an intermediate twist-free rotation of e_i^1. Based on the quantities defined via equations 5.5 - 5.8 we can define the generalized curvature Ω_i for every node via

$$\Omega_i^1 = -\frac{\Theta_i}{\sin(\Theta_i)} e_i^2 \cdot e_{i+1}^3, \tag{5.9}$$

$$\Omega_i^2 = +\frac{\Theta_i}{\sin(\Theta_i)} e_i^1 \cdot e_{i+1}^3, \tag{5.10}$$

$$\Omega_i^3 = \phi_i. \tag{5.11}$$

The definition of the curvature in equations 5.9-5.11 is suitable to define the shape of a helix and therefore suitable to define the shape of the flagella.

5.1.2 Equations of motion

Based on the definitions in the previous section we can now define the equations of motion describing the interaction of the bacterium with its environment. Based on these equation it will be possible to simulate bacteria locomotion. We assume that the bacterium moves through an incompresible Newtonian fluid at zero Reynolds number (see section 2.2.2). Furthermore we assume that each component k of the swimmer (cell-body and flagellum), is force and torque free. Therefore the whole bacterium is force and torque free. All external dynamics like elasticity (el), steric interactions (ster), application of motor torque (mot) and constraints (C) are balanced by the hydrodynamic drag (D). This can be quantified via the equations

$$F_k^{\mathrm{D}} + F_k^{\mathrm{el}} + F_k^{\mathrm{ster}} + F_k^{\mathrm{mot}} + F_k^{\mathrm{C}} = \mathbf{0} \tag{5.12}$$

$$T_k^{\mathrm{D}} + T_k^{\mathrm{el}} + T_k^{\mathrm{ster}} + T_k^{\mathrm{mot}} + T_k^{\mathrm{C}} = \mathbf{0} \tag{5.13}$$

In the following we will discuss all quantities in equations 5.12 and 5.13. Here a subscript $k = \mathrm{b}$ denotes cell body and $k = i$ denotes the ith flagella-segment. We scale torques with T, lengths with R_b, forces with $\frac{T}{R_b}$, velocities with $\frac{T}{R_b \zeta_b}$ and times with $\frac{\zeta_b R_b^2}{T}$. The standard-geometry of our swimmer is defined by $L_{\mathrm{h}} = 0.28$, $R = 0.28$, $\lambda = 4$, $a = 0.028$ and $L = 9$, reflecting a good estimate for *E. coli* [119].

Hydrodynamics

To treat the hydrodynamics of the flagella, we use a discretized slender body theory. Due to the imposed torque on the flagellum we must additionally track the rotational phase ϕ_i of the filament. We quantify the velocity of each node $\boldsymbol{x}_i$ as v_i and the angular velocity of each edge $\boldsymbol{e}_i$ as $\omega_i = \dot{\phi}_i$. Due to the moving nodes $\boldsymbol{x}_i$, the surrounding fluid exerts a Stokes law drag force on it, denoted as $\boldsymbol{F}_i^{\mathrm{D}}$. The force $\boldsymbol{F}_i^{\mathrm{D}}$ can be calculated as

$$\boldsymbol{F}_i^{\mathrm{D}} = \boldsymbol{\eta}_i \left[\left(\boldsymbol{v}_{i,\infty}^{\mathrm{f}} + \boldsymbol{v}_{i,\infty}^{\mathrm{b}} - \boldsymbol{v}_i \right) \right]. \tag{5.14}$$

The tree contributions to equation 5.14 arise from

1. $\boldsymbol{v}_i$: A local contribution from the motion of node $\boldsymbol{x}_i$.
2. $\boldsymbol{v}_{i,\infty}^{\mathrm{f}}$: Far field contribution from all other nodes.
3. $\boldsymbol{v}_{i,\infty}^{\mathrm{b}}$: Far field contribution from the cell-body.

Rather than assuming spherical nodes, we threat the nodes as small rods, resulting in the anisotropic friction coefficient

$$\boldsymbol{\eta}_i = \eta_\perp \delta + \left(\eta_\parallel - \eta_\perp \right) \boldsymbol{t}_i \boldsymbol{t}_i \tag{5.15}$$

for a slender rigid rod of aspect ratio $\frac{l}{a}$. Here $\eta_\parallel$ and $\eta_\perp$ are the scalar tangential and perpendicular friction coefficients. By neglecting rotlets the drag from rotating edge i along its axis simplifies to

$$\boldsymbol{T}_i^{\mathrm{D}} \cdot \boldsymbol{e}_i^3 = -\eta_i^{\mathrm{r}} \omega_i, \tag{5.16}$$

where the superscript r denotes rotlet and the corresponding parameter is given as $\eta_i^{\mathrm{r}} = 4\pi\nu a^2 l$.
To compute the field $\boldsymbol{v}_{i,\infty}^{\mathrm{f}}$ from equation 5.14 arising from hydrodynamic interactions between the flagella, we treat each node as a regularized point force acting on the fluid. This approach is summarized in Fig. 5.2. To obtain the whole flow-field $\boldsymbol{v}_{i,\infty}^{\mathrm{f}}$, we have fo sum over each single contribution $\boldsymbol{F}_j$ as

$$\boldsymbol{v}_{i,\infty}^{\mathrm{f}} = \sum_{i \neq j} \boldsymbol{M}_{\mathrm{f}} \left(\boldsymbol{x}_i, \boldsymbol{x}_j \right) \cdot \boldsymbol{F}_j, \tag{5.17}$$

where $\boldsymbol{F}_j = -\boldsymbol{F}_j^{\mathrm{D}}$ is the force exerted on the fluid by node $\boldsymbol{x}_j$ and $\boldsymbol{M}_f$ is the mobility tensor. The exact expression for the body induced flow $\boldsymbol{v}_{i,\infty}^{\mathrm{b}}$ from equation 5.14 is usually a linear function of the force and torque exerted by the sphere on the fluid:

$$\boldsymbol{v}_{i,\infty}^{\mathrm{b}} = \boldsymbol{M}_{\mathrm{b}} \left(\boldsymbol{x}_i - \boldsymbol{x}_{\mathrm{b}} \right) \cdot \boldsymbol{M}_{\mathrm{b}} + \boldsymbol{M}_{\mathrm{b}}^{\mathrm{r}} \left(\boldsymbol{x}_i - \boldsymbol{x}_{\mathrm{b}} \right) \cdot \boldsymbol{T}_{\mathrm{b}}, \tag{5.18}$$

The remaining drag contribution $\boldsymbol{F}_{\mathrm{b}}^{\mathrm{D}}$ from the cell-body can be calculated by applying Faxén's law, yielding

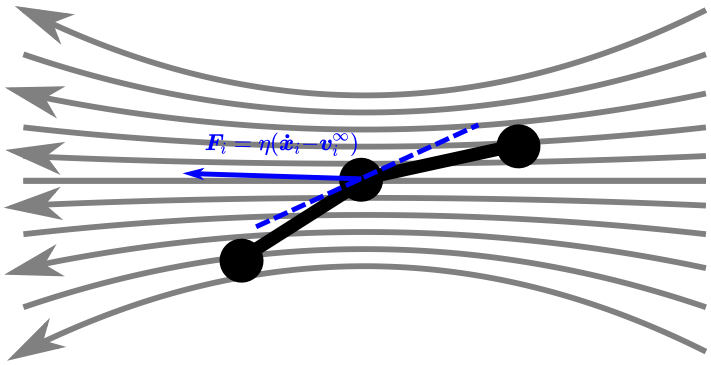

FIGURE 5.2: Representation of the flow-field (gray lines) created by a regularized point-force.

$$F_b^D = \eta \left[-v_b + \left(1 + \frac{R_b^2}{6} \nabla^2 \right) v_\infty \right] |_{x_b}, \tag{5.19}$$

$$T_b^D = \eta_b^r \left[-\omega_b + \frac{1}{2} (\nabla \times v_\infty) \right] |_{x_b}, \tag{5.20}$$

where $\eta = 6\pi\nu R_b$ and $\eta_b^r = 8\pi\nu R_b^3$ are the translational and rotational drag coefficients for the sphere. Here each flagellum and any additional interaction of the cell body with the flow domain has contributions to the flow v_∞, which can be quantified for any point x in the flow domain as

$$v_\infty(x) = \sum_j M_f(x, x_j) \cdot F_j + M_b^* \cdot F_b + M_b^{r*} \cdot T_b. \tag{5.21}$$

To summarize, both contributions of the hydrodynamic interactions regarding the flagellum (force: equation 5.14 and torque: equation 5.16) and cell-body (force: equation 5.20 and torque: equation 5.20) have been introduced.

Elasticity

The elasticity describes forces and torques arising when the shape of the flagellum differs from the *equal*-state, defined via $\Omega_{i,eq}$. The elasticity is especially important to perform polymorphic transformation, as will be discussed later on in section 5.2.1. By applying a discrete version of Kirchhoff's classical theory to write the elastic energy E^{el} we obtain

$$E^{el} = \frac{K_{Bh}}{L_h} (\Theta_0 - \Theta_{0,eq})^2 + \frac{K_B}{l} \sum_{i=1}^{N-2} \left[\sum_{\beta=1}^{2} \left(\Omega_i^\beta - \Omega_{i,eq}^\beta \right)^2 + \Gamma \left(\Omega_i^3 - \Omega_{i,eq}^3 \right) \right]. \tag{5.22}$$

We se that the elastic energy increases in if the shape of the flagellum differs from the shape defined via the *equal*-parameters $\Omega_{i,eq}$. Differences in shape

are *punished* via the term $\left(\Omega_i^j - \Omega_{i,\mathrm{eq}}^j\right)$ in equation 5.22.
By derivating the energy E^{el} defined via equation 5.22 we obtain the corresponding forces

$$\boldsymbol{F}_i^{\mathrm{el}} = \frac{\partial \mathrm{E}^{\mathrm{el}}}{\partial \boldsymbol{x_i}} \tag{5.23}$$

and torques

$$\boldsymbol{T}_i^{\mathrm{el}} = -\frac{\partial \mathrm{E}^{\mathrm{el}}}{\partial \phi_i} \boldsymbol{e}_i^3. \tag{5.24}$$

Forces and torques on the flagella anchors are transferred to the cell body via

$$\boldsymbol{F}_{\mathrm{b}}^{\mathrm{el}} = \sum_{\mathrm{flag.}} \boldsymbol{F}_0^{\mathrm{el}}, \tag{5.25}$$

$$\boldsymbol{T}_{\mathrm{b}}^{\mathrm{el}} = R_{\mathrm{b}} \sum_{\mathrm{flag.}} \boldsymbol{e}_0^3 \times \boldsymbol{F}_0^{\mathrm{el}}, \tag{5.26}$$

where we sum over all flagella.

Steric repulsion

To avoid that flagella-nodes $\boldsymbol{x}_i$ approach other flagella-nodes $\boldsymbol{x}_j$ or the cell-body $\boldsymbol{x}_{\mathrm{b}}$ to closely, we introduce repulsive steric forces. These forces are inspired by the Lennard-Jones potential, which in general has a repulsive and attractive part, as can be seen via the blue curve in Fig. 5.3. By applying

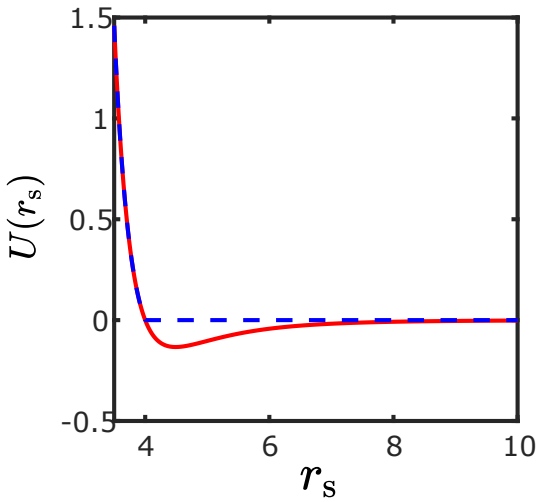

FIGURE 5.3: Representation of the Lennard-Jones-Potential U_{LJ} (red) and the truncated Lennard-Jones-Potential $U_{\mathrm{LJ,t}}$ (blue).

a Heaviside-function H, we truncate the general Lennard-Jones potential so that only the repulsive part remains. The resulting potential $U_{\mathrm{LJ,t}}$ reads

$$U_{\mathrm{LJ,t}} = U_{\mathrm{LJ}} \mathrm{H}\left(2^{\frac{1/6}{r_s}}\right) = \frac{F_{\mathrm{s}}\sigma}{6}\left[\left(\frac{\sigma}{r_{\mathrm{s}}}\right)^{12} - \left(\frac{\sigma}{r_{\mathrm{s}}}\right)^{6}\right] \mathrm{H}\left(2^{\frac{1/6}{r_s}}\right), \tag{5.27}$$

where r_s is the distance between components, σ the cut-off distance, and F_s the repulsion strength. We denote with $f_{p,q}$ the force on component p due to component q. The force on the cell-body can be written as

$$\boldsymbol{F}_b^{ster} = \sum_i \boldsymbol{f}_{b,i}, \tag{5.28}$$

the force on a certain flagella-node $\boldsymbol{x}_i$ as

$$\boldsymbol{F}_i^{ster} = \boldsymbol{f}_{i,b} + \sum_{j \neq i} \boldsymbol{f}_{i,j}. \tag{5.29}$$

Let us denote the vector connecting closest points of contact as

$$\boldsymbol{r}_s = r_s \hat{\boldsymbol{r}}_s. \tag{5.30}$$

Using this definition, we can calculate the force based on the potential energy introduced in equation 5.27 to

$$\boldsymbol{f}_{p,q}^* = -\frac{\mathrm{d}U_{LJ,p}(r_s)}{\mathrm{d}\boldsymbol{r}_s}. \tag{5.31}$$

Based on equation 5.31 we are able to calculate the forces $\boldsymbol{F}_b^{ster}$ and $\boldsymbol{F}_i^{ster}$ from equation 5.28 and 5.29.

Motor

The motor torque $\boldsymbol{T}_1^{mot}$ is only applied on the first segment (hook) and can be written as

$$\boldsymbol{T}_1^{mot} = \frac{T}{2}\left(\boldsymbol{e}_0^3 + \boldsymbol{e}_1^3\right). \tag{5.32}$$

In case of no hook bending ($\Theta_0 = 0$), equation 5.32 simplifies to $\boldsymbol{T}_1^{mot} = T\boldsymbol{e}_0^3$. The force $\boldsymbol{F}_{0,1}^{mot}$ on adjacent nodes 0 and 1 is calculated to

$$\boldsymbol{F}_{0,1}^{mot}. \tag{5.33}$$

If we take into account Newton's third law, the torque $\boldsymbol{T}_1^{mot}$ applied on the flagellum is balanced by a torque $-\boldsymbol{T}_1^{mot}$ on the body for each flagellum. This leads to a counter-rotation of the body, what is generally denotes as *wobbling*. The total torque $\boldsymbol{T}_b^{mot}$ and force $\boldsymbol{F}_b^{mot}$ on the cell-body can be calculated via

$$\boldsymbol{T}_b^{mot} = \sum_{flag.} \left[-\boldsymbol{T}_1^{mot} + R_b \boldsymbol{e}_0^3 \times \boldsymbol{F}_0^{mot}\right], \tag{5.34}$$

$$\boldsymbol{T}_b^{mot} = \sum_{flag.} \boldsymbol{F}_0^{mot}. \tag{5.35}$$

Constraints

There are two different possibilities to keep the general setup of the modeled bacterium:

1. Using stiff springs.
2. Using constraints.

In the code we use, constraints are applied to keep the general setup of the swimmer. The advantage is a smaller calculation time. The three constraints are visualized in Fig. 5.4. The first constraint from Fig. 5.4 (a) represents

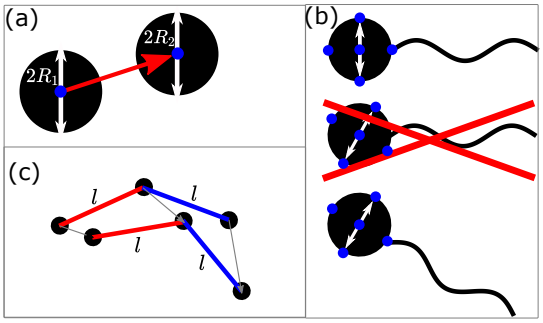

FIGURE 5.4: Representation of the constraints quantified via equation 5.36 (a), 5.37 (b) and 5.38 (c).

the fact that the cell-body represented via q_b remains a unit quaternion. This means the cell-body only undergoes rotations, but does not change it's shape ($R_1 = R_2 = R_b$). The second constraint visualized in Fig. 5.4 (b) means that the flagella anchors undergo rigid body-motion. This means that the anchors follow the body-surface. The third constraint is visualized in Fig. 5.4 (b). This constraint represents the fact that the flagella segments are inextensible, their length is fixed to l. These three constraints can be quantified via

$$q_b q_b - 1 = 0, \tag{5.36}$$

$$q_b x_0^{(b)} q_b^{-1} - (x_0 - x_b) = \mathbf{0}, \tag{5.37}$$

$$(x_{i+1} - x_i) \cdot (x_{i+1} - x_i) - l^2 = 0. \tag{5.38}$$

Here $x_0^{(b)}$ represents a constant vector denoting the anchor point in the body-fixed frame of reference. The quaternion q_b rotates the vector $x_0^{(b)}$ in the laboratory frame.

5.1.3 Time evolution

After we have summarized the model and the relevant interactions with the environment, we can focus now on the description of the time-evolution. The state of the swimmer can be fully described by the orientation of the cell body, represented as quaternion q_b, the position of the cell-body x_b and the position of flagella nodes x_f. We condense the swimmer's position variables

in a single vector

$$\boldsymbol{y} = \begin{bmatrix} \boldsymbol{q}_\mathrm{b} \\ \boldsymbol{x}_\mathrm{b} \\ \boldsymbol{x}_\mathrm{f} \end{bmatrix}. \tag{5.39}$$

The dynamic variables are condensed in the vector

$$\boldsymbol{f} = \begin{bmatrix} \boldsymbol{t}_\mathrm{b} \\ \boldsymbol{F}_\mathrm{b} \\ \boldsymbol{F}_\mathrm{f} \end{bmatrix}. \tag{5.40}$$

As there are M flagella with N nodes, we have $\boldsymbol{x}_\mathrm{f}, \boldsymbol{F}_\mathrm{f} \in \mathcal{R}^{3NM}$, so that $\boldsymbol{y} \in \mathcal{R}^{3NM+7}$. As we assume linear flow, we can write the relation between velocities $\dot{\boldsymbol{y}}$ and forces $\boldsymbol{f}$ via the mobility matrix $\boldsymbol{M}$ as

$$\dot{\boldsymbol{y}} = \boldsymbol{M}\boldsymbol{f}. \tag{5.41}$$

We split the time-evolution from equation 5.41 in two different steps, as summarized in Fig. 5.5. In a first step, we neglect the constraints and make an

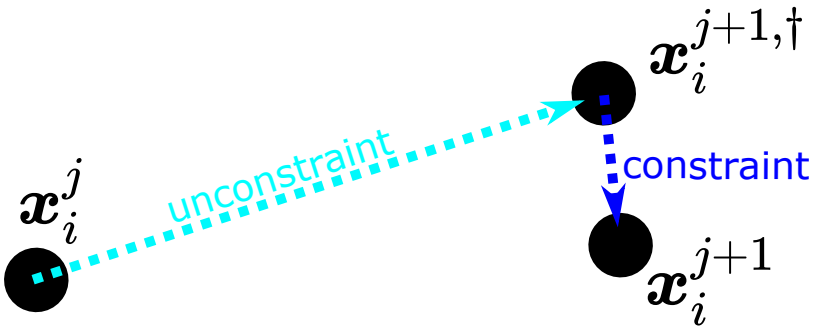

FIGURE 5.5: Representation of the unconstraint timestep, and the application of the constraints.

unconstraint-timestep, moving nodes $\boldsymbol{x}_i^j$ to $\boldsymbol{x}_i^{j+1,\dagger}$, where the superscript † denotes an unconstrained position. After all nodes have moved, the constraints are taken into account, moving nodes $\boldsymbol{x}_i^{j+1,\dagger}$ to $\boldsymbol{x}_i^{j+1}$. To quantify this method, we split equation 5.41 to

$$\dot{\boldsymbol{y}} = \boldsymbol{M} \cdot \left[\boldsymbol{f}^\dagger - \nabla \boldsymbol{C}^\mathrm{T} \cdot \boldsymbol{\Lambda} \right] = \dot{\boldsymbol{y}}^\dagger - \boldsymbol{M} \cdot \nabla \boldsymbol{C}^\mathrm{T} \cdot \Lambda. \tag{5.42}$$

Here we can calculate $\boldsymbol{f}^\dagger$ from $-T_k^\mathrm{D}$ and $-F_k^\mathrm{D}$ introduced in the equations of motion 5.12 and 5.13. The vector $\boldsymbol{C} \in \mathcal{R}_\mathcal{C}^N$ contains the constraint-equations introduced in equations 5.36-5.38. The Lagrange-multipliers $\boldsymbol{\Lambda}$ have to satisfy the constraint

$$\boldsymbol{C} = \boldsymbol{0}. \tag{5.43}$$

To solve equation 5.42 with respect to the constraints, we perform the following steps:

1. Calculate the unconstrained solution $\boldsymbol{y}^* = \boldsymbol{y}^\dagger\,(t_{n+1})$.

2. Repeat steps (3)-(5) while $|\boldsymbol{C}(\boldsymbol{y}^*)| > \epsilon$.
3. Solve $\Delta t \left[\nabla \boldsymbol{C} \cdot \boldsymbol{M} \cdot \nabla \boldsymbol{C}^{\mathrm{T}}\right] \Lambda = \boldsymbol{C}$ for $\boldsymbol{\nabla}$.
4. Solve $\delta \boldsymbol{y} = -\Delta t \boldsymbol{M} \cdot \boldsymbol{C}^{\mathrm{T}} \cdot \boldsymbol{\nabla}$ for $\delta \boldsymbol{y}$
5. Update: $\boldsymbol{y}^* + \delta \boldsymbol{y} \rightarrow \boldsymbol{y}^*$.
6. Constrained solution: $\boldsymbol{y}(t_{n+1}) = \boldsymbol{y}^*$

By applying above steps 1 to 5 we find the constrained solution to the initial equation 5.41 describing the dynamics of the swimmer.

5.1.4 Simulate the running state

Based on the model defined in previous sections 5.1.1-5.1.3, we are able to simulate the running state of a bacterium. In this section we briefly show the main results of Frank's work, before we go on to section 5.2 with simulating the tumbling state. If we have a look at Fig. 5.6, we see the results for the simulation of bacterium with one flagellum. To quantify the efficiency in swimming, we can introduce the quantity

$$D^2 = \sum_{\text{flag.}} \frac{1}{N} \sum_{\text{nodes}} |\boldsymbol{x}_i - \boldsymbol{x}_{\mathrm{b}}|^2, \tag{5.44}$$

where large values correspond to a stretched, well-defined helical shape of the flagellum. The swimmer was simulated for various combinations of the flexibility of the hook $\mathrm{FL_h}$ and the flexibility of the flagellum FL. Combinations resulting in straight swimming are represented as blue dots, combinations for non-stable swimming as orange squares in Fig. 5.6 (a). The corresponding evolution for the quantity D introduced in equation 5.44 is represented in Fig. 5.6 (b). The initial state and the state after $t = 28$ for certain combinations of $\mathrm{FL_h}$ and FL is represented in Fig. 5.6 (c)-(f). If we compare the results obtained for the Uni-flagella case with the results for four flagella, represented in Fig. 5.7, we see a *flip* in the stability regimes. In Fig. 5.7 (a), parameter-regimes where a bundling of the four flagella occurs, resulting in straight swimming, are marked as blue dots. Regimes with efficient swimming, but no bundling, are marked as green triangles. And regimes with no bundling and no swimming are marked as orange squares. The corresponding evolution of the quantity D is represented in Fig. 5.7 (b), the initial state and the state after $t = 28$ for four different combinations of $\mathrm{FL_h}$ and FL are represented in Fig. 5.7 (c)-(f). The reason for the *flipping* of the stability regime represented in Fig. 5.6 (a) and Fig. 5.7 (a) can be explained via the impact of the hook. In the Uni-flagella case, a stiff hook is required to avoid buckling. In case of the Quad-flagella case, a stiff hook avoids building bundles, resulting in a directed swimming, due to the stiffness. Bundling only occurs in case of a flexible hook and relatively stiff flagella. In the following section 5.2 we extend the model to introduce tumbling-events. We will see that for tumbling-events, the flexibility of the flagellum plays a major role.

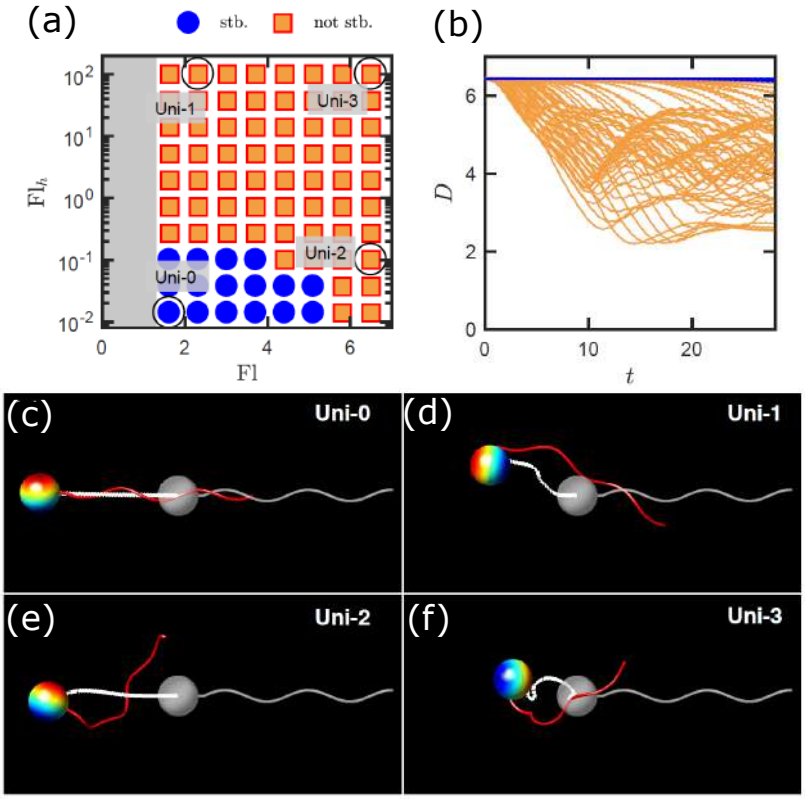

FIGURE 5.6: (a) Visualization of the stability regime for a simulated bacterium with one flagellum, where blue dots correspond to stable swimming, and orange squares correspond to non-stable swimming. (b) Representation of the quantity D defined in equation 5.44 to quantify the swim-efficiency. (c)-(f) Initial state (gray) and state after $t = 20$ (colored) of the swimmer for the four parameter-settings represented in (a). Images taken from [119].

5.2 Simulate tumbling-events

The trajectories of free swimming bacteria usually consist of running and tumbling states. In the previous section 5.1 we introduced a model from Frank Nguyen developed for the simulation of the running state. In this section we extend this model to include tumbling-events. We know that in the running state, all flagella rotate counterclockwise (CCW), resulting in a flagella bundle. When some of the flagella motors start rotating clockwise (CW), an undundling process starts, resulting in a change of the swimming course [42, 90, 166]. The flagella rotating CW undergo polymorphic transformations through several shapes, before the CCW rotation changes the shape back to the *normal* running shape. The filament is connected to the cell-body via the hook, which is typically $50 - 80$ nm in length [25, 50, 148]. The hook transfers this torque to the filament, and can bend up to $90°$. The ability of the hook beeing able to bend, is essential for flagella bundling [18, 29]. There are several reasons for triggering the polymorphic transformations, such as

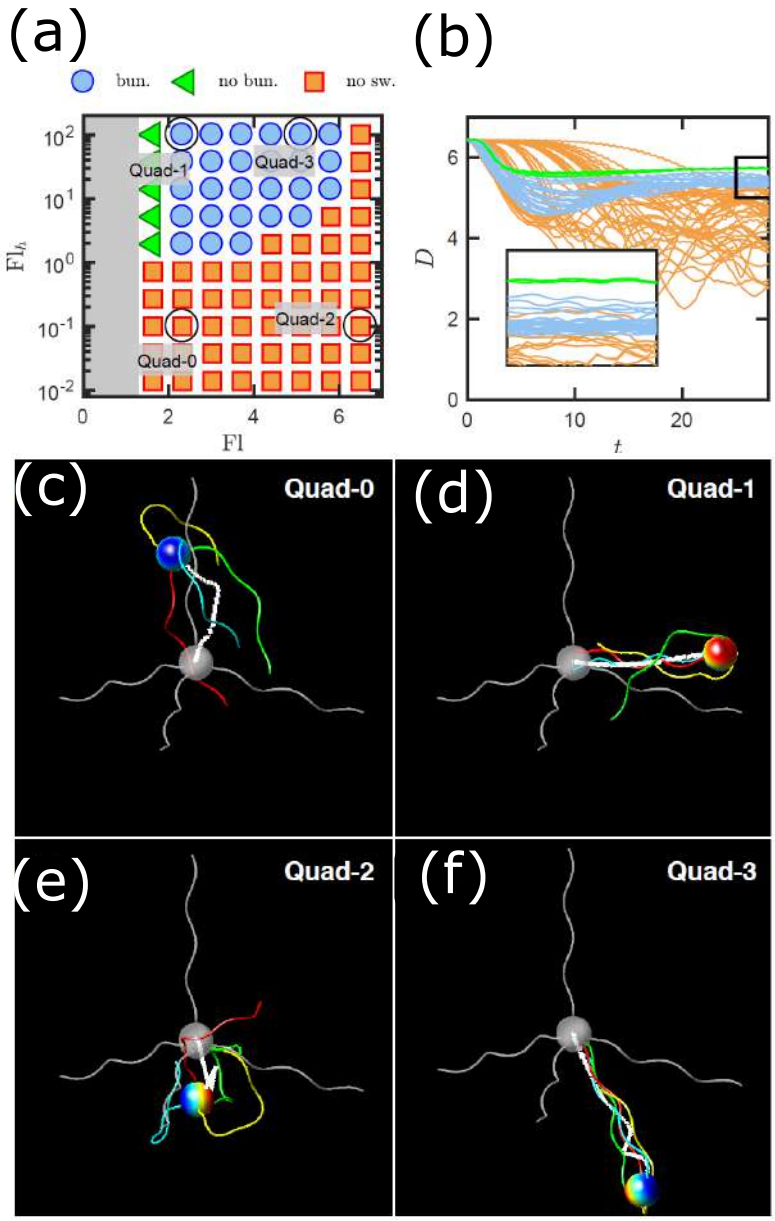

FIGURE 5.7: (a) Visualization of the stability regime for a simulated bacterium with four flagella, where blue dots correspond to bundling and stable swimming, orange squares correspond to no swimming and green triangles correspond to swimming without bundling. (b) Representation of the quantity D defined in equation 5.44 to quantify the swim-efficiency. (c)-(f) Initial state (gray) and state after $t = 20$ (colored) of the swimmer for the four parameter-settings represented in (a). Images taken from [119].

external forces and hydrodynamic torques [43, 66, 108]. Other reasons include changes in solvent conditions [60, 67, 77, 149, 153]. There are several models for the simulation of these polymorphic transformations. Based on the work from Asakura [5], Calladine [31–33] presented a geometric model which is suitable to predict 12 different helical forms. Other models are based

on Brownian dynamics [172] or use an elastic model for the flagellum based on Kirchhoffs theory [170]. There is also a continuum model of a single flagellum proposed by and Stark [171], to describe polymorphic transformations in response to an applied motor torque. In our work, we tried two different models to induce polymorphic transformations. The first model consists of a double-well potential for the shape of the flagellum, similar to [157], the second model has a state-dependent potential, based on the desired flagella-shape, as described in [95]. In the following we consider three shapes for the simulation, the normal shape (running state), semicoiled-state (beginning of tumbling-state) and the curly-I-state (end of tumbling-state).

5.2.1 Manipulation of the polymorphic shape

In section 5.1.2 we defined five different forces (and torques) which determine the dynamics of the simulated swimmer. The only force arising due to deformation of the flagellum is the elasticity force F^{el} based on the energy introduced in equation 5.22. In this section we manipulate this energy-landscape to perform polymorphic transformations. We tried two different approaches to manipulate this energy-landscape, which can be seen in Fig. 5.8. We try to change the initial normal form of the flagellum, represented as the blue curve in Fig. 5.8 (a)-(c) to the semicoiled form, represented as the cyan curve. Every node $\boldsymbol{x}_i$ of the helix has assigned a certain curvature $\Omega_i^{1,2}$ and a twist Ω_i^3. Initially we set all these values to $\Omega_i^{1,2} = 1.3$ and $\Omega_i^3 = -2.08$, corresponding to experimental values from table 2.1. These initial parameters $\Omega_i^{1,2}$ and Ω_i^3 for each node are visualized in Fig. 5.8 (d) and (e). After initializing the flagellum in the running state, we keep it rotating with a negative torque $T = -1$, and after a certain time $t = t_1$ we change the torque to $T = 1$, which should trigger the polymorphic transformation (Fig. 5.8 (f)). Therefore, in Fig. 5.8 (d) we show a potential with two different minima, where the second minimum corresponds to the semicoiled shape of the flagellum. In Fig. 5.8 (e) we show a time-dependent potential, where for times $t < t_1$ the potential is given as the blue lines, and for times $t \geq t_1$ the potential corresponds to the cyan lines. In the following we will discuss both approaches.

Multi-minima potential

First we discuss the potential introduced in Fig. 5.8 (d). This potential can be quantified via

$$\mathrm{E}^{\mathrm{el,m}} = \min\left(\mathrm{E}^{\mathrm{el}}\left(\kappa_0^{\mathrm{n}}, \tau_0^{\mathrm{n}}\right) + \delta, \mathrm{E}^{\mathrm{el}}\left(\kappa_0^{\mathrm{s}}, \tau_0^{\mathrm{s}}\right)\right), \tag{5.45}$$

where the superscript k in κ_0^k and τ_0^k refers to the normal- (n) and semicoiled-state (s). The quantity δ is an artificial energy gap. The potential $\mathrm{E}^{\mathrm{el}}\left(\kappa_0^{\mathrm{n}}, \tau_0^{\mathrm{n}}\right)$

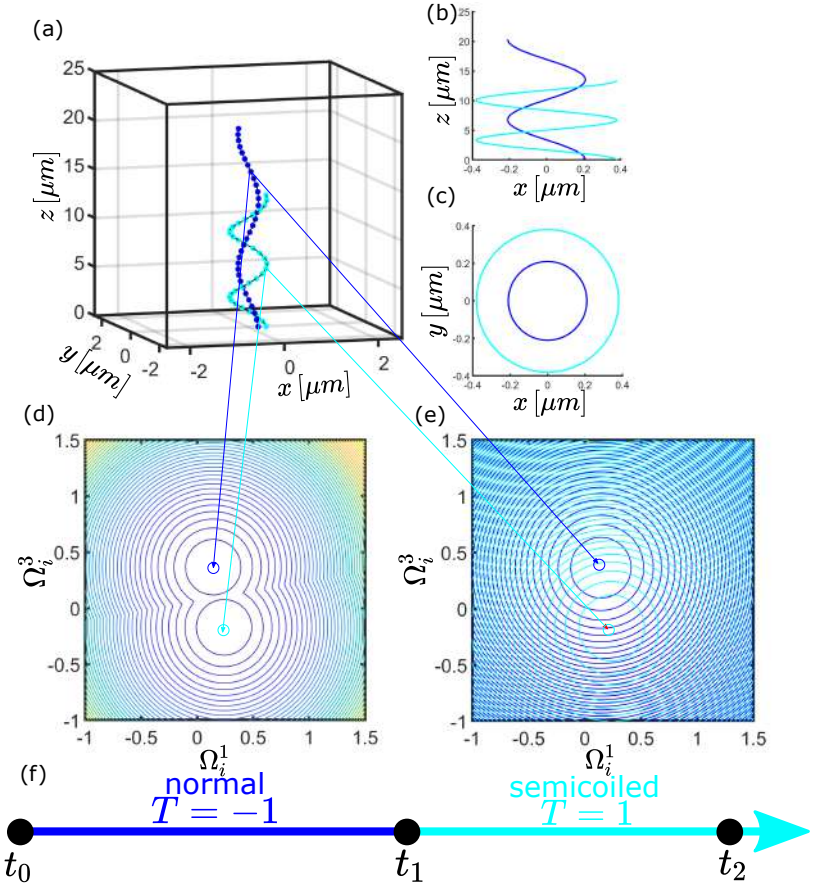

FIGURE 5.8: (a) Representation of a helix in the normal (blue) and semicoiled (cyan)-state. (b),(c) Projection of the helix visualized in (a) in the xz- and xy-plane. (d) Time-independent multi-minima potential, where the minima correspond to the normal and the semicoiled state. (e) Time-dependent potential corresponding to the blue lines for $t \leq t_1$ and the cyan lines for $t > t_1$. (f) Visualization of the process to induce polymorphic-transformations with a negative torque $T = -1$ for $t \leq t_1$ and a positive torque $T = 1$ for $t > t_1$.

is defined as

$$\mathrm{E}^{\mathrm{el}}\left(\kappa_0^k, \tau_0^k\right) = \frac{K_{\mathrm{Bh}}}{L_{\mathrm{h}}}\left(\Theta_0 - \Theta_{0,\mathrm{eq}}\right)^2 + \frac{K_{\mathrm{B}}}{l}\sum_{i=1}^{N-2}\left[\sum_{\beta=1}^{2}\left(\Omega_i^\beta - \kappa_0^k\right)^2 + \Gamma\left(\Omega_i^3 - \tau_0^k\right)\right]. \tag{5.46}$$

Let us set $\delta = 0$. In Fig. 5.9 (a) we see the flagellum at $t = 0$ (red), $t = t_1$ (blue) and $t \gg t_1$ (cyan). We see that there is nearly no change in flagellum shape. Also by observing the corresponding curvature and twist values Ω_i^1 and Ω_i^3 in Fig. 5.9 (b) obeys that nearly no change of flagellum-shape occured. This can be explained due to the parameter settings with relatively high values for the flexural rigidity K_{B} and twist-to-bend ratio Γ. Therefore we tried to either reduce the flexural rigidity K_{B} (Fig. 5.9 (c)-(d)) or to reduce the twist-to-bend ratio Γ (Fig. 5.9 (e)-(f)). We see that a reduction in the flexural rigidity K_{B} or the twist-to-bend ratio Γ increases the ability of the flagellum to change

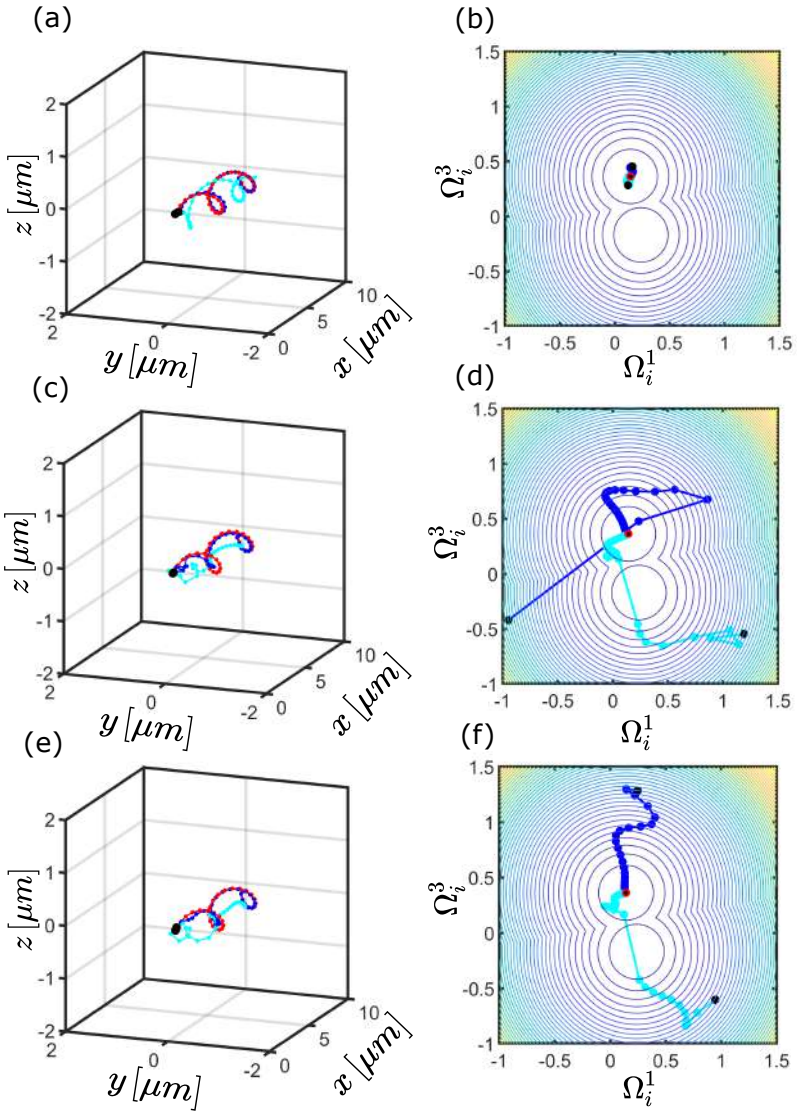

FIGURE 5.9: Visualization of the flagellum and the corresponding curvature and twist values $\mathbf{\Omega}$ after $t = 0$ (red), $t = t_1$ (blue) and $t \gg t_1$ (cyan) for $(K_B, \Gamma) = (K_{B,0}, \Gamma_0)$ (a,b), $(K_B, \Gamma) = \left(\frac{K_{B,0}}{4}, \Gamma_0\right)$ (c,d) and $(K_B, \Gamma) = \left(K_{B,0}, \frac{\Gamma_0}{4}\right)$ (e,f).

their curvature- and twist-values Ω_i, and even a certain amounts flips to the desired negative part of twist-values Ω_i^3, but none of them end up at the desired position and even a certain amount of parameters Ω_i does not change their value at all. We could not find a parameter setting of flexural rigidity K_B and twist-to-bend ratio Γ where the parameters Ω_i moved to the positions corresponding to the semicoiled shape. Therefore in a next step we tried to vary the parameter δ from equation 5.45. In Fig. 5.10 we show the energy-difference

$$\Delta_{n,s} = E^{el}\left(\kappa_0^n, \tau_0^n\right) + \delta - E^{el}\left(\kappa_0^s, \tau_0^s\right) \tag{5.47}$$

for $t = t_0$ (a), $t = t_1$ (b) and $t = t_2 \gg t_1$ (c). The initial energy-difference is given as $\Delta_{n,s}(t = 0) = 3.15$. The curves correspond to $\delta = 0$ (red), $\delta = 3.1$ (cyan) and $\delta = 3.2$ (blue). We see that the only for $\delta > \Delta_{n,s}(t = 0)$ the

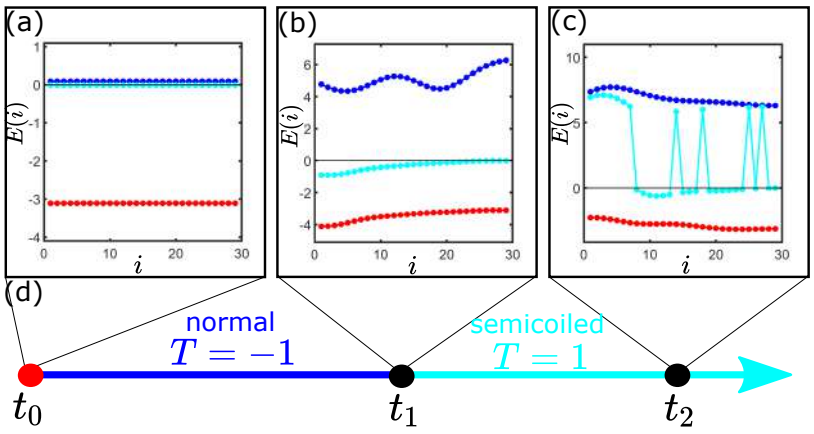

FIGURE 5.10: Plot of the elastic energy $E(i)$ for node $\boldsymbol{x}_i$ for $t = 0$ (red), $t = t_1$ (blue) and $t = t_2 \gg t_1$ (cyan) corresponding to $\delta = 0$ (a), $\delta = 3.1$ (b) and $\delta = 3.2$ (c). (d) Visualization of the process to induce polymorphic-transformations with a negative torque $T = -1$ for $t \leq t_1$ and a positive torque $T = 1$ for $t > t_1$.

energy-gap to move to the semicoiled state can be overcome, resulting in purely positive value for $\Delta_{n,s}(t_2)$ in Fig. 5.10 (c). The corresponding flagella and curvature and twist values Ω_i^1 and Ω_i^3 are represented in Fig. 5.11. Here the parameters correspond to $\delta = 0$ (a) and (b), $\delta = 3.1$ (c) and (d) and $\delta = 3.2$ (e) and (f). We see in Fig. 5.11 (c) that a part of the flagellum (cyan) has already changed its shape, whereas in Fig. 5.11 (e) the whole flagella transforms into the semicoiled shape. Therefore by adapting the energy-gap δ we are able to perform polymorphic changes. But the problem is that it is now impossible to go back to the normal state, as the energy gap introduced by $\delta = 3.2$ is too high to overcome. Also the polymorphic transformation from normal to semicoiled occurs now independently of whether we change the torque from $T = -1$ to $T = 1$ or keep the torque at it's negative value $T = -1$.
To summarize, we could not find a combination of the flexural rigidity K_B, the twist-to-bend ratio Γ and the energy-gap δ to trigger polymorphic changes from the normal shape to the semicoiled-state and back to normal by changing the torque from $T = -1$ to $T = 1$ and back to $T = -1$. Therefore we use another approach to trigger polymorphic transformations.

Time-dependent potential

As we could not find a static potential allowing us to perform polymorphic transformations, we introduce a time-dependent potential suitable to perform these transformations. The potential is represented in Fig. 5.8 (e) and can be quantified via

$$\mathrm{E}^{\mathrm{el,t}} = \begin{cases} \mathrm{E}^{\mathrm{el}}\left(\kappa_0^n, \tau_0^n\right) & t \leq t_1 \\ \mathrm{E}^{\mathrm{el}}\left(\kappa_0^s, \tau_0^s\right) & t_1 < t. \end{cases} \tag{5.48}$$

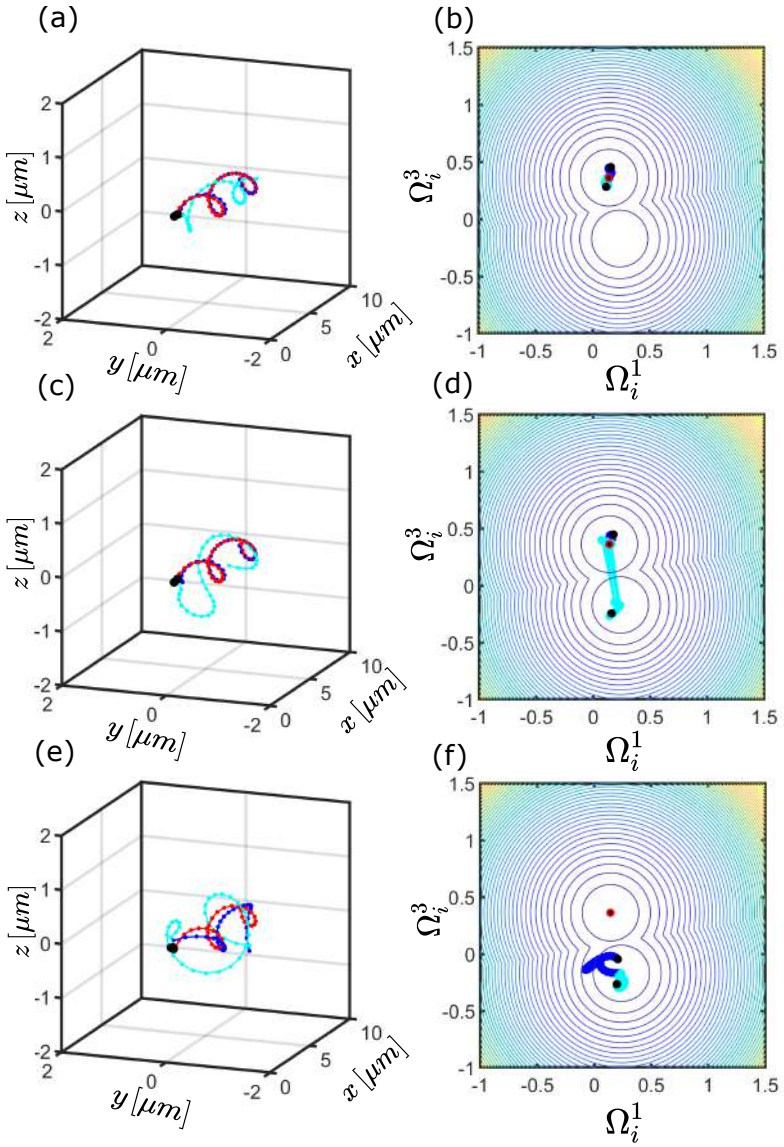

FIGURE 5.11: Visualization of the flagellum and the corresponding curvature and twist values $\mathbf{\Omega}$ after $t = 0$ (red), $t = t_1$ (blue) and $t \gg t_1$ (cyan) for $\delta = 0$ (a,b), $\delta = 3.1$ (c,d) and $\delta = 3.3$ (e,f).

The results after applying above potential are visualized in Fig. 5.12. We see in Fig. 5.12 (a) a polymorphic transformation from the initial ($t = 0$, red) normal-state to the final ($t \gg t_1$, cyan) semicoiled-state. The corresponding curvature and twist values Ω_i^1 and Ω_i^3 in Fig. 5.12 (b). In the following we use the potential introduced in equation 5.49 to trigger polymorphic-transformations.

5.2.2 Simulate tumbling-events

In above section we investigated two different approaches to trigger polymorphic transformations. In this section we use the second approach, the time-dependent potential, to trigger these polymorphic transformations and

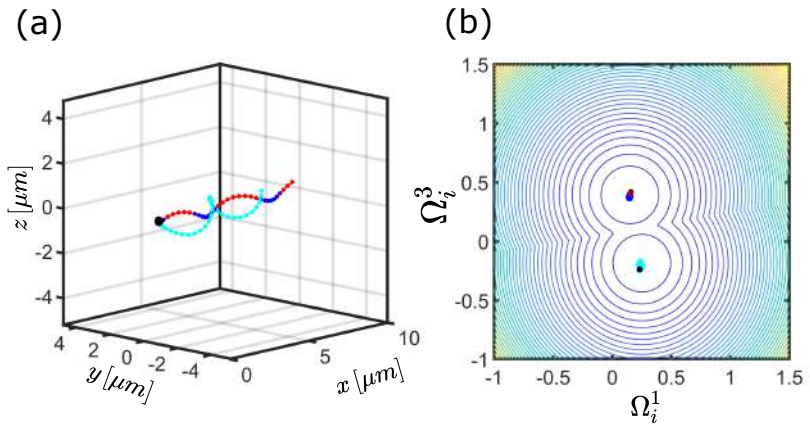

FIGURE 5.12: Visualization of the flagellum (a) and the corresponding curvature and twist values $\mathbf{\Omega}$ (b) after $t = 0$ (red), $t = t_1$ (blue) and $t \gg t_1$ (cyan) for the potential defined in equation 5.49.

to simulate tumbling-events. The potential is given as

$$\mathrm{E}^{\mathrm{el,t}} = \begin{cases} \mathrm{E}^{\mathrm{el}}\left(\kappa_0^n, \tau_0^n\right) & t \leq t_1 \\ \mathrm{E}^{\mathrm{el}}\left(\kappa_0^s, \tau_0^s\right) & t_1 < t \leq t_2 \\ \mathrm{E}^{\mathrm{el}}\left(\kappa_0^c, \tau_0^c\right) & t_2 < t \leq t_3 \\ \mathrm{E}^{\mathrm{el}}\left(\kappa_0^n, \tau_0^n\right) & t_3 < t \leq t. \end{cases} \tag{5.49}$$

The evolution of a tumbling event is summarized in Fig. 5.13. In the following we simulate tumbling-events for one, two, three and four different flagella.

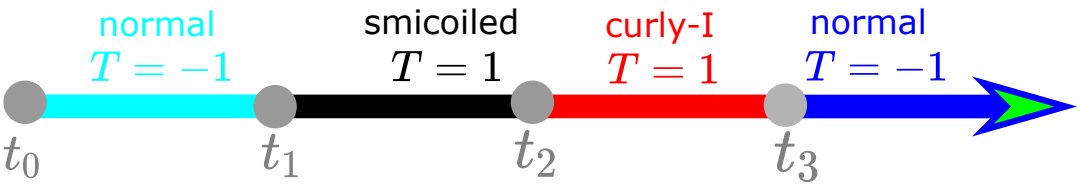

FIGURE 5.13: Schematic representation of a tumbling event consisting of the flagellum being in the normal state. A switch of the torque from $T = -1$ to $T = 1$ at $t = t_1$ induces a polymorphic transformation from the normal to the semicoiled state. After $t = t_2$ the flagellum changes to the curly-I shape before it switches back to the normal state at $t = t_3$ when the torque switches back from $T = 1$ to $T = -1$.

Uni-flagella

In a first step, we simulated a tumbling event for a bacterium with one single flagellum. The obtained trajectory is represented as the black curve in Fig. 5.14 (a). We marked the times $t = t_1$ (red), $t = t_2$ (blue), $t = t_3$ (cyan) and the last timepoint (magenta) as dots. We also fit a line through the initial

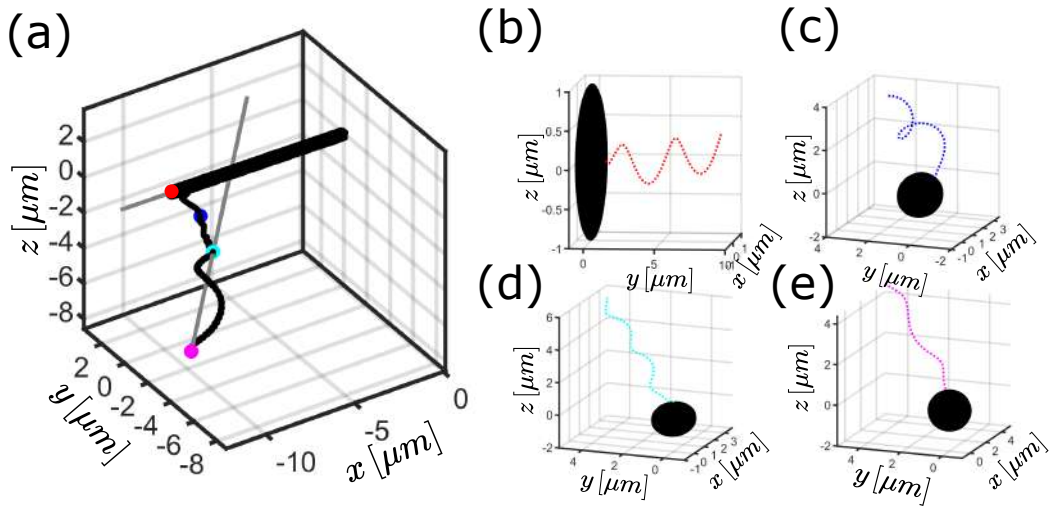

FIGURE 5.14: (a) Trajectory of a simulated bacterium with one flagellum (black), where the times $t = t_1$ (red), $t = t_2$ (blue), $t = t_3$ (cyan) and the last timepoint (magenta) are marked as dots. Gray lines represent a linear fit through the initial and final part of the trajectory. (b)-(e) Visualization of the flagellum at the positions marked with the colored dots in (a).

running-state and the last running-state to make the obtained tumbling-angle Θ_t clearly visible. In Fig. 5.14 (b)-(e) we show the flagella shape for the times marked in Fig. 5.14 (a). We see a clear transformation of the flagellum from the initial normal state (Fig. 5.14 (b)) to the semicoiled state (Fig. 5.14 (c)), the curly-I state (Fig. 5.14 (d)) and back to the final normal state (Fig. 5.14 (e)). Furthermore we see a clear change in the direction of bacteria locomotion when the tumbling event starts at $t = t_1$.

Bi-flagella

We also simulated a bacterium with two different flagella. The trajectory is represented in Fig. 5.15 (a). We marked the times $t = t_1$ (red), $t = t_2$ (blue), $t = t_3$ (cyan) and the last timepoint (magenta) as dots. We also fit a line through the initial running-state and the last running-state to make the obtained tumbling-angle Θ_t clearly visible. In Fig. 5.15 (b)-(e) we represent the tumbling flagella as dotted, the non-tumbling flagella as solid line. We see a clear bundle of flagella in Fig. 5.15 (b) and Fig. 5.15 (e), whereas in Fig. 5.15 (c) and (d) the tumbling flagellum has changed it's shape and unbundled from the other flagellum. At the last timestep the calculation crashed. The crash happened due to numerical problems as the flagella approached too close. We found no parameter setting for the flagellum to maintain a long running state after a tumbling event. It seems that due to the tumbling event it is impossible for the bacterium to recreate a smooth bundle as has already existed before the tumbling event. We will discuss this aspect later on.

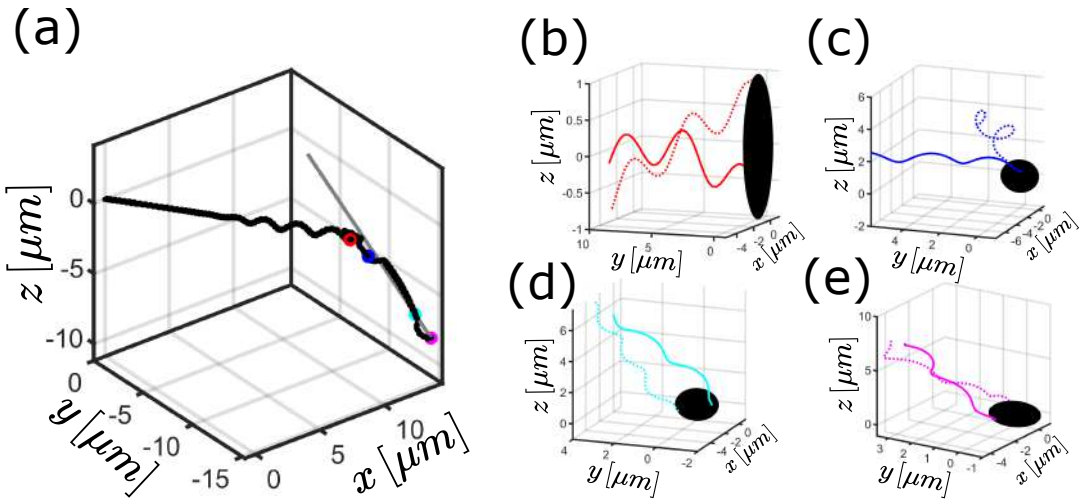

FIGURE 5.15: (a) Trajectory of a simulated bacterium with two flagella (black), where the times $t = t_1$ (red), $t = t_2$ (blue), $t = t_3$ (cyan) and the last timepoint (magenta) are marked as dots. Gray lines represent a linear fit through the initial and final part of the trajectory. (b)-(e) Visualization of the flagellum at the positions marked with the colored dots in (a).

Tri-and Quad-flagella

The trajectory of a bacterium with three flagella is represented in Fig. 5.16 (a). We marked the times $t = t_1$ (red), $t = t_2$ (blue), $t = t_3$ (cyan) and the last time-

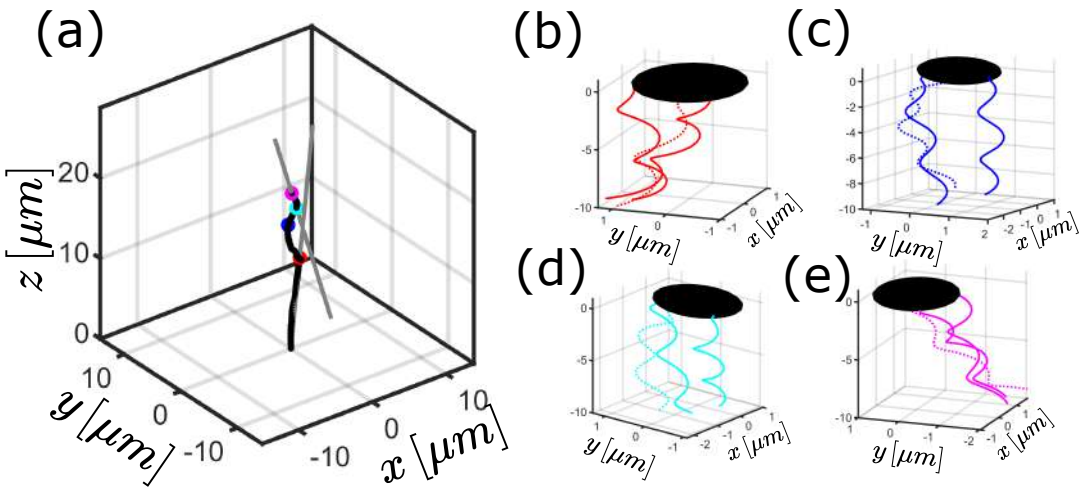

FIGURE 5.16: (a) Trajectory of a simulated bacterium with three flagella (black), where the times $t = t_1$ (red), $t = t_2$ (blue), $t = t_3$ (cyan) and the last timepoint (magenta) are marked as dots. Gray lines represent a linear fit through the initial and final part of the trajectory. (b)-(e) Visualization of the flagellum at the positions marked with the colored dots in (a).

point (magenta) as dots. We also fit a line through the initial running-state and the last running-state to make the obtained tumbling-angle Θ_t clearly visible. In Fig. 5.15 (b)-(e) we represent the tumbling flagella as dotted, the

non-tumbling flagella as solid line. We see a clear bundle in of flagella in Fig. 5.15 (b) and Fig. 5.15 (e), whereas in Fig. 5.15 (c) and (d) the flagella unbundled, but we do not see a clear semicoiled- or curly-I-shape as in the uni- or bi-flagella case. This can be explained through the impact of the other two flagella, remaining in running state and keeping up the propulsion, which has a direct impact on the tumbling flagellum-shape. We also see from Fig. 5.16 (a) that there is a smaller tumbling angle as in the uni- and bi-flagella-case. The same observation can be made for the quad-flagella-case, represented in Fig. 5.17. We see an even smaller tumbling-angle in Fig. 5.17 (a)

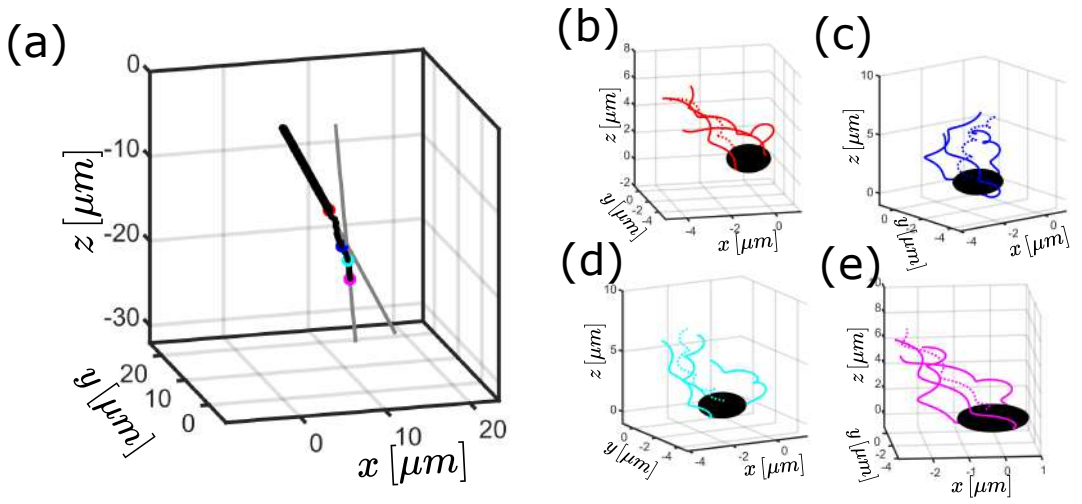

FIGURE 5.17: (a) Trajectory of a simulated bacterium with four flagella (black), where the times $t = t_1$ (red), $t = t_2$ (blue), $t = t_3$ (cyan) and the last timepoint (magenta) are marked as dots. Gray lines represent a linear fit through the initial and final part of the trajectory. (b)-(e) Visualization of the flagellum at the positions marked with the colored dots in (a).

due to the strong propulsion of the three flagella remaining in the running-state. Similar to the three flagella-case we see a bundle in Fig. 5.17 (b) and (e), whereas in Fig. 5.17 (c) and (d) no bundle is visible. Due to the presence of three flagella in the running state, keeping up the propulsion of the bacterium, the tumbling event only leads to unbundling, but the shape of the tumbling flagellum can barely be adapted.

Numerical stability

In the above cases of uni-, bi- tri and quad-flagella simulations, only the uni-flagellum case could finish the simulation without numerical problems resulting in the crash of the simulations. For all other cases the simulations crashed due to a too close approach of flagella. In Fig. 5.18 we investigated the stability of the simulation by varying times t_1 and t_2. If a simulation crashed during the semicoiled-state, we represent this as a black dot, a crash during the curly-I-state is represented as a red dot, a crash during the final running-state as blue dot, and if the simulation finished, we represent it as

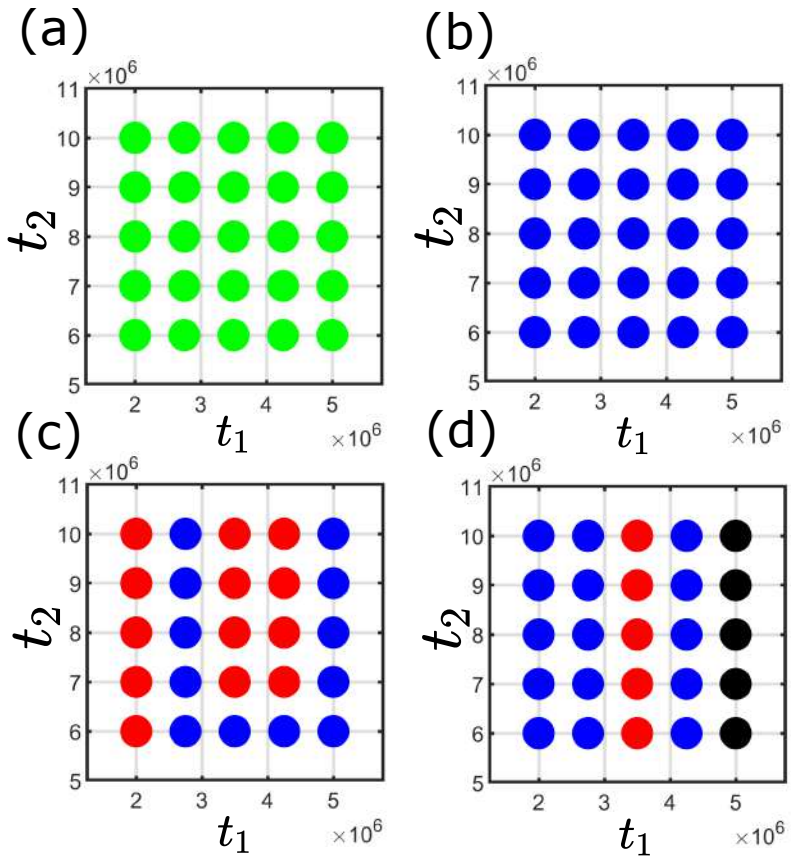

FIGURE 5.18: Performance in the simulation of tumbling-events for a bacterium with one (a), two (b), three (c) and four (d) flagella. Green dots correspond to a completely successful simulation, blue dots correspond to a crash of the simulation during the last running-state, red dots correspond to a crash of the simulation during the curly-I state and black dots correspond to a crash of the simulation during the semicoiled-state.

a green dot. The results for the Uni-flagella case are represented in Fig. 5.18 (a), the Bi-flagella case in Fig. 5.18 (b), the Tri-flagella case in Fig. 5.18 (c) and the Quad-flagella case in Fig. 5.18 (d). We see that only in the case of one single flagellum all simulations finished. In case of two flagella all simulations crashed during the last running state. This indicates that due to the tumbling event the bacterium is not able to restore it's initial, stable bundle. In case of three flagella, some calculations even crash during the curly-I-state, and for the four-flagella case even some simulations crashed during the semicoiled-state. Due to these numerical problems we restrict our analysis to a bacterium with two flagella.

Impact flagella-position

In this section we investigate the impact of the flagella positioning on the bacteria locomotion. Therefore we simulated the tumbling event represented in Fig. 5.13 for six different initial flagella positions represented in Fig. 5.19

(a)-(e), corresponding to $\Phi_{\text{Initial}} = \frac{5\pi}{5}$ (a), $\Phi_{\text{Initial}} = \frac{4\pi}{5}$ (b), $\Phi_{\text{Initial}} = \frac{3\pi}{5}$ (c), $\Phi_{\text{Initial}} = \frac{2\pi}{5}$ (d) and $\Phi_{\text{Initial}} = \frac{1\pi}{5}$ (e). Here the initial position can be defined via the angle Φ_{Initial} between both flagella. The obtained trajectories are rep-

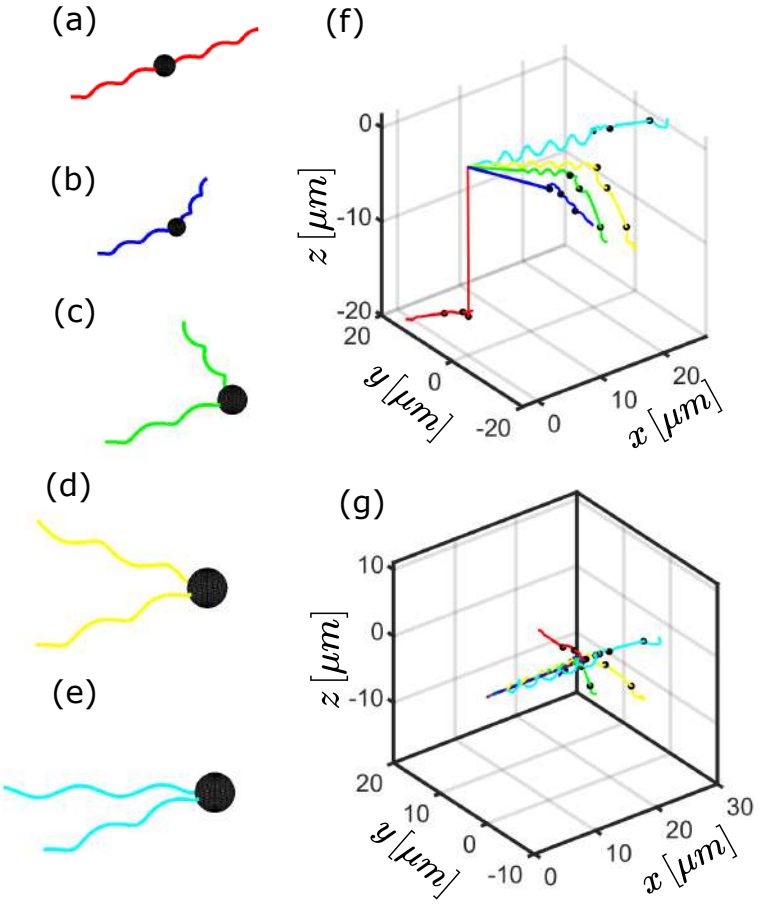

FIGURE 5.19: Visualization of the impact of flagella positioning for a bacterium with two flagella with initial conditions corresponding to $\Phi_{\text{Initial}} = \frac{5\pi}{5}$ (a), $\Phi_{\text{Initial}} = \frac{4\pi}{5}$ (b), $\Phi_{\text{Initial}} = \frac{3\pi}{5}$ (c), $\Phi_{\text{Initial}} = \frac{2\pi}{5}$ (d) and $\Phi_{\text{Initial}} = \frac{1\pi}{5}$ (e). The corresponding trajectories are represented in (f). A representation where the first running-state of all simulations is aligned is represented in (g). Black dots correspond to t_1, t_2 and t_3.

resented in Fig. 5.19 (g), where we marked times $t = t_1$, $t = t_2$ and $t = t_3$ as black dots. A clearer representation where we aligned the axis of the initial running-state is visualized in Fig. 5.19 (h). The first observation is the helical shape of the initial running state, whose radius increases for smaller angles Φ_{Initial}. We qualitatively see that the tumbling angles Θ_t increases for larger values of Φ_{Initial}. This qualitative observation is quantified by Fig. 5.20, where we show the tumbling angle Θ_t for different flagella-angles Φ_{Initial}. The general trend visualized in Fig. 5.20 was an expected result and can be explained to the higher impact of the tumbling flagellum to the trajectory the further its distance to the other flagellum. In case of $\Phi_{\text{Initial}} = \pi$, a tumbling-events of one flagellum sets the bacterium in a state where on one side the flagellum has full propulsion, whereas on the opposite side of the bacterium

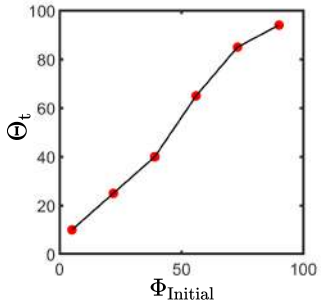

FIGURE 5.20: Simulated impact of initial flagella-positioning Φ_{Initial} on the tumbling-angle Θ_t.

the flagellum exerts a force on the other direction, resulting in a change of orientation by about $\Theta_t = \pi$. In case of $\Phi_{\text{Initial}} \approx 0$, a tumbling event does not change the direction as both flagella are close together. A tumbling only leads to a drop in velocity with barely a change in orientation. We further analyzed the speed v and the quantity D introduced in equation 5.44 to quantify whether efficient swimming occurs. These quantities are represented in Fig. 5.21 (a) and (b). The times $t = t_1$, $t = t_2$ and $t = t_3$ are visualized as black

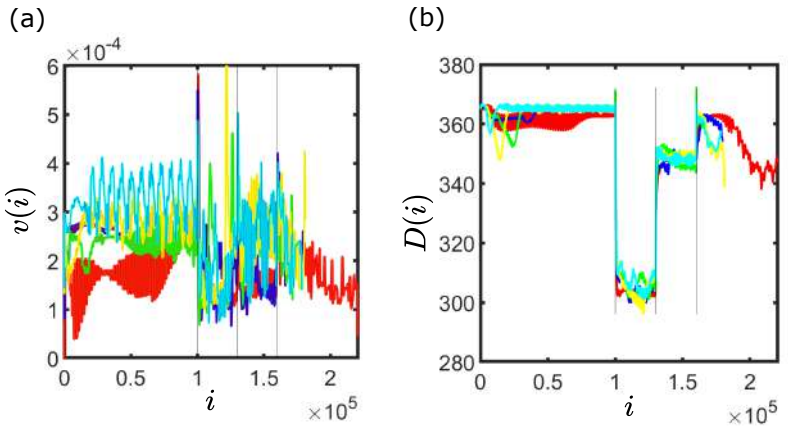

FIGURE 5.21: Representation of speed $v(i)$ (a) and quantity $D(i)$ (b) defined in equation 5.44 for $\Phi_{\text{Initial}} = \frac{5\pi}{5}$ (red), $\Phi_{\text{Initial}} = \frac{4\pi}{5}$ (blue), $\Phi_{\text{Initial}} = \frac{3\pi}{5}$ (green), $\Phi_{\text{Initial}} = \frac{2\pi}{5}$ (yellow) and $\Phi_{\text{Initial}} = \frac{1\pi}{5}$ (cyan). Times t_1, t_2 and t_3 are marked via black vertical lines. Both quantities v and D show a drop at time $t = t_1$ and jump back to approximately the initial stable value at $t = t_3$ but are not able to maintain this state.

vertical lines. We see a clear drop in the speed v during the semicoiled- and curly-I-state. During the final running-state the speed v initially increases, but does not reach it's value from the initial running state. This is a clear indication that the swimming in the final running-state is not as efficient as in the initial running-state. This observation is clearly supported by the quantity D represented in Fig. 5.21 (b). In the first running-state D oscillates around a relatively high value, whereas there is an - expected - drop during the semicoiled- and curly-I-state. During the final running-state the value of

D rises again to the same relatively high value as in the initial running-state, but after a certain time the value drops, resulting in less efficient swimming. The drop of D in the final running-state is a clear indication that the tumbling event not only changes the swimming-properties during this event, but also avoids the system to regain it's initial efficient swimming state, resulting in an unstable bundle of the two flagella, which after a certain time approach too close, resulting in numerical problems crashing the calculation.

5.3 Discussion

In this section we presented a qualitative model for the simulation of bacteria locomotion. This model simulates the swimmer as a combination of a spherical body and the flagellum. The flagellum consists of the hook, which connects the helical filament to the cell-body. Each segment of the flagellum has the fixed length l. The motor torque generated inside the cell-body is transferred from one segment to the next segment, forcing the flagellum to rotate. The helical shape of the flagellum is defined via the curvature and the twist value, which remain equal in the running-state. We extended the model of Frank Nguyen to simulate the tumbling-state, characterized via a change in the flagellum rotation-direction and change in flagellum shape. We were not able to simulate tumbling-events applying a time-independent potential, consisting of several minima, where each minimum in the energy-landscape corresponds to a certain flagellum-shape. We either had the problem that a relatively flat potential was not able to create a stable state, or a too steep potential was not able to allow changes in flagellum-shape. Therefore we introduced a time-dependent potential, where the current potential is suitable to generate the desired flagellum-shape at the current time of the tumbling-process. In the uni-flagellum case we were able to simulate tumbling processes, where the flagellum is initially in the normal state. During the tumbling state, the flagellum changes it's shape to the semicoiled-state, followed by the curly-I state. After the tumbling process ends, the flagellum changes it's shape back to the normal state. In case of two flagella, the tumbling process from normal- to semicoiled- to curly-I- and back to normal-state can be simulated, but after a certain time in the second normal state, the calculations crash due to numerical problems. In case of three or four flagella, the calculations already crash during the semicoiled- or curly-I state, as can be seen from Fig. 5.18. It is interesting to see that calculations for three flagella can crash during the semicoiled-state, but remain in tact for longer times in the four-flagella case and only crash in the subsequent curly-I state for the same parameter setting. The reason for the crash of the simulations is a too close approach of flagella, resulting in numerical problems. As it is impossible to determine the crash-point of a simulation and simulations for three or four flagella can take several weeks, we restricted our analysis to swimmer with only two flagella. We were interested in the impact on flagella-positioning on the tumbling-dynamics. Therefore we initialized swimmer with different flagella-positions characterized via the angle Φ_{Initial}, as represented in Fig. 5.19. The relation between the tumbling-angle and

the flagella-positioning can be seen in Fig. 5.20. The result proves our expectation, that a larger distance between anchor points of flagella-positions lead to a larger tumbling-angle Θ_t. The largest tumbling-angle Θ_t was obtained for a swimmer, where flagella were positioned at opposite sides of the cell-body. During a tumbling-event, the propulsion in the direction of movement for the non-tumbling-flagellum remains, whereas the tumbling-flagellum rotates in the opposite direction, pulling in the opposite direction relative to the current direction of motion. This effect of pulling is reduced for smaller distances of the anchor points of the flagella, resulting in smaller tumbling angles Θ_t for smaller angles Φ_{Initial}. The speed v (a) as well as the quantity D (b) representing the effectiveness in swimming are represented in Fig. 5.21 (a) ((b)). We see a clear dip in v and D during the tumbling-state. After a certain time in the second normal-state after the tumbling-event, the calculations start to crash. If we have a look at the quantity D from Fig. 5.21 (b) we see that the value of D after the tumbling event increases, but cannot maintain the level previous to the tumbling. This is a clear indication that the tumbling-event introduces a certain distortion to the system. The initial stable bundle in the initial running-state is irreversible destroyed through the tumbling event. In the second running-state, this initial stable bundle of both flagella cannot be recreated. Hence the second running-state is a meta-stable running-state where after a certain time the flagella approach so close that numerical problems crash the simulation. This can clearly be seen through the decaying of the quantity D in the second running-state from Fig. 5.21 (b). To conclude, we have extended the model of Frank Nguyen for the simulation of the running state to also simulate the tumbling-state, where polymorphic transformations of the swimmer are induced via a time-dependent potential.

Chapter 6

Summary & Outlook

6.1 3D Particle-Tracking

In chapter 3 we extended an optical microscope via an electrically focus tunable lens (ETL), allowing us to track particles in three dimensions. The tracking algorithm consists of two different steps, where we initially track particles in the xy-plane. Subsequently we calculate the sharpness of the tracked particle. Over a certain range of the past n tracked positions we assign the particle height z to the focal plane z_f for which we obtained the sharpest image of the particle. This method allows us to track particles up to $1\,mm$ in the z-range and several mm in the x- and y-range. To quantify the tracking-performance we tracked beads and could show a good agreement between the theoretical and measured (rotational) diffusion coefficient $D_{(r)}$. Application of the tracking algorithm on bacteria allowed us to obtain bacteria-trajectories over several minutes, showing a clear transition from the initial ballistic regime of the MSD to the diffusive regime. Furthermore we have seen that the maximal adaptable width Δz_a of the focal plane depends on the distance L between camera and ETL. This possibility in the adaption of Δz_a extends the possible application of the ETL to several phenomena arising at different scales. As a last advantage of the ETL we would like to point out that with costs of *only* about 400 €, the ETL is a very cost efficient method in adapting the focal plane z_f compared to e.g. xyz-mountable stages in the range of several thousands of €. Currently we have to initialize every tracking process manually although, once started, the tracking-process is fully automated. In future work the tracking-process could be adapted to be completely automatic. Therefore it would be necessary to automatically distinguish between dust particles and the particles we are interested to track. To solve this problems, neural networks have proven to be very efficient. Applying neural networks would allow for a completely automatic tracking-process. Another improvement of our tracking algorithm could be the determination of the height z. Currently we only can restrict the height z of a particle between two different layers and have no method to efficiently map a quantity to the distance Δz between particle and foal plane z_f. The biggest problem is the restriction to relatively low magnifications due to the ETL. It would be interesting to see if neural networks would be capable of mapping an image of a bacterium to the distance Δz. Furthermore it would be interesting to compare the MS(A)D for several different bacteria. Also the

difference in swimming-dynamics at different areas inside the sample would be an interesting topic to investigate.

6.2 Trajectory-Evaluation

In chapter 4 we introduced the Kalman-Filter as an efficient tool to evaluate bacteria trajectories. Furthermore the KF has several extensions, e.g. the IMM-filter, suitable to distinguish between different states of a system. We showed that an initial application of the KF on trajectories allows for a more efficient determination of the rotational diffusion coefficient D_r. The IMM-filter allowed us to present a powerful method for the distinction of the running- and tumbling-state. Rather than conventional methods, the application of the IMM-filter allows an intrinsic distinction of these two states. We have seen that by using the IMM-filter, wobbling-events will not be detected as tumbling-events anymore, changing the double-peak distribution for the tumbling-angle Θ_t obtained for conventional method to a single-peak distribution for the IMM-method. We furthermore use the IMM-filter to detect tumbling-events of three-dimensional trajectories obtained with the tracking algorithm introduced in chapter 3. We could show that the evaluation of three-dimensional trajectories leads to a higher mean in the distribution of running-times t_r compared to the evaluation of two-dimensional trajectories obtained with a conventional microscope. This effect occurs due to the missing z-information by only evaluating the two-dimensional projection of bacteria locomotion. In future work it would be interesting to refine the model applied in the Kalman-Filter. Currently we distinguish between running- and tumbling-state. This model could be refined to a running state, a running-tumbling-transition, the tumbling-state and the tumbling-running-transition. This refining of the model would probably give a simpler policy for the detection of tumbling-events. Furthermore it would be interesting to compare the run- and tumbling-dynamics of multiple different bacteria.

6.3 Qualitative Trajectory-Simulation

In chapter 5 we extended the method from Frank [119] developed for the qualitative simulation of the running-state of bacteria locomotion to simulate tumbling-events. We could show a clear relation between flagella-positioning on the cell-body and tumbling-dynamics. A larger distance between flagella has the effect of larger tumbling-angles Θ_t. In our analysis we were restricted to the investigation of bi-flagellated bacteria. A larger number of flagella leads to numerical problems, resulting in a crash of simulations. These numerical problems arise from too-close approaches of flagella due to the tumbling-event. To avoid these tumbling-events, the steric repulsion between flagella-nodes has to be adapted. Furthermore we faced the problem that we were not able to induce polymorphic transformations of flagella with a time-independent potential, as has been done in other publications as

e.g. [171]. The main difference between our model and the model of [171] is the simulation for the flagellum, which in our case consists of stiff segments, whereas in case of [171] if consist of several springs, allowing the flagellum to adapt its length. In future work, our model could be adapted similar to [171], allowing to induce polymorphic-changes for a time-independent potential, resulting in more realistic tumbling-events.

Bibliography

[1] Gabriel Amselem et al. “A Stochastic Description of Dictyostelium Chemotaxis”. en. In: *PLoS ONE* 7.5 (May 2012). Ed. by Adrian John Harwood, e37213. ISSN: 1932-6203. DOI: 10.1371/journal.pone.0037213.

[2] Dmitry Apel and Michael G. Surette. “Bringing Order to a Complex Molecular Machine: The Assembly of the Bacterial Flagella”. en. In: *Biochimica et Biophysica Acta (BBA) - Biomembranes* 1778.9 (Sept. 2008), pp. 1851–1858. ISSN: 00052736. DOI: 10.1016/j.bbamem.2007.07.005.

[3] J P Armitage and R M Macnab. “Unidirectional, Intermittent Rotation of the Flagellum of Rhodobacter Sphaeroides.” en. In: *Journal of Bacteriology* 169.2 (1987), pp. 514–518. ISSN: 0021-9193, 1098-5530. DOI: 10.1128/JB.169.2.514-518.1987.

[4] J. P. Armitage and R. Schmitt. “Bacterial Chemotaxis: Rhodobacter Sphaeroide and Sinorhizobium Meliloti - Variations on a Theme?” en. In: *Microbiology* 143.12 (Dec. 1997), pp. 3671–3682. ISSN: 1350-0872, 1465-2080. DOI: 10.1099/00221287-143-12-3671.

[5] S. Asakura. “Polymerization of Flagellin and Polymorphism of Flagella”. eng. In: *Advances in Biophysics* 1 (1970), pp. 99–155. ISSN: 0065-227X.

[6] Karen Asatryan et al. “Optical Lens with Electrically Variable Focus Using an Optically Hidden Dielectric Structure”. en. In: *Optics Express* 18.13 (June 2010), p. 13981. ISSN: 1094-4087. DOI: 10.1364/OE.18.013981.

[7] Yaakov Bar-Shalom, Xiao-Rong Li, and Thiagalingam Kirubarajan. *Estimation with Applications to Tracking and Navigation*. New York: Wiley, 2001. ISBN: 978-0-471-41655-5.

[8] F. Bartumeus and S. A. Levin. “Fractal Reorientation Clocks: Linking Animal Behavior to Statistical Patterns of Search”. en. In: *Proceedings of the National Academy of Sciences* 105.49 (Dec. 2008), pp. 19072–19077. ISSN: 0027-8424, 1091-6490. DOI: 10.1073/pnas.0801926105.

[9] Bahareh Behkam and Metin Sitti. “Bacterial Flagella-Based Propulsion and on/off Motion Control of Microscale Objects”. en. In: *Applied Physics Letters* 90.2 (Jan. 2007), p. 023902. ISSN: 0003-6951, 1077-3118. DOI: 10.1063/1.2431454.

[10] O. Bénichou et al. “Intermittent Search Strategies”. en. In: *Reviews of Modern Physics* 83.1 (Mar. 2011), pp. 81–129. ISSN: 0034-6861, 1539-0756. DOI: 10.1103/RevModPhys.83.81.

[11] O. Bénichou et al. “Optimal Search Strategies for Hidden Targets”. en. In: *Physical Review Letters* 94.19 (May 2005), p. 198101. ISSN: 0031-9007, 1079-7114. DOI: 10.1103/PhysRevLett.94.198101.

[12] H. C. Berg. *E. coli in Motion*. German. Berlin, Heidelberg: Springer Berlin Heidelberg, 2004. ISBN: 978-0-387-21638-6.

[13] H. C. Berg and L. Turner. “Chemotaxis of Bacteria in Glass Capillary Arrays. Escherichia Coli, Motility, Microchannel Plate, and Light Scattering”. eng. In: *Biophysical Journal* 58.4 (Oct. 1990), pp. 919–930. ISSN: 0006-3495. DOI: 10.1016/S0006-3495(90)82436-X.

[14] H.C. Berg and E.M. Purcell. “Physics of Chemoreception”. en. In: *Biophysical Journal* 20.2 (Nov. 1977), pp. 193–219. ISSN: 00063495. DOI: 10.1016/S0006-3495(77)85544-6.

[15] Howard C. Berg. “How to Track Bacteria”. en. In: *Review of Scientific Instruments* 42.6 (June 1971), pp. 868–871. ISSN: 0034-6748, 1089-7623. DOI: 10.1063/1.1685246.

[16] Howard C. Berg. *Random Walks in Biology*. Expanded ed. Princeton, N.J: Princeton University Press, 1993. ISBN: 978-0-691-00064-0.

[17] Howard C. Berg. “The Rotary Motor of Bacterial Flagella”. en. In: *Annual Review of Biochemistry* 72.1 (June 2003), pp. 19–54. ISSN: 0066-4154, 1545-4509. DOI: 10.1146/annurev.biochem.72.121801.161737.

[18] Howard C. Berg and Robert A. Anderson. “Bacteria Swim by Rotating Their Flagellar Filaments”. en. In: *Nature* 245.5425 (Oct. 1973), pp. 380–382. ISSN: 0028-0836, 1476-4687. DOI: 10.1038/245380a0.

[19] Howard C. Berg and Douglas A. Brown. “Chemotaxis in Escherichia Coli Analysed by Three-Dimensional Tracking”. en. In: *Nature* 239.5374 (Oct. 1972), pp. 500–504. ISSN: 0028-0836, 1476-4687. DOI: 10.1038/239500a0.

[20] James O. Berger. *Statistical Decision Theory and Bayesian Analysis*. 2nd ed. Springer Series in Statistics. New York: Springer-Verlag, 1993. ISBN: 978-0-387-96098-2.

[21] José M. Bernardo, Adrian F. M. Smith, and Thomas Bayes. *Bayesian Theory*. eng. Wiley Series in Probability and Mathematical Statistics. Chichester: Wiley, 2000. ISBN: 978-0-471-49464-5.

[22] Silvio Bianchi, Filippo Saglimbeni, and Roberto Di Leonardo. “Holographic Imaging Reveals the Mechanism of Wall Entrapment in Swimming Bacteria”. en. In: *Physical Review X* 7.1 (Jan. 2017), p. 011010. ISSN: 2160-3308. DOI: 10.1103/PhysRevX.7.011010.

[23] Peter J. Bickel and Kjell A. Doksum. *Mathematical Statistics: Basic Ideas and Selected Topics*. 2nd ed. Upper Saddle River, N.J: Pearson Prentice Hall, 2007. ISBN: 978-0-13-230637-9.

[24] David S. C. Biggs and Mark Andrews. “Acceleration of Iterative Image Restoration Algorithms”. en. In: *Applied Optics* 36.8 (Mar. 1997), p. 1766. ISSN: 0003-6935, 1539-4522. DOI: 10.1364/AO.36.001766.

[25] Steven M. Block, David F. Blair, and Howard C. Berg. "Compliance of Bacterial Flagella Measured with Optical Tweezers". en. In: *Nature* 338.6215 (Apr. 1989), pp. 514–518. ISSN: 0028-0836, 1476-4687. DOI: 10.1038/338514a0.

[26] M. Blum et al. "Compact Optical Design Solutions Using Focus Tunable Lenses". In: *SPIE Optical Systems Design*. Marseille, France, Sept. 2011, 81670W. DOI: 10.1117/12.897608.

[27] Manuele Brambilla et al. "Swarm Robotics: A Review from the Swarm Engineering Perspective". en. In: *Swarm Intelligence* 7.1 (Mar. 2013), pp. 1–41. ISSN: 1935-3812, 1935-3820. DOI: 10.1007/s11721-012-0075-2.

[28] Alfred Brown and Harold J. Benson. *Benson's Microbiological Applications: Laboratory Manual in General Microbiology, Complete Version*. eng. 10th ed. Boston: McGraw-Hill, 2007. ISBN: 978-0-07-299272-4 978-0-07-125416-8.

[29] M. T. Brown et al. "Flagellar Hook Flexibility Is Essential for Bundle Formation in Swimming Escherichia Coli Cells". en. In: *Journal of Bacteriology* 194.13 (July 2012), pp. 3495–3501. ISSN: 0021-9193. DOI: 10.1128/JB.00209-12.

[30] S. Bubendorfer et al. "Secondary Bacterial Flagellar System Improves Bacterial Spreading by Increasing the Directional Persistence of Swimming". en. In: *Proceedings of the National Academy of Sciences* 111.31 (Aug. 2014), pp. 11485–11490. ISSN: 0027-8424, 1091-6490. DOI: 10.1073/pnas.1405820111.

[31] C. R. Calladine. "Construction of Bacterial Flagella". en. In: *Nature* 255.5504 (May 1975), pp. 121–124. ISSN: 0028-0836, 1476-4687. DOI: 10.1038/255121a0.

[32] C.R. Calladine. "Design Requirements for the Construction of Bacterial Flagella". en. In: *Journal of Theoretical Biology* 57.2 (Apr. 1976), pp. 469–489. ISSN: 00225193. DOI: 10.1016/0022-5193(76)90016-3.

[33] C.R. Calldine. "Change of Waveform in Bacterial Flagella: The Role of Mechanics at the Molecular Level". en. In: *Journal of Molecular Biology* 118.4 (Feb. 1978), pp. 457–479. ISSN: 00222836. DOI: 10.1016/0022-2836(78)90285-1.

[34] Alfred S. Carasso. "APEX Blind Deconvolution of Color Hubble Space Telescope Imagery and Other Astronomical Data". en. In: *Optical Engineering* 45.10 (Oct. 2006), p. 107004. ISSN: 0091-3286. DOI: 10.1117/1.2362579.

[35] S. Chattopadhyay et al. "Swimming Efficiency of Bacterium Escherichia Coli". en. In: *Proceedings of the National Academy of Sciences* 103.37 (Sept. 2006), pp. 13712–13717. ISSN: 0027-8424, 1091-6490. DOI: 10.1073/pnas.0602043103.

[36] Suddhashil Chattopadhyay. *Study of Bacterial Motility Using Optical Tweezers*. Jan. 2009.

[37] Suddhashil Chattopadhyay and Xiao-Lun Wu. "The Effect of Long-Range Hydrodynamic Interaction on the Swimming of a Single Bacterium". en. In: *Biophysical Journal* 96.5 (Mar. 2009), pp. 2023–2028. ISSN: 00063495. DOI: 10.1016/j.bpj.2008.11.046.

[38] Fook Chiong Cheong, Bhaskar Jyoti Krishnatreya, and David G. Grier. "Strategies for Three-Dimensional Particle Tracking with Holographic Video Microscopy". en. In: *Optics Express* 18.13 (June 2010), p. 13563. ISSN: 1094-4087. DOI: 10.1364/OE.18.013563.

[39] Jacinta C. Conrad et al. "Flagella and Pili-Mediated Near-Surface Single-Cell Motility Mechanisms in P. Aeruginosa". en. In: *Biophysical Journal* 100.7 (Apr. 2011), pp. 1608–1616. ISSN: 00063495. DOI: 10.1016/j.bpj.2011.02.020.

[40] G. Corkidi et al. "Tracking Sperm in Three-Dimensions". en. In: *Biochemical and Biophysical Research Communications* 373.1 (Aug. 2008), pp. 125–129. ISSN: 0006291X. DOI: 10.1016/j.bbrc.2008.05.189.

[41] Ricardo Cortez, Lisa Fauci, and Alexei Medovikov. "The Method of Regularized Stokeslets in Three Dimensions: Analysis, Validation, and Application to Helical Swimming". en. In: *Physics of Fluids* 17.3 (Mar. 2005), p. 031504. ISSN: 1070-6631, 1089-7666. DOI: 10.1063/1.1830486.

[42] T. Darnige et al. "Lagrangian 3D Tracking of Fluorescent Microscopic Objects in Motion". en. In: *Review of Scientific Instruments* 88.5 (May 2017), p. 055106. ISSN: 0034-6748, 1089-7623. DOI: 10.1063/1.4982820.

[43] N. C. Darnton et al. "On Torque and Tumbling in Swimming Escherichia Coli". en. In: *Journal of Bacteriology* 189.5 (Mar. 2007), pp. 1756–1764. ISSN: 0021-9193. DOI: 10.1128/JB.01501-06.

[44] Nicholas Darnton et al. "Moving Fluid with Bacterial Carpets". en. In: *Biophysical Journal* 86.3 (Mar. 2004), pp. 1863–1870. ISSN: 00063495. DOI: 10.1016/S0006-3495(04)74253-8.

[45] Nicholas C. Darnton and Howard C. Berg. "Force-Extension Measurements on Bacterial Flagella: Triggering Polymorphic Transformations". en. In: *Biophysical Journal* 92.6 (Mar. 2007), pp. 2230–2236. ISSN: 00063495. DOI: 10.1529/biophysj.106.094037.

[46] Michael W. Davidson and Mortimer Abramowitz. "Optical Microscopy". en. In: *Encyclopedia of Imaging Science and Technology*. Ed. by Joseph P. Hornak. Hoboken, NJ, USA: John Wiley & Sons, Inc., Jan. 2002, img074. ISBN: 978-0-471-44339-1. DOI: 10.1002/0471443395.img074.

[47] Kanjar De and V. Masilamani. "Image Sharpness Measure for Blurred Images in Frequency Domain". en. In: *Procedia Engineering* 64 (2013), pp. 149–158. ISSN: 18777058. DOI: 10.1016/j.proeng.2013.09.086.

[48] Jan K. G. Dhont. *An Introduction to Dynamics of Colloids*. Studies in Interface Science vol. 2. Amsterdam, Netherlands ; New York: Elsevier, 1996. ISBN: 978-0-444-82009-9.

[49] Sebastian Doniach. "*Biological Physics: Energy, Information, Life* **Biological Physics: Energy, Information, Life** , Philip Nelson (with the Assistance of Marko Radosavljević and Sarina Bromberg) W. H. Freeman, New York, 2003. $92.00 (598 Pp.). ISBN 0-7167-4372-8". en. In: *Physics Today* 57.11 (Nov. 2004), pp. 63–64. ISSN: 0031-9228, 1945-0699. DOI: 10.1063/1.1839381.

[50] Terence C. Flynn and Jianpeng Ma. "Theoretical Analysis of Twist/Bend Ratio and Mechanical Moduli of Bacterial Flagellar Hook and Filament". en. In: *Biophysical Journal* 86.5 (May 2004), pp. 3204–3210. ISSN: 00063495. DOI: 10.1016/S0006-3495(04)74368-4.

[51] Benjamin Friedrich. "A Mesoscopic Model for Helical Bacterial Flagella". en. In: *Journal of Mathematical Biology* 53.1 (July 2006), pp. 162–178. ISSN: 0303-6812, 1432-1416. DOI: 10.1007/s00285-006-0380-8.

[52] Yiin-Kuen Fuh, Jui-Kuan Chen, and Pin-Wen Chen. "Characterization of Electrically Tunable Liquid Lens and Adaptive Optics for Aberration Correction". en. In: *Optik* 126.24 (Dec. 2015), pp. 5456–5459. ISSN: 00304026. DOI: 10.1016/j.ijleo.2015.09.105.

[53] C. W. Gardiner and C. W. Gardiner. *Stochastic Methods: A Handbook for the Natural and Social Sciences*. 4th ed. Springer Series in Synergetics. Berlin: Springer, 2009. ISBN: 978-3-540-70712-7.

[54] J. GRAY. "The Movement of Sea-Urchin Spermatozoa". In: *Journal of Experimental Biology* 32.4 (1955), pp. 775–801. ISSN: 0022-0949. eprint: https://jeb.biologists.org/content/32/4/775.full.pdf.

[55] J. GRAY and G. J. HANCOCK. "The Propulsion of Sea-Urchin Spermatozoa". In: *Journal of Experimental Biology* 32.4 (1955), pp. 802–814. ISSN: 0022-0949. eprint: https://jeb.biologists.org/content/32/4/802.full.pdf.

[56] Mohinder S Grewal and Angus P Andrews. *Kalman Filtering: Theory and Practice Using MATLAB*. English. New York: Wiley, 2001. ISBN: 978-0-471-39254-5 978-0-471-26638-9.

[57] Benjamin F. Grewe et al. "Fast Two-Layer Two-Photon Imaging of Neuronal Cell Populations Using an Electrically Tunable Lens". en. In: *Biomedical Optics Express* 2.7 (July 2011), p. 2035. ISSN: 2156-7085, 2156-7085. DOI: 10.1364/BOE.2.002035.

[58] G. Hancock. "The Self-Propulsion of Microscopic Organisms through Liquids". en. In: *Proceedings of the Royal Society of London. Series A. Mathematical and Physical Sciences* 217.1128 (Mar. 1953), pp. 96–121. ISSN: 0080-4630, 2053-9169. DOI: 10.1098/rspa.1953.0048.

[59] J. Hartikainen, A. Solin, and S. Saerkkae. *Optimal Filtering with Kalman Filters and Smoothers - a Manual for the Matlab Toolbox EKF/UKF*. Aug. 2007.

[60] Etsuko Hasegawa, Ritsu Kamiya, and Sho Asakura. "Thermal Transition in Helical Forms of Salmonella Flagella". en. In: *Journal of Molecular Biology* 160.4 (Oct. 1982), pp. 609–621. ISSN: 00222836. DOI: 10.1016/0022-2836(82)90318-7.

[61] Kazuya Hasegawa, Ichiro Yamashita, and Keiichi Namba. "Quasi- and Nonequivalence in the Structure of Bacterial Flagellar Filament". en. In: *Biophysical Journal* 74.1 (Jan. 1998), pp. 569–575. ISSN: 00063495. DOI: 10.1016/S0006-3495(98)77815-4.

[62] Dirk Helbing. "Traffic and Related Self-Driven Many-Particle Systems". en. In: *Reviews of Modern Physics* 73.4 (Dec. 2001), pp. 1067–1141. ISSN: 0034-6861, 1539-0756. DOI: 10.1103/RevModPhys.73.1067.

[63] William R. Hesse et al. "Bacterial Nanofluidic Structures for Medicine and Engineering". en. In: *Small* 6.8 (Apr. 2010), pp. 895–909. ISSN: 16136810, 16136829. DOI: 10.1002/smll.200901576.

[64] William R. Hesse et al. "Mineralization of Flagella for Nanotube Formation". en. In: *Materials Science and Engineering: C* 29.7 (Aug. 2009), pp. 2282–2286. ISSN: 09284931. DOI: 10.1016/j.msec.2009.05.018.

[65] Timothy J. Holmes et al. "Light Microscopic Images Reconstructed by Maximum Likelihood Deconvolution". en. In: *Handbook of Biological Confocal Microscopy*. Ed. by James B. Pawley. Boston, MA: Springer US, 1995, pp. 389–402. ISBN: 978-1-4757-5350-9 978-1-4757-5348-6. DOI: 10.1007/978-1-4757-5348-6_24.

[66] Hirokazu Hotani. "Micro-Video Study of Moving Bacterial Flagellar Filaments". en. In: *Journal of Molecular Biology* 156.4 (Apr. 1982), pp. 791–806. ISSN: 00222836. DOI: 10.1016/0022-2836(82)90142-5.

[67] Hirokazu Hotani. "Micro-Video Study of Moving Bacterial Flagellar Filaments II. Polymorphic Transition in Alcohol". en. In: *Biosystems* 12.3-4 (Jan. 1980), pp. 325–330. ISSN: 03032647. DOI: 10.1016/0303-2647(80)90030-1.

[68] Daisuke Iwai et al. "Speeded-Up Focus Control of Electrically Tunable Lens by Sparse Optimization". en. In: *Scientific Reports* 9.1 (Dec. 2019), p. 12365. ISSN: 2045-2322. DOI: 10.1038/s41598-019-48900-z.

[69] Joey M. Jabbour et al. "Optical Axial Scanning in Confocal Microscopy Using an Electrically Tunable Lens". en. In: *Biomedical Optics Express* 5.2 (Feb. 2014), p. 645. ISSN: 2156-7085, 2156-7085. DOI: 10.1364/BOE.5.000645.

[70] P. J. A. Janssen and M. D. Graham. "Coexistence of Tight and Loose Bundled States in a Model of Bacterial Flagellar Dynamics". en. In: *Physical Review E* 84.1 (July 2011), p. 011910. ISSN: 1539-3755, 1550-2376. DOI: 10.1103/PhysRevE.84.011910.

[71] Peter A. Jansson, ed. *Deconvolution of Images and Spectra*. 2nd ed. San Diego: Academic Press, 1997. ISBN: 978-0-12-380222-4.

[72] R.E. Johnson and C.J. Brokaw. "Flagellar Hydrodynamics. A Comparison between Resistive-Force Theory and Slender-Body Theory". en. In: *Biophysical Journal* 25.1 (Jan. 1979), pp. 113–127. ISSN: 00063495. DOI: 10.1016/S0006-3495(79)85281-9.

[73] Christopher J. Jones et al. "Stoichiometric Analysis of the Flagellar Hook-(Basal-Body) Complex of Salmonella Typhimurium". en. In: *Journal of Molecular Biology* 212.2 (Mar. 1990), pp. 377–387. ISSN: 00222836. DOI: 10.1016/0022-2836(90)90132-6.

[74] R. E. Kalman. "A New Approach to Linear Filtering and Prediction Problems". en. In: *Journal of Basic Engineering* 82.1 (1960), p. 35. ISSN: 00219223. DOI: 10.1115/1.3662552.

[75] R. Kamiya et al. "Transition of Bacterial Flagella from Helical to Straight Forms with Different Subunit Arrangements". en. In: *Journal of Molecular Biology* 131.4 (July 1979), pp. 725–742. ISSN: 00222836. DOI: 10.1016/0022-2836(79)90199-2.

[76] Ritsu Kamiya and Sho Asakura. "Flagellar Transformations at Alkaline pH". en. In: *Journal of Molecular Biology* 108.2 (Dec. 1976), pp. 513–518. ISSN: 00222836. DOI: 10.1016/S0022-2836(76)80133-7.

[77] Ritsu Kamiya and Sho Asakura. "Helical Transformations of Salmonella Flagella in Vitro". en. In: *Journal of Molecular Biology* 106.1 (Sept. 1976), pp. 167–186. ISSN: 00222836. DOI: 10.1016/0022-2836(76)90306-5.

[78] U. Benjamin Kaupp, Nachiket D. Kashikar, and Ingo Weyand. "Mechanisms of Sperm Chemotaxis". en. In: *Annual Review of Physiology* 70.1 (Mar. 2008), pp. 93–117. ISSN: 0066-4278, 1545-1585. DOI: 10.1146/annurev.physiol.70.113006.100654.

[79] M. Kim et al. "A Macroscopic Scale Model of Bacterial Flagellar Bundling". en. In: *Proceedings of the National Academy of Sciences* 100.26 (Dec. 2003), pp. 15481–15485. ISSN: 0027-8424, 1091-6490. DOI: 10.1073/pnas.2633596100.

[80] Min Jun Kim and Kenneth S. Breuer. "Microfluidic Pump Powered by Self-Organizing Bacteria". en. In: *Small* 4.1 (Jan. 2008), pp. 111–118. ISSN: 16136810, 16136829. DOI: 10.1002/smll.200700641.

[81] MunJu Kim and Thomas R. Powers. "Deformation of a Helical Filament by Flow and Electric or Magnetic Fields". en. In: *Physical Review E* 71.2 (Feb. 2005), p. 021914. ISSN: 1539-3755, 1550-2376. DOI: 10.1103/PhysRevE.71.021914.

[82] MunJu Kim and Thomas R. Powers. "Hydrodynamic Interactions between Rotating Helices". en. In: *Physical Review E* 69.6 (June 2004), p. 061910. ISSN: 1539-3755, 1550-2376. DOI: 10.1103/PhysRevE.69.061910.

[83] P. E. Kloeden and E. Platen. *Numerical Solution of Stochastic Differential Equations*. German. Berlin, Heidelberg: Springer Berlin Heidelberg, 1992. ISBN: 978-3-662-12616-5.

[84] A. J Kluyver and Cornelis Bernardus van Niel. *The Microbe's Contribution to Biology*. English. 1956. ISBN: 978-0-674-18869-3.

[85] K. Kobayashi et al. "Purification and Characterization of the Flagellar Basal Body of Rhodobacter Sphaeroides". en. In: *Journal of Bacteriology* 185.17 (Sept. 2003), pp. 5295–5300. ISSN: 0021-9193. DOI: 10.1128/JB.185.17.5295-5300.2003.

[86] Arthur L. Koch. "Control of the Bacterial Cell Cycle by Cytoplasmic Growth". en. In: *Critical Reviews in Microbiology* 28.1 (Jan. 2002), pp. 61–77. ISSN: 1040-841X, 1549-7828. DOI: 10.1080/1040-840291046696.

[87] S. Kudo et al. "Asymmetric Swimming Pattern of Vibrio Alginolyticus Cells with Single Polar Flagella". In: 242.2 (Jan. 2005), pp. 221–225.

[88] S. H. Larsen et al. "Chemomechanical Coupling without ATP: The Source of Energy for Motility and Chemotaxis in Bacteria". en. In: *Proceedings of the National Academy of Sciences* 71.4 (Apr. 1974), pp. 1239–1243. ISSN: 0027-8424, 1091-6490. DOI: 10.1073/pnas.71.4.1239.

[89] Steven H. Larsen et al. "Change in Direction of Flagellar Rotation Is the Basis of the Chemotactic Response in Escherichia Coli". en. In: *Nature* 249.5452 (May 1974), pp. 74–77. ISSN: 0028-0836, 1476-4687. DOI: 10.1038/249074a0.

[90] Eric Lauga. "Bacterial Hydrodynamics". en. In: *Annual Review of Fluid Mechanics* 48.1 (Jan. 2016), pp. 105–130. ISSN: 0066-4189, 1545-4479. DOI: 10.1146/annurev-fluid-122414-034606.

[91] Eric Lauga and Thomas R Powers. "The Hydrodynamics of Swimming Microorganisms". In: *Reports on Progress in Physics* 72.9 (Sept. 2009), p. 096601. ISSN: 0034-4885, 1361-6633. DOI: 10.1088/0034-4885/72/9/096601.

[92] Eric Lauga et al. "Swimming in Circles: Motion of Bacteria near Solid Boundaries". eng. In: *Biophysical Journal* 90.2 (Jan. 2006), pp. 400–412. ISSN: 0006-3495. DOI: 10.1529/biophysj.105.069401.

[93] P. Läuger. "Torque and Rotation Rate of the Bacterial Flagellar Motor". en. In: *Biophysical Journal* 53.1 (Jan. 1988), pp. 53–65. ISSN: 00063495. DOI: 10.1016/S0006-3495(88)83065-0.

[94] Sang Yup Lee, ed. *Systems Biology and Biotechnology of Escherichia Coli*. Dordrecht: Springer, 2009. ISBN: 978-1-4020-9393-7 978-1-4020-9394-4.

[95] Wanho Lee et al. "Bacterial Flagellar Bundling and Unbundling via Polymorphic Transformations". en. In: *Physical Review E* 98.5 (Nov. 2018), p. 052405. ISSN: 2470-0045, 2470-0053. DOI: 10.1103/PhysRevE.98.052405.

[96] Don S. Lemons and Anthony Gythiel. "Paul Langevin's 1908 Paper "On the Theory of Brownian Motion" ["Sur La Théorie Du Mouvement Brownien," C. R. Acad. Sci. (Paris) **146** , 530–533 (1908)]". en. In: *American Journal of Physics* 65.11 (Nov. 1997), pp. 1079–1081. ISSN: 0002-9505, 1943-2909. DOI: 10.1119/1.18725.

[97] Anat Levin et al. "Understanding and Evaluating Blind Deconvolution Algorithms". In: *2009 IEEE Conference on Computer Vision and Pattern Recognition*. Miami, FL: IEEE, June 2009, pp. 1964–1971. ISBN: 978-1-4244-3992-8. DOI: 10.1109/CVPR.2009.5206815.

[98] Guanglai Li et al. "Accumulation of Swimming Bacteria near a Solid Surface". en. In: *Physical Review E* 84.4 (Oct. 2011), p. 041932. ISSN: 1539-3755, 1550-2376. DOI: 10.1103/PhysRevE.84.041932.

[99] Martin Li. *Experimental Study of Swimming Flagellated Bacteria and Their Collective Behaviour in Concentrated Suspensions*. Jan. 2010.

[100] James Lighthill. "Flagellar Hydrodynamics". en. In: *SIAM Review* 18.2 (Apr. 1976), pp. 161–230. ISSN: 0036-1445, 1095-7200. DOI: 10.1137/1018040.

[101] M. J. Lighthill. *Mathematical Biofluiddynamics*. eng. CBMS-NSF Regional Conference Series in Applied Mathematics 17. Philadelphia: Society for Industrial and Applied Mathematics, 1989. ISBN: 978-0-89871-014-4.

[102] Hung-Chun Lin, Ming-Syuan Chen, and Yi-Hsin Lin. "A Review of Electrically Tunable Focusing Liquid Crystal Lenses". In: *Transactions on Electrical and Electronic Materials* 12.6 (Dec. 2011), pp. 234–240. DOI: 10.4313/TEEM.2011.12.6.234.

[103] S. G. Lipson, H. Lipson, and D. S. Tannhauser. *Optical Physics*. 3rd ed. Cambridge ; New York, NY, USA: Cambridge University Press, 1995. ISBN: 978-0-521-43047-0 978-0-521-43631-1.

[104] B. Liu et al. "Helical Motion of the Cell Body Enhances Caulobacter Crescentus Motility". en. In: *Proceedings of the National Academy of Sciences* 111.31 (Aug. 2014), pp. 11252–11256. ISSN: 0027-8424, 1091-6490. DOI: 10.1073/pnas.1407636111.

[105] R. Liu and H. Ochman. "Stepwise Formation of the Bacterial Flagellar System". en. In: *Proceedings of the National Academy of Sciences* 104.17 (Apr. 2007), pp. 7116–7121. ISSN: 0027-8424, 1091-6490. DOI: 10.1073/pnas.0700266104.

[106] J. Lowy and M. Spencer. "Structure and Function of Bacterial Flagella". eng. In: *Symposia of the Society for Experimental Biology* 22 (1968), pp. 215–236. ISSN: 0081-1386.

[107] Rolf H. Luchsinger, Birger Bergersen, and James G. Mitchell. "Bacterial Swimming Strategies and Turbulence". en. In: *Biophysical Journal* 77.5 (Nov. 1999), pp. 2377–2386. ISSN: 00063495. DOI: 10.1016/S0006-3495(99)77075-X.

[108] R. M. Macnab. "Bacterial Flagella Rotating in Bundles: A Study in Helical Geometry." en. In: *Proceedings of the National Academy of Sciences* 74.1 (Jan. 1977), pp. 221–225. ISSN: 0027-8424, 1091-6490. DOI: 10.1073/pnas.74.1.221.

[109] R. M. Macnab. "The Bacterial Flagellum: Reversible Rotary Propellor and Type III Export Apparatus". eng. In: *Journal of Bacteriology* 181.23 (Dec. 1999), pp. 7149–7153. ISSN: 0021-9193.

[110] Luc Maffli et al. "Ultrafast All-Polymer Electrically Tunable Silicone Lenses". en. In: *Advanced Functional Materials* 25.11 (Mar. 2015), pp. 1656–1665. ISSN: 1616301X. DOI: 10.1002/adfm.201403942.

[111] Yukio Magariyama et al. "Difference in Bacterial Motion between Forward and Backward Swimming Caused by the Wall Effect". en. In: *Biophysical Journal* 88.5 (May 2005), pp. 3648–3658. ISSN: 00063495. DOI: 10.1529/biophysj.104.054049.

[112] M. D. Manson et al. "A Protonmotive Force Drives Bacterial Flagella." en. In: *Proceedings of the National Academy of Sciences* 74.7 (July 1977), pp. 3060–3064. ISSN: 0027-8424, 1091-6490. DOI: 10.1073/pnas.74.7.3060.

[113] M. C. Marchetti et al. "Hydrodynamics of Soft Active Matter". en. In: *Reviews of Modern Physics* 85.3 (July 2013), pp. 1143–1189. ISSN: 0034-6861, 1539-0756. DOI: 10.1103/RevModPhys.85.1143.

[114] J.-B. Masson et al. "Noninvasive Inference of the Molecular Chemotactic Response Using Bacterial Trajectories". en. In: *Proceedings of the National Academy of Sciences* 109.5 (Jan. 2012), pp. 1802–1807. ISSN: 0027-8424, 1091-6490. DOI: 10.1073/pnas.1116772109.

[115] Pasquale Memmolo et al. "Recent Advances in Holographic 3D Particle Tracking". en. In: *Advances in Optics and Photonics* 7.4 (Dec. 2015), p. 713. ISSN: 1943-8206. DOI: 10.1364/AOP.7.000713.

[116] Faith A. Morrison. *An Introduction to Fluid Mechanics*. Cambridge ; New York: Cambridge University Press, 2013. ISBN: 978-1-107-00353-8.

[117] Douglas B. Murphy and Michael W. Davidson. *Fundamentals of Light Microscopy and Electronic Imaging*. 2nd ed. Hoboken, N.J: Wiley-Blackwell, 2013. ISBN: 978-0-471-69214-0.

[118] Javad Najafi et al. "Flagellar Number Governs Bacterial Spreading and Transport Efficiency". en. In: *Science Advances* 4.9 (Sept. 2018), eaar6425. ISSN: 2375-2548. DOI: 10.1126/sciadv.aar6425.

[119] Frank T. M. Nguyen and Michael D. Graham. "Impacts of Multiflagellarity on Stability and Speed of Bacterial Locomotion". en. In: *Physical Review E* 98.4 (Oct. 2018), p. 042419. ISSN: 2470-0045, 2470-0053. DOI: 10.1103/PhysRevE.98.042419.

[120] Bernt K. Øksendal. *Stochastic Differential Equations: An Introduction with Applications*. eng. Sixth edition, sixth corrected printing. Universitext. Berlin Heidelberg New York Dordrecht London: Springer, 2013. ISBN: 978-3-642-14394-6 978-3-540-04758-2.

[121] Fernando Peruani and Luis G. Morelli. "Self-Propelled Particles with Fluctuating Speed and Direction of Motion in Two Dimensions". en. In: *Physical Review Letters* 99.1 (July 2007), p. 010602. ISSN: 0031-9007, 1079-7114. DOI: 10.1103/PhysRevLett.99.010602.

[122] Oleg Pishnyak, Susumu Sato, and Oleg D. Lavrentovich. "Electrically Tunable Lens Based on a Dual-Frequency Nematic Liquid Crystal". en. In: *Applied Optics* 45.19 (July 2006), p. 4576. ISSN: 0003-6935, 1539-4522. DOI: 10.1364/AO.45.004576.

[123] Oliver Pohl et al. "Inferring the Chemotactic Strategy of P. Putida and E. Coli Using Modified Kramers-Moyal Coefficients". en. In: *PLOS Computational Biology* 13.1 (Jan. 2017). Ed. by Marcus J Tindall, e1005329. ISSN: 1553-7358. DOI: 10.1371/journal.pcbi.1005329.

[124] Marco Polin et al. "*Chlamydomonas* Swims with Two "Gears" in a Eukaryotic Version of Run-and-Tumble Locomotion". en. In: *Science* 325.5939 (July 2009), pp. 487–490. ISSN: 0036-8075, 1095-9203. DOI: 10.1126/science.1172667.

[125] John Postgate. *Microbes and Man*. en. /core/books/microbes-and-man/8E3BBACAAC9A7 Feb. 2000. DOI: 10.1017/CBO9780511612008.

[126] Noëlle Pottier. *Nonequilibrium Statistical Physics: Linear Irreversible Processes*. Oxford Graduate Texts. Oxford: Oxford University Press, 2010. ISBN: 978-0-19-955688-5.

[127] Karl Przibram. "Über die ungeordnete Bewegung niederer Tiere". de. In: *Pflüger, Archiv für die Gesammte Physiologie des Menschen und der Thiere* 153.8-10 (Aug. 1913), pp. 401–405. ISSN: 0031-6768, 1432-2013. DOI: 10.1007/BF01686480.

[128] E. M. Purcell. "Life at Low Reynolds Number". en. In: *American Journal of Physics* 45.1 (Jan. 1977), pp. 3–11. ISSN: 0002-9505, 1943-2909. DOI: 10.1119/1.10903.

[129] Zijie Qu et al. "Changes in the Flagellar Bundling Time Account for Variations in Swimming Behavior of Flagellated Bacteria in Viscous Media". en. In: *Proceedings of the National Academy of Sciences* 115.8 (Feb. 2018), pp. 1707–1712. ISSN: 0027-8424, 1091-6490. DOI: 10.1073/pnas.1714187115.

[130] Sriram Ramaswamy. "The Mechanics and Statistics of Active Matter". en. In: *Annual Review of Condensed Matter Physics* 1.1 (Aug. 2010), pp. 323–345. ISSN: 1947-5454, 1947-5462. DOI: 10.1146/annurev-conmatphys-070909-104101.

[131] M. Reichert and H. Stark. "Synchronization of Rotating Helices by Hydrodynamic Interactions". en. In: *The European Physical Journal E* 17.4 (Aug. 2005), pp. 493–500. ISSN: 1292-8941, 1292-895X. DOI: 10.1140/epje/i2004-10152-7.

[132] Ian Reid. *Estimation II*. 2001.

[133] Shang Yik Reigh, Roland G. Winkler, and Gerhard Gompper. "Synchronization and Bundling of Anchored Bacterial Flagella". en. In: *Soft Matter* 8.16 (2012), p. 4363. ISSN: 1744-683X, 1744-6848. DOI: 10.1039/c2sm07378a.

[134] B. Rodenborn et al. "Propulsion of Microorganisms by a Helical Flagellum". en. In: *Proceedings of the National Academy of Sciences* 110.5 (Jan. 2013), E338–E347. ISSN: 0027-8424, 1091-6490. DOI: 10.1073/pnas.1219831110.

[135] P. Romanczuk et al. "Active Brownian Particles: From Individual to Collective Stochastic Dynamics". en. In: *The European Physical Journal Special Topics* 202.1 (Mar. 2012), pp. 1–162. ISSN: 1951-6355, 1951-6401. DOI: 10.1140/epjst/e2012-01529-y.

[136] F. Saglimbeni et al. "Three-Axis Digital Holographic Microscopy for High Speed Volumetric Imaging". en. In: *Optics Express* 22.11 (June 2014), p. 13710. ISSN: 1094-4087. DOI: 10.1364/OE.22.013710.

[137] Fadel A. Samatey et al. "Structure of the Bacterial Flagellar Hook and Implication for the Molecular Universal Joint Mechanism". en. In: *Nature* 431.7012 (Oct. 2004), pp. 1062–1068. ISSN: 0028-0836, 1476-4687. DOI: 10.1038/nature02997.

[138] Fadel A. Samatey et al. "Structure of the Bacterial Flagellar Protofilament and Implications for a Switch for Supercoiling". en. In: *Nature* 410.6826 (Mar. 2001), pp. 331–337. ISSN: 0028-0836, 1476-4687. DOI: 10.1038/35066504.

[139] J. Saragosti et al. "Directional Persistence of Chemotactic Bacteria in a Traveling Concentration Wave". en. In: *Proceedings of the National Academy of Sciences* 108.39 (Sept. 2011), pp. 16235–16240. ISSN: 0027-8424, 1091-6490. DOI: 10.1073/pnas.1101996108.

[140] Jonathan Saragosti, Pascal Silberzan, and Axel Buguin. "Modeling E. Coli Tumbles by Rotational Diffusion. Implications for Chemotaxis". en. In: *PLoS ONE* 7.4 (Apr. 2012). Ed. by Tom Waigh, e35412. ISSN: 1932-6203. DOI: 10.1371/journal.pone.0035412.

[141] B. Scharf. "Real-Time Imaging of Fluorescent Flagellar Filaments of Rhizobium Lupini H13-3: Flagellar Rotation and pH-Induced Polymorphic Transitions". en. In: *Journal of Bacteriology* 184.21 (Nov. 2002), pp. 5979–5986. ISSN: 0021-9193. DOI: 10.1128/JB.184.21.5979-5986.2002.

[142] M. Schienbein and H. Gruler. "Langevin Equation, Fokker-Planck Equation and Cell Migration". en. In: *Bulletin of Mathematical Biology* 55.3 (May 1993), pp. 585–608. ISSN: 0092-8240, 1522-9602. DOI: 10.1007/BF02460652.

[143] Mark J. Schnitzer. "Theory of Continuum Random Walks and Application to Chemotaxis". en. In: *Physical Review E* 48.4 (Oct. 1993), pp. 2553–2568. ISSN: 1063-651X, 1095-3787. DOI: 10.1103/PhysRevE.48.2553.

[144] Robin Schubert et al. "Enhanced Quantitative Phase Imaging in Self-Interference Digital Holographic Microscopy Using an Electrically Focus Tunable Lens". en. In: *Biomedical Optics Express* 5.12 (Dec. 2014), p. 4213. ISSN: 2156-7085, 2156-7085. DOI: 10.1364/BOE.5.004213.

[145] Frank Schweitzer, Werner Ebeling, and Benno Tilch. "Complex Motion of Brownian Particles with Energy Depots". en. In: *Physical Review Letters* 80.23 (June 1998), pp. 5044–5047. ISSN: 0031-9007, 1079-7114. DOI: 10.1103/PhysRevLett.80.5044.

[146] Cynthia L. Sears. "A Dynamic Partnership: Celebrating Our Gut Flora". en. In: *Anaerobe* 11.5 (Oct. 2005), pp. 247–251. ISSN: 10759964. DOI: 10.1016/j.anaerobe.2005.05.001.

[147] David Selmeczi et al. "Cell Motility as Persistent Random Motion: Theories from Experiments". en. In: *Biophysical Journal* 89.2 (Aug. 2005), pp. 912–931. ISSN: 00063495. DOI: 10.1529/biophysj.105.061150.

[148] A. Sen. "Elasticity of Flagellar Hooks". en. In: *Journal of Electron Microscopy* 53.3 (June 2004), pp. 305–309. ISSN: 0022-0744, 1477-9986. DOI: 10.1093/jmicro/53.3.305.

[149] Mark Seville, Takeshi Ikeda, and Hirokazu Hotani. "The Effect of Sugars on the Morphology of the Bacterial Flagellum". en. In: *FEBS Letters* 332.3 (Oct. 1993), pp. 260–262. ISSN: 00145793. DOI: 10.1016/0014-5793(93)80645-B.

[150] Deepan S. H. Shah et al. "The Flagellar Filament of Rhodobacter Sphaeroides: pH-Induced Polymorphic Transitions and Analysis of the fliC Gene". en. In: *Journal of Bacteriology* 182.18 (2000), pp. 5218–5224. ISSN: 1098-5530, 0021-9193. DOI: 10.1128/JB.182.18.5218-5224.2000.

[151] T. R. Shaikh et al. "A Partial Atomic Structure for the Flagellar Hook of Salmonella Typhimurium". en. In: *Proceedings of the National Academy of Sciences* 102.4 (Jan. 2005), pp. 1023–1028. ISSN: 0027-8424, 1091-6490. DOI: 10.1073/pnas.0409020102.

[152] Samuel Shian, Roger M. Diebold, and David R. Clarke. "Tunable Lenses Using Transparent Dielectric Elastomer Actuators". en. In: *Optics Express* 21.7 (Apr. 2013), p. 8669. ISSN: 1094-4087. DOI: 10.1364/OE.21.008669.

[153] Katsuhiko Shimada, Ritsu Kamiya, and Sho Asakura. "Left-Handed to Right-Handed Helix Conversion in Salmonella Flagella". en. In: *Nature* 254.5498 (Mar. 1975), pp. 332–334. ISSN: 0028-0836, 1476-4687. DOI: 10.1038/254332a0.

[154] Michael Silverman and Melvin Simon. "Flagellar Rotation and the Mechanism of Bacterial Motility". en. In: *Nature* 249.5452 (May 1974), pp. 73–74. ISSN: 0028-0836, 1476-4687. DOI: 10.1038/249073a0.

[155] Yoshiyuki Sowa and Richard M. Berry. "Bacterial Flagellar Motor". en. In: *Quarterly Reviews of Biophysics* 41.2 (May 2008), pp. 103–132. ISSN: 0033-5835, 1469-8994. DOI: 10.1017/S0033583508004691.

[156] C Speier, R Vogel, and H Stark. "Modeling the Bacterial Flagellum by an Elastic Network of Rigid Bodies". In: *Physical Biology* 8.4 (Aug. 2011), p. 046009. ISSN: 1478-3975. DOI: 10.1088/1478-3975/8/4/046009.

[157] Srikanth V. Srigiriraju and Thomas R. Powers. "Continuum Model for Polymorphism of Bacterial Flagella". en. In: *Physical Review Letters* 94.24 (June 2005), p. 248101. ISSN: 0031-9007, 1079-7114. DOI: 10.1103/PhysRevLett.94.248101.

[158] Srikanth V. Srigiriraju and Thomas R. Powers. "Model for Polymorphic Transitions in Bacterial Flagella". en. In: *Physical Review E* 73.1 (Jan. 2006), p. 011902. ISSN: 1539-3755, 1550-2376. DOI: 10.1103/PhysRevE.73.011902.

[159] S. Suzuki and K. Abe. "Topological Structural Analysis of Digitized Binary Images by Border Following". In: *Computer Vision, Graphics, and Image Processing* 30.1 (Apr. 1985), pp. 32–46.

[160] Johannes Taktikos. *Modeling the Random Walk and Chemotaxis of Bacteria: Aspects of Biofilm Formation*. 2013.

[161] Yuankai K. Tao, Sunil K. Srivastava, and Justis P. Ehlers. "Microscope-Integrated Intraoperative OCT with Electrically Tunable Focus and Heads-up Display for Imaging of Ophthalmic Surgical Maneuvers". en. In: *Biomedical Optics Express* 5.6 (June 2014), p. 1877. ISSN: 2156-7085, 2156-7085. DOI: 10.1364/BOE.5.001877.

[162] K.M. Taute et al. "High-Throughput 3D Tracking of Bacteria on a Standard Phase Contrast Microscope". en. In: *Nature Communications* 6.1 (Dec. 2015), p. 8776. ISSN: 2041-1723. DOI: 10.1038/ncomms9776.

[163] MATTHIAS THEVES. *Bacterial Motility and Growth in Openand Confined Environments*. Mar. 2014.

[164] Matthias Theves et al. "A Bacterial Swimmer with Two Alternating Speeds of Propagation". en. In: *Biophysical Journal* 105.8 (Oct. 2013), pp. 1915–1924. ISSN: 00063495. DOI: 10.1016/j.bpj.2013.08.047.

[165] Shlomo Trachtenberg et al. "Pairwise Perturbation of Flagellin Subunits". en. In: *Journal of Molecular Biology* 190.4 (Aug. 1986), pp. 569–576. ISSN: 00222836. DOI: 10.1016/0022-2836(86)90242-1.

[166] L. Turner, W. S. Ryu, and H. C. Berg. "Real-Time Imaging of Fluorescent Flagellar Filaments". en. In: *Journal of Bacteriology* 182.10 (May 2000), pp. 2793–2801. ISSN: 0021-9193. DOI: 10.1128/JB.182.10.2793-2801.2000.

[167] Linda Turner et al. "Visualizing Flagella While Tracking Bacteria". en. In: *Biophysical Journal* 111.3 (Aug. 2016), pp. 630–639. ISSN: 00063495. DOI: 10.1016/j.bpj.2016.05.053.

[168] Siebe B van Albada, Sorin Tănase-Nicola, and Pieter Rein ten Wolde. "The Switching Dynamics of the Bacterial Flagellar Motor". en. In: *Molecular Systems Biology* 5.1 (Jan. 2009), p. 316. ISSN: 1744-4292, 1744-4292. DOI: 10.1038/msb.2009.74.

[169] Gandhimohan M. Viswanathan, ed. *The Physics of Foraging: An Introduction to Random Searches and Biological Encounters*. Cambridge ; New York: Cambridge University Press, 2011. ISBN: 978-1-107-00679-9.

[170] R. Vogel and H. Stark. "Force-Extension Curves of Bacterial Flagella". en. In: *The European Physical Journal E* 33.3 (Nov. 2010), pp. 259–271. ISSN: 1292-8941, 1292-895X. DOI: 10.1140/epje/i2010-10664-5.

[171] Reinhard Vogel and Holger Stark. "Rotation-Induced Polymorphic Transitions in Bacterial Flagella". en. In: *Physical Review Letters* 110.15 (Apr. 2013), p. 158104. ISSN: 0031-9007, 1079-7114. DOI: 10.1103/PhysRevLett.110.158104.

[172] H. Wada and R. R. Netz. "Discrete Elastic Model for Stretching-Induced Flagellar Polymorphs". In: *EPL (Europhysics Letters)* 82.2 (Apr. 2008), p. 28001. ISSN: 0295-5075, 1286-4854. DOI: 10.1209/0295-5075/82/28001.

[173] H Wada and R. R Netz. "Stretching Helical Nano-Springs at Finite Temperature". In: *Europhysics Letters (EPL)* 77.6 (Mar. 2007), p. 68001. ISSN: 0295-5075, 1286-4854. DOI: 10.1209/0295-5075/77/68001.

[174] Hirofumi Wada and Roland R. Netz. "Model for Self-Propulsive Helical Filaments: Kink-Pair Propagation". en. In: *Physical Review Letters* 99.10 (Sept. 2007), p. 108102. ISSN: 0031-9007, 1079-7114. DOI: 10.1103/PhysRevLett.99.108102.

[175] George H. Wadhams and Judith P. Armitage. "Making Sense of It All: Bacterial Chemotaxis". en. In: *Nature Reviews Molecular Cell Biology* 5.12 (Dec. 2004), pp. 1024–1037. ISSN: 1471-0072, 1471-0080. DOI: 10.1038/nrm1524.

[176] Michael J. Waites, ed. *Industrial Microbiology*. Osney Mead, Oxford ; Malden, MA: Blackwell Science, 2001. ISBN: 978-0-632-05307-0.

[177] W. B. Whitman, D. C. Coleman, and W. J. Wiebe. "Prokaryotes: The Unseen Majority". en. In: *Proceedings of the National Academy of Sciences* 95.12 (June 1998), pp. 6578–6583. ISSN: 0027-8424, 1091-6490. DOI: 10.1073/pnas.95.12.6578.

[178] Norbert Wiener. *Time Series*. 5. print. MIT 9. Cambridge/Mass: MIT Pr, 1977. ISBN: 978-0-262-73005-1.

[179] M. Wu et al. "Collective Bacterial Dynamics Revealed Using a Three-Dimensional Population-Scale Defocused Particle Tracking Technique". en. In: *Applied and Environmental Microbiology* 72.7 (July 2006), pp. 4987–4994. ISSN: 0099-2240. DOI: 10.1128/AEM.00158-06.

[180] L. Xie et al. "Bacterial Flagellum as a Propeller and as a Rudder for Efficient Chemotaxis". In: 6 (Feb. 2011), pp. 2246–2251.

[181] Ichiro Yamashita et al. "Structure and Switching of Bacterial Flagellar Filaments Studied by X-Rayfiber Diffraction". In: *Nature Structural Biology* 5.7 (July 1998), pp. 612–612. ISSN: 1072-8368. DOI: 10.1038/872.

[182] Koji Yonekura, Saori Maki-Yonekura, and Keiichi Namba. "Complete Atomic Model of the Bacterial Flagellar Filament by Electron Cryomicroscopy". en. In: *Nature* 424.6949 (Aug. 2003), pp. 643–650. ISSN: 0028-0836, 1476-4687. DOI: 10.1038/nature01830.

[183] Yongchao Zou et al. "Miniature Adjustable-Focus Endoscope with a Solid Electrically Tunable Lens". en. In: *Optics Express* 23.16 (Aug. 2015), p. 20582. ISSN: 1094-4087. DOI: 10.1364/OE.23.020582.